NOVEL PERFORMANCE ANALYSIS TECHNIQUES WITH APPLICATION TO THE SCALING PROPERTIES OF SILICON MICROMOTOR STRUCTURES

by

D. Kyle MacKay, B.Eng.

A Thesis

Submitted to the School of Graduate Studies

in Partial Fulfilment of the Requirements

for the Degree

Doctor of Philosophy

McMaster University

September 2000

NOVEL PERFORMANCE ANALYSIS TECHNIQUES WITH APPLICATION TO THE SCALING PROPERTIES OF SILICON MICROMOTOR STRUCTURES

DOCTOR OF PHILOSOPHY (2000)
(Electrical Engineering)

McMaster University
Hamilton, Ontario

TITLE: NOVEL PERFORMANCE ANALYSIS TECHNIQUES WITH APPLICATION TO THE SCALING PROPERTIES OF SILICON MICROMOTOR STRUCTURES

AUTHOR: D. Kyle MacKay, B. Eng. (McMaster University)

SUPERVISOR: Dr. Raymond Findlay, Department of Electrical and Computer Engineering

NUMBER OF PAGES: xx, 267

ABSTRACT

An output coefficient extracted from motor design sizing calculations is cast into a form whereby it can be implemented as an actuation independent measure of performance. The way in which this measure scales for both electrically actuated motors and magnetically actuated motors is investigated. An engineering process for judging the advantages and disadvantages of each actuation scheme as it applies to particular motor designs is discussed.

The performance capabilities of an electrically actuated variable capacitance motor are compared to those of a magnetically actuated alternative using the output coefficient as a comparative measure. A transition point is estimated which represents the scale at which the benefits of electrical actuation over magnetic actuation put electrically actuated devices in the realm of practical consideration.

The two axis or **dq0** method of analysing conventional magnetically actuated machines is extended and applied to the topology of an electrically actuated variable capacitance silicon micromotor. A "conventional" finite element technique is used to obtain estimates for the direct axis and quadrature axis synchronous capacitive susceptances. The energy based formulation employed eliminates the need to extract self and mutual phase capacitances and produces the desired axis capacitances directly. This novel method brings attention to higher order harmonics in the direct axis and quadrature axis charge waveforms. A physical explanation based on positive, negative and zero sequence phase charge is derived accounting for the observed rotor position-dependent characteristics.

A dual bounds approach is applied to a typical two-dimensional micromotor structure.

The direct axis capacitance is computed for the conditions of maximum stator pole-rotor pole overlap with the excitation EMF placed in two "extreme" conditions. The first condition is placement along the rotor's direct axis and the second condition is placement along the rotor's quadrature axis.

Quadrilaterals are used to discretize a ninety degree (electrical) section of a silicon micromotor structure with a stator pole to rotor pole ratio of three to two. Two separate discretizations are considered , one for each of the stator EMF conditions previously noted. A method in which the same quadrilateral discretization can be used for both the upper and lower capacitance bound is presented.

The notion of a stationary solution for the method of dual bounds is shown to exist. A simple two dimensional example is given in order to illustrate how the linear equations are derived and to bring to out the ability to control the coupling of the resultant linear equations. Substantial computational savings, especially in the three-dimensional case can be realized (when compared to the finite element method) and warrant future examination and application in both electrically actuated and magnetically actuated problems.

The encouraging two-dimensional results lead to a full three dimensional extension of the theory, in particular, the development of novel geometrical constructs necessary for dual bound analysis. Formal methods for determining the placement of equipotential slices and flux tube walls inside fundamental cuboid structures are presented. Actual numerical results are presented for two simple three dimensional constructs. A discretization process is given that shows how a complete three-dimensional silicon micromotor model can be discretized using the geometrical primitives derived in this thesis.

ACKNOWLEDGMENTS

I would like first and foremost to acknowledge my supervisor, Dr. Raymond Findlay for his guidance, patience and understanding throughout the course of this research. I would also like to acknowledge the members of my supervisory committee, Drs. Alden, Szabados and Dableh for their help in defining the final stages of this work.

Many thanks go to Dr. Ronnie Belmans at the Katholieke Universiteit Leuven in Belgium for suggesting the subject of this research and for getting me started on the Finite Element software package MagNet.

I gratefully acknowledge the assistance provided by the following staff members of McMaster University and the Power Research Laboratory; Steve Spencer, Adam Marianski, Bruce Chariot and Fran Hustak.

To all of my colleagues at the PRL and CRL; you, above all, have made my time spent here at McMaster most enjoyable and rewarding.

To Mom, Kristen and Fred, thank you for your encouragement, it means a lot to me.

I would like to extend my sincere appreciation to the Natural Sciences and Engineering Council of Canada as well as to the Department of Electrical and Computer Engineering at McMaster University for providing financial support.

CHERYL . . . a very special thank you to the one who provided me with the motivation and the reason for completing this work. THANK YOU FOR WAITING !

Dedicated to my daughter **KASSIDY**.

TABLE OF CONTENTS

LIST OF FIGURES

LIST OF PRINCIPAL SYMBOLS

Symbol	Description	Units
$\mathbf{A}$	Magnetic vector potential	Wb/m
$\mathbf{A}_{cu}$	Area of copper	m^2
$\mathbf{A}_{plate}$	Area of capacitor plate	m^2
$\mathbf{A}_{pole}$	Area of magnetic pole	m^2
$\|\mathbf{B}\|$	Magnitude of magnetic flux density vector	T
$\mathbf{B}_m$	Magnetic flux density (in a permanent magnet)	T
$\mathbf{C}$	Capacitance	F
$\mathbf{C}_d$	Direct axis synchronous capacitance	F/m
$\mathbf{C}_q$	Quadrature axis synchronous capacitance	F/m
$\|\mathbf{D}\|$	Magnitude of electric flux density vector	C/m^2
$\|\mathbf{E}\|$	Magnitude of electric field vector	V/m
$\mathbf{E}_f$	Rotor "speed" voltage	V/m
$\mathbf{f}$	Instantaneous force	N
$\|\mathbf{H}\|$	Magnitude of magnetic field strength	A/m
$\mathbf{H}_m$	Magnetic field strength (in a permanent magnet)	A/m
$\mathbf{i}$	Instantaneous current	A
$\mathbf{I}_{ad}$	Direct axis component of phase current	A
$\mathbf{I}_{aq}$	Quadrature axis component of phase current	A
$\mathbf{I}_\phi$	RMS phase current	A
$\mathbf{J}$	Current density	A/m^2
ℓ_m	Length of a permanent magnet	m
$\mathbf{L}$	Inductance	H
$\mathbf{L}_d$	Direct axis synchronous inductance	H/m
$\mathbf{L}_q$	Quadrature axis synchronous inductance	H/m
$\mathbf{M}$	Mutual inductance	H

LIST OF PRINCIPAL SYMBOLS CONTINUED

Symbol	Description	Units
N_p	Number of poles	dimensionless
p	Instantaneous power	W or W/m
P	Average power	W or W/m
q	Instantaneous charge	C
Q_{cd}	Direct axis component of phase charge	C/m
Q_{cq}	Quadrature axis component of phase charge	C/m
R_{eff}	Effective resistance	ohm
s	Scaling parameter	dimensionless
t	Time	s
v	Instantaneous voltage	V
V_{ad}	Direct axis component of phase voltage	V or V/m
V_{aq}	Quadrature axis component of phase voltage	V or V/m
V_ϕ	RMS phase voltage	V/m
W_e	Electric Energy	J or J/m
W'_e	Electric Co-energy	J or J/m
W_m	Magnetic Energy	J or J/m
W'_m	Magnetic Co-energy	J or J/m
x	Displacement	m
X_{sd}	Direct axis synchronous inductive reactance	ohm/m
β_{cd}	Direct axis synchronous capacitive susceptance	S/m
β_{cq}	Quadrature axis synchronous capacitive susceptance	S/m
δ	Power angle	rad
θ	Angular displacement	rad
λ	Flux Linkages	Wb
λ_{ad}	Direct axis component of phase flux linkages	Wb/m

LIST OF PRINCIPAL SYMBOLS CONTINUED

Symbol	Description	Units
λ_{aq}	Quadrature axis component of phase flux linkages	Wb/m
ξ_0	Output coefficient	J/m^4
ρ	Electrical resistivity	ohm·m
τ	Instantaneous torque	Nm
φ	Magnetic flux	Wb
ω_r	Angular velocity of rotor (mechanical)	rad/s
ω_s	Angular velocity of electrical supply	rad/s

LIST OF TABLES

CHAPTER 1

INTRODUCTION

1.1 BACKGROUND AND MOTIVATION

Motors, solenoids and other magnetically actuated devices are some of the most important elements that make up electromechanical energy conversion systems. Magnetic fields capable of exerting useful forces on current carrying conductors and magnetically permeable structures are relatively easy to generate. As a result, magnetic actuators have enjoyed an enormous amount of success to date. Evidence to support this notion surrounds us in many aspects of everyday life. Without exception, the actuating mechanism behind any electric power tool or common household appliance is a magnetically actuated device, most likely a rotational "electric" motor of one sort or another. Quotation marks are placed around the word electric to indicate the fact that even though it is customary to refer to conventional machines as electrical machines, they are in reality magnetically actuated.

In spite of their longer history [1,76], actuators utilizing the electric field as the coupling field have not met with much success at all. Because of their size, most systems constructed to date can be classified as macro domain systems [2]. At this scale, electric field strengths of the order of millions of volts per centimetre are required before electric actuation becomes competitive with magnetic actuation. Since the maximum electric field strength (at

atmospheric pressure) that can be tolerated across the air-gap of a macroscopic actuator is only about 30,000 volts per centimetre [3], it is not at all surprising that magnetic actuators have so far been the actuators of choice. At smaller scales, however, electric actuation is favoured over magnetic actuation. The threshold level of electrical breakdown as well as the strength of electrostatic forces relative to other forces (inertial, magnetic etc.) increases as system dimensions shift into the micro domain [2].

Recent developments in the field of silicon micromechanics have made the construction of extremely small electric machines possible. These machines, which are built using processes similar to those used in the manufacture of integrated circuits, possess unconstrained elements that are free to rotate or slide over the surface of a substrate [4]. Tiny motors have been fashioned on silicon wafers using these newly developed micro machining techniques, but such devices have not reached a large scale commercial stage of development yet. Methods of extracting mechanical power and information regarding friction and wear characteristics are still under investigation [5,6]. Nevertheless, the prospect that micro mechanical systems may one day be feasible offers new opportunities for research and for the development of novel applications in a domain that has yet to be explored.

1.2 A GENERAL OVERVIEW OF THE PROBLEMS

Motor Performance ... How is it Measured ?

There are a number of defined quantities such as average power, average torque, etc. that are familiar measures of the performance of a rotating machine. What is important to note about these measures is that they characterize an individual machine and express a single

machine's performance capabilities without reference to others'. Although useful as ratings by setting maximum recommended safe operating levels, they do not provide a meaningful method on which to base comparisons. With some manipulation however, such indices can be used as a means of evaluating the benefits of one machine relative to those of another.

In addition to output capability and physical size, a motor's efficiency is also a concern. Although the losses of a micromotor (be it electrically or magnetically actuated) might not be appreciable on absolute terms, the losses of one machine relative to those of another is still an important factor to consider in the process of selecting a motor. This is especially true in cases where the nature of the application places limits or restrictions on the kind of power supply used. Some applications demand local or mobile power supplies like batteries. If, for example, a device is to be implanted inside the human body, then maximizing the battery's lifetime is obviously of paramount importance. By comparing the current density requirements of electrically and magnetically actuated motors at various size scales, the question of relative efficiency can be addressed.

A method, or more specifically an index, which takes into account both output capability and overall physical size must be employed if electrically and magnetically actuated motors are to be matched against one another at different size scales.

Scaling Properties ... How Does this Measure Scale ?

Because of the duality which exists between electrically actuated machines and their magnetic counterparts, a comparative study assessing the merits of electrical actuation in the micro domain seems fitting. While such an assessment is appropriate for actuating

mechanisms in general, this thesis focuses on rotational motors since they are the most frequently encountered type of actuator. The problem here is to establish a scale at which we can expect the benefits of electric actuation to be realized using practical motor designs belonging to both actuation schemes.

Derive a General Framework for Analysis

It is equally important that before any comparisons be made, the techniques needed for analysing variable capacitance (VC) machines and for obtaining the necessary performance measures using presently available numerical tools be devised. Since magnetically actuated motors have been in practical use for such an extended period of time, the procedures required to analyse them are well established. Therefore, developing techniques that involve concepts already familiar to the designers of conventional rotating machines is essential.

The concepts familiar to the designers of conventional magnetically actuated machines are applied routinely in practice to two-dimensional models. The primary reason for this is that the axial length or stack length of such machines is usually larger than the stator's outer diameter. Except at the two end-regions, the distribution of the magnetic field within any plane which is perpendicular to the axis of the rotor remains essentially unchanged along the length of the shaft. Therefore, the edge-effects are secondary influences and not the primary phenomena determining the output capability of a conventional magnetically actuated motor.

Because of the integrated circuit fabrication techniques employed to construct electrically actuated micromotors, the outer diameter of the stator is necessarily and significantly greater than the axial length of the device. The electric field distribution which

determines the output capability of the machine is dominated by the edge-effects. Applying any analysis strategy to a two-dimensional model under such circumstances may produce highly inaccurate estimates for the performance of the real device.

To reiterate, the framework or foundation of the theoretical analysis must implement concepts familiar to machine designers. Although in the past most techniques have been applied exclusively to two-dimensional structures in practise, the newly developed methods must be general because of the nature of the silicon micromotor. That is, they must not be specific to two or three dimensional problems alone, but must be adaptable to both. This constraint leads us into a lumped parameter based framework since it is equally applicable to both two dimensional problems and three dimensional problems.

Derive a Finite Element Based Solution

The finite element technique has become arguably the most popular numerical method for solving distributed problems like electromagnetic field problems in both two and three dimensions. What must be developed is a numerical method in which we can calculate any necessary parameters required by the performance index we adopt. A numerical solution is needed since it is unlikely that closed form solutions for the complex geometric structures used in this work can readily be found.

Formulate a Computationally Less Expensive Three Dimensional Solution

Based on current research, it appears that a radial-gap configuration has emerged as the most promising design for variable capacitance silicon micromotors [7-13]. In a radial-gap configuration the lines of electric flux cross the air-gap separating overlapping surfaces of the rotating and stationary members essentially in the plane of the rotor (figure 1.1). This is in contrast to an axial-gap configuration in which the lines of electric flux are, for the most part, directed parallel to the axis of the rotating member (figure 1.2). Under certain circumstances, because of the small axial-length to air-gap width ratio common to most radial-gap machines, it may be necessary to model the three dimensional electric field. The primary reason for this is that a significant fraction of the total energy stored by the electric field may be contained in the out-of-rotor-plane fringing field (figure 1.3) as opposed to the

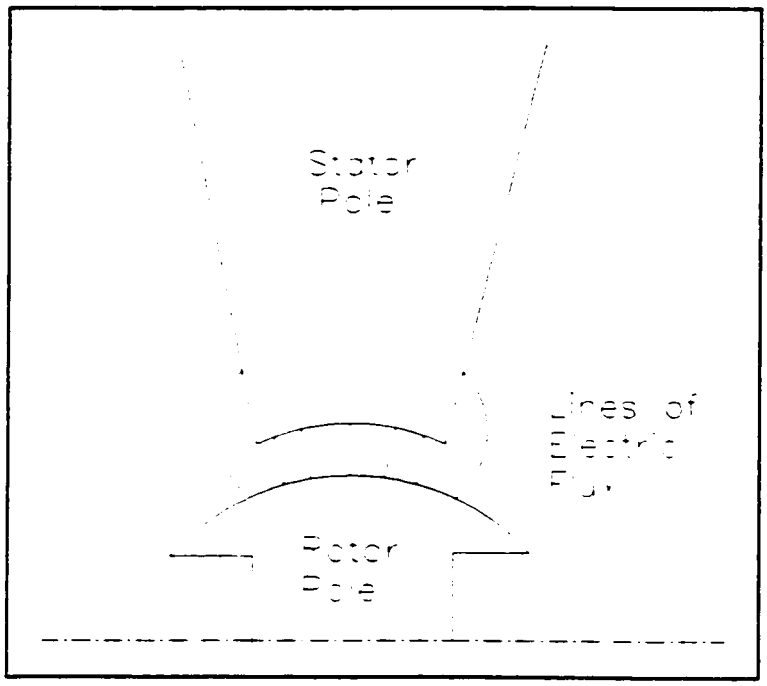

Figure 1.1: A radial-gap configuration.

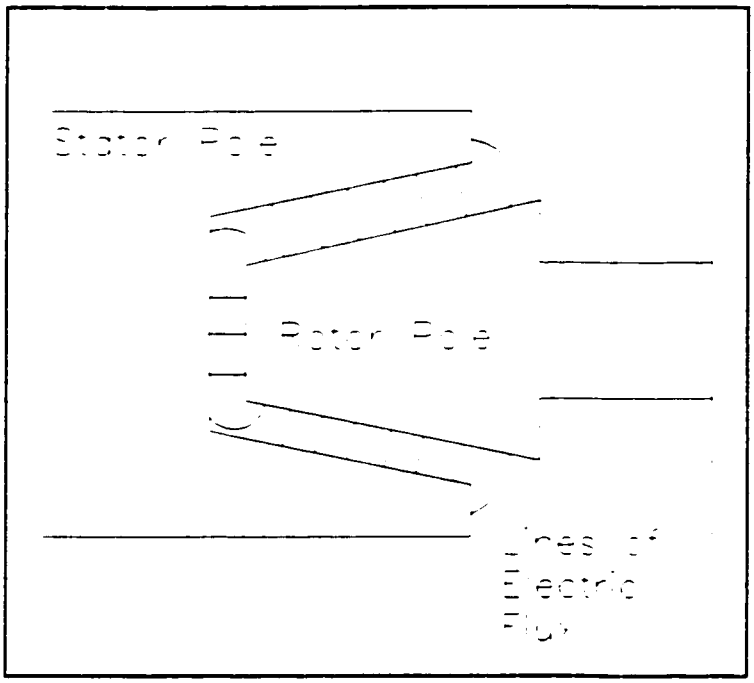

Figure 1.2: An axial-gap configuration.

air-gap field. If this is the case, then ignoring such edge effects could result in largely inaccurate values for the leakage capacitance and generated torque estimates.

Figure 1.3 is an axial plane view depicting a "cut" through one rotor pole and one stator electrode of a radial-gap VC motor at the point of maximum overlap between the two surfaces. A number of scalar equipotential lines are illustrated on this diagram. Lines of electric flux leave and terminate normally on conducting surfaces, and in between, the flux lines cross the equipotential lines orthogonally. The strength of the electric field at any point depends upon the spacing between adjacent equipotential lines. Stronger electric fields are found in regions of closely spaced equipotential lines. As an example, note how the equipotential lines in the rotor/stator air-gap region are crowded together, indicating a region

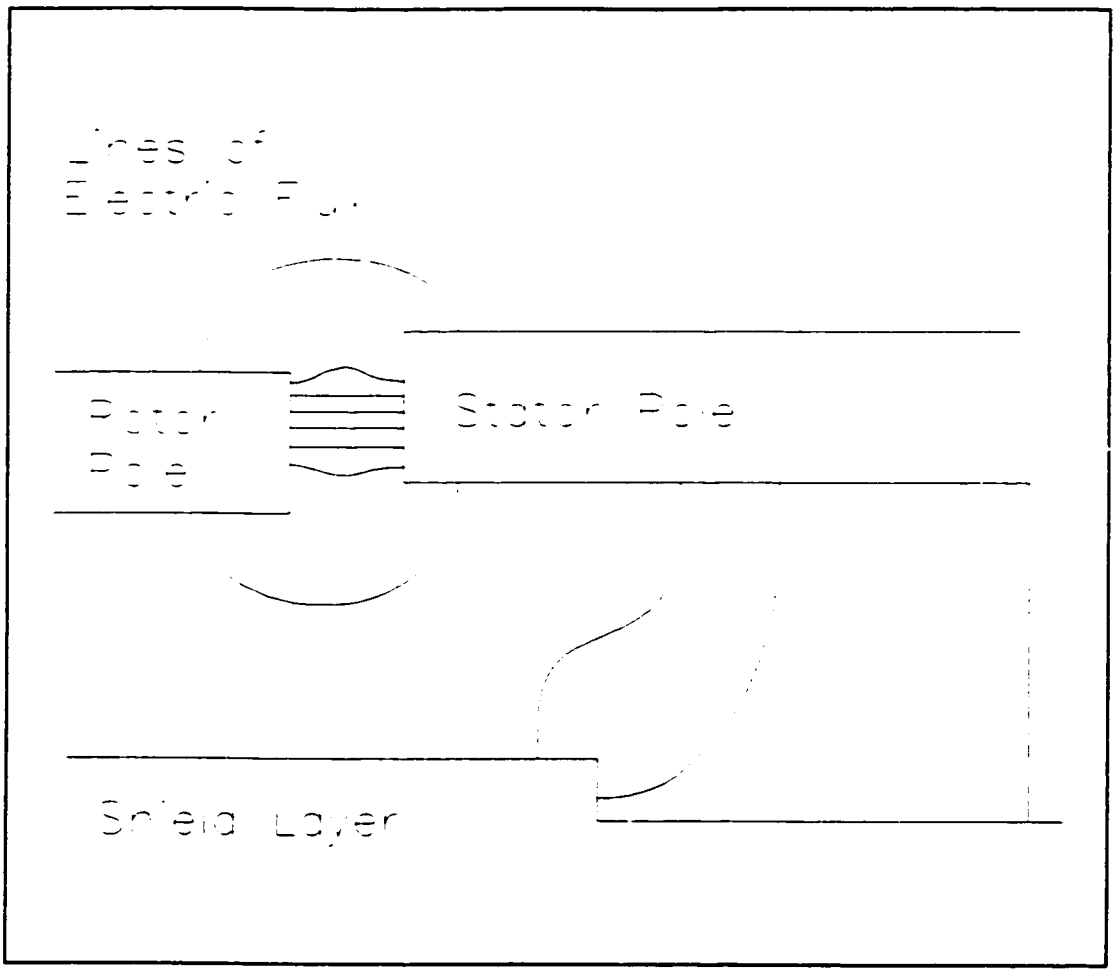

Figure 1.3: Electric flux lines demonstrating out-of-rotor-plane effects.

of higher electric field intensity.

The out-of-rotor-plane fields of interest originate on the upper and lower surfaces of the stator electrode and terminate on the rotor-pole and shield respectively. More intense out-of-rotor-plane electric fields are expected on the underside of the stator where the stator/shield clearance may be as small as the stator/rotor air-gap width. Constant amounts of energy stored in the out-of-rotor-plane regions will contribute to the leakage capacitance.

Variations in the amount of stored electrical energy that take place as the rotor's

position is altered will affect the generated torque. Taking the three dimensional aspects of the problem into consideration in a practical manner and assessing the margin of error is the final task to be examined. The "traditional' approach to solving such three dimensional problems is to construct a single three-dimensional finite element mesh and use the amount of stored electrical energy in the problem domain to calculate the required capacitance values. The desired mechanical output power or torque can be computed subsequently. Alternatively, two finite element meshes can be generated corresponding to two slightly different rotor positions. A solution for each mesh is obtained and the change in stored energy with respect to position used to calculate torque.

As mentioned earlier in section §1.2, the amount of computational effort involved in a detailed three-dimensional finite element solution is likely to be enormous. Presently, it is quite common to find two-dimensional meshes with tens of thousands of degrees of freedom (nodes). Extrapolating and carrying this level of detail into a three-dimensional model will involve hundreds of thousands of nodes. It is possible to reduce the computational burden involved in a three-dimensional finite element solution by reducing the level of discretization. This reduction however is achieved at the expense of solution accuracy. It is necessary therefore, to gain some sense or feeling about the accuracy and reliability of the computed results. Experimental verification is of course the best way to test a model. However, with silicon micromotor structures, we are dealing on a scale at which the necessary test instruments do not exist. Furthermore, a means of fabricating a test machine is not readily available to us. An alternative mechanism for checking the sensibility of the computed results is essential.

Even with the computing power available with modern workstations, the accurate prediction of three-dimensional electromagnetic field distributions remains a formidable task. In fact some detailed two-dimensional field simulations will push the capabilities of powerful workstations to their limits and tie-up the processor for days. Solving three-dimensional electromagnetic field problems within a practical time frame involves reducing the detail or the amount of discretization used in the three dimensional model. This tradeoff may result in poor approximate solutions to the three dimensional model, yielding results that are of as little value as a two-dimensional model which completely ignores the three-dimensional nature of the problem in the first place. The last problem addressed in this work is one of investigating the possibility of reducing the computational burden associated with simulating three-dimensional electric field distributions surrounding variable capacitance silicon micromotor structures.

Five main problems have been identified and mentioned thus far. The remainder of §1.2 summarizes the aforementioned problems and serves to clarify the scope of the work.

1.2.1 Performance Measures

As mentioned earlier in this chapter, the "traditional' measures of performance such as power, torque, efficiency etc. do not explicitly contain any information regarding scale. What we seek is a measure that includes scale information so that we can investigate the behaviour of this measure as machine dimensions change. The motivation behind this is a specific comparison between an electrically actuated device and an equivalent magnetically actuated counterpart.

1.2.2 Scaling Analysis - Locating a Transition "Point"

A typical problem that an engineer faces in practice today is that of choosing a motor for a particular application. At the moment, this problem, which is not simple by any standard, is restricted to making a choice from a collection of magnetically actuated motor designs. However, because of the advancements in silicon micro machining technology that are being made by researchers in that field, practising engineers may someday have an additional option to ponder. Choosing the best actuation scheme (ie. electric or magnetic) is a factor that is not presently considered by engineers, but whose relevance will become increasingly important as developments in electric micromotor technology occur. Therefore, specific guidelines need to be set down that will assist in choosing an actuation scheme.

An engineering process for selecting an actuation scheme (ie. electric or magnetic) needs to be developed The process must addresses the criteria needed to establish whether a particular electrically actuated motor would be favoured over a particular conventional magnetically actuated motor.

1.2.3 Analysis Strategy

Another objective is to demonstrate how one of the classical concepts of rotating machine theory (namely the two axis or **dq0** method) applies to electrically actuated VC motors. The **dq0** transformation enables excitation schemes involving no more than three independent stator electrode voltages at any instant in time to be represented. Although the technique is ideally suited for balanced three phase sinusoidal excitation, it can be used in the general case since any vector containing three instantaneous phase quantities can be mapped

into **dq0** variables using an appropriate transformation.

In previous works describing variable capacitance silicon micromotor performance, other authors [7,10,17] have made use of the virtual work concept to express the mechanical output capability of these machines. Mechanical force or torque estimates can be readily obtained through finite element analysis using the virtual work technique but the results are specific to the stator electrode voltages used to excite the motor for that simulation. Furthermore, some interesting characteristics about variable capacitance machines such as the harmonic content of the electrode charge/current are not immediately available or apparent after virtual work analysis. The two axis approach adopted in this work highlights some of these characteristics.

1.2.4 Determination of Lumped Parameters

After extending and applying the **dq0** formulation to variable capacitance machines, the problem of computing the lumped parameter quantities defined in the two axis framework remains. The solution to this problem must employ procedures that are compatible with current state-of-the-art computer-aided-engineering (CAE) finite element (FE) software. Furthermore, the techniques have to ensure practicability in terms of the amount of computational labour involved and stay within the limitations of the available software.

1.2.5 Three Dimensional Field Simulation

A two-dimensional field simulation strategy based on two bounded solutions is presented by Hammond in references [63-66]. In this method, the value of a lumped

parameter electrical circuit element (ie. resistance, inductance, capacitance) is estimated using two approximations for the distributed field within the problem domain. One of the estimates is an upper bound and the other estimate a lower bound for the true solution. The final estimate for the value of the circuit parameter is the average of the two solutions. A three dimensional extension of the procedure is only proposed and no development is undertaken.

In this thesis, a complete and thorough specification of the constraints that a three-dimensional extension of the method must adhere to for its application to silicon micromotor structures is presented. A derivation of the fundamental elements of construction and proof of the existence of the three dimensional equipotential slices and flux tubes is sought.

1.3 SIGNIFICANCE

Several authors have outlined the advantages of electric actuation at small scales [2,3,7,14,15]. However, these investigations only consider the scaling properties of very simple structures. Until recently [16, 17], devices more akin to real machines have not been examined in a comparative framework.

Quantitative studies have been conducted on a number of micromotor designs [7,11, 69] but just how well these devices measure up against possible magnetic alternatives is not entirely clear. Such appraisals will be significant if advances in micro machining technology are successful in reducing the size of mechanical systems to the point where electrically actuated devices become viable [68]. By comparing figures of merit, one can establish whether an electrically actuated machine would render any benefits over a particular magnetic machine in terms of size or mass reduction.

The state space representation of a dynamical system consists of a set of ordinary differential equations in which lumped parameter values appear as coefficients. Because system control and stability studies entail solving these equations [18-21], it is essential that methods for calculating the required lumped parameter values be available. Furthermore, the procedures used by the author in this work can be applied to VC micromotors whose designs differ from that of the example machine.

An economical solution to three-dimensional electric field problems has widespread use in other areas of machine design. The concepts can be applied to complicated magnetic field problems and perhaps to coupled electromagnetic field problems as well. For example, the problem of calculating the leakage reactance of stator end-windings or of rotor end-rings in alternating current induction motors is an application that can benefit from more efficient solutions to three-dimensional magnetic field distributions. Dynamic applications in which the impedance of a three dimensional structure is required is another potential application [16, 21, 49].

The non ideal effects of the fringing fields in the inherently low profile radial-gap variable capacitance silicon micromotor structures can be accounted for with a viable three dimensional solution methodology. Curves such as those presented in chapter five (for direct axis and quadrature axis phase charge versus rotor angular position) are practical to generate at the design phase since the time frame for their production is significantly reduced.

A means of assessing the accuracy of the computed results is made available by implementing the method of tubes and slices. Each topology generates a bound on the desired true capacitance. The average value can then be used with a known window of

uncertainty in the result.

1.4 CONTRIBUTIONS

1) A novel application of a sizing equation is presented. In this application, an output coefficient is extracted from the formulation and used as a performance measure for both electrically actuated machines as well as magnetically actuated machines. We show how this index can be a employed as a practical tool for scaling analysis and demonstrate that this index allows a direct comparison between machines with different actuation schemes.

2) With an index relating motor performance and physical size now at our disposal, some decisions can be made regarding the best method of actuation for a particular size scale. An engineering process that utilizes the performance index referred to above is developed for comparing motors of differing actuation schemes. This procedure outlines a series of steps, enabling a decision to be made about the best type of actuation (ie. electric or magnetic) for a particular size scale. A cross-over point/scale is established for which electrically actuated motors would provide advantageous when compared to magnetically actuated alternatives.

3) The two-axis method (or **dq0** method) was initially developed for, and has since been used in the analysis of conventional (magnetically actuated) rotating machines. In this thesis, it is shown how to apply the two-axis method to electrically actuated rotating machines using the case of a three phase VC motor as an example. Power/torque equations for a variable capacitance silicon micromotor are derived in the synchronous frame. The primary advantage of this method lies in the fact that the parameters used in the formulation are lumped parameter values. Therefore, the concepts hold whether the geometry is two dimensional or

three dimensional in nature.

4) Distributed models capable of simulating internal field conditions are an elegant means of evaluating lumped parameter values for equivalent circuits. MagNet 2D, a commercial finite element package commonly used in the analysis and design of electromagnetic devices, is used to calculate the direct axis and quadrature axis synchronous capacitive susceptances present in the two axis model of a three phase variable capacitance motor. The method derived in this thesis is capable of predicting harmonics in the phase quantities that are a result of air-gap space harmonics. Conventionally, these harmonics are calculated by numerically differentiating the air-gap potential distribution to obtain the field in the air-gap and then performing a harmonic analysis of the resultant field.

Because of the numerical differentiation, some level of accuracy is lost and some quantization is introduced. Using the energy based two axis methods derived in this work, no differentiation of the potential field is necessary in order to obtain the same information.

5) A two-dimensional dual bounds analysis is performed using the concepts of equipotential slices and flux tubes on an actual variable capacitance silicon micromotor structure. To date, no other researches in the field have attempted a dually bounded solution when addressing the problem of estimating the equivalent circuit parameter values of VC micromotors. Successful quadrilateral discretization of a ninety (electrical) degree section of a variable capacitance motor is realized for two extreme cases of stator EMF alignment relative to the rotor's direct axis. Capacitance estimates are obtained for each configuration.

From the two-dimensional dually bounded results it is determined that careful placement of the equipotential slices and flux tubes is sufficient for accurate capacitance

estimates. It is shown that an optimization process can be carried out as well if so desired using this method.

6) Novel geometrical constructs are devised for the application of the method of tubes and slices to three-dimensional structures. A complete derivation of the placement of equipotential slices in the three dimensional slice discretization, and the placement of flux tube walls in the three dimensional tube discretization is presented. The derivations presented in this thesis guarantee continuity of internal slice/tube surfaces, and the ability to be cascaded. The latter is essential for discretization of complex three dimensional structures.

1.5 OUTLINE OF THESIS

Chapter 2

Chapter two lists a number of advantages and applications of small mechanical systems. Basic energy conversion principles needed to derive expressions for various performance measures are reviewed. These expressions are applied to simple energy conversion devices in order to demonstrate the factors motivating the study and comparison of more realistic machines.

Chapter 3

Micro mechanical device fabrication processes are examined in brief. Previous research conducted in the area of radial-gap silicon micromotors is reviewed. After stating some design considerations the topology of the radial-gap VC micromotor under consideration in thesis is presented. Analytical methods for evaluating average power and

torque for three phase VC motors are derived and the concept of a two axis approach for studying the example silicon micromotor is introduced.

Chapter 4

Partial differential equations governing the behaviour of the scalar potential fields of electrostatic and magnetostatic systems are stated. The foundations for the "direct" calculation of the axis capacitances for the example VC micromotor are set by first presenting the mathematical definitions of self and mutual inductance and capacitance. Alternative methods for calculating these lumped parameter values for "physically tangible" coils and electrodes are listed. In particular, for inductance calculations, a fundamental method based on flux linkages or a derived energy-based method can be used. For capacitance calculations, the fundamental method is a charge-based method while the derived method is once again an energy-based method.

The inductance and capacitance calculation methodologies are extended and applied to the task of obtaining fictitious direct and quadrature axis quantities. The suitability of the finite element method for "direct" calculation of **dq0** axis parameters is pointed out.

Chapter 5

In chapter five, a performance index which is referred to as an output coefficient is detailed. The concepts presented in chapters three and four are combined and put into practice. Electric scalar potential fields, the outcome of a series of finite element simulations performed on the VC motor, are used to "directly" calculate the direct axis and quadrature

axis capacitances and subsequently the output coefficient of the representative silicon micromotor. A similar kind of analysis is conducted for a simple permanent magnet motor in preparation for the calculation of its output coefficient.

The last section of this chapter probes further into the physical meaning of the axis charge versus rotor position curves obtained from the finite element simulations. Coupling between the direct axis and the quadrature axis is investigated as is the existence of zero sequence phase currents in the absence of zero sequence content in the phase voltages.

Chapter 6

Two dimensional rotor plane comparisons are made among the output coefficient of the VC micromotor, the projected value for the output coefficient of a "good" magnetic motor and the output coefficient of the permanent magnet motor. Scaling laws are applied to investigate the region in which the VC motor outperforms alternative magnetic machines. The variable reluctance machine can be analysed by the maximum current density relation and the difference between **Xd** and **Xq** assuming infinitely permeable iron. This difference will change as the permeability changes.

Chapter 7

The concepts underlying a capacitance-based torque calculation bounded by an upper capacitance limit and a lower capacitance limit are described in this chapter. Variational principles and moment-based methods employing basis functions are compared. The ability to generate both an upper capacitance bound as well as a lower capacitance bound with each

method is demonstrated. Computational savings realized by the application of the method of dual bounds is highlighted.

Geometrical discretization of a problem domain into a collection of either flux tubes or equipotential slices is described. The concepts discussed in this chapter are then applied to a practical two-dimensional silicon micromotor structure. Actual geometrical discretization schemes are shown and the direct axis capacitance is calculated using two extreme stator EMF configurations. A discussion illustrating the possibility of incorporating stationary functionals in the method of tubes and slices is included.

Chapter 8

Chapter eight includes a complete derivation of the placement of equipotential slices and flux tubes in a three dimensional problem. We prove the continuity of the potential surfaces as well as the flux tube walls within the proposed fundamental discretization structure. We then go on to prove that the proposed schemes are general enough to permit the discretization of an arbitrary three dimensional structure. Some examples of the application of the method are presented.

Chapter 9

The contributions of this work are summarized and conclusions based on the results obtained in the thesis are drawn. Recommendations for future work in the area of micromotor analysis are made.

CHAPTER 2

MICROSYSTEMS AND

SCALING LAWS

2.1 SMALL SYSTEMS

2.1.1 Advantages of Small Systems[1]

Future manufacturing endeavours will most likely bring about the need for smaller machines and systems. There are already some situations in which the presence of minute mechanical systems would be welcome. Consider the electronics industry. Rapid progress in manufacturing techniques has reduced the dimensions of individual electronic components to micron levels. Complete electronic systems can now be integrated onto a single silicon substrate. In the manufacturing environment these tiny silicon "chips" are packaged and transported from one work area to another by means of awkward sized robots that are much larger than the actual devices being manoeuvred. In such instances, smaller machines better suited for handling and manipulating minuscule objects would be preferable.

There are several advantages to using machines whose dimensions are comparable to those of the parts being handled: Reduced point to point transport distances may enable micro

---

I) This section summarizes the main points contained in [2] and [14].

fabrication systems to function faster and complete jobs in less time than larger systems. Mechanical vibrations and physical deformations resulting from thermal expansion and contraction are not as severe. Hence the position control of automated systems may be simplified and the accuracy of their movements could be improved. The likelihood of component damage during processing is lessened since the forces required to move the machine's mass are considerably smaller. Decreased system volumes permit substances, normally prohibited from large scale use because of their price, to serve as primary construction materials. Because of their superior electrical and/or mechanical properties, there are some performance benefits to be gained through the use of such materials. Finally, smaller systems occupy substantially less space and thereby allow machines to be placed in closer proximity to one another.

2.1.2 Applications

At this time, it is impossible to furnish a complete list of the various disciplines in which micro mechanical systems could eventually be employed. The technology is still in its infancy (micro machined joints, gears, springs etc. started to appear around 1987 [22,23]) and most of the potential applications have yet to be envisioned. Nevertheless, the prospects for micro mechanical systems seem very promising. The micro domain remains a relatively unexplored territory and thus presents a wealth of opportunities for research. Many new and innovative ideas introducing novel applications for small systems await discovery. As Trimmer [2] points out, there is probably more room in the near future for the development of systems in the micro domain than there is in the macro domain.

As of yet, micro mechanisms exhibiting unrestrained motion have not been implemented in commercial products. However, some silicon micro machined devices exhibiting limited dynamic capabilities are finding use in sensor applications. Moveable members typically consist of flexible diaphragms or beams fixed in at least one position and restricted to small deflections spanning only a few micrometers. For example, tiny pieces of silicon suspended above hollow cavities by thin silicon beams act as proof masses and make up the foundations of a new class of micro accelerometers [9]. Other examples include pressure sensors [24], light modulator arrays, micro mechanical switches [25] and ink jet printing nozzles [26] and others in the automotive [72] and computer [77] industries.

Planar mechanisms analogous to their macroscopic counterparts can now be fashioned on silicon substrates using processes similar to those used in the manufacture of integrated circuits. Micron-sized pin joints, self constraining joints, gears, cranks, springs and other mechanisms containing multiple parts have been machined from silicon wafers as integrated units without the need for piecewise assembly [22,23]. Unconstrained mechanisms like these can transmit mechanical power from force-producing elements to mechanical loads and are vital to the operation of any robotic system. It has been suggested that these micro mechanisms form the basis of future micro robotic systems in much the same way as conventional mechanisms form the basis of present day robotic systems [22].

Additional uses for future micro mechanical systems have been proposed by several authors [70,73,74,75]. Micro positioning and other micro control systems consisting of sensors, actuators and control electronics integrated onto a single substrate [4] could be used to control light for optical signal processing applications [9,23,27,28]. A collection of tiny

valves, pumps and chemical reactors placed on the same chip and functioning together as a single "plant" would constitute a micro fabrication system [9,27]. In the field of medicine, the advent of micro mechanical systems may lead to new types of artificial organs, produce valuable micro surgical instruments or give rise to life saving micro surgical procedures that are presently beyond the limits of human ability [29].

2.2 ENERGY CONVERSION - BASIC PRINCIPLES

Quasistatic electrical and magnetic systems are adequately modelled by lumped parameter circuits [30]. In a quasistatic electrical system, the force or torque exerted on a moveable member by the electrical coupling network in the displacement direction can be expressed as [31] :

$$f = -\frac{\partial W_e(v,x)}{\partial x} + \sum_{k=1}^{\ell} v_k \frac{\partial q_k}{\partial x}$$
$$f = \frac{\partial W_e'(v,x)}{\partial x} \qquad \textbf{(2.1)}$$

where ℓ is the number of purely electrical ports. The formulation given in equation (2.1) requires that voltage **v** and displacement **x** function as independent variables. If it is desired to use charge **q** and displacement **x** as independent variables, then the formulation presented in equation (2.2) should be used :

$$f = -\frac{\partial W_e(q,x)}{\partial x}$$
$$f = \frac{\partial W_e'(q,x)}{\partial x} - \sum_{k=1}^{\cdot} q_k \frac{\partial v_k}{\partial x} \qquad (2.2)$$

Similar equations can also be derived for quasistatic magnetic systems. With current **i** and displacement **x** treated as independent variables :

$$f = -\frac{\partial W_m(i,x)}{\partial x} + \sum_{k=1}^{n} i_k \frac{\partial \lambda_k}{\partial x}$$
$$f = \frac{\partial W_m'(i,x)}{\partial x} \qquad (2.3)$$

and with flux linkages λ and displacement **x** serving as the independent variables :

$$f = -\frac{\partial W_m(\lambda,x)}{\partial x}$$
$$f = \frac{\partial W_m'(\lambda,x)}{\partial x} - \sum_{k=1}^{n} \lambda_k \frac{\partial i_k}{\partial x} \qquad (2.4)$$

where **n** represents the number of purely magnetic ports.

2.3 PERFORMANCE MEASURES

2.3.1 Static Force

To demonstrate the advantages of electric actuation at small scales, the two simple static force-producing structures shown in figures 2.1 and 2.2 will be utilized.

Neglecting edge effects and assuming linearity, the force of attraction between the two parallel plates in figure 2.1 can be obtained from equation (2.2). As a first step, express the energy stored in the air-gap electric field in terms of the plate separation and the plate charge

$$W_e = \frac{1}{2} qv$$
$$W_e = \frac{1}{2} \frac{q^2 x}{\varepsilon_0 A_{plate}} \qquad (2.5)$$

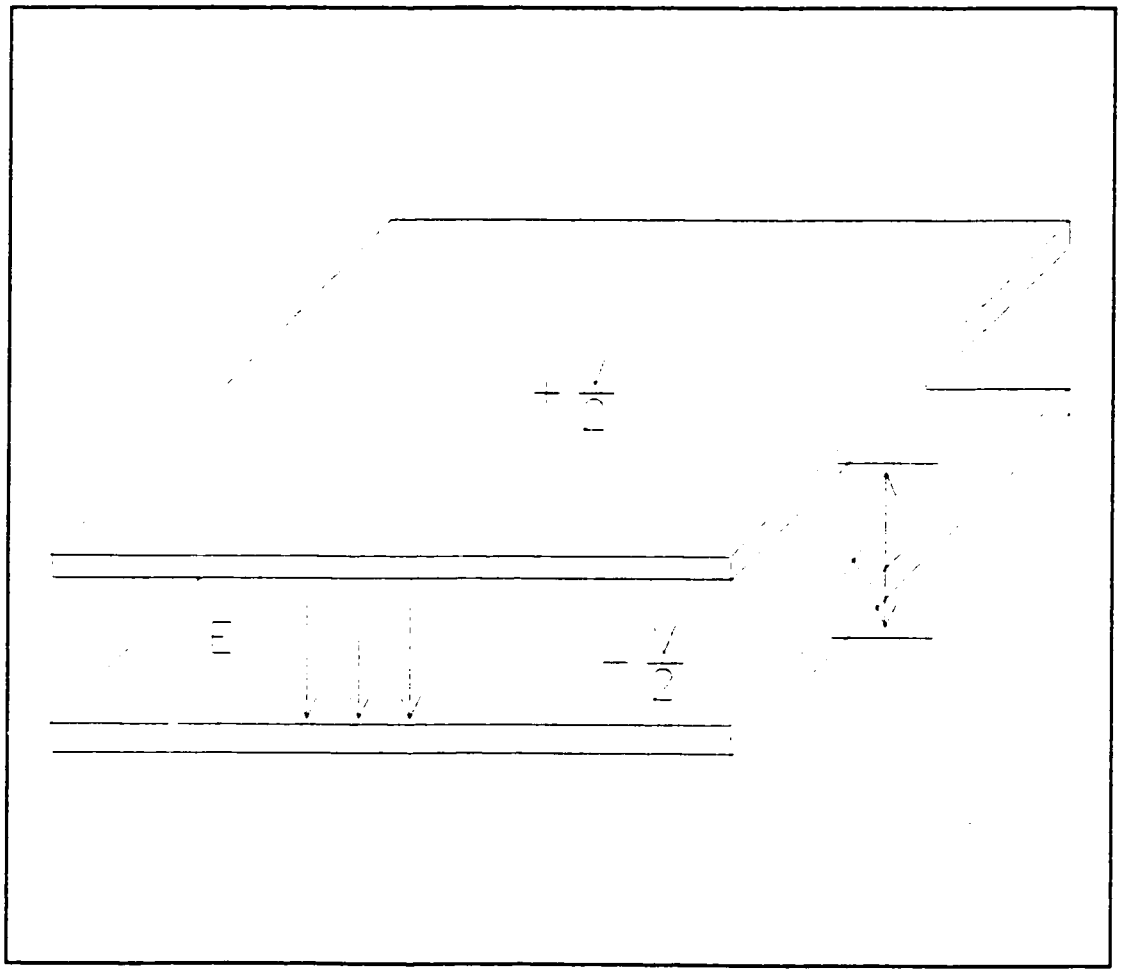

Figure 2.1: A simple electric actuator.

where **x** represents the plate separation, **q** the plate charge, **E** the electric field strength and ε_0 the permitivity of free space.. According to equation (2.2), the magnitude of the force tending to pull the plates together is :

$$f = \frac{1}{2}\frac{q^2}{\varepsilon_0 A_{plate}}$$
$$f = \frac{\varepsilon_0 A_{plate} V^2}{2x^2} \qquad \textbf{(2.6)}$$

For the structure portrayed in figure 2.2, the energy stored in the air-gap magnetic field and the force exerted on the plunger tending to move it in such a way as to reduce the size of the air-gap are given by equations (2.7) and (2.8) respectively :

$$W_m = \frac{1}{2}\lambda i$$
$$W_m = \frac{1}{2}\frac{\lambda^2 x}{\mu_0 A_{pole}} \qquad \textbf{(2.7)}$$

$$f = \frac{1}{2}\frac{\lambda^2}{\mu_0 A_{pole}}$$
$$f = \frac{\mu_0 A_{pole} J^2 A_{cu}^2}{2x^2} \qquad \textbf{(2.8)}$$

where μ_0 is the permeability of free space and λ the flux linkages.

2.3.2 Torque Production in Continuous Motion Devices

When the ideas presented in §2.2 are applied to continuous motion devices they yield the generated torque as a function of rotor angular velocity. The single phase variable reluctance motor shown in figure 2.3 and the single phase variable capacitance motor shown in figure 2.4 will serve as models for this exercise [32]. In response to an applied stator excitation, each rotor will experience a periodic mechanical torque exerted on it by the coupling field that is a function of the rotor's angular position.

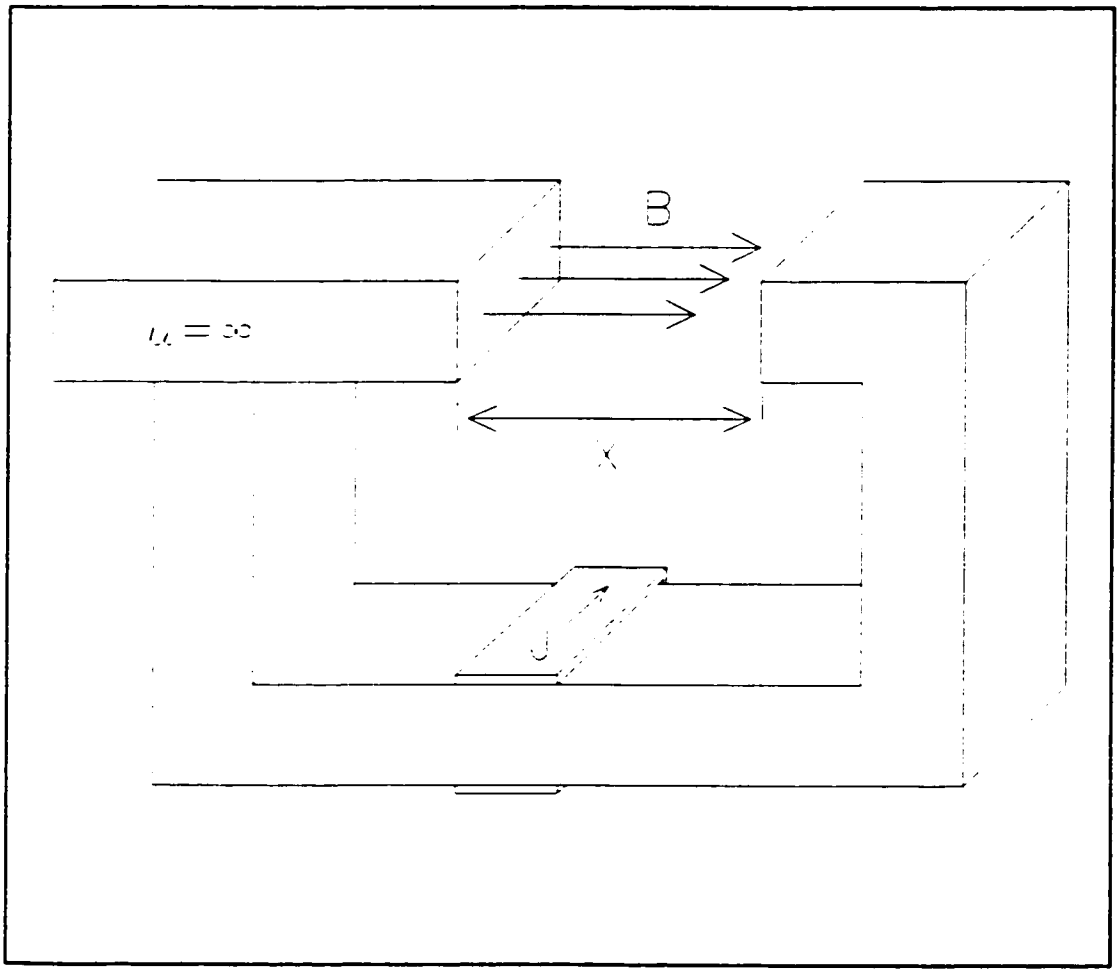

Figure 2.2: A simple magnetic actuator.

Since there is only one magnetic port, the generated torque for the single phase variable reluctance motor can be expressed simply as :

$$\tau = -\frac{\partial W_m(\lambda,\theta)}{\partial \theta}$$

$$\tau = \frac{\partial W_m'(i,\theta)}{\partial \theta} \qquad \textbf{(2.9)}$$

Similarly, for the single phase variable capacitance motor with one electrical port :

$$\tau = -\frac{\partial W_e(q,\theta)}{\partial \theta}$$

$$\tau = \frac{\partial W_e'(v,\theta)}{\partial \theta} \qquad \textbf{(2.10)}$$

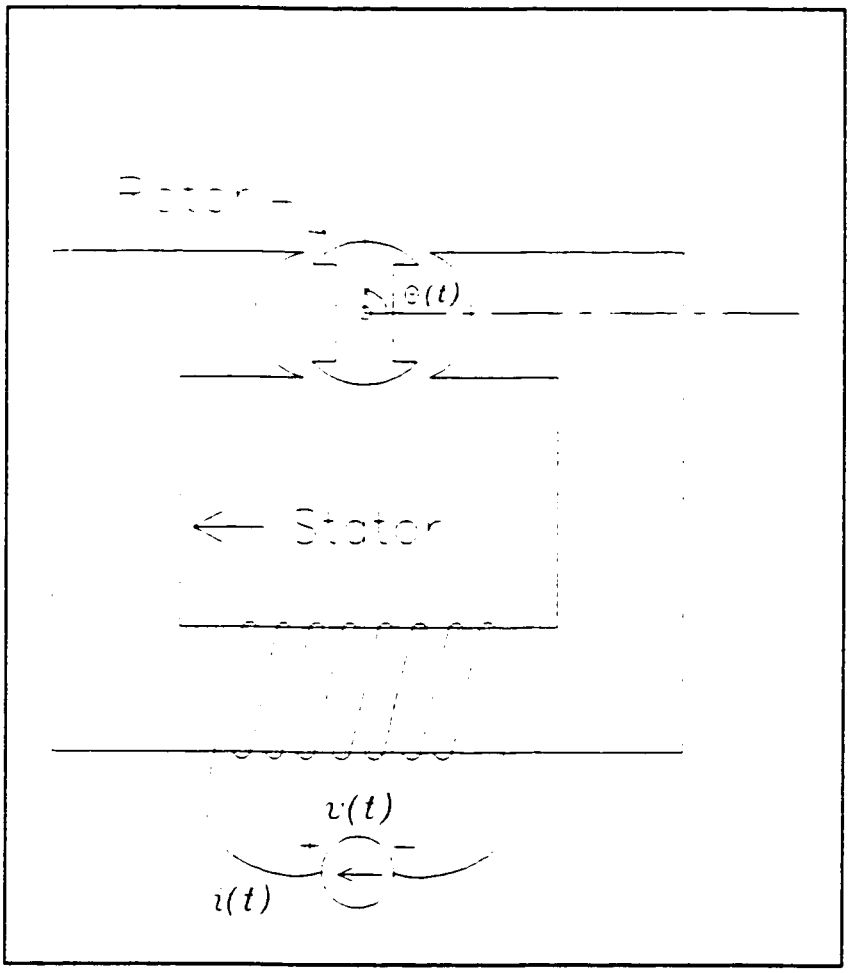

Figure 2.3: Single phase variable reluctance motor.

Assuming that both systems are linear, the respective energy and co-energy in each case will be equal and can be used interchangeably [32]. For the linear magnetic system, flux linkages λ and current **i** are related by $L=\lambda/i$. For the linear electric system, charge **q** and voltage **v** are related by $C=q/v$. Because of the symmetrical nature of the devices, both the inductance **L** and the capacitance **C** are periodic and even functions of θ.

Under sinusoidal steady state operating conditions, only certain values of rotor angular velocity ω_r and excitation radian frequency ω_s will produce an average torque over time.

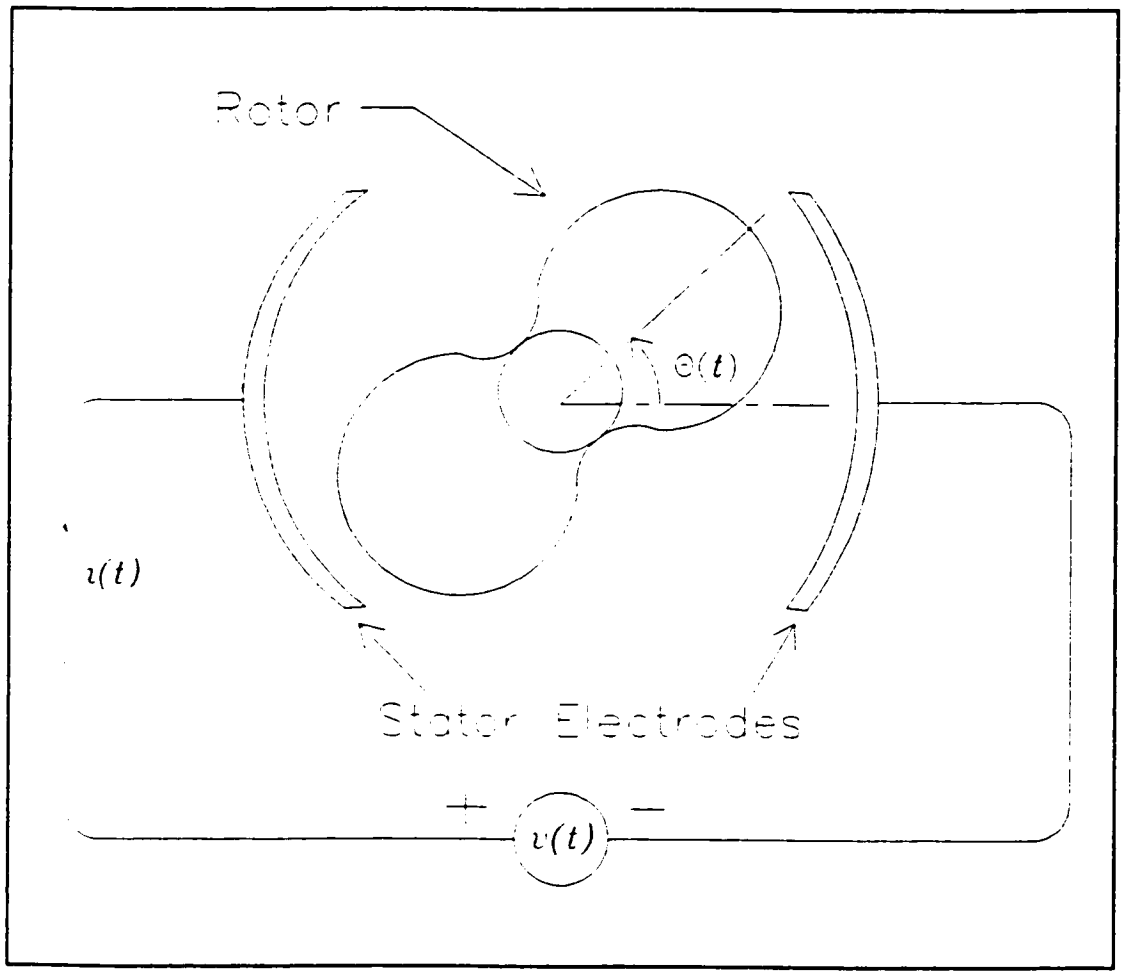

Figure 2.4: Single phase variable capacitance motor.

Table 2.1 lists the average torque values which correspond to the second harmonic (dominant) component of **L(θ)** and **C(θ)**. In each case the angular position **θ**'s functional dependence on time is :

$$\theta=\omega_r t+\delta \qquad \textbf{(2.11)}$$

The current in the drive coil of the variable reluctance machine and the voltage across the plates of the variable capacitance machine are :

$$\begin{aligned} i(t)&=I_{max}\sin(\omega_s t)\\ v(t)&=V_{max}\sin(\omega_s t)\end{aligned} \qquad \textbf{(2.12)}$$

Table 2.1: Average steady state torque - Single phase synchronous motors.

$\frac{\omega_r}{\omega_s}$	Average torque	
	Variable reluctance	Variable capacitance
1.0	$\frac{1}{4}I_{max}^2 L_2 \sin(2\delta)$	$\frac{1}{4}V_{max}^2 C_2 \sin(2\delta)$

2.3.3 Output Power

The average power which is developed can be evaluated once the rotor angular velocity and the average torque have been determined. It is simply the product of the average torque and rotor angular velocity :

$$P_{av} = \tau_{av} \omega_r \tag{2.13}$$

For the variable reluctance machine of figure 2.3 :

$$P_{av} = \frac{\omega_r}{4} I_{max}^2 L_2 \sin(2\delta) \tag{2.14}$$

For the variable capacitance machine of figure 2.4 :

$$P_{av} = \frac{\omega_r}{4} V_{max}^2 C_2 \sin(2\delta) \tag{2.15}$$

2.3.4 Efficiency

a) ***Static Force Production***

The generation of force through electrostatic means is a highly efficient process. Some power dissipation is unavoidable during the process of establishing the charge due to conduction losses in the electrodes and connections. At the same time, non-ideal dielectric material will contribute additional losses. Additional amounts of power (albeit very small) will be consumed while maintaining the force if charge leaks from the electrodes.

On the other hand, sustaining a static magnetic force requires a much larger continuous flow of electric charge. Resistance in the drive coil results in $\mathbf{I^2R}$ losses. This loss term can be expressed as :

$$\begin{aligned} P_{loss} &= I^2 R_{eff} \\ P_{loss} &= (J A_{cu})^2 R_{eff} \end{aligned} \tag{2.16}$$

b) ***Continuous Motion Devices***

For the single phase variable capacitance machine, the current which results from the repeated charging and discharging of the electrodes leads to conduction current losses. Small amounts of power dissipation arising from lossy dielectrics may also be encountered. Similarly, the variable reluctance machine will suffer from conduction current losses generated by the drive coil excitation current and also from hysteresis loss due to the periodic re-orientation of magnetic domains. Magnetically actuated machines will also suffer to some degree from eddy current losses, a source of loss not normally present in electrically actuated devices.

Dielectric, hysteresis and eddy current losses are very difficult to quantify. The inclusion of these losses in the scaling properties of machine efficiencies is not considered in this work. At small scales the losses incurred due to ohmic dissipation in the conductors will probably dominate anyway. Consequently, equation (2.16) accounts for all sources of loss considered to be "electrical" in nature.

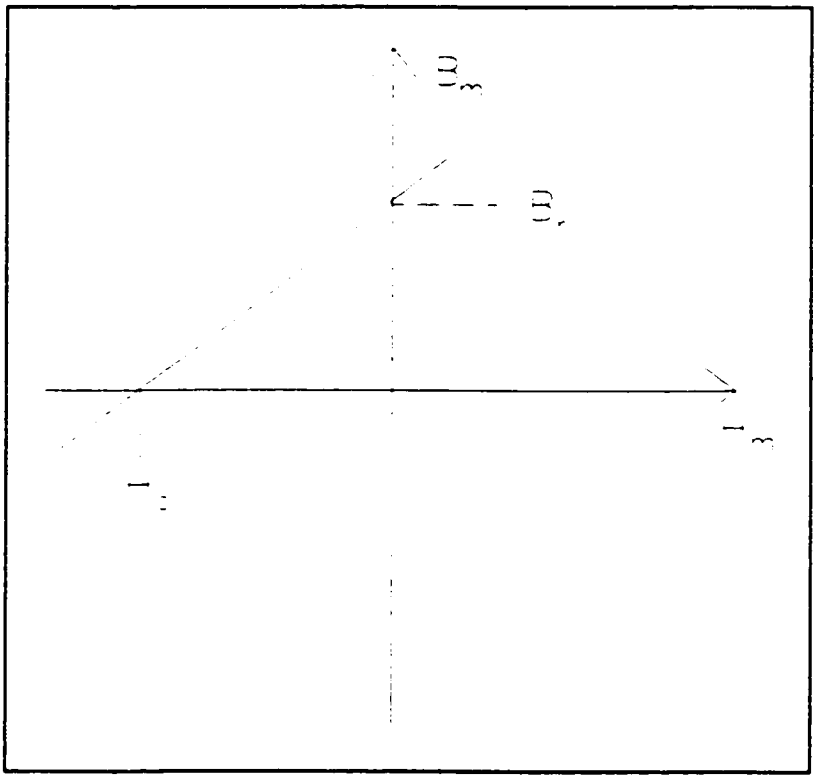

Figure 2.5: Recoil line of a permanent magnet.

2.3.5 Permanent Magnet Machines

a) *Static Magnetic Force*

Consider the production of a static magnetic force through the use of a permanent magnet. The drive coil of figure 2.1 has been replaced by a permanent magnet whose B-H characteristic [33] is shown in figure 2.5.

Mathematically, the permanent magnet material is modelled as soft magnetic material wrapped in a current sheet of appropriate strength [34]. A force is exerted on the moveable member so as to reduce the size of the air-gap. From equation (2.8) the magnitude of this force is given by :

$$f=\frac{1}{2}\frac{B_m^2 A_{pole}}{\mu_0} \qquad (2.17)$$

The magnetic flux density in the magnet $\mathbf{B_m}$ must be consistent with the B-H curves of both the permanent magnet material and of the air. It will take on a value equal to that which exists at the point of intersection between the two materials' characteristic curves. For an illustrative example see figure 2.6.

$\mathbf{B_m}$ is obtained algebraically by simultaneously solving the linear system in figure 2.6 and the integral equation given in equation (2.18) :

$$\oint \mathbf{H}\cdot\mathbf{dl}=I_{enclosed} \qquad (2.18)$$

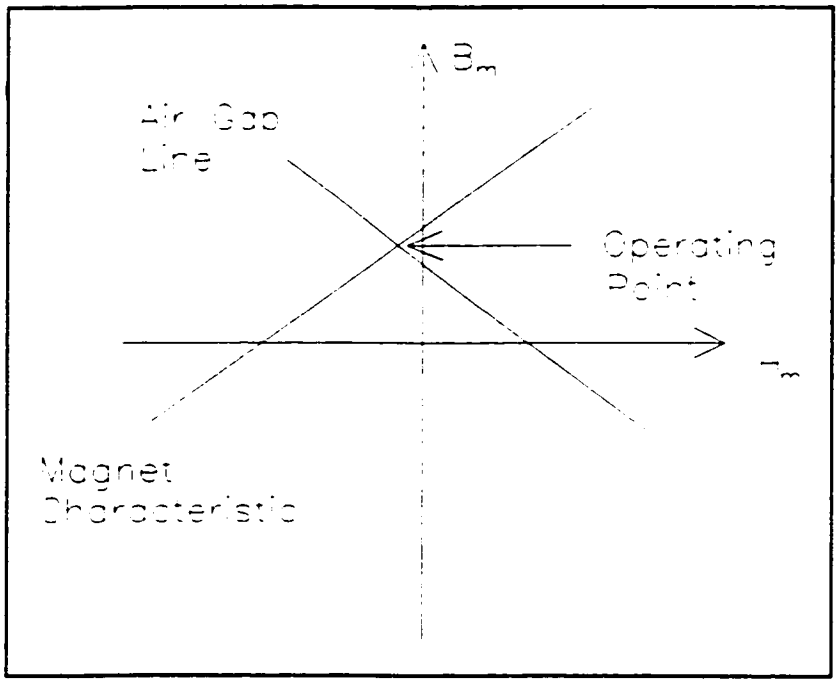

Figure 2.6: Determining the magnet operating point.

After substituting equation (2.18) into equation (2.17), the resulting expression for the attractive force becomes :

$$f=\left(\frac{2}{\mu_0}\right)\left(\frac{A_{pole}B_r^2\ell_m^2}{(\mu_r x+\ell_m)^2}\right) \qquad \textbf{(2.19)}$$

where ℓ_m is the length of the magnet.

b) ***Synchronous Motor Torque***

A simple continuous motion device incorporating a permanent magnet can be realized from the structure of figure 2.3 by replacing the soft iron salient pole rotor by a permanent magnet. Retaining the current sheet model for the hard magnetic material allows us to treat this new single phase synchronous motor as a multiply excited machine [32]. Once again linearity will be assumed. The total stator flux linkages λ_s and rotor flux linkages λ_r can be expressed as functions of the drive coil current i_1 and the effective rotor current i_2 :

$$\begin{aligned}\lambda_s&=L_s(\theta)i_1+L_m(\theta)i_2\\ \lambda_r&=L_m(\theta)i_1+L_r(\theta)i_2\end{aligned} \qquad \textbf{(2.20)}$$

The total energy stored in the magnetic field is :

$$W_m=\frac{1}{2}(L_s(\theta)i_1^2+L_r(\theta)i_2^2)+L_m(\theta)i_1i_2 \qquad \textbf{(2.21)}$$

L_s and L_r represent the stator and rotor self inductances respectively. Like the self inductances, the stator to rotor mutual inductance L_m is a periodic and even function of rotor angular position. The mutual inductance term differs from the self inductance terms in the

sense that its harmonics are multiples of θ rather than 2θ and it has an average value of zero.

From equation (2.3), the torque exerted on the rotor by the magnetic coupling field is given by :

$$\tau = \frac{1}{2}\left(i_1^2 \frac{dL_s}{d\theta} + i_2^2 \frac{dL_r}{d\theta}\right) + i_1 i_2 \frac{dL_m}{d\theta} \qquad \textbf{(2.22)}$$

With the rotor angular position θ given by equation (2.11) and the drive coil current $i_1(t)$ given by the first expression in equation (2.12) the developed torque at synchronous speed will have an average value over time of :

$$\tau_{av} = \frac{1}{4} I_{max}^2 L_{s,2} \sin(2\delta) + \frac{1}{2} L_{m,1} I_2 I_{max} \cos(\delta) \qquad \textbf{(2.23)}$$

As before, $L_{s,2}$ and $L_{m,1}$ represent only the dominant harmonics which contribute to an average value of torque. Using the current sheet model for the permanent magnet the effective rotor current i_2 is constant and is equal to the product of the permanent magnet material's coercive force H_c and the magnet's length ℓ_m :

$$i_2 = I_2 = H_c \ell_m \qquad \textbf{(2.24)}$$

c) ***Synchronous Motor Output Power***

Now that an expression for the average torque has been derived we can calculate the average power :

$$P_{av}=\tau_{av}\omega_r$$

$$P_{av}=\left(\frac{1}{4}I_{max}^2 L_{s,2}\sin(2\delta)+\frac{1}{2}L_{m,1}I_2 I_{max}\cos(\delta)\right)\omega_r \qquad \textbf{(2.25)}$$

d) ***Efficiency***

Hysteresis and eddy current losses will of course be present, but since the machines of interest are quite small, conduction current losses will probably dominate. As such, equation (2.16) will yield the power dissipated in the drive coil.

2.4 THE PASCHEN EFFECT

One of the most interesting natural phenomena lending favour to electric actuation at small scales is known as the Paschen effect. Experiments indicate that the breakdown electric field strength of air is a function of the air-gap spacing air-gap pressure product [3]. Of particular notice is the tendency for the breakdown electric field strength of air to increase for decreasing product values. Figure 2.7 (taken from [7]) depicts this relationship for air at 20° Celsius.

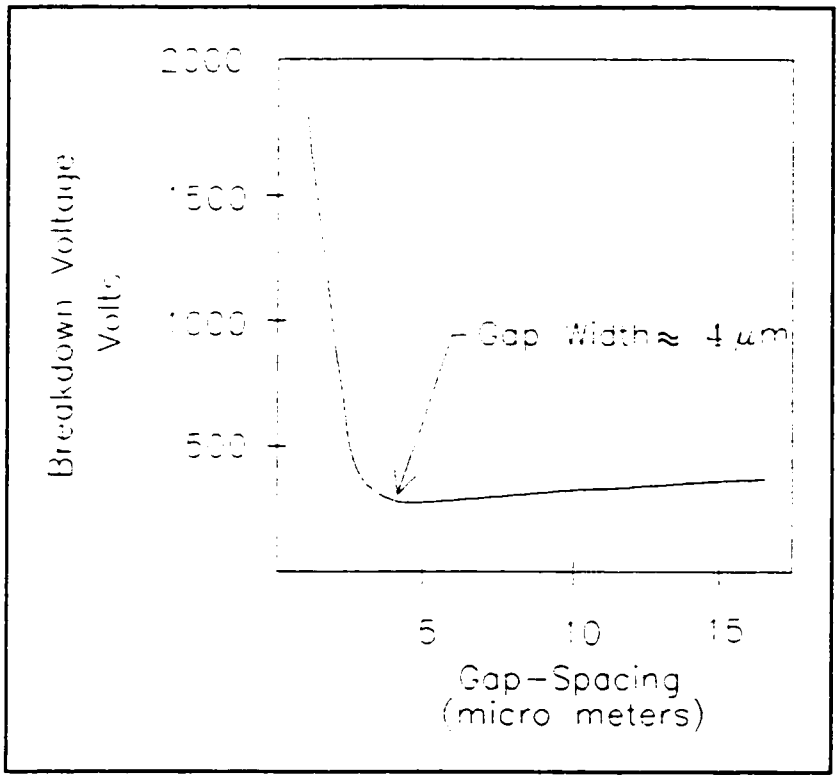

Figure 2.7: Paschen curve for air at 20° Celsius.

The breakdown voltage of air at atmospheric pressure at 20° C starts to rise as the gap width nears 4 micrometers. Electrically actuated machines possessing air-gap spacings in this range can attain significantly higher energy densities than analogous devices with macro domain sized air-gaps. It is at this point and primarily for this reason that electrically actuated devices become viable and could conceivably compete with magnetically actuated machines.

2.5 ELECTRIC VS MAGNETIC ACTUATION

The expressions presented in §2.3 for the different performance measures (ie. static force, torque, output power and efficiency) will now be examined. Our aim is to establish in a qualitative manner the general scaling trends these performance measures follow. For comparison purposes, various terms in §2.3.1 and §2.3.5a have been assigned numerical values so that the relationships can be displayed graphically. By plotting the functions on a common set of axes, the effects of scale and the benefits of electrical actuation in the micro domain can be portrayed in a clear and concise manner.

2.5.1 Static Force Scaling Properties

Figure 2.8 graphically depicts the effect of the current density function on the static force For comparison, electric forces within the applicable range are also shown. The attractive force magnitude has been calculated at selected intervals representing a variety of "machine" sizes spanning from the micro to the macro domain. The relationships are plotted against the air-gap width for a range of gap values extending from one micrometer to one millimeter. It has been assumed that all measurements scale proportionally and at the same rate as the air-gap width **d**.

The legend for the numbered force curves in figure 2.8 is :

1 ... constant electric field, E=3 MV per metre.

2 ... constant electric field, E=300 MV per metre.

3 ... current density function; J=2 MA per square metre.

4 ... hard magnetic material - Samarium Cobalt (B_r=0.92 T; H_c=705 KA/m) [35].

5 ... current density function; $J=J(d^{-1.1})$.

6 ... current density function; $J=J(d^{-1})$.

The initial conductor area $\mathbf{A_{cu}}$ for cases 5 and 6 and the magnet length ℓ_m for case 4 were calculated after stipulating that the macroscopic air-gap flux density have a value of 0.8 Tesla. A macroscopic air-gap is considered to be an air-gap measuring 1 millimeter in width or greater.

There are a number of important features contained in figure 2.8 that deserve notice.

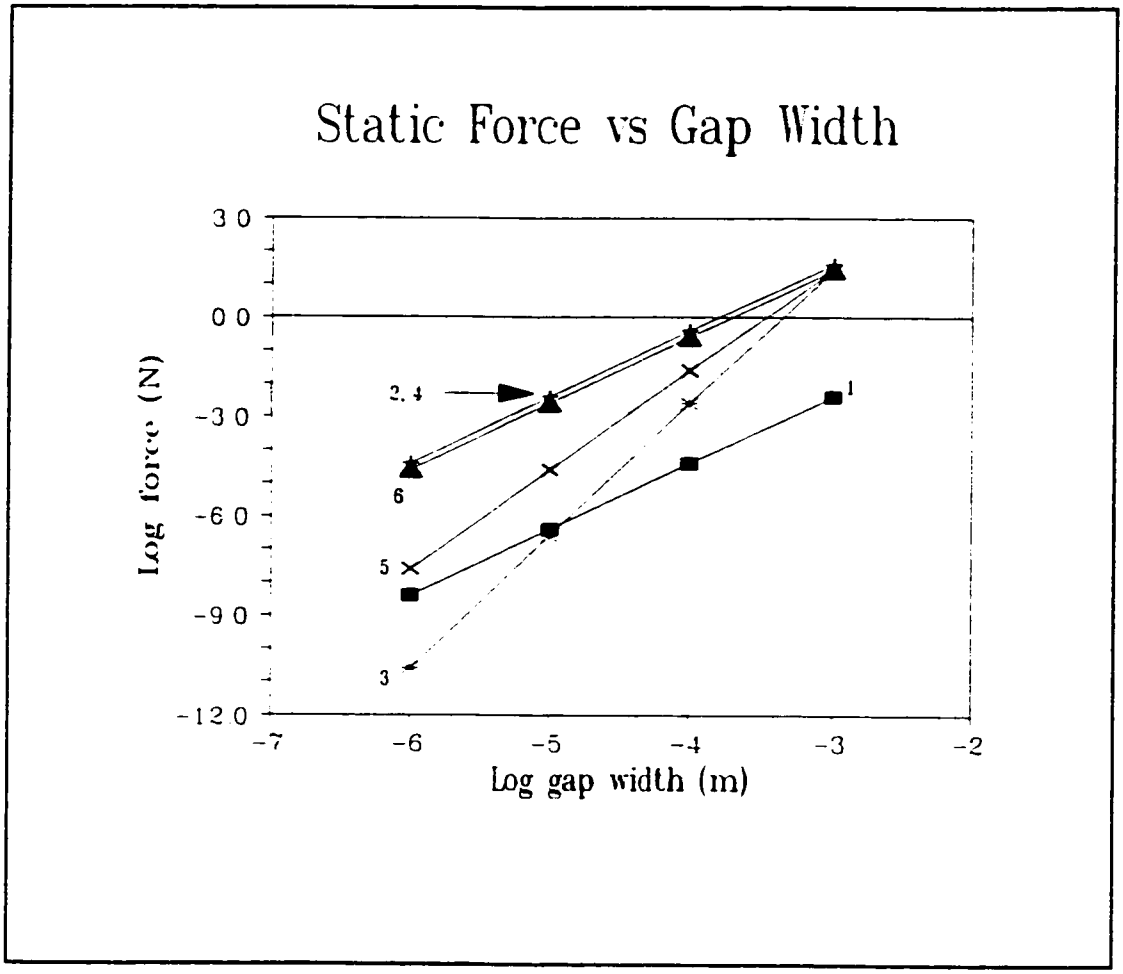

Figure 2.8: Scaling of static forces.

Some of the fundamental differences between the way electric and magnetic forces scale are brought out in this diagram. For example, it is quite clear that under conditions of constant electric field strength and constant current density, forces of electric origin decrease at a slower rate than do those of magnetic origin. Compare, for example, the slope of curves 1 and 2 to that of curve 3. A direct consequence of this rate discrepancy is the existence of a "transition" point denoting the air-gap width at which the electric and magnetic actuators produce forces of equal magnitude. Any subsequent size reduction will result in a decrease in magnetic force magnitude in excess of that experienced by the electrically actuated device. By increasing the threshold level of electrical breakdown it is possible to shift the transition point in a direction which tends to move it closer to the macro domain.

The inclusion of hard magnetic materials (curve 4) in the magnetic actuator's construction also has an effect on the location of this transition point. In fact, in so far as static forces are concerned, the presence of hard magnetic materials actually eliminates the rate discrepancy. Both types of forces now scale at the same rate. The question as to which device is capable of producing the greater force will depend on the magnitudes of the permissible breakdown electric field strength and macroscopic air-gap magnetic flux density values used.

It is also evident that scaling rates and consequently transition points are affected by differing levels of electric current density. Each of the current density relationships used possesses some physical significance. The implication of constant current density (curve 3) is constant heat generation per unit volume inside the conductor. The inverse square root dependence of current density on air-gap width (curve 5) corresponds to constant heat flow

per unit area out of the conductor and the inverse relationship (curve 6) pertains to a constant temperature differential between a conductor and its surroundings [2].

To summarize, static forces of electrical origin decrease at a slower rate than do those of magnetic origin when current density levels in magnetic actuators remain constant. We can compensate for this rate discrepancy by modelling the current density function in magnetic devices differently or by including permanent magnet materials in the construction of magnetic actuators.

2.5.2 Other Scaling Laws

In §2.5.1 we examined the scaling properties of one particular performance measure - static force. The graphical analysis presented in that section shows how the favoured actuation scheme can change at some scale. This is exemplified by the fact that some of the curves in figure 2.8 cross. A so called "transition" point is located where two curves representing the same performance measure but different actuation schemes intersect.

Static force is just one of the performance measures referred to in §2.3. The balance of performance measures that remain are more relevant to rotating machines. They include average torque, average power and efficiency. Using the equations developed in §2.3, the scaling properties of these remaining performance measures will be addressed. However, instead of the graphical approach taken in the previous section, a notation found in the literature is used. Establishing approximate transition points for this group of performance measures requires techniques developed in later chapters and hence precludes any numerical work at this time.

The bracket notation adopted here is the same one introduced by Trimmer [2]. In this notation, the parameter **s** represents any measurement that characterizes the size of a device and the power to which it is raised indicates the functional dependence of the particular quantity on this parameter. The vertical bracket notation is a compact way of conveying the various scaling laws. The different slopes shown in figure 2.8 correspond to different powers of **s**. The fact that the behaviour of electrically and magnetically actuated devices is different and their performance measures scale at different rates is the main factor motivating the comparison between these two types of machines.

The current density and breakdown electric field strength scaling matrices are given in equation (2.26) :

$$J=\begin{bmatrix} s^{0} \\ s^{-0.5} \\ s^{-1} \end{bmatrix} \quad E=\begin{bmatrix} s^{0} \\ s^{-0.5} \end{bmatrix} \tag{2.26}$$

Holding the excitation frequency ω_s constant, the scaling matrices for the variable reluctance machine's average torque, average power and ohmic conduction loss expressed as powers of **s** are :

$$\tau_{av}=P_{av}=\begin{bmatrix} s^{5} \\ s^{4} \\ s^{3} \end{bmatrix} \quad P_{loss}=\begin{bmatrix} s^{3} \\ s^{2} \\ s^{1} \end{bmatrix} \tag{2.27}$$

For the variable capacitance machine :

$$\tau_{av}=P_{av}=\begin{bmatrix} s^3 \\ s^2 \end{bmatrix} \quad P_{loss}=\begin{bmatrix} s^3 \\ s^2 \end{bmatrix} \tag{2.28}$$

For the permanent magnet machine :

$$\tau_{av}=P_{av}=\begin{bmatrix} s^4 \\ s^{3.5} \\ s^3 \end{bmatrix} \quad P_{loss}=\begin{bmatrix} s^3 \\ s^2 \\ s^1 \end{bmatrix} \tag{2.29}$$

The excitation frequency is scaled as s^{-1} so that we obtain, for the variable reluctance machine :

$$\tau_{av}=\begin{bmatrix} s^5 \\ s^4 \\ s^3 \end{bmatrix} \quad P_{av}=\begin{bmatrix} s^4 \\ s^3 \\ s^2 \end{bmatrix} \quad P_{loss}=\begin{bmatrix} s^3 \\ s^2 \\ s^1 \end{bmatrix} \tag{2.30}$$

For the variable capacitance machine :

$$\tau_{av}=\begin{bmatrix} s^3 \\ s^2 \end{bmatrix} \quad P_{av}=\begin{bmatrix} s^2 \\ s^1 \end{bmatrix} \quad P_{loss}=\begin{bmatrix} s^1 \\ s^0 \end{bmatrix} \tag{2.31}$$

For the permanent magnet machine :

$$\tau_{av}=\begin{bmatrix} s^4 \\ s^{3.5} \\ s^3 \end{bmatrix} \quad P_{av}=\begin{bmatrix} s^3 \\ s^{2.5} \\ s^2 \end{bmatrix} \quad P_{loss}=\begin{bmatrix} s^3 \\ s^2 \\ s^1 \end{bmatrix} \tag{2.32}$$

There is some physical significance attached to the scaling of the excitation frequency ω_s as a power of s^{-1}. Since the rotor radius scales as s^1 and the tip velocity of the rotor is obtainable from the product of rotor radius and rotor angular velocity, the rotor tip velocity will be constant if ω_s scales as s^{-1}.

Under constant frequency excitation the variable capacitance machine's torque and power producing abilities are most favorable in the micro domain. The variable capacitance machine is followed first by the permanent magnet machine and then by the variable reluctance machine. Ohmic conduction losses scale at the same rate for each device but it should be noted that the absolute losses may be markedly different because of the disparate current requirements of each of the machines. For example, it is expected that the current requirements of the variable capacitance machine will be substantially less than those of the other two machines.

By adjusting the excitation frequency in a way that keeps the rotor tip velocity constant, we encounter a situation in which the developed torque scales exactly as it did under constant frequency excitation, however, the power which is developed now decreases at a slower rate. All the powers of s in the power vertical bracket have decreased by 1. Additionally, there has been a noticeable change in the ohmic power loss bracket for the variable capacitance machine. The consequences of the reduced powers of s in the power loss bracket are important and should not be overlooked. A smaller exponent implies a slower rate of decline. Therefore, at some "point", the losses incurred by an electrically actuated device will actually be larger than those experienced by a magnetically actuated device of similar size.

In summary, when torque and output power are of concern, smaller powers of **s** imply the existence of a transition point obviously favoring the use of electric actuation at small scales. As long as angular velocities remain fixed, no relative change in power lost to ohmic dissipation is experienced. However, if rotor tip velocities are held constant, $\mathbf{I^2R}$ losses for VC motors decrease at a slower rate than those of magnetically actuated motors. In other words, for scales to the "left" of the loss transition point, electric actuation is not favoured. Any comparison between a magnetically actuated device and an electrically actuated device should make some attempt at determining the peak operating current density of each device. If for example, it is discovered that two particular devices develop the requisite amount of power at one scale, the losses incurred by one machine may be much larger than those of the other.

It seems as if a statement which advocates the use of electrically actuated devices at small scales cannot be made using a cursory examination or simple rule of thumb. There does not seem to be a definitive or general answer. The problem needs to be examined more closely and should entail a fairly accurate assessment of the specific devices in question on a case by case basis.

Take as a simple example the benefit-of-scale concept illustrated in figure 2.9. The two curves represent the torque generated by two actuators, one electric and one magnetic. Per unit (normalized) generated torque is plotted on the y-axis against actuator size on the x-axis. The parameter used in this section to represent actuator size is air-gap width but any parameter that characterizes an actuator's size could be used. For example, stator outer diameter is a measurable quantity that can be used to characterize the size of a rotating machine. In general, any quantity that conveys information regarding physical size could be

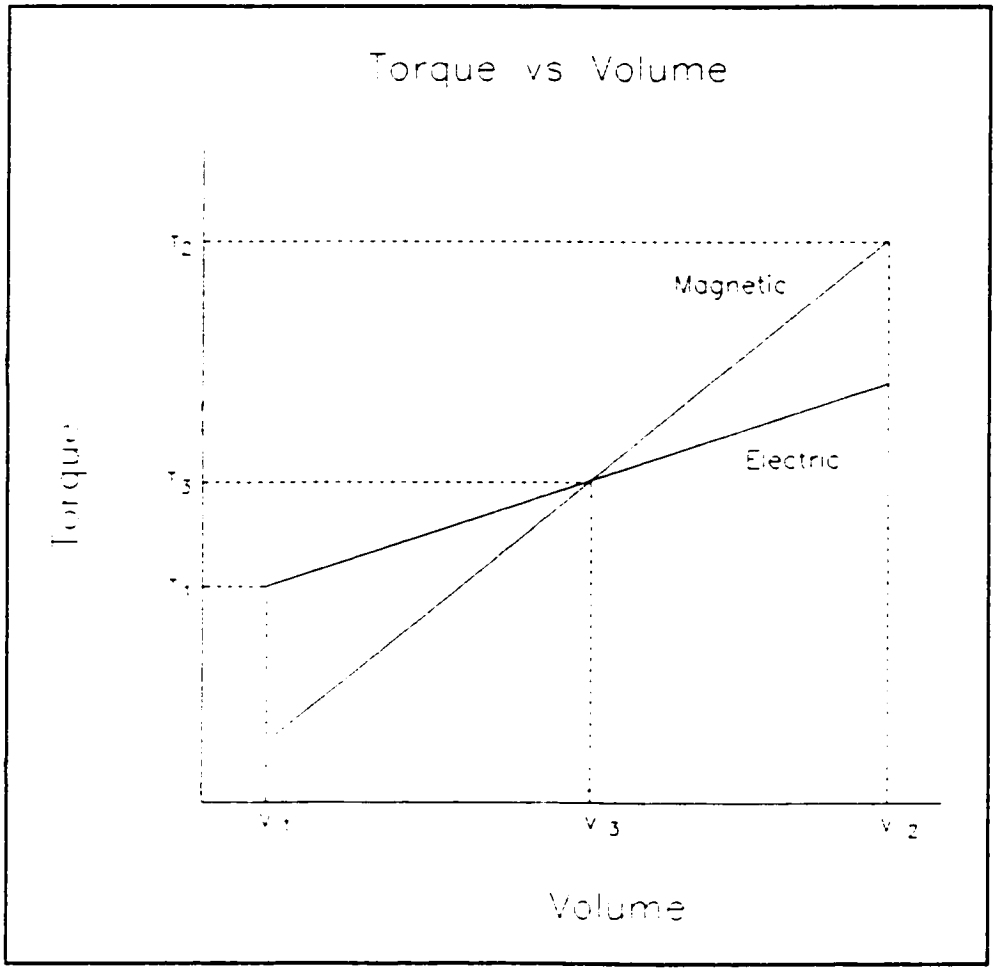

Figure 2.9: Locating a transition "point".

substituted.

Figure 2.9 serves to introduce the notion of a transition "point" and illustrates how one type of actuation can be more desirable than another at a certain size scale. The diagram is interpreted as follows :

For applications requiring actuators capable of generating torques of magnitude near $\mathbf{T_1}$ with actuator characteristic dimensions near $\mathbf{V_1}$ electric actuation is favoured. The reason is that at this small scale the magnetic actuator of equivalent size does not yield the required amount of torque. Similar considerations favour the use of magnetic actuation for applications where torques of magnitude near $\mathbf{T_2}$ need to be generated with actuators of size close to $\mathbf{V_2}$. It is an objective of this work to estimate the location of a "point" analogous to that of $\mathbf{V_3}$ for an example variable capacitance micromotor design.

The magnetic counterparts considered as alternatives to the variable capacitance machine include an interior type permanent magnet motor as well as conventional (rotor field-current excitation) synchronous and variable reluctance motor designs. The decision making process is based upon an index referred to as an output coefficient. While a specific interior type permanent magnet motor design is proposed and analysed in detail, the latter two categories of design alternatives are considered indirectly through the output coefficient calculation.

The concept of an output coefficient is described in detail in chapter five. For the moment, it is sufficient to state that the output coefficient is a powerful construct for comparative studies involving scale because it is a general index and does not require specific construction detail for its implementation.

CHAPTER 3

FABRICATION & ANALYSIS OF THREE PHASE SILICON MICRO MOTORS

In chapter 2, the main factors motivating the comparison between electrically and magnetically actuated motors were revealed. As indicated in figure 2.8, one of the principal requirements that must be met before electrically actuated devices can be expected to compete with magnetic machines is the attainment of an air-gap electric field strength far in excess of the macroscopic 3 MV per metre level. At standard pressure (101.3 kPa) and without the assistance of special insulating gases, the use of micron sized air-gaps seems to be the only alternative mechanism by which these elevated levels of electric field strength can be achieved.

In recent years, a number of researchers have successfully constructed tiny mechanical elements on the surface of silicon wafers using processes similar to those used in the manufacture of integrated circuits [7,8,10,11,12,22,23,71]. Some of these devices possess fully detached members that can rotate or slide freely over the substrate surface. A certain class of these machines is designed in such a way as to permit one of the unrestrained components (usually a disk type structure) to rotate in response to an applied electric field. These types of mechanical machines are referred to as silicon micro motors. Although no

practical means of extracting mechanical power from these devices exists at the time of this writing, the conversion of electrical energy into mechanical motion using the electric field as the coupling field has been demonstrated [7,8,10,11,12].

Such tiny electrically actuated machines hold promise because the micrometre scale clearances necessary for useful electro mechanical energy conversion are readily achieved through the photo lithographic techniques and silicon micro machining methods employed in the fabrication of integrated circuits. The very same advancements that have been so instrumental in reducing the size of electronic components may one day duplicate their achievements with mechanical systems.

We begin with a review of some basic fabrication steps compatible with integrated circuit (IC) manufacturing technology currently employed in the construction of silicon micro motors. Several design considerations involved in the process of choosing a motor configuration are presented. Details of the example micro motor whose performance capabilities are matched against those of a "rival" magnetic machine are introduced. This chapter closes by establishing the theoretical foundations upon which future analysis of the example three phase VC silicon motor is based.

3.1 SILICON MICRO MACHINING

Two principal silicon micro machining techniques have so far been utilized in the construction of micro mechanical devices [9]. A brief account of each method is given in the following sections.

3.1.1 Bulk Micro Machining [9]

The underlying concept behind the bulk micro machining of silicon lies with the uneven rates at which different planes of the silicon crystal are etched by alkaline solutions such as potassium hydroxide and hydrazine [4]. Masking selected areas of the wafer with either a silicon dioxide or silicon nitride film allows for the careful definition of lateral dimensions. Silicon doped heavily with boron serves as an effective method of stopping the etching process from going beyond a pre-specified depth.

A process for constructing thin metalized insulating members suspended over a cavity and attached to the silicon substrate at one end is described in [25]. Silicon dioxide serves as a masking layer with highly boron doped silicon used as a stop etch. A special etchant (EDP) which does not appreciably attack metals like chromium or gold but rapidly undercuts the "convex" corners of a mask can be used to create rectangular pits in the silicon with the overhanging elements taking on any desired shape. This technique, however, is not considered to be a standard MOS process [36].

Moveable silicon plates supported by polyamide beams in conjunction with on-chip, integrated position-sensing has been accomplished and is described in [28].

3.1.2 Surface Micro Machining [9]

By successively depositing structural layers and etching away sacrificial ones, it is possible to furnish an entirely assembled mechanical structure on the surface of a silicon wafer. Typically, polycrystalline silicon is used as the structural layer with silicon dioxide acting as the sacrificial spacer layer. Both films can be grown on the wafer using a chemical

vapour deposition (CVD) process that is able to deposit the films over uneven surfaces with a high degree of consistency.

The tremendous resolution that can be attained with present day plasma etching techniques and photolithographic processes permits the lateral dimensions of components and the clearances between them to be accurately defined [4]. One drawback of this process is the problem of surface planarization. As the surface of the structure becomes rougher through repeated depositions, the effectiveness of the photolithographic process deteriorates.

Aluminum and polyamide represent a set of sacrificial/structural materials that are congruous with the processes involved in the integration of MOS circuitry and could possibly enable micro mechanical systems and prefabricated MOS electronics to be located on a common substrate. It is advantageous to have both the electronic and mechanical systems on the same chip because the interconnections are much easier to handle and the parasitic capacitances associated with external connections are significantly reduced. There are, however, some complications that arise when attempting to combine surface micro machining procedures with the electronic fabrication process. Such matters will be addressed briefly in a section on practical construction difficulties.

In [36] a surface micro machining process that is largely compatible with conventional planar MOS fabrication methods is described. The technique is used to construct polysilicon micro mechanical beams. A silicon dioxide layer is first grown or deposited on the silicon wafer and a window subsequently opened in the oxide layer. A poly silicon layer is deposited and later etched to form a beam. Finally, the oxide layer is removed by immersing the wafer in a buffered solution of hydrofluoric acid (HF).

Mehregany *et al.* [22] describe a surface micro machining process by which they produce integrated poly silicon mechanisms like turbines, gear trains and mechanical tongs. The fabrication of three types of silicon micro motors using similar methods is described in [10].

Fan *et al.* [23] outline the micro machining of integrated moveable pin joints, self constraining joints, gears, cranks and springs all with micro metre scale dimensions. Their process entails the use of poly silicon as the structural material and phosphosilicate glass as the sacrificial layer. An undercut and refill operation is used to form restraining flanges. An extension of the same process has furnished several working micro motor designs. The design, fabrication and operation of these devices is presented in [8].

A standard MOS VLSI processing technique has recently been used to fabricate radial-gap variable capacitance micro motors [12]. The local oxidation of silicon (LOCOS) differs from standard surface micro machining in the way that a LOCOS step is performed before any depositions or patterns are made. With this process, a high degree of planarization between the SiO_2 and Si_3N_4 layers can be achieved.

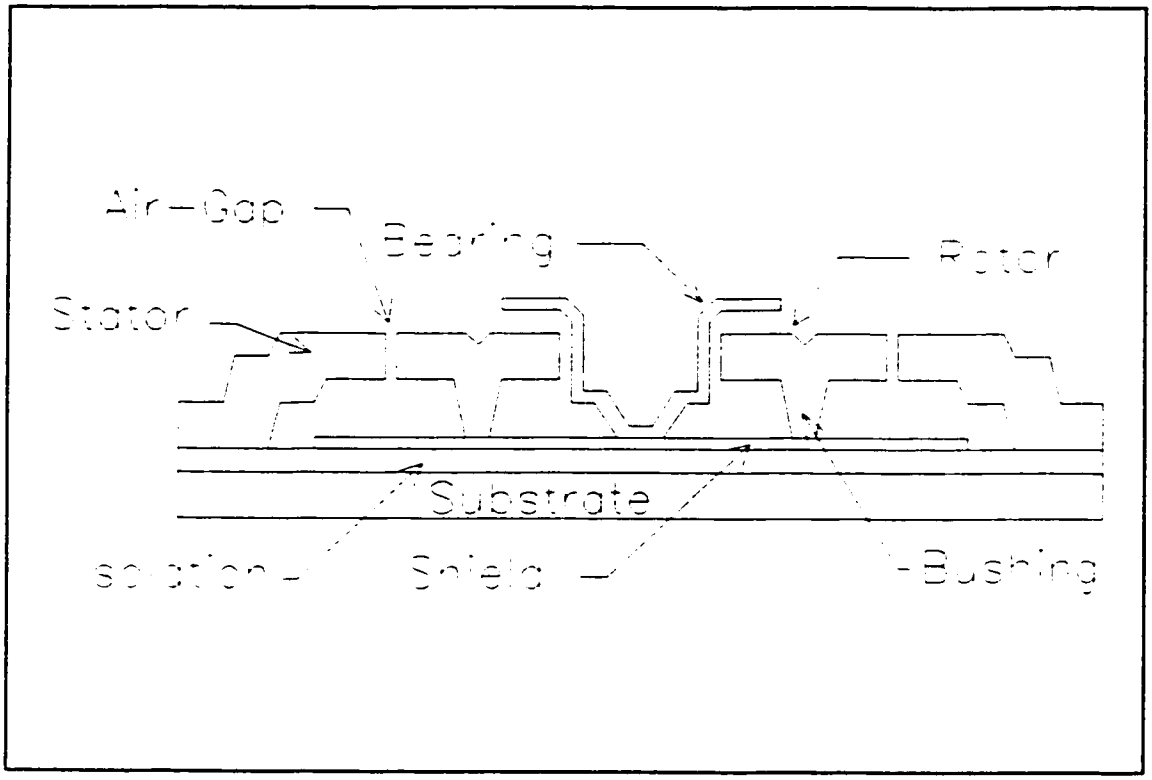

Figure 3.1: Cross sectional view of a silicon micro motor.

a) ***A Surface Micro Machined Silicon Micro Motor*** [7]

Figure 3.1 shows the cross section of a typical radial-gap variable capacitance silicon micro motor with the various components labelled on the diagram. An overview of the micro machining procedure employed in its construction can be found in the thesis by Bart [7] and a more detailed description can be seen in Mehregany's thesis [37].

Figure 3.2 shows a scanning electron micrograph (SEM) view of the top of a 12 stator pole, 8 rotor pole radial-gap variable capacitance silicon micro motor.

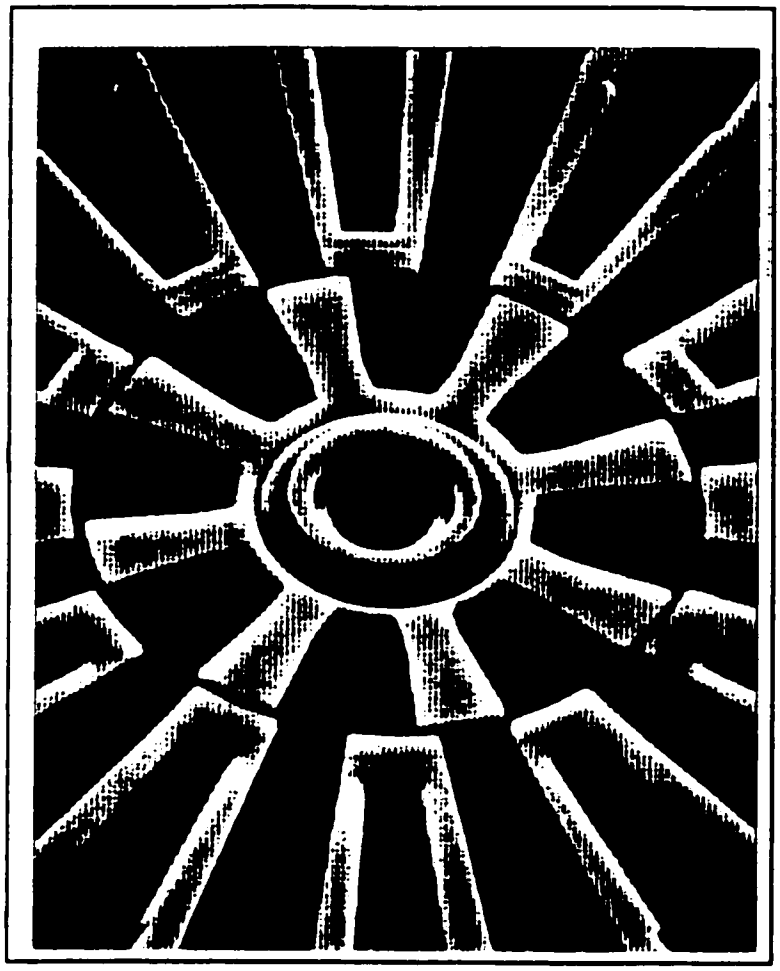

Figure 3.2: SEM of a VC silicon micro motor.

3.2 DESIGN CONSIDERATIONS

In a recent study of several silicon micro motor topologies, it was concluded that with the micro fabrication technologies currently available, radial-gap variable capacitance micro motors appear to be the most advantageous and least problematic design [7,78]. Some of the salient features about the "optimal" configuration arrived at in [7] are discussed below.

A 3:2 ratio (number of stator electrodes:number of rotor poles) rather than the conventional 3:1 ratio normally adopted for three phase machines was used as an "optimal"

design criterion. This decision was arrived at by calculating the maximum average torque exerted on the rotor over one complete rotor revolution assuming synchronous conditions and what effectively corresponds to a maximum rotor angle. Making such an assumption, of course, presumes that some form of rotor position sensing is available in order to switch the stator phases at the proper times.

Operation is thus similar to a switched reluctance motor [38]. However, the consequence of using a 3:2 ratio is a reduction by a factor of 2 in the synchronous speed. Since the maximum average torque may not necessarily double, the maximum average developed power could actually decrease on the whole. Therefore, the effects of this 3:2 ratio must be carefully weighed.

An air-gap spacing as small as possible is most desirable. Taking the limited resolution of the lithography and etching process into consideration, a clearance of approximately 1.5 μm between stator and rotor is about the best that one can hope for.

For structures with an equal number of teeth on the rotor and stator, Mukherji [39] and Bollée [40] determined that the maximum average torque results when :

- the air-gap is as small as possible.
- the tooth width to tooth pitch ratio is approximately 0.38.
- the tooth pitch to gap width ratio is around 8.

Furthermore, the tooth slot depth need not be more than 5 times the air-gap width as long as the tooth pitch is less than 30 times the air-gap width. Based upon the above considerations, Bart [7] recommends a design consisting of 24 stator electrodes, 16 rotor poles, a 1.5 μm air-gap and a 50 μm rotor radius.

3.3 PRACTICAL DIFFICULTIES

The design of a working silicon micro motor is a formidable task. Since the entire field of silicon micromechanics is relatively new in its own right, there are still a number of obstacles to overcome before any micro mechanical system is ready for commercial use. Some of the most important and problematic issues are outlined in brief in the subsequent sections. For the most part, these are difficulties which have not yet been completely resolved at the time of this writing. As mentioned earlier, no practical methods for the extraction of mechanical power from a radial-gap silicon micro motor are available, a fact that reflects to some degree the challenges facing researchers in this field and the infancy of the technology.

3.3.1 Friction and Wear

Frictional forces and mechanical wear characteristics have surfaced as two problems worthy of immediate attention. So far, the retarding frictional forces have emerged as a major stumbling block to successful micro motor development [8,10,11]. Larger than expected drive voltages and exceedingly small rpm levels indicate that frictional forces are significant [8,11]. Air levitation of the rotor structures has been required in several designs [10]. Special friction-reducing mechanisms are already included in some prototype motor designs. One such feature places hemispherical bushings on the under side of the rotor to reduce the contact surface area between rotor and substrate [8]. In another design, a flanged hub is used in an attempt to reduce the length of the frictional moment arm and hopefully produce a smaller frictional counter torque [8,11]. A couple of material combinations have also been tried. The main purpose is to use a pair of materials exhibiting a small coefficient of friction

[8]. Silicon nitride spacers placed on the vertical walls of the rotor and stator and between the rotor and hub serve as friction reducing lubricants and protection from mechanical wear [8,11]. Coplanar rotor and stator structures and ensuring good electrical connection between the rotor and the grounding plane help reduce the magnitude of undesirable vertical pull-down forces [8,10].

The dynamic coefficient of friction for polysilicon on silicon has been estimated to lie in the range 0.25 to 0.35 [5]. The source of friction in that work was considered to be the sliding of the polysilicon bushing on the underside of the rotor over the silicon substrate. An additional viscous drag term was also included in the model. The frictional force was assumed to be dependent only on the mass of the rotor and the radius of the bushing. The viscous drag force was calculated from a continuum model based on the shear force exerted on the underside of the rotor assuming laminar flow conditions. A laser tachometer was used to record the rotor velocity and a least squares fit was carried out to find the best estimate for the dynamic coefficient of friction after the removal of the air drive.

Estimates for the dynamic coefficient of friction between polysilicon and silicon nitride lie in the range 0.21 to 0.38 [6]. In that analysis, the retarding torque is assumed to originate from a constant term due to trapped charges at the surface of the rotor and hub and a position dependent term resulting from lateral movement of the rotor. The dynamical equation of motion was solved for various coefficient values and compared to videotaped rotor movements showing the number of velocity reversals.

In both of the experiments reported on in [5] and [6], the authors estimated the lifetime of their devices at about 1 million revolutions before rotation stopped.

Bart [7] uses stroboscopic dynamometry to produce a position versus time response of a selected radial-gap micro motor to an applied step voltage. Several different parameters were included in the proposed model and a least squares fit was done on the data in order to obtain estimates of these parameters. Included in the model are :

- a viscous drag term.
- a constant friction term.
- a voltage dependent sliding friction term.

The statistical analysis reported in Bart's thesis demonstrated that the postulated constant component of frictional torque (possibly due to trapped charges in the rotor, bearing or substrate coupled with inadequate grounding of the rotor due to oxide formation on polysilicon surfaces) was not important. Total frictional torque seems to be around 10% of the available drive torque. By carefully designing the bushing structures, the frictional torque arising from bushing-substrate contact can be made small relative to the rotor-bearing frictional torque (due to side pull). While viscous drag torque is negligible at low speeds, it becomes appreciable at higher speeds (estimated at 8% of total drive torque for a rotor speed near 48,000 rpm).

3.3.2 Rotor Instability

In radial-gap motors, the rotor is free to both rotate and translate. Vertical forces are not so problematic. Grounding the rotor by ensuring good electrical contact between the

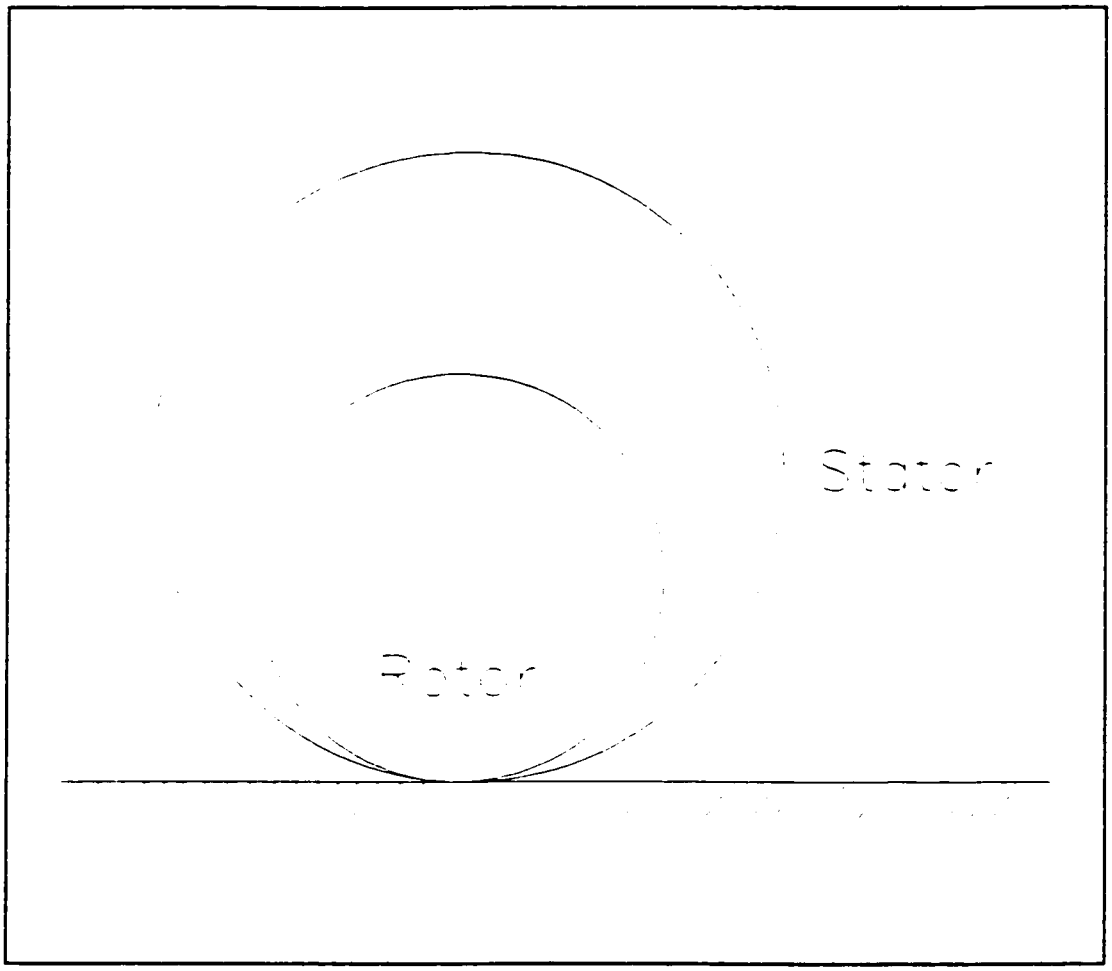

Figure 3.3: Concept of a wobble motor.

bushings and the shield helps reduce the forces tending to clamp the rotor down to the substrate. Forces pulling the rotor up into the plane of the stator are beneficial since this effect alleviates some of the frictional sliding forces between the bushings and the ground plane [10]. Lateral forces on the rotor are cancelled by mechanical reaction forces produced by the centre bearing. However, these forces produce frictional counter torques dependent on both the size of the lateral force and the radius of the bearing structure.

3.3.3 Lack of Active Surface Area

Because of the restrictions placed on the thickness of the rotor and stator structures, one of the concessions that must be made when adopting a radial-gap variable capacitance micro motor topology is a reduction in the active area of rotor - stator overlap. The result is a smaller generated torque. Harmonic motors or "wobble" motors (figure 3.3) do not suffer from this problem [27,41]. Furthermore, the unwanted clamping forces which plague other micro motor designs are the driving forces in these machines. The basic concept of the wobble motor is to cause a structure of lesser circumference to roll around inside the surface of a second structure of larger circumference. Because the two structures possess different circumferences, a differential rotation of the member containing the smaller of the two circumferences results. Another attribute related to harmonic or wobble motors is a smaller retarding frictional force. Since the rotor does not slide but rolls, the coefficient of friction is reduced. Motors of this type are not considered in this work.

3.3.4 Warpage of Thin Films

The thin film nature of both stator and rotor structures makes warpage of these parts a concern [4]. It is possible for polysilicon films to possess a compressive residual stress that could cause the film to bend [36,42]. Through high temperature annealing or simply by increasing the thickness of the films, this problem can be satisfactorily dealt with [4].

3.3.5 Integration with Electronics [4]

Integrated rotor position sensing necessitates that electronic circuit components and

micro mechanical devices be integrated onto a common substrate. Off chip drive electronics may introduce intolerable parasitic capacitances which severely restrict the performance of electric micro motors. Although micro machining technology uses conventional electronic thin films, the delicate process requirements involved in the fabrication of electronic components place stringent limits upon techniques employed in the fabrication of micro mechanical devices.

3.4 THE CHOSEN DESIGN

One specific electric micro motor design is studied in detail in this work. It should be noted, however, that all material presented in the remainder of this thesis applies equally to other configurations. Some of the design particulars are:

- 12 stator electrodes.
- 4 salient rotor poles.
- rotor outer diameter = 50 μm.
- stator outer diameter = 75 μm.
- air-gap spacing = 1.5 μm.
- stator electrode width to pitch ratio = 0.4
- rotor pole width to pitch ratio = 5:18

A 3:1 stator electrode:rotor-pole ratio is chosen instead of the 3:2 configuration adopted by Bart [7] so that the electrically actuated device rotates at the same speed as the example permanent magnet motor when driven with the same excitation frequency. No rotor-position sensing mechanisms are assumed to be present and the motor is run open-loop. With

balanced three phase sinusoidal voltage excitation, the VC motor is an electrically actuated analog of the classical three phase variable reluctance synchronous motor. Vernier type synchronous motors like the ones discussed in [43] and [44] are not considered.

As a result of the decision to use only 4 rotor poles, the number of teeth on the stator and rotor differ considerably. Hence the criteria necessary for the optimal guidelines of §3.2 to be valid are not met. For the type of motor under consideration here, the maximum average torque is a function of ;

- the rotor or power angle δ.
- the magnitude of the second harmonic component of mutual capacitance.

No attempt is made to optimize the design. Machine dimensions are chosen to be consistent with current micro machining fabrication procedures. A rotor plane cross sectional view appears in figure 3.4. This particular micro motor is similar to a design which has already been built [7].

3.5 ANALYTICAL ANALYSIS

Since steady state motor operation under balanced three phase voltage excitation is the principal framework in which the performance of the electrically actuated device is being assessed, we shall start the analysis by considering only the fundamental components of the various phase quantities. The evaluation of torque and power is carried out under the assumption that all electrical input power to the machine originates solely from the fundamental components of phase voltage and phase current.

3.5.1 Three Phase Analysis

Consider the three stator electrodes numbered 2, 4 and 6 in figure 3.4. The charge residing on these electrodes can be written as :

$$\begin{aligned} q_a &= c_{11}(v_a - v_r) - c_{12}(v_b - v_r) - c_{13}(v_c - v_r) \\ q_b &= -c_{21}(v_a - v_r) + c_{22}(v_b - v_r) - c_{23}(v_c - v_r) \\ q_c &= -c_{31}(v_a - v_r) - c_{32}(v_b - v_r) + c_{33}(v_c - v_r) \end{aligned} \qquad \textbf{(3.1)}$$

where ;

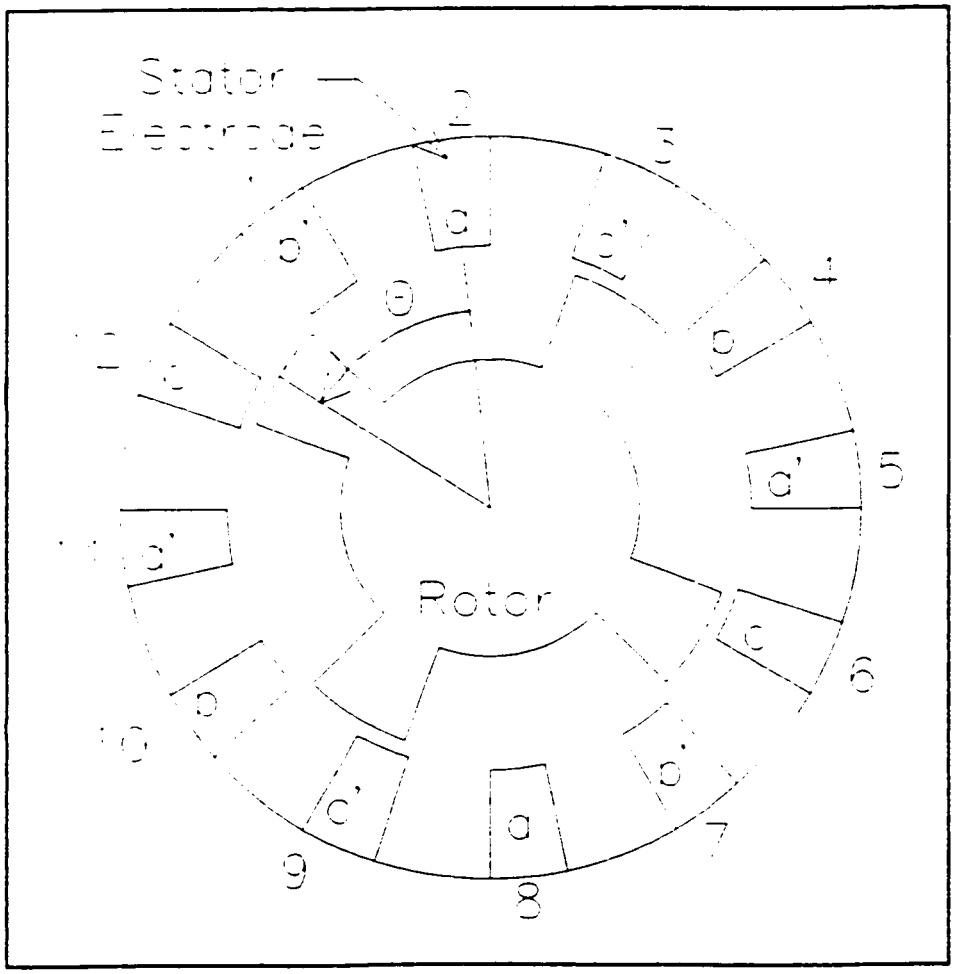

Figure 3.4: Rotor plane view of the VC micro motor under study.

- (v_a-v_r), (v_b-v_r) and (v_c-v_r) represent the potential differences existing between each of the electrodes (2, 4, 6 respectively) and the rotor which serves as a reference potential.
- c_{11}, c_{22} and c_{33} represent the self capacitance of each electrode.
- c_{12}, c_{21}, c_{23}, c_{32}, c_{13}, c_{31} represent the mutual capacitances between the electrodes.

The mutual capacitance terms reflect the fact that there is some degree of coupling between an electrode and the electrodes immediately on either side. Coupling between electrodes that are not directly adjacent to each other is negligible when the rotor is held at a fixed potential.

With sinusoidal voltage excitation and with the rotor turning at synchronous speed $\omega_r=2\omega_s/N_p$, only the average and second harmonic components of the self and mutual capacitances will produce a fundamental current harmonic. The self capacitances can be written as :

$$\begin{aligned} c_{11} &= C_0 + C_2\cos(2\theta) \\ c_{22} &= C_0 + C_2\cos(2\theta - \frac{2\pi}{3}) \\ c_{33} &= C_0 + C_2\cos(2\theta + \frac{2\pi}{3}) \end{aligned} \qquad \textbf{(3.2)}$$

and the mutual capacitances as :

all phase quantities (current, voltage and charge) as the sum of two "orthogonal" sinusoids. The technique derives its name from the method used to determine the amplitude of each function. For an illustration of the method, see the following discussion.

a) ***Direct Axis Quantities***

Consider the hypothetical phase 'a' electrode voltage and current waveforms shown in figure 3.5. Our aim is to express each of these functions as a sum of two orthogonal

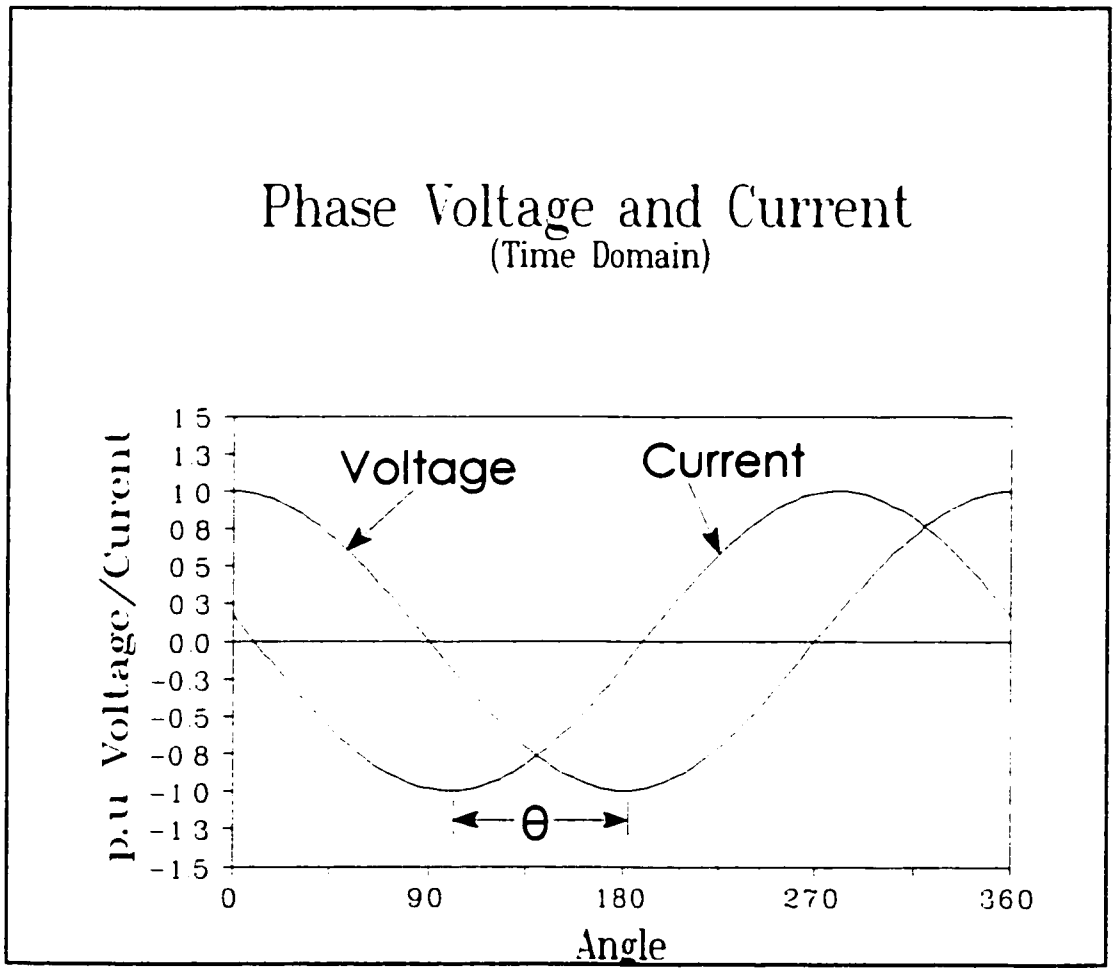

Figure 3.5: Phase 'a' fundamental components.

sinusoids. Because we are dealing strictly with sinusoidal functions of equal frequency, it will be easier to work with phasors rather than the actual time domain waveforms. The phasor diagram in figure 3.6 represents the chosen electrode quantities at the instant the voltage on the phase 'a' electrode reaches its peak value.

In this particular situation, the axis of the rotor poles, called the direct axis, subtends an angle of $-\delta$ radians measured counter clockwise from the axis of the phase 'a' electrode. The instantaneous value of any one of these quantities can be obtained by projecting the

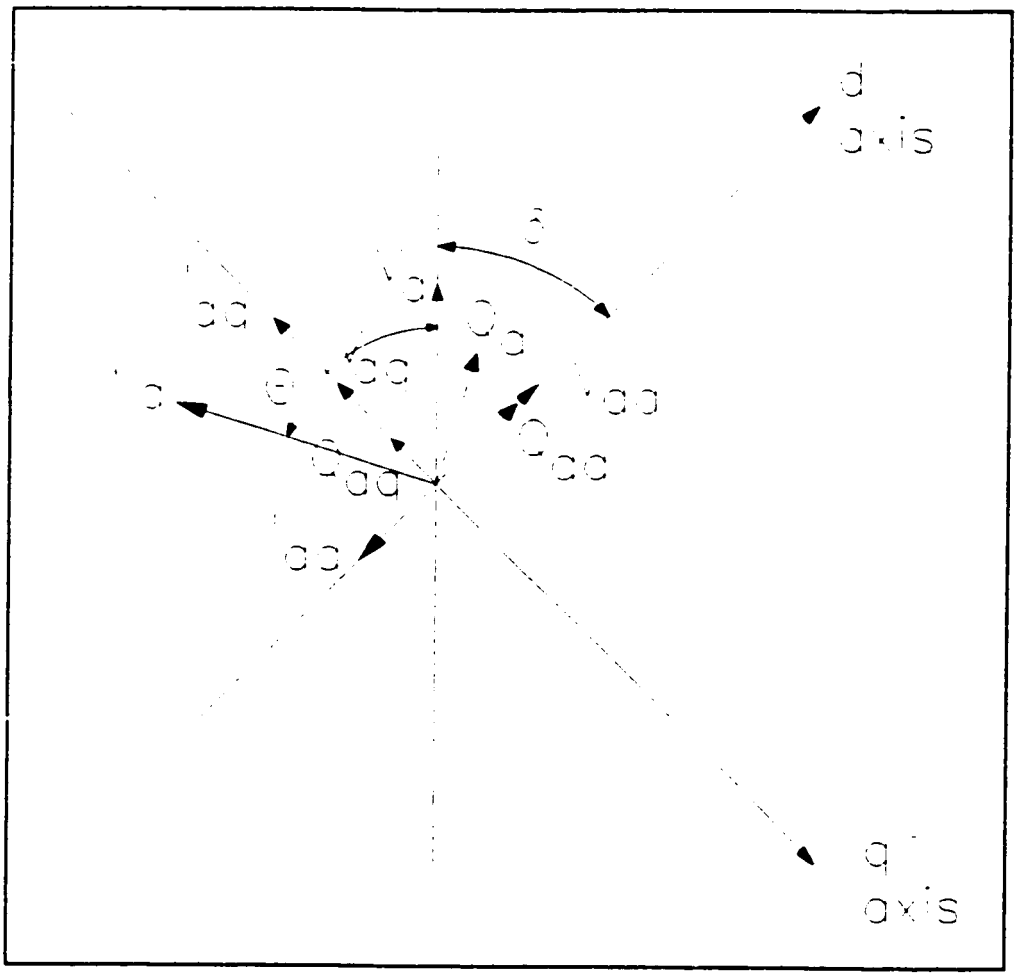

Figure 3.6: Phasor diagram representing phase 'a' quantities.

corresponding phasor onto the vertical axis.

Having outlined the circumstances portrayed by the phasor diagram of figure 3.6, we now proceed with a series of definitions. The projection of the current phasor onto the direct axis is given the symbol $\mathbf{I_{ad}}$ and defines the direct axis current. In a similar way, we define the direct axis voltage $\mathbf{V_{ad}}$ as the projection of the voltage phasor onto the same axis. The projection of these phasors onto the direct axis establishes the instantaneous value of each electrode quantity when the direct axis coincides with the axis of the phase 'a' electrode.

The direct axis synchronous capacitive susceptance $\boldsymbol{\beta_{cd}}$ is defined as :

$$\beta_{cd}=\omega_s C_d \qquad \textbf{(3.6)}$$

where $\mathbf{C_d}$ is termed the direct axis capacitance and $\boldsymbol{\omega_s}$ is the radian frequency of the supply. The direct axis capacitance $\mathbf{C_d}$ is defined as the ratio of direct axis charge $\mathbf{Q_{ad}}$ to direct axis voltage $\mathbf{V_{ad}}$.

b) ***Quadrature Axis Quantities***

In order to obtain the quadrature axis quantities, we simply project the current and voltage phasors onto the axis which lies perpendicular to the direct axis. These two projections are referred to as the quadrature axis current $\mathbf{I_{aq}}$ and the quadrature axis voltage $\mathbf{V_{aq}}$ respectively. Just as we did in the direct axis case, we define a quadrature axis synchronous capacitive susceptance $\boldsymbol{\beta_{cq}}$ as :

$$\beta_{cq}=\omega_s C_q \qquad \textbf{(3.7)}$$

where $\mathbf{C_q}$ is termed the quadrature axis capacitance. The quadrature axis capacitance $\mathbf{C_q}$ is obtained in a manner similar to the one used to calculate the direct axis capacitance. $\mathbf{C_q}$ is defined as the ratio of quadrature axis charge $\mathbf{Q_{aq}}$ to quadrature axis voltage $\mathbf{V_{aq}}$.

Once $\mathbf{C_d}$ and $\mathbf{C_q}$ have been obtained, it is possible to express $\mathbf{I_{ad}}$ and $\mathbf{I_{aq}}$ in terms of $\boldsymbol{\beta_{cd}}$ and $\boldsymbol{\beta_{cq}}$:

$$\begin{aligned} I_{ad} &= \omega_s Q_{aq} = \omega_s C_q V_{aq} = \beta_{cq} V_{aq} \\ I_{aq} &= -\omega_s Q_{ad} = -\omega_s C_d V_{ad} = -\beta_{cd} V_{ad} \end{aligned} \qquad \textbf{(3.8)}$$

3.6 dq0 ANALYSIS: GENERAL CASE

In this section, a more mathematical approach to the **dq0** axis transformations than the one offered in the previous section is given. Whereas the discussion of §3.5 dealt specifically with the sinusoidal steady state, the concepts behind the direct and quadrature axis analysis can be extended and applied to a general dynamical treatment of the device.

In §3.5, we were able to find two "orthogonal" voltage phasors that, when superposed, produced an overall excitation equivalent to that of a balanced three phase set of voltages. In the general case however, it may be necessary to include a third voltage (the zero sequence component) in order to replicate, by superposition, the effects of the original three phase voltages. The matrix which maps the phase voltages into the **dq0** voltages is given by equation (3.9) [32].

$$[T]=\frac{2}{3}\begin{bmatrix} \cos(\theta) & \cos(\theta-\frac{2\pi}{3}) & \cos(\theta+\frac{2\pi}{3}) \\ -\sin(\theta) & -\sin(\theta-\frac{2\pi}{3}) & -\sin(\theta+\frac{2\pi}{3}) \\ \frac{1}{2} & \frac{1}{2} & \frac{1}{2} \end{bmatrix} \qquad \textbf{(3.9)}$$

A physical interpretation of equation (3.9) can be found in most textbooks written on the subject of rotating machines. However, since the machines considered in those works are magnetic in nature, the intuitive approach adopted by their authors makes use of magnetomotive force (MMF) concepts rather than voltages. Regardless, the pre-multiplication of a column vector containing any three phase quantities by **[T]** will map them into **dq0** variables. The following two paragraphs offer a brief account of the main ideas.

The essential part of the method entails breaking up the vector containing the instantaneous stator phase EMF's and expressing it as a linear combination of three groups of three phasors; a direct axis set, a quadrature axis set and a zero sequence set. Within each group, the phasors are of equal magnitude. The phasors within the direct axis group and the quadrature axis group lie at 120° electrical intervals. The zero sequence phasors are all in phase and therefore lie along a common axis.

To calculate the group of direct axis EMF phasors;

i) vectorially sum the stator EMF's using the spatial axis of each phase as a direction indicator and the instantaneous phase value as a scalar multiplier. Project the resultant onto the direct axis and scale this

vector by a factor of ⅔.

ii) the balanced set of time domain EMF phasors which produce this EMF along the direct axis constitute the direct axis set of EMF phasors.

The group of quadrature axis time domain phasors can be obtained in the same way except the resultant vector should be projected onto the quadrature axis instead of the direct axis. Zero sequence phasors can be found by subtracting the direct and quadrature axis time domain phasors from the appropriate stator EMF phasor.

By pre-multiplying a column vector of **dq0** variables by $[\mathbf{T}]^{-1}$ we can recover the original phase quantities. The inverse of the transformation matrix [**T**] is given by :

$$[T]^{-1} = \begin{bmatrix} \cos(\theta) & -\sin(\theta) & 1 \\ \cos(\theta-\frac{2\pi}{3}) & -\sin(\theta-\frac{2\pi}{3}) & 1 \\ \cos(\theta+\frac{2\pi}{3}) & -\sin(\theta+\frac{2\pi}{3}) & 1 \end{bmatrix} \qquad \textbf{(3.10)}$$

Perhaps the most appealing aspect of this transformation is the outcome of the matrix products which appear in equations (3.11) and (3.12) :

$$[C_{dq}] = [T][C][T]^{-1} \qquad \textbf{(3.11)}$$

$$[L_{dq}] = [T][L][T]^{-1} \qquad \textbf{(3.12)}$$

As long as the elements of the capacitance matrix [**C**] and the inductance matrix [**L**] possess only average values and appropriately related harmonic terms dependent on 2θ, the matrix product operation will remove any dependence on rotor angular position. Hence, the governing ordinary differential equations become somewhat easier to solve. This is especially true for sinusoidal steady state operation. In this case, the differential equations reduce to algebraic equations.

3.7 AVERAGE POWER: SINUSOIDAL STEADY

In §3.5.1 instantaneous power and torque were formulated in terms of the phase currents and phase voltages. When only the fundamental components are considered, the average power consumed by the variable capacitance motor over one cycle of the electrical supply is given by :

$$P_{3\varphi} = 3N_p V_\varphi I_\varphi \cos(\alpha) \qquad \textbf{(3.13)}$$

where α is the angular phase shift between current and voltage for any one of the phases and V_φ and I_φ are the RMS magnitudes of the phase voltage and line current respectively.

For reasons which will become apparent in the next chapter, it is desirable to express the average power in terms of the previously defined direct and quadrature axis values. After the **dq0** decomposition, V_{sd} and I_{sd} are in phase as are V_{sq} and I_{sq}. Therefore, the average power for a phase 'a' electrode is simply :

$$
\begin{aligned}
P_{\varphi} &= \frac{1}{2}(V_{ad}I_{ad} + V_{aq}I_{aq}) \\
&= \frac{1}{2}(V_{ad}\beta_{cq}V_{aq} - V_{aq}\beta_{cd}V_{ad}) \\
&= \frac{1}{2}V_{ad}V_{aq}(\beta_{cq} - \beta_{cd})
\end{aligned}
\tag{3.14}
$$

Since $\mathbf{V_{ad}}$ and $\mathbf{V_{aq}}$ are related to the electrode voltage $\mathbf{V_a}$ by :

$$
\begin{aligned}
V_{ad} &= V_a \cos(\delta) \\
V_{aq} &= -V_a \sin(\delta)
\end{aligned}
\tag{3.15}
$$

the total average power expressed in **dq0** axis parameters is :

$$
P_{3\varphi} = (\frac{3}{2}) N_p V_a^2 \frac{\sin(2\delta)}{2} [\beta_{cd} - \beta_{cq}] \tag{3.16}
$$

With equation (3.13) and equation (3.16) we now have at our disposal two means by which the average power of a VC motor can be obtained. What remains is to develop a procedure through which the necessary lumped parameter values can be obtained. For example, in equation (3.16) values for $\boldsymbol{\beta_{cd}}$ and $\boldsymbol{\beta_{cq}}$ must be known before the average power can be computed. Similar consideration given to equation (3.13) shows that the elements of the phase capacitance matrix in equation (3.17) must be known in order to calculate the phase current $\mathbf{I_{\varphi}}$.

$$
[C] = \begin{bmatrix} c_{11} & -c_{12} & -c_{13} \\ -c_{21} & c_{22} & -c_{23} \\ -c_{31} & -c_{32} & c_{33} \end{bmatrix} \tag{3.17}
$$

The form of each matrix element in equation (3.17) is given in equation (3.2) and equation (3.3). These phase capacitance coefficients need to be calculated if we are to use equation (3.13) to calculate average power. Chapter 4 considers the calculation of lumped parameter values using the finite element method. A technique for obtaining the **dq0** axis parameters for a VC motor without intermediate phase capacitance calculations is presented.

CHAPTER 4

NUMERICAL CALCULATION

OF LUMPED PARAMETERS

The two axis or **dq0** method has proven to be a very versatile tool in both the design of conventional rotating machines and in the analysis of large interconnected systems (the electrical power grid for example). Until recently quantitative examinations of silicon micro motors have not included this type of analysis [16,17]. The main contribution made by this chapter includes extending the techniques used by conventional machine designers for the purpose of estimating direct and quadrature axis synchronous inductive reactances, to the calculation of the direct and quadrature axis synchronous capacitive susceptances for the micro motor shown in figure 3.4. Once evaluated, these values will be used to scrutinize the performance capabilities of the example micro motor.

4.1 GOVERNING EQUATIONS

The expressions for power and torque developed in chapter three assume prior knowledge of a number of lumped electrical parameters. For example, implied in equation (3.16) is the fact that values for the direct axis capacitance $\mathbf{C_d}$ and the quadrature axis capacitance $\mathbf{C_q}$ are known. Furthermore, the operation of a simple permanent magnet

synchronous motor will also be of interest for comparative purposes. When examining this device, it will be necessary to calculate an inductance parameter $\mathbf{L_d}$ in order to obtain an estimate for the direct axis synchronous inductive reactance of this machine.

4.1.1 Electric Scalar Potential

Once solved for the unknown nodal potential fields, the governing partial differential equations shown below in equations (4.1) and (4.3) yield the information needed to calculate the above mentioned lumped parameter values. Restricting the analysis to two dimensions the equations are as follows [45] :

$$-\varepsilon(x,y)\nabla^2\varphi(x,y)=\rho(x,y) \qquad \textbf{(4.1)}$$

where ε is the permittivity of the material (assumed to be linear), φ is the electric scalar potential and ρ is the volume electric charge density. For electric field problems pertaining to silicon micro motors, the electric scalar potential within a given region can be uniquely prescribed via the boundary conditions. Surface charges reside on electrode surfaces but no volume charge density exists anywhere inside the region. Under these circumstances equation (4.1) reduces to :

$$\nabla^2\varphi=0 \qquad \textbf{(4.2)}$$

4.1.2 Magnetic Vector Potential

$$\nabla \times \frac{1}{\mu} \nabla \times A_z = J_z \qquad (4.3)$$

where μ is the magnetic permeability, $\mathbf{A_z}$ is the z axis component of the magnetic vector potential and $\mathbf{J_z}$ is the z axis component of the volume current density.

While equation (4.2) is linear in all cases equation (4.3) is not. The magnetic permeability μ is, in general, a nonlinear function of the magnetic flux density **B**. Since magnetic flux density and magnetic vector potential **A** are related by :

$$B = \nabla \times A \qquad (4.4)$$

equation (4.3) is a nonlinear partial differential equation. Note that in a two dimensional analysis variations of any quantity in the axial direction are ignored.

4.2 THE FINITE ELEMENT METHOD

The finite element method today is a popular and widely accepted method for the numerical solution of partial differential equations. Those who deal with the solution of field problems (electromagnetic, fluid, thermal, structural etc.) find the technique particularly useful. Much of its success can be attributed to the relative ease with which the method copes with nonlinear material behaviour and complicated geometries.

Together, these two factors make the finite element method an extremely valuable tool for the analysis and design of conventional magnetic machines. In this thesis, the study of an example silicon micro motor is facilitated by the use of a commercial finite element package

(MagNet 2D). By employing the finite element method, lumped parameter values related to electrically and magnetically actuated devices can be estimated. Configurations that resemble actual machine geometries (and materials exhibiting nonlinear characteristics if so desired) can be included in the two dimensional models.

4.2.1 Basic Concepts

The mathematical basis of the finite element method is extensively documented in the literature. See for example Hoole [45] or Silvester and Ferrari [46]. In this section, only a very brief account of the method is presented.

Essentially, the finite element method obtains values for a finite number of unknown nodal potentials by attempting to minimize an objective function or satisfy some optimality criterion. The problem domain is discretized by dividing it up into a number of small elements. In our case the elements are triangular. Over each element a trial function is defined. The trial function's independent variables consist of the unknown nodal potentials as well as spatial position. For triangular elements with nodes located only at element vertices, the trial functions are linear (first order) in their dependence on spatial position. With higher order elements, higher order interpolating polynomials can be used by increasing the number of unknowns associated with each element. First order triangular elements are used exclusively in this work.

For problems involving electric scalar potential fields, the finite element method arrives at an approximate solution by minimizing the functional in equation (4.5). This functional is stationary when φ satisfies equation (4.1) :

$$L[\varphi]=\iint\{\frac{1}{2}\varepsilon[\nabla\varphi]^2-\rho\varphi\}\,dR \qquad (4.5)$$

The corresponding functional for magnetostatic cases is :

$$L[A_z]=\iint\{\frac{1}{2\mu}[\nabla A_z]^2-J_zA_z\}\,dR \qquad (4.6)$$

4.2.2 Functional Minimization

Having discretized the solution region into a number of small elements, the integrations appearing in the functionals of equations (4.5) and (4.6) can be evaluated as a sum of individual element integrals. That is, each element will contribute a part to the total integral. Moreover, because the unknown potential fields have been assigned trial functions over each of the elements, the integration can be carried over each element analytically. What we are left with is a function of **n** unknowns. The **n** unknowns are the "weights" of the unknown nodal potentials. For this function to have a local minimum, the **n** partial derivatives must all be zero. It is shown in [45] that the resulting equations constitute a set of **n-k** equations in **n-k** unknowns where **k** is the number of prescribed or Dirichlet boundary conditions.

4.2.3 Equation Solving

In the electrostatic case, these equations are always linear. However, this is not necessarily true for magnetostatic problems. The presence of iron and/or other nonlinear magnetic materials makes these equations nonlinear. The MagNet system [47] uses a Newton iteration technique to solve nonlinear problems. At each linear step of the Newton iteration, and for linear problems, a preconditioned conjugate gradient method is employed. The incomplete Choleski conjugate gradient method is the actual method used by the MagNet system.

4.3 POSTPROCESSING

Post processing is arguably the most important stage of any numerical field simulation carried out in the field of electrical engineering. With the exception of a few special cases, it is not the potential field that is of interest. Instead, it is normally some lumped electrical circuit parameter that one is seeking. Such is the case in this thesis. The performance comparisons undertaken in this work require the evaluation of a number of inductance and capacitance values. The reason for this being that the classical two axis method of analysing synchronous machines has been chosen. In all cases, the average power and torque are functions of direct and quadrature axis parameters. In this section, methods of extracting lumped parameter values from the information contained in a numerical potential field solution are given.

4.3.1 Inductance Calculations

Inductance calculations shall be considered first since the material-based non linearities make them slightly more involved than the calculation of lumped capacitance values. Furthermore, once the concepts underlying inductance calculations have been outlined, capacitance calculations follow almost by "similarity". Only the two-dimensional formulations of the various formulas are presented since variations in the axial direction are neglected.

The two primary definitions generally accepted for inductance calculations differ in that method 1, which is fundamental, makes use of the concept of flux linkages while method 2, which is derived, utilizes the total energy stored in the magnetic field [48].

1. Flux linkage definition; total flux linkages divided by coil current.
2. Energy-based definition; total magnetic energy divided by one half the coil current squared.

Both methods yield what can be considered as saturated inductances when nonlinear or even piecewise linear material models are used. Furthermore, these particular definitions do not apply to incremental inductances since total, ***not*** incremental, flux linkages and coil current values are employed.

a) *Self Inductance of a Coil*

The two methods furnish equal inductance values for linear systems but different values for nonlinear systems (in which the definition of inductance is not clear). Mathematically, the two techniques can be expressed as follows. Using flux linkages, the

inductance of a coil per unit axial length is [48] :

$$L=\frac{1}{i^2}\int_S A_z J_z dS \tag{4.7}$$

In this formulation, the flux linkages per unit length are :

$$\lambda=\frac{1}{i}\int_S A_z J_z dS \tag{4.8}$$

and **i** is the total coil current.

Using the energy-based method **L** is obtained as :

$$L=\frac{2}{i^2}\int_S \{\int_0^B |H|(|B|)d|B|\}dS \tag{4.9}$$

where $|\mathbf{H}|(|\mathbf{B}|)$ is the magnetic field strength in A/m. The dependence of **H** on **B** is nonlinear in many materials and can vary with direction if the material is anisotropic. The latter energy-based method assumes initially that the system is linear and uses the following familiar relationship between stored magnetic energy and inductance :

$$W_m=\frac{1}{2}Li^2 \tag{4.10}$$

Note that equation (4.8) can also be used to calculate the stored magnetic energy if the system is linear :

$$\begin{aligned} W_m &= \frac{1}{2}\lambda i \\ &= \frac{1}{2}\int_S A_z J_z dS \end{aligned} \tag{4.11}$$

The MagNet system actually makes use of this relationship when it evaluates magnetic co-energy. Magnetic co-energy is defined as :

$$W_m' = \int_S \{ \int_0^{|H|} |B|(|H|) d|H| \} dS \qquad \textbf{(4.12)}$$

and is employed in static magnetic force/torque calculations. This integral is not actually carried out by the system. Instead, it is obtained indirectly by first taking twice the value resulting from equation (4.11) and then subtracting from that value the amount of stored magnetic energy.

Since material curves are stored by the MagNet system as relative reluctivity versus flux density squared, it is more efficient to evaluate the following integral which really represents twice the stored magnetic energy :

$$2W_m = \int_S \{ \int_0^{|B|^2} \frac{1}{\mu} d|B|^2 \} dS$$

$$2W_m = \int_S \{ \int_0^{|B|^2} \nu(|B|^2) d|B|^2 \} dS \qquad \textbf{(4.13)}$$

b) ***Mutual Inductance Between Coils***

Just as there are two alternative methods for the calculation of a coil's self inductance, there are two analogous methods for the determination of the mutual inductance between coils. As expected, one can use either a flux linkage method or an energy-based method.

The mutual inductance between two coils is defined as the total number of flux linkages of one coil (carrying zero current) caused by a current flowing in the second coil. Therefore the mutual inductance between two coils, coil 1 and coil 2, can be thought of as either the flux linking coil 1 due to a current in coil 2 ($\mathbf{M}_{12}$) or as the flux linking coil 2 due to a current in coil 1 ($\mathbf{M}_{21}$). Conservation of energy considerations [32] demand that $\mathbf{M}_{12}=\mathbf{M}_{21}$.

From a finite element field solution, the mutual inductance per unit axial length $\mathbf{M}_{12}$ can be estimated from :

$$M_{12}=\frac{1}{i_1 i_2}\int_S A_z J_{1z}\,dS \qquad \textbf{(4.14)}$$

The vector potential field used must be the one obtained by exciting coil 2 only. The current density in coil 1 serves only as a "filter" and permits the calculation of flux linkages using the method of equation (4.8).

Using the energy-based method, two finite element solutions are necessary. In the first run, coil 1 and coil 2 carry currents $\mathbf{i}_1$ and $\mathbf{i}_2$ respectively. The total stored magnetic energy is calculated and denoted as $\mathbf{W}_1$. For the second run we reverse the direction of one of the currents and calculate the energy $\mathbf{W}_2$. The mutual inductance $\mathbf{M}_{12}$ per unit axial length can then be obtained using :

$$M_{12}=\frac{W_1-W_2}{2i_1 i_2} \qquad \textbf{(4.15)}$$

4.3.2 Capacitance Calculations

The linearity of electrostatic field problems in air alleviates the ambiguity problem we encountered when dealing with inductance calculations. Just as there are two methods available for the evaluation of inductance parameter values, there are also two methods for the calculation of capacitance values. Either a charge based method or an energy-based method can be employed. Both techniques shall be demonstrated in the ensuing discussion.

a) ***Self Capacitance***

The total charge **Q** residing on a conductor held at a potential of **V** Volts above some reference conductor with all other conductors at the same potential as the reference conductor is proportional to that voltage. Being a linear system, this proportionality term is constant and does not depend on **V** :

$$Q = C\,V \tag{4.16}$$

By integrating the normal component of the negative gradient of the electric scalar potential field around a contour immediately surrounding the electrode, it is possible to obtain a numerical estimate for the value of **Q**. The scalar potential field can be attained from a finite element simulation.

$$Q = \int_{\Omega} (-\varepsilon \nabla \varphi) \cdot \hat{n}\, d\Omega \tag{4.17}$$

Here, **Ω** represents the contour of integration surrounding the electrode of interest. Actually, equation (4.17) yields the charge per unit axial length owing to the two dimensional

nature of the field problem.

Using an energy-based method similar to the one used when calculating inductances, the capacitance can be found from the following equation :

$$C = \frac{2W_e}{V^2} \tag{4.18}$$

where $\mathbf{W_e}$ is the stored electrical energy. From a finite element field solution, we can find $\mathbf{W_e}$ using :

$$W_e = \int_S \{ \int_0^{E} |D|(|E|)\, d|E| \}\, dS$$
$$W_e = \int_S \{ \int_0^{E} \varepsilon |E|\, d|E| \}\, dS \tag{4.19}$$

where $|\mathbf{D}|$ is the electric flux density in C/m^2. For most materials $|\mathbf{D}|$ is linearly dependent on $|\mathbf{E}|$.

Again, keep in mind that this formulation yields energy and hence capacitance per unit axial length.

b) ***Mutual Capacitance***

The concept of a mutual capacitance between two conductors is very much the same as the concept of a mutual inductance between two coils. Given conductor 1 and conductor 2, the mutual capacitance between them is defined as :

$$C_{12} = C_{21} = \frac{Q_{12}}{V_2} \tag{4.20}$$

where $\mathbf{Q_{12}}$ is the charge which resides on conductor 1 when it is at the same potential as the reference conductor and conductor 2 is held at a potential of $\mathbf{V_2}$ Volts above the reference conductor.

If a finite element solution is obtained with $\mathbf{V_1}$=0 and $\mathbf{V_2}$ set to some non-zero value, then equation (4.17) can be used to find the charge on conductor 1 and equation (4.20) will yield the mutual capacitance per unit axial length.

Using an energy-based method, two finite element solutions are needed. In the first run, set conductor 1 at a potential of $\mathbf{V_1}$ Volts above the reference and conductor 2 at a potential of $\mathbf{V_2}$ Volts above reference. Next, calculate the stored electrical energy $\mathbf{W_1}$. For the second run, reverse the sign of one of the potentials and calculate the stored electrical energy $\mathbf{W_2}$ for this case. The mutual capacitance per unit axial length $\mathbf{C_{12}}$ is then obtained using :

$$C_{12} = \frac{W_1 - W_2}{2V_1V_2} \qquad \textbf{(4.21)}$$

A word of caution is called for when using the energy-based formulations given in equations (4.15) and (4.21) to calculate mutual coupling terms. As mentioned by Lowther & Silvester [48], if $\mathbf{W_1}$ and $\mathbf{W_2}$ are nearly equal, the finite precision limitations common to all digital computers will result in a loss of significant figures. To circumvent this problem, we propose a direct calculation of the **dq0** axis parameters in order to bypass the computation of any mutual inductances or capacitances. The techniques are described in §4.4.

4.4 DIRECT AND QUADRATURE AXIS QUANTITIES

The methods introduced in §4.3 dealt with the calculation of "real" or physical quantities. These methods represent techniques which can be used to estimate the self and mutual inductance/capacitance of clearly identifiable coils/electrodes. Unfortunately, when dealing with polyphase machines, it is much too cumbersome to manipulate the governing dynamical state equations in their phase form. Self and mutual phase inductances/capacitances are readily obtained from finite element simulations, but for machines possessing saliency, these quantities are functions of rotor position (see for example equations (3.2) and (3.3)). This feature makes it rather difficult to even determine a machine's sinusoidal steady state operating point for given excitation and load conditions.

The two axis or **dq0** method of treating rotating machines has been used for many years and can be found in almost any textbook written on the subject of conventional rotating machines. It is a very powerful and useful technique. The principal reason is that the transformations produce lumped parameter values (traditionally inductances) which, in the ideal case, no longer possess any dependence on rotor position. As far as sinusoidal steady state operation is concerned, a machine's operating point can be determined simply with the aid of a phasor diagram provided we have knowledge of the pertinent direct and quadrature axis quantities. This concept was discussed in chapter 3. In this section methods of calculating these direct and quadrature axis quantities from the results of a finite element simulation are presented.

Expressions that relate the direct and quadrature axis inductances to the self and mutual components of the phase inductances can be found in some textbooks [32]. However,

calculating the **dq0** parameters in this fashion requires the evaluation of second harmonic mutual inductance terms. For reasons stated earlier this can be undesirable. Furthermore, unless the elements in the phase inductance matrix [**L**] consist strictly of an average value and second harmonic self and mutual inductance terms with appropriately related coefficients, the Park transformation will not yield constant values for the direct and quadrature axis inductances at all rotor positions.

The proposed method for obtaining direct axis and quadrature axis synchronous capacitive susceptances eliminates the need for calculating any harmonic mutual phase capacitance coefficients. This so-called "direct" method originates from ideas put forth by other authors studying conventional magnetically actuated machines.

4.4.1 Direct and Quadrature Axis Inductances

In §4.3.1 two methods for computing coil inductance values from the results of a finite element simulation were given. As expected, two methods also exist for the computation of direct and quadrature axis inductances. Ashtiani and Lowther [49] report on their use of a flux linkage technique while Pavlik *et al.* describe an energy-based formulation [50].

a) *Flux Linkage Method*

Taking phase 'a' as an example, the direct axis inductance $\mathbf{L_d}$ is defined as the ratio of the direct axis component of phase 'a' flux linkages to the direct axis component of phase 'a' current. By aligning the rotor poles along the axis of the phase 'a' coil in the finite element mesh, the task of decomposing the resultant MMF into direct and quadrature axis components

is eliminated. The reason is that if we assume the phase current in that coil is at its maximum value, then the resultant stator MMF vector will lie along the direct axis. We then simply use equation (4.8) to find the flux linkages and divide by the magnitude of the phase current. A similar procedure conducted with the rotor poles positioned in the quadrature axis yields $\mathbf{L_q}$.

Now, if the inductance matrix [**L**] were of "ideal" composition, the outcome of equation (4.8) would be independent of rotor position. The direct and quadrature axis inductance parameters given by :

$$L_d = \frac{\lambda_{ad}}{I_{ad}}$$
$$L_q = \frac{\lambda_{aq}}{I_{aq}} \qquad (4.22)$$

respectively, would exhibit no changes resulting from variations in the rotor's position relative to the magnetic axis of phase 'a'. Unfortunately, because of the presence of space harmonics, the inductance matrix [**L**] cannot be considered ideal. Consequently, $\mathbf{L_d}$ and $\mathbf{L_q}$ must be estimated using a number of finite element simulations in which the rotor's position relative to the axis of phase 'a' is continuously altered.

b) ***Energy-Based Method***

With the rotor poles positioned along the axis of one of the phase coils and with the current in that coil at its maximum value, there will be no quadrature axis component of current. Therefore, if the total energy stored in the magnetic field is :

$$W_m = \frac{1}{2}\lambda_{ad} I_{ad} + \frac{1}{2}\lambda_{aq} I_{aq} \qquad (4.23)$$

and $I_{aq}=0$, then :

$$\lambda_{ad} = \frac{2W_m}{I_{ad}} \qquad (4.24)$$

A similar procedure is conducted to obtain the quadrature axis flux linkages. Align the resultant stator MMF with the quadrature axis and re-solve the finite element problem. The quadrature axis flux linkages are given by :

$$\lambda_{aq} = \frac{2W_m}{I_{aq}} \qquad (4.25)$$

4.4.2 Direct and Quadrature Axis Capacitances

The underlying theory on which the two axis approach is based as well as the essentials of capacitance calculations have already been dealt with. To this effect, little else remains to be said other than a few words regarding the combined application of the finite element method and two axis theory to electrically actuated devices.

a) *Charge Method*

To calculate the direct axis capacitance, align the rotor poles along the axis of one of the phase electrodes. Set the phase voltages such that the applied voltage on the electrode collinear with the direct axis is at its maximum value. The ratio of phase charge obtained

from equation (4.17) to phase voltage for the direct axis electrode will yield the direct axis capacitance. Repeat the procedure with the rotor turned by 90° electrically in order to estimate the quadrature axis capacitance.

b) *Energy-Based Method*

With the direct axis positioned along the axis of one of the phase electrodes, there will be no quadrature axis component of voltage. Therefore, the total energy stored in the air-gap electric field $\mathbf{W_e}$ can be expressed as :

$$W_e = \frac{1}{2} Q_{ad} V_{ad} \qquad \textbf{(4.26)}$$

re-arranging and solving for $\mathbf{Q_{ad}}$ we get :

$$Q_{ad} = \frac{2W_e}{V_{ad}} \qquad \textbf{(4.27)}$$

Using the same voltage excitation but with the rotor displaced 90° electrically from its previous position in the direct axis, the quadrature axis capacitance is obtained using :

$$Q_{aq} = \frac{2W_e}{V_{aq}} \qquad \textbf{(4.28)}$$

Notice that in §4.4.1b) and §4.4.2b) it is the axis flux linkages and axis charge which are given and not the desired axis inductance or capacitance. More will be said of this in chapter 5 when the finite element simulation results are presented.

CHAPTER 5

FINITE ELEMENT RESULTS AND OUTPUT COEFFICIENT CALCULATIONS

This chapter begins with the definition of an output coefficient which serves as a quantitative measure of performance. The methods outlined in chapter four which describe the calculation of lumped parameter values based on finite element simulation results are implemented. Specifically, the direct and quadrature axis synchronous capacitive susceptances for the electrically actuated variable capacitance micro motor of figure 3.4 and the direct axis synchronous inductive reactance of the interior type permanent magnet motor of figure 5.3 are evaluated.

5.1 THE PERFORMANCE INDEX

The performance index used in this work is based upon the output coefficient derived by Honsinger [50]. The output coefficient serves as a kind of "goodness factor" since it relates machine size to output power and speed. In one form, the output coefficient is defined as :

$$\xi_0 = \frac{P}{n_s D_0^3} \tag{5.1}$$

where **P** is the average output power in Watts per metre, $\mathbf{n_s}$ the synchronous speed of the motor in rpm and $\mathbf{D_0}$ the outer diameter of the stator in metres.

Equation (5.1) is a convenient method for calculating the output coefficient of any machine since it is general and can thus be used for both electrically and magnetically actuated devices provided the average output power **P** can be computed.

In its alternate form, the output coefficient is expressed as a function of several key physical quantities which we already know from chapter 2 determine the scaling properties of magnetically actuated machines :

$$\xi_0 \propto B_g J \eta \cos(\theta) \frac{V}{E} f_0(\zeta) \tag{5.2}$$

In equation (5.2), $\mathbf{B_g}$ is the peak value of an assumed sinusoidally distributed air-gap magnetic flux density, **J** is the volume current density, $\boldsymbol{\eta}$ is the machine efficiency, $\cos(\boldsymbol{\theta})$ is the power factor, **V/E** is the ratio of terminal voltage to air-gap voltage, $\boldsymbol{\zeta}$ is the ratio of stator inner diameter $\mathbf{D_i}$ to stator outer diameter $\mathbf{D_0}$ and $\mathbf{f_0(\zeta)}$ is a maximizing function.

5.2 VC MOTOR ANALYSIS

5.2.1 Boundary Conditions

Since the rotor is assumed to be in contact at all times with a ground plane through bushings on the underside of the rotor it is treated as an equipotential surface and its interior region is not discretized. The final finite element mesh contains 2748 nodes and 4972 elements. Boundary conditions on the stator consist of specified or Dirichlet conditions on the equipotential stator poles and natural or Neuman boundary conditions on the arcs connecting the stator poles. Physically, this implies that no lines of electric flux are sourced by or terminate on conductors outside the problem domain. This extremely important fact allows us to choose one of the conductors inside the problem domain and use it as a reference. The potential of the reference conductor relative to any another conductors outside the region is irrelevant. Only the potential differences between the reference conductor and other equipotential surfaces inside the region are of importance.

A bipolar parallel stator electrode connection scheme is used. By this we mean that electrode pairs in figure 3.4 with similar labels are connected together. Relative to the rotor, the electric scalar potential of the primed electrodes is negative that of the corresponding un-primed electrodes. If the stator is driven by a balanced three phase set of voltages, bipolar excitation ensures that the rotor potential remains at the same level as the ground plane. This eliminates any rotor-substrate clamping forces which may be caused by poor bushing-ground plane contact.

5.2.2 Capacitance Calculation Strategy

As mentioned in §4.4, there are two strategies which can be adopted for the evaluation of the direct and quadrature axis capacitances. Method one uses electrode self and mutual capacitances. With this method, it is necessary to obtain coefficient values for the elements of the phase capacitance matrix [**C**] defined in equations (3.2) and (3.3). This method is undesirable because it requires a harmonic analysis of the results in order to extract the pertinent second harmonic self and mutual phase capacitance terms.

The second approach entails evaluating both $\mathbf{C}_d$ and $\mathbf{C}_q$ directly. The energy-based method is used because the finite element method itself is "geared" towards energy-based calculations. Recall from §4.2 that the nodal potentials emerging from a finite element simulation are those which minimize the appropriate energy functional. The charge-based method requires numerical differentiation of the scalar potential field in order to obtain the electric field. The accuracy of the energy-based method is therefore one order higher than that of the charge-based method. It is therefore preferable to use a more accurate global quantity like stored energy, which is directly minimized by the FE method, rather than local information which is not. Results obtained from energy-based calculations are presented in the following sections as axis charge in Coulombs per metre versus rotor angular position.

5.2.3 Requirement for Multiple FE Simulations

Constant direct and quadrature axis capacitances are not anticipated at all rotor positions. The reason is that the presence of higher order spatial harmonics in the self and mutual phase capacitances are expected to produce direct and quadrature axis capacitances

dependent upon the rotor's position relative to the axis of the phase 'a' electrode. As such, to extract the constant component of both $\mathbf{C_d}$ and $\mathbf{C_q}$, a direct calculation of each quantity must be done for a number of rotor positions.

The need for a number of simulations places constraints on the finite element mesh. In particular, if a new mesh were to be constructed for each rotor position, the process would be prohibitively long and especially tedious. Instead, nodes are placed on a circular boundary between the rotor and the air-gap at 2.5° mechanical intervals. This allows us to rotate the rotor mesh and join it with the air-gap/stator mesh without having to construct an entirely new mesh.

A script file (contained in appendix C) contains the Prob2D setup information for each new rotor position. Script files are also used to direct the meshing package, MESH, to rotate the rotor by a pre- specified amount and join it with the air-gap/stator mesh and to drive the postprocessing unit Post2D. The script files themselves are altered via a set of utility programs written in C. The entire process executes from a DOS batch file which loops until an appropriate error level is detected.

5.2.4 Finite Element Results - Direct Axis Excitation

A balanced set of three phase voltages is assigned to the stator electrodes. The peak value of the scalar potential difference between a phase electrode and the rotor is 75 Volts. While this voltage is limited in practice by the maximum permissible electric field strength, it has no influence on capacitance calculations. For every angle from 0° to 90° measured mechanically from the axis of the phase 'a' electrode, the rotor's position is advanced in a

counter clockwise direction at 2.5° intervals. At the same time the applied stator voltages are advanced by 5° electrically in time so that the resultant voltage "vector" continually coincides with the direct axis. The direct axis lies along the centre of the rotor poles. Because the rotor revolves counter clockwise, the phase sequence of the stator voltages must be ***acb*** owing to the spatial arrangement of the phase electrodes in figure 3.4.

After a solution is obtained, the MagNet 2D postprocessor is invoked to calculate the stored electrical energy. The energy values are written to a file for storage and used for further processing. Equation (4.27) is used to calculate the direct axis charge. The results of this simulation are plotted in figure 5.1.

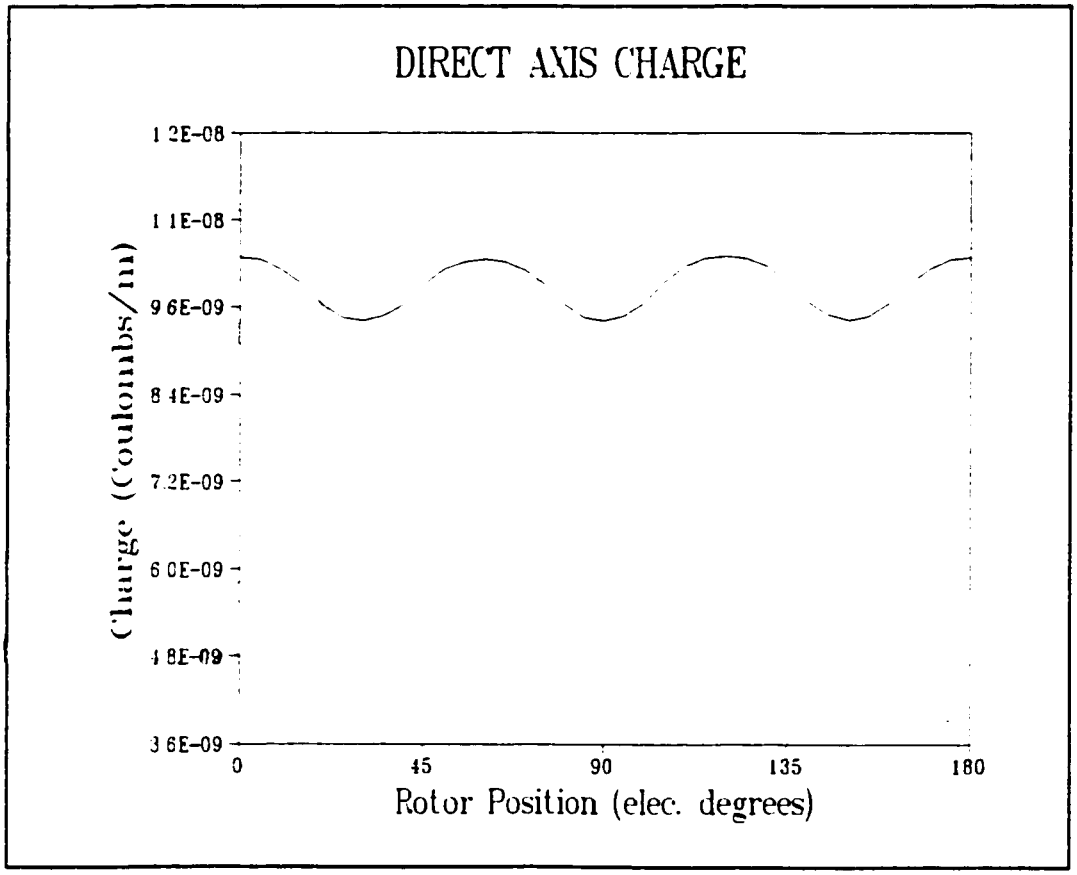

Figure 5.1: Direct axis charge versus rotor position.

5.2.5 Finite Element Results - Quadrature Axis Excitation

A procedure similar to that described in §5.2.3 is used to evaluate the quadrature axis charge for the same rotor positions. However, rather than aligning the resultant voltage "vector" along the direct axis, it is aligned with the quadrature axis. The quadrature axis lies 90° electrically (or 45° mechanically in this case) ahead of or behind the direct axis. The results of the quadrature axis simulation are plotted in figure 5.2.

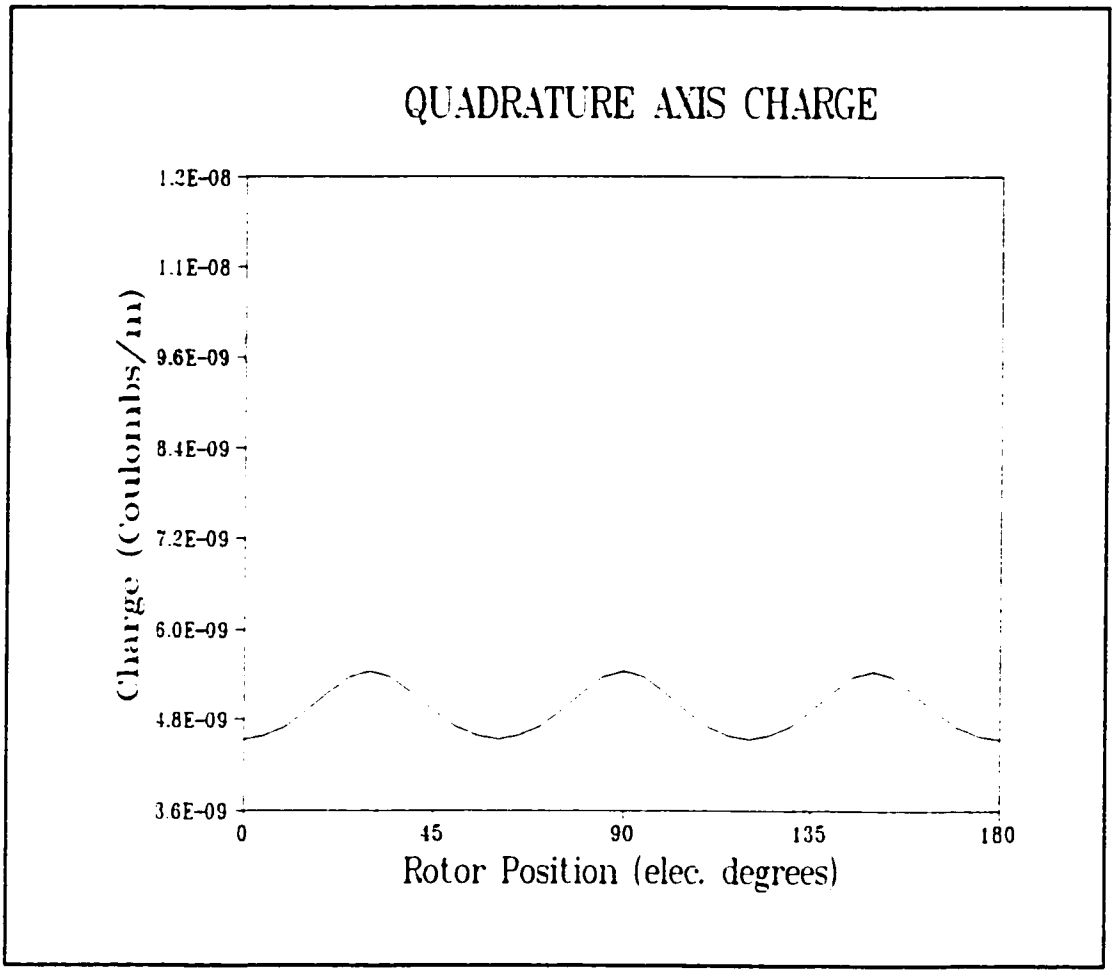

Figure 5.2: Quadrature axis charge versus rotor position.

5.2.6 Determining the Axis Capacitances

From figures 5.1 and 5.2 the direct and quadrature axis capacitances must be extracted. As anticipated, the axis charges (and hence capacitances) are not independent of rotor position. However, it is the sinusoidal steady state operation of the device that we are interested in. The effects of space harmonics are not of any concern and must be "filtered" out if we are to use equation (3.16) to calculate the average power for the electrically actuated micro motor.

Under balanced three phase voltage excitation $\mathbf{V_{ad}}$ and $\mathbf{V_{aq}}$ are constant. Any axis capacitance terms that are responsible for generating harmonics in the axis charge waveforms of order other than zero do not contribute to the average power. Therefore, the components we seek are the constant terms or the average values of each of the curves in figures 5.1 and 5.2. Table 5.1 contains the direct axis and quadrature axis capacitance obtained by averaging the required axis charge curve.

Table 5.1: Direct and Quadrature Axis Capacitances

Voltage (Volts)	Average Energy (Joules/m)	Average Charge (Coulombs/m)	Capacitance (F/m)
$\mathbf{V_{ad}}$=75	$\mathbf{W_c}$=8.35E-07	$\mathbf{N_p Q_{ad}}$=9.89E-09	$\mathbf{N_p C_d}$=1.32E-10
$\mathbf{V_{aq}}$=75	$\mathbf{W_c}$=4.17E-07	$\mathbf{N_p Q_{aq}}$=4.94E-09	$\mathbf{N_p C_q}$=6.59E-11

5.2.7 Performance Index for the VC Motor

We are now in a position to calculate the performance index for the variable capacitance motor. The first step is to calculate the average output power. Equation (3.16), restated below, is used for this purpose :

$$P = \frac{3}{2} N_p V_s^2 \frac{\sin(2\delta)}{2} [\beta_{cd} - \beta_{cq}] \qquad \textbf{(3.16)}$$

With a 1.5 μm air-gap, electric field strengths of 3×10^8 V/m have been sustained without electrical breakdown. In our model this corresponds to an RMS electrode voltage of $V_s/\sqrt{2}=(3\times10^8)(1.5\times10^{-6})/\sqrt{2}= 318$ V.

The direct axis and quadrature axis synchronous capacitive susceptances depend on excitation frequency. Assume for purposes of comparison that ω_s=377 rad/s. Equations (3.6) and (3.7) then determine β_{cd} and β_{cq} :

$$\begin{aligned} N_p\beta_{cd} &= 377\times1.32\times10^{-10} = 4.98\times10^{-8} \text{ S/m} \\ N_p\beta_{cq} &= 377\times6.59\times10^{-11} = 2.48\times10^{-8} \text{ S/m} \end{aligned} \qquad \textbf{(5.4)}$$

In our example motor, the number of poles, N_p, is equal to four and the entire four pole structure of the VC motor is meshed. Therefore, the energy values obtained from the postprocessor after each finite element simulation are four times larger than those which would result if only one "pole" were to be modelled.

With $\sin(2\delta)$ set to a maximum value of 1.0, the output coefficient for the example variable capacitance micro motor using equation (5.1) is :

$$\xi_0 = \frac{3}{2}\left[\frac{318^2 \times (4.98 - 2.48)}{1800 \times (75 \times 10^{-6})^3} \times 10^{-8}\right] \approx 5.0 \times 10^6 \quad \frac{J}{m^4} \qquad (5.5)$$

5.3 PERMANENT MAGNET MOTOR ANALYSIS

The scaling of devices incorporating permanent magnet materials was found to be favourable in chapter 2. In that chapter however, no attempt was made at estimating the size of the machine required to achieve the same performance (ie average output power) as an electrically actuated micromotor. In this section, the results of finite element simulations conducted on a three phase permanent magnet motor are presented. A cross sectional view representative of the example permanent magnet motor is shown in figure 5.3. It is a four pole interior type permanent magnet machine [34] using Samarium Cobalt magnets.

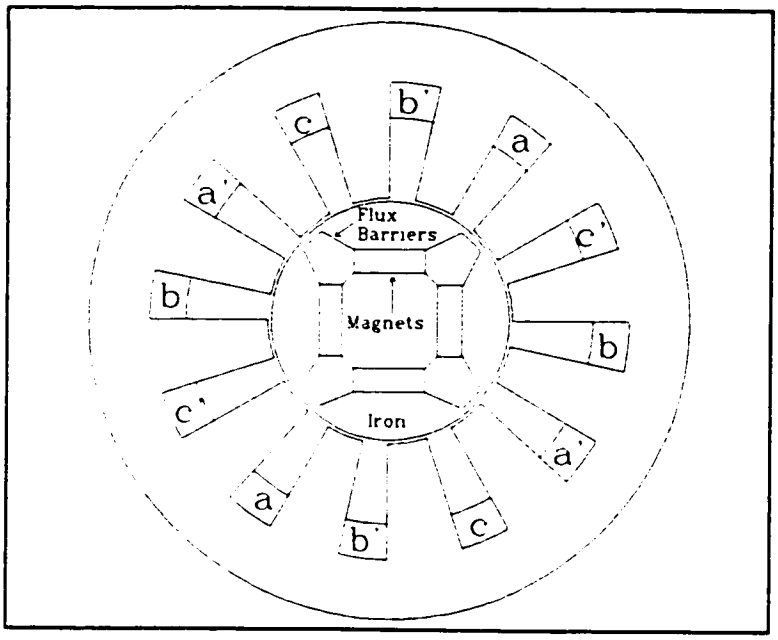

Figure 5.3: An interior type permanent magnet motor.

5.3.1 Average Output Power of a Doubly Excited Motor

Equation (3.16) gives the output power of a three phase variable capacitance motor in terms of direct axis and quadrature axis synchronous capacitive susceptances. A similar expression exists for the average output power of a three phase synchronous motor (with a source of magnetic flux on the rotor) involving direct and quadrature axis synchronous inductive reactances [51] :

$$P = \frac{3V_{\varphi}E_f}{X_{sd}}\sin(\delta) + \frac{3}{2}V_{\varphi}^2\left(\frac{1}{X_{sq}} - \frac{1}{X_{sd}}\right)\sin(2\delta) \qquad \textbf{(5.6)}$$

where $\mathbf{V_\varphi}$ and $\mathbf{E_f}$ are RMS values. As mentioned earlier, the axis parameters $\mathbf{X_{sd}}$ and $\mathbf{X_{sq}}$ appearing in equation (5.6) are obtainable through finite element simulations. The second term in equation (5.6) is a saliency term. Since we are most interested in the effects of the permanent magnets, we will consider only the first term which represents the average power developed by the rotor - stator coupling. From the finite element analysis we will need to determine $\mathbf{X_{sd}}$ and $\mathbf{E_f}$ only.

5.3.2 Finite Element Results - Direct Axis Excitation

The direct axis inductance $\mathbf{L_d}$ is determined using an energy-based technique and equations (4.23) and (4.24). In this simulation, the magnets are "turned off" and given the magnetic properties of free space because of their linearity and near unity relative permeability. The magnetic properties of the core material are those of M19 electrical steel, a typical material used in the construction of small motors. Results are plotted in figure 5.4 as direct axis flux linkages versus rotor position relative to the magnetic axis of the phase 'a'

coil.

5.3.3 Finite Element Results - Field Excitation

Because the rotor voltage is the result of mutual coupling between rotor and stator, energy-based calculations require two FE simulation per rotor position and the subsequent subtraction of two possibly nearly equal energy values. Therefore, to determine $\mathbf{E}_r$, the component of the terminal voltage caused by the rotor flux, a method based on flux linkages is used.

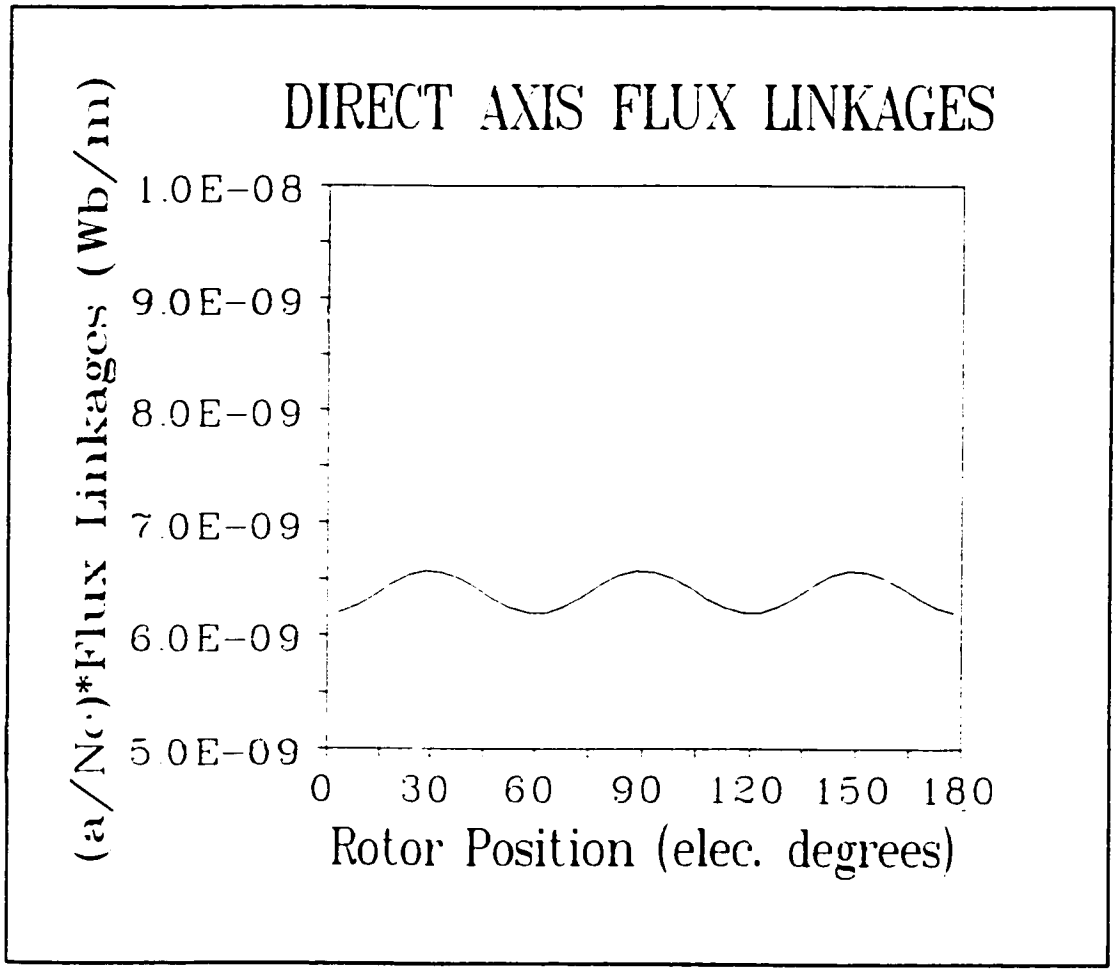

Figure 5.4: Direct axis flux linkages versus rotor position.

Equation (4.14) is the principal expression upon which the flux linkage method is based. The magnetic vector potential fields used in the flux linkage calculations come from simulations with only the magnets excited. The current density field is merely a screening function used to pick out vector potential field values over coil regions. Using the MagNet system's post-processor, a current density field is entered one phase at a time so that phase coil flux linkages can be plotted individually. Results are plotted in figure 5.5 as phase flux linkages versus rotor position relative to the magnetic axis of the phase 'a' coil. In figure 5.4 and figure 5.5, **a** represents the number of parallel current paths in the machine and $\mathbf{N_c}$ is the number of turns per coil. It is assumed that all coils contain an equal number of turns.

One last point warrants mention. In chapter 2 the notion of an operating point for a permanent magnet material was introduced. In figure 2.6 the operating point is determined graphically. Using the finite element technique the procedure is not quite so simple. The size of the magnets must be chosen carefully so as to ensure that, at all points within the magnet, the material is "biassed" properly. A trial and error method is used in this work, continually adjusting the thickness of the magnets until satisfactory magnet sizes are found.

5.3.4 Determination of L_d and E_f

Table 5.2 presents the results of the averaging process designed to estimate the direct axis inductance $\mathbf{L_d}$ and table 5.3 gives the results of the rotor voltage $\mathbf{E_f}$ determination problem.

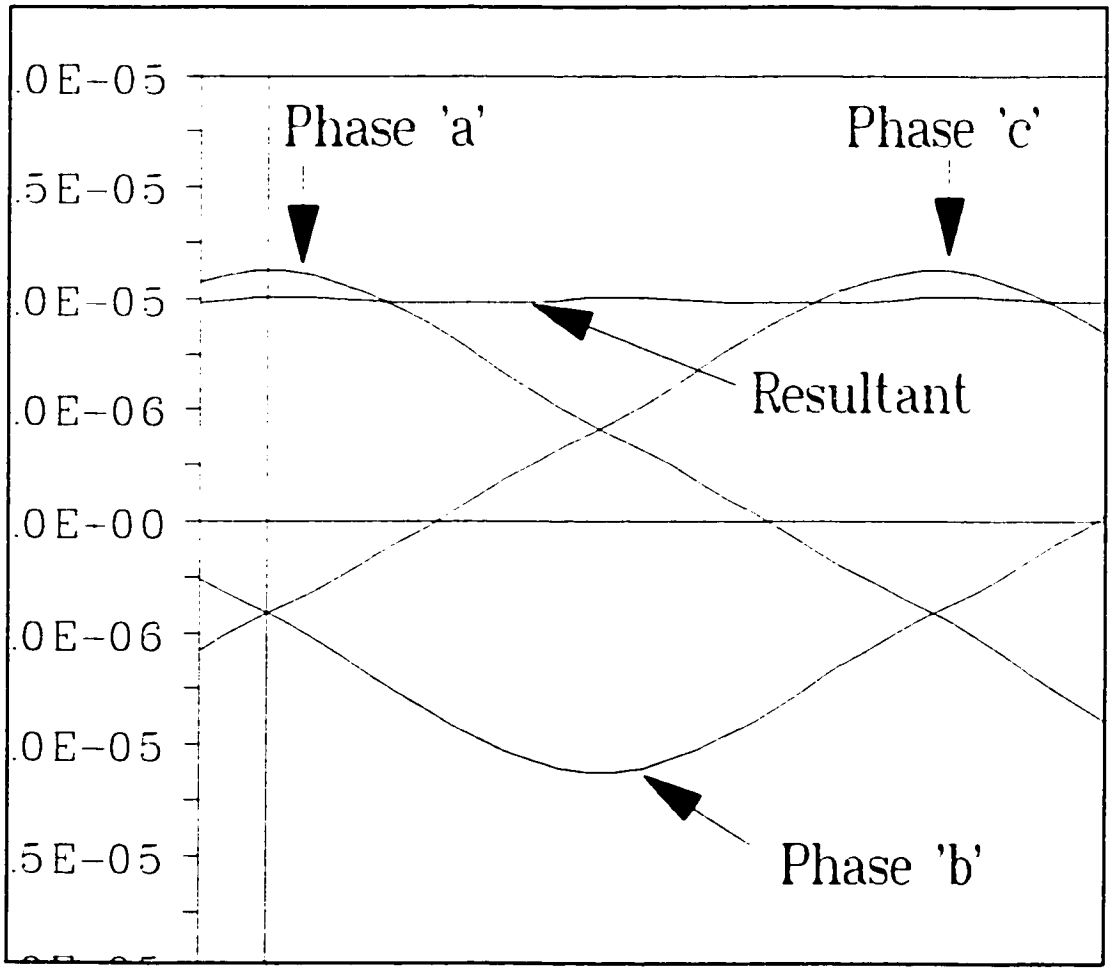

Figure 5.5: Phase flux linkages versus rotor position.

Table 5.2: Determination of the Direct Axis Inductance

Current (Amps) $\times 10^{-4}$	Average Energy (Joules/m)	Average Flux Linkages (Wb/m) $\times 10^{-9}$	Inductance (H/m) $\times 10^{-5}$
$(N_c/a)\times I_{ad}$=4.92	W_m=3.53E-12	$(a/N_c)\times\lambda_{ad}$=6.39	$(a/N_c)^2\times L_d$=1.30

Table 5.3: Determination of the Rotor Voltage E_f

Average Flux Linkages (Wb/m) $\times 10^{-6}$	Electrical Frequency (rad/s)	Parallel Current Paths	Rotor Voltage(Volts/m) $\times 10^{-3}$
$(a/N_c)\lambda_f$=9.90	ω_s=377	**a**=1	$(1/N_c)E_f$=3.73

5.3.5 Performance Index for the Permanent Magnet Motor

The first term in equation (5.5) is the component of the average output power due to the coupling between the permanent magnets' field and the stator field. Restated below, the expression is :

$$P=\frac{3V_\varphi E_f}{X_{fd}}\sin(\delta) \qquad \textbf{(5.7)}$$

To obtain the direct axis synchronous inductive reactance X_{fd}, the direct axis inductance L_d is multiplied by the electrical excitation frequency ω_s.

$$X_{fd}=\omega_s L_d=377\times 1.30\times 10^{-5}\times N_c^2=N_c^2\times 4.90\times 10^{-3}\ \Omega/m \qquad \textbf{(5.8)}$$

Now, let us assume a value for the power angle δ of 90° so that sin (δ)=1. Since sin(δ), cos(θ), E_f, X_{fd} and I_φ are related by :

$$\frac{E_f}{X_{fd}}\sin(\delta)=I_\varphi\cos(\theta) \qquad \textbf{(5.9)}$$

the RMS value of the phase current I_φ will depend on the power factor. With δ set

to 90° the effect of differing power factor values can be seen in figure 5.6.

Using the previously calculated values for $\mathbf{E_f}$ and $\mathbf{X_{id}}$ and assuming a power factor of 0.9 lagging, we get :

$$N_c I_\varphi = N_c \frac{E_f}{0.9 X_{ld}} = 0.60 \text{ A} \qquad \textbf{(5.10)}$$

$\mathbf{V_\varphi}$ is calculated using :

$$V_\varphi^2 + E_f^2 = (X_{:d} I_\varphi)^2 \qquad \textbf{(5.11)}$$

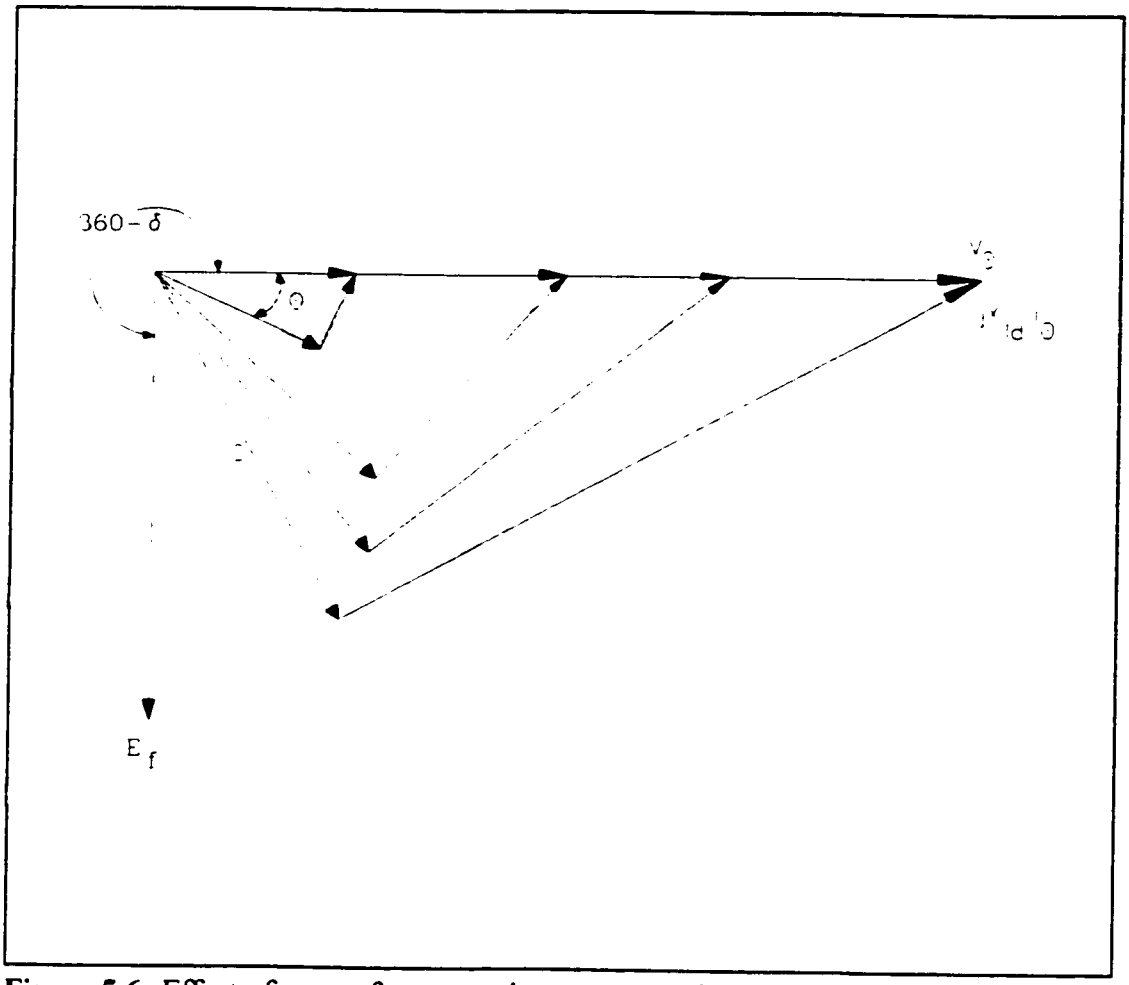

Figure 5.6: Effect of power factor on phase current with δ=90°.

and the result substituted into equation (5.6) to get the average power. Equation (5.1) yields a value for the output coefficient of :

$$\xi_0 = 3\left[\frac{V_\varphi E_f}{X_{:d} n_s D_0^3}\right] = 3\left[\frac{1.3\times10^{-3}\times2.64\times10^{-3}}{4.90\times10^{-3}\times1800\times(80\times10^{-6})^3}\right] = 2.3\times10^6 \quad \frac{J}{m^4} \qquad \textbf{(5.12)}$$

5.4 VC MOTOR MODELLING: AXIS COUPLING

In this final section, a more detailed interpretation of the finite element results obtained from our examination of the variable capacitance motor is given. The motivation is to better understand the physical aspects of the axis charge versus rotor positions curves.

5.4.1 Direct Axis - Quadrature Axis Coupling

The self and mutual phase capacitances in the general case will contain components other than an average value plus a second harmonic. Some of these harmonics will generate motoring torque when the corresponding temporal voltage harmonic is present. Such capacitances are said to generate positive sequence currents. Other harmonics generate currents whose interaction with their corresponding temporal voltage harmonic produce a counter torque. These currents are the negative sequence currents.

In a three phase machine, the fundamental of course, as well as the 7^{th}, 13^{th}, 19^{th} and so on current harmonics are positive sequence harmonics. To calculate the harmonic number **k** of a positive sequence term use the following equation :

$$k = 3(2i) + 1 \qquad i = 0, 1, 2, \ldots \qquad \textbf{(5.13)}$$

The harmonic numbers of the negative sequence components are given by :

$$k = 3(2(i+1)) - 1 \qquad i = 0, 1, 2, \ldots \qquad \textbf{(5.14)}$$

The rotor of our example VC machine in figure 3.4 revolves counter clockwise as do the positive sequences. Negative sequences move in a clockwise direction. Therefore, during the period of one cycle of the electrical supply's fundamental, the 5^{th} and 7^{th} phase charge harmonics generate a charge "vector" which aligns itself with the direct axis and quadrature axis six times. Consequently, we expect the direct and quadrature axis charge versus rotor position curves to exhibit a 6^{th} harmonic oscillation. Referring to figures 5.1 and 5.2, a 6^{th} harmonic (among others) is indeed present.

The amount of coupling between the direct axis and quadrature axis is obtainable from finite element solutions. An energy-based method analogous to that described in §4.3.2b) is used. For each rotor position, two FE simulations are conducted. In the first problem configuration, the resultant voltage vector must contain both direct axis and quadrature axis voltage components but no zero sequence component. Then, in the second run, the sign of one of the axis voltages is reversed. For each case the stored electrical energy is computed.

The difference between the two energy values is proportional to the charge on the direct/quadrature axis due to the quadrature/direct axis component of phase voltage. Figure 5.7 is a plot of the mutual coupling between the direct axis and the quadrature axis for our example VC motor.

Notice that the curve in figure 5.7 has an average value of zero. Because only fundamental voltage components are used in exciting the motor, no average power can be generated through the higher order positive and negative sequence current harmonics. If

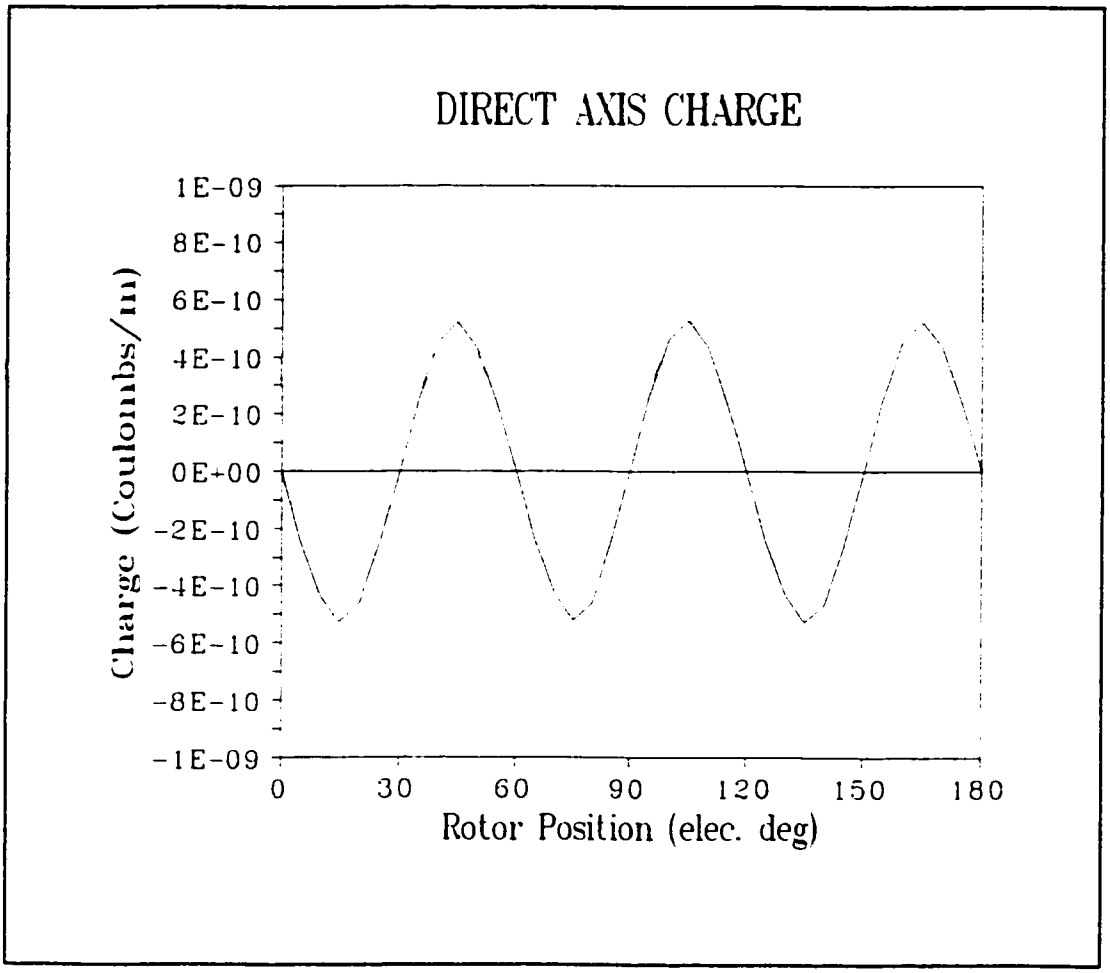

Figure 5.7: Direct axis charge due to quadrature axis voltage.

however, voltage harmonics are present in the electrical supply feeding the machine's electrodes, average torques and counter torques in addition to pulsating torques will be developed.

The curve in figure 5.7 was verified by comparing the total energy stored in the electric field for one of the runs with the outcome of the following equation :

$$W_e = \frac{1}{2}C_d V_d^2 + \frac{1}{2}C_q V_q^2 + C_{dq} V_d V_q \qquad \textbf{(5.15)}$$

Conservation of energy considerations demand that $\mathbf{C_{dq}}=\mathbf{C_{qd}}$.

5.4.2 Zero Sequence Coupling

In this section we investigate the possible existence of zero sequence phase currents in the absence of a zero sequence component of phase voltage. The second harmonic self and mutual phase inductance coefficients for the variable reluctance motor [32] preclude the existence of such voltage harmonics under balanced three phase current excitation. In a three phase machine, the harmonic number **k** of a zero sequence current is given by :

$$k = 3(2i+1) \qquad i = 0,\ 1,\ 2,\ \ldots \qquad \textbf{(5.16)}$$

If any zero sequence currents are present, the third harmonic would most likely be dominant. We cannot, however, detect its presence with the direct axis or quadrature axis charge versus rotor position curves previously described. Another set of simulations must be conducted.

Using the energy-based technique, two finite element simulations per rotor position are again necessary. In the first run, the phase voltages are assigned a zero sequence component plus one of either a direct axis or quadrature axis component. In the second run, the sign of the zero sequence voltage is reversed. Figures 5.8 and 5.9 show the zero sequence charge versus rotor position due to direct axis and quadrature axis voltage excitation respectively. Note the presence of the third harmonic (one and one half cycles in 180 electrical degrees in the case shown in figure 5.8)

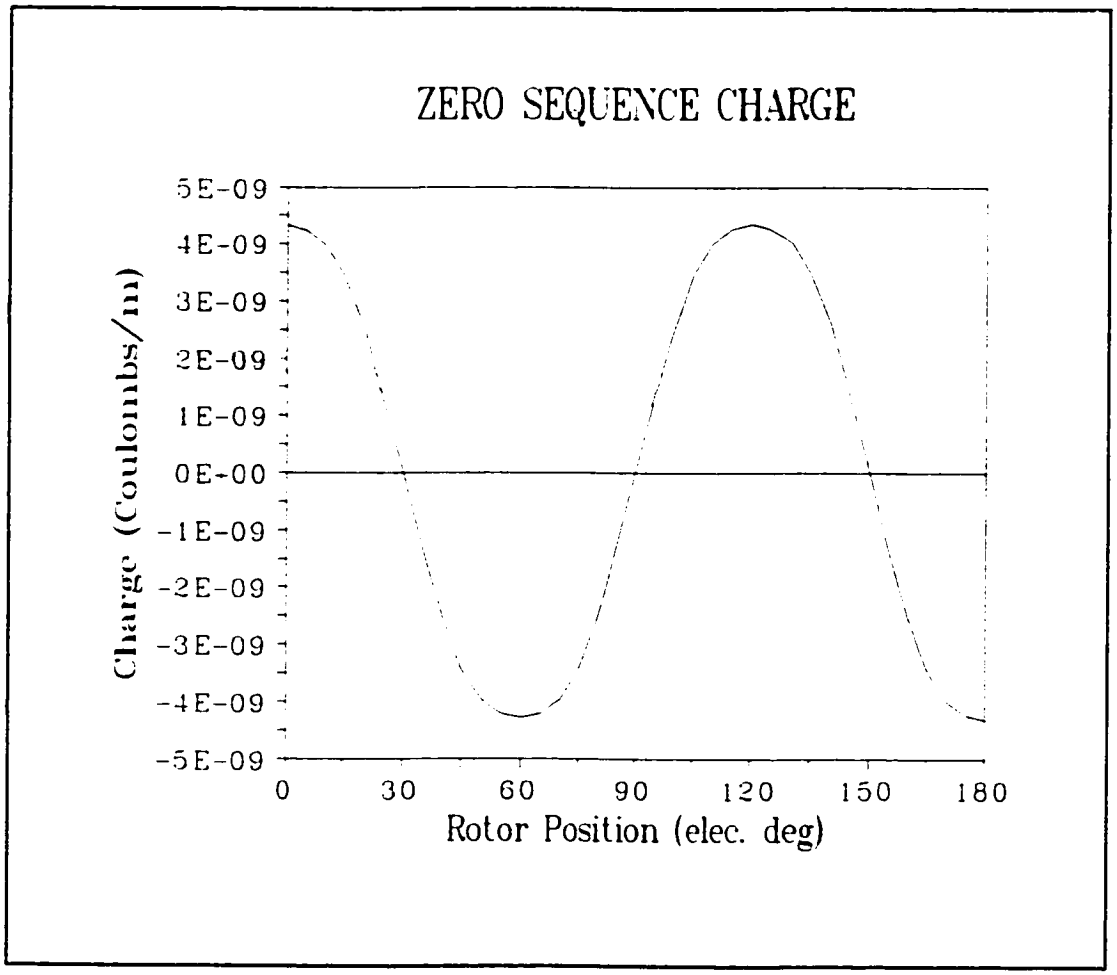

Figure 5.8: Zero sequence charge due to direct axis voltage.

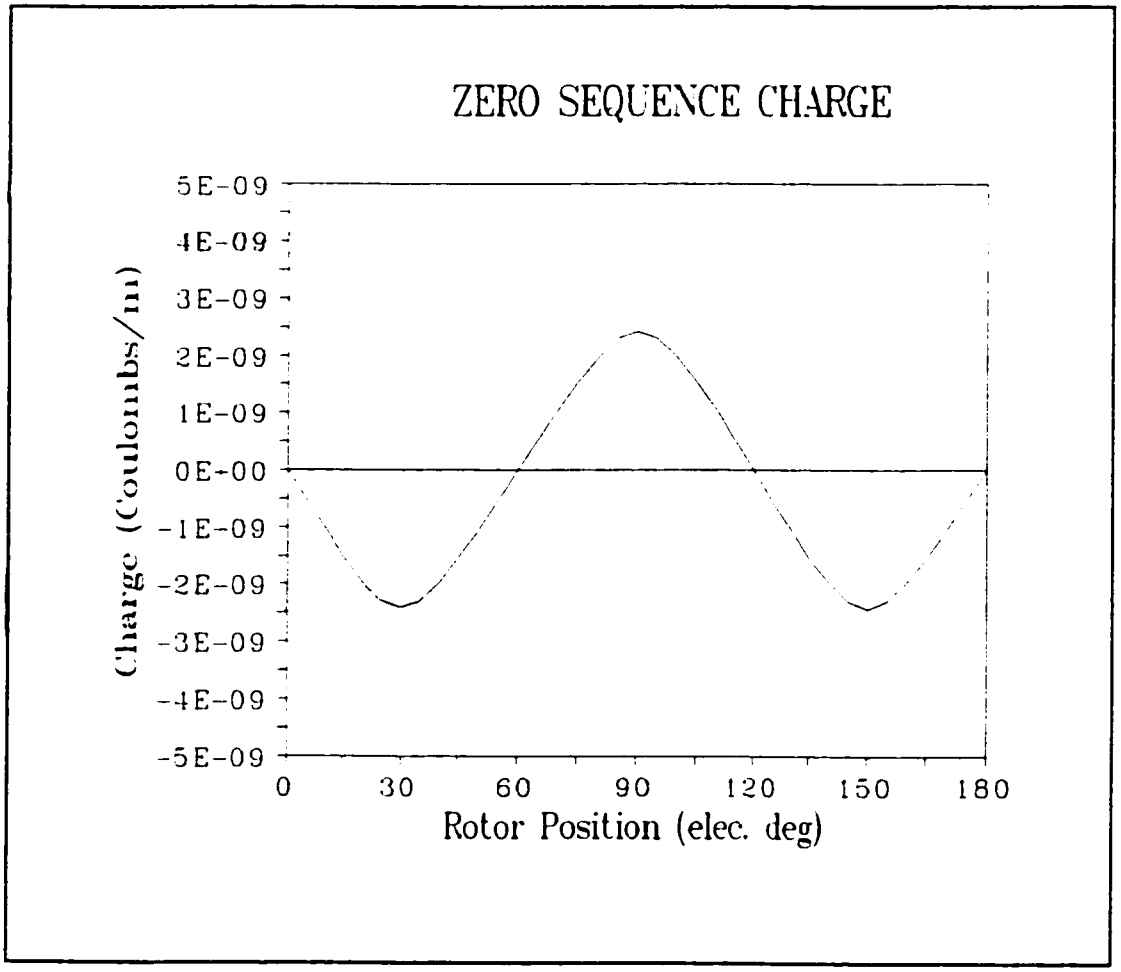

Figure 5.9: Zero sequence charge due to quadrature axis voltage.

CHAPTER 6

SCALING LAW

RESULTS

Chapter six discusses the results of the output coefficient calculations performed in chapter five and assess the merits of electrical actuation based on the computed output capability of the example silicon micro motor. We estimate the output coefficient of a "good" magnetic machine design based on equation (5.2) and the size of a magnetic machine possessing an output capability equivalent to that of the example variable capacitance machine. The scaling laws presented in chapter two are applied to probe for a transition point indicating the approximate scale at which electrical actuation becomes more desirable than magnetic actuation according to the values of the performance indices for the two micro motor designs.

6.1 DISCUSSION OF OUTPUT COEFFICIENTS

Having obtained output coefficients for both an electrically actuated machine as well as a magnetically actuated permanent magnet motor, we make the first of our assessments by comparing the performance indices of the two similarly sized machines.

The maximum output coefficient of our example VC motor is estimated at 5×10^{6}.

This value is obtained using a peak stator electrode voltage of 450 volts across a 1.5 μm air-gap. The power angle δ is set to 45° so that sin (2δ) takes on its maximum value of 1.0. Such operating conditions are physically realizable in practice. Electric field strengths of the order of 3×10^8 V/m can be sustained across micrometre scale air-gaps without electrical breakdown. Furthermore, it will be shown that at 60 Hz, current densities are well within permissible limits, allowing for the use of substantially higher operating frequencies.

The peak current density in a stator electrode is estimated by calculating the electrode current per unit axial length and dividing by the inner arc length of a stator electrode. Using equations (3.8) and (3.15) :

$$N_p\sqrt{I_{ad}^2+I_{aq}^2} = 1.77\times10^{-5}\ \text{A/m} \qquad \textbf{(6.1)}$$

This value must be divided by the number of poles, N_p, in order to establish the current in each individual electrode. Therefore, $I_a=4.43\times10^{-6}$ A/m which is ¼ of the value in equation (6.1). The resulting estimate for the peak current density is :

$$J_{peak} = \frac{4.43\times10^{-6}}{26.5\times10^{-6}\times12(\frac{\pi}{180})} = 0.8\ \text{A/m}^2 \qquad \textbf{(6.2)}$$

since the inner radius of the stator electrodes is 26.5μm and the pole width is 12° measured mechanically. Macroscopic current densities are of the order 2×10^6 A/m^2 and allowances can be made for an increase as system dimensions are reduced. Current densities at 60 Hz are certainly permissible for this VC machine.

Without any regard for current density limits, our estimate for the maximum output

coefficient of the permanent magnet motor is 2.3×10^6. The assumption of $\delta=90°$ with $a=1$ and $\cos(\theta)=0.9$ gives :

$$\sqrt{2}N_c I_\varphi = \sqrt{2}(.6) = 0.85 \text{ amps} \qquad \textbf{(6.3)}$$

For the peak current density in the phase coils :

$$\sqrt{2}N_c I_\varphi = J_{peak} A_{slot} = 0.85 \text{ amps} \qquad \textbf{(6.4)}$$

we get $J_{peak} = 1.0\times10^{10}$ A/m^2.

With a peak current density of 1.0×10^{10} A/m^2, an output coefficient of 2.3×10^6 J/m^4 is probably not realistic for a permanent magnet motor of this size. We now estimate a new output coefficient for the permanent magnet motor using a peak current density of 10 A/mm^2, a value used by Belmans *et al.* [17].

From equation (6.4), the RMS value of the phase current I_φ is :

$$N_c I_\varphi = \frac{10.0\times10^6 \times 8.2\times10^{-11}}{\sqrt{2}} = 5.8\times10^{-4} \text{ amps} \qquad \textbf{(6.5)}$$

This small phase current restricts δ, the rotor or "power" angle, to values substantially less than 90°. Therefore, rather than assigning values to δ and $\cos(\theta)$ as before, we apply the cosine law to the triangle formed by V_φ, E_f and $jX_{sd}I_\varphi$ and solve equation (6.6) :

$$\cos(\delta) = \frac{V_\varphi^2 + E_f^2 - (X_{sd} I_\varphi)^2}{2E_f V_\varphi} \qquad \textbf{(6.6)}$$

With $V_\varphi = E_f$, the new estimate for the output coefficient of the permanent magnet

motor becomes :

$$\xi_0 = \frac{3(2.64\times10^{-3})^2}{4.9\times10^{-3}} 1.1\times10^{-3} \times \frac{1}{1800\times(80\times10^{-6})^3} = 5.0\times10^{3} \quad \frac{J}{m^4} \qquad (6.7)$$

This output coefficient for the permanent magnet motor is considered to be more realistic than the previous one. Note that it is three orders of magnitude smaller than the output coefficient of the VC motor.

6.2 OUTPUT COEFFICIENT - ALTERNATIVE FORMULATION

An alternative expression (applying strictly to magnetically actuated devices) for the output coefficient appears in equation (5.2). Typical macroscopic parameter values for $\mathbf{B_g}$, $\mathbf{J}$, η, $\cos(\theta)$, $\mathbf{V/E}$ and $f_0(\zeta)$ are substituted into equation (5.2) to estimate the output coefficient of a "good" conventional magnetic machine design. Assumptions about the parameters in equation (5.2) consist of :

- $\mathbf{B_g}$=0.8 T
- $\mathbf{J}$=2.0 amps/mm^2
- η=0.9
- $\cos(\theta)$=0.8
- $\mathbf{V/E}\approx 1.0$

Following the work of Honsinger [50], the ratio of peak stator core flux density to peak stator tooth flux density is set to 0.8. For a four pole machine with a copper-iron ratio of 0.5, the maximum value of $f_0(\zeta)$ is approximately 0.16. With these values, an estimate for the output coefficient of a "good" magnetic machine design is of the order 5×10^3 J/m^4.

6.3 APPLICATION OF SCALING LAWS

6.3.1 Variable Capacitance Machine

In §6.1 an estimate of 0.8 A/m^2 at 60 Hz was made for the peak current density in a stator electrode of the example VC machine. With increasing frequency, the output coefficient of this motor remains constant because the axis capacitive susceptances scale linearly with frequency. Using 2.0 A/mm^2 as a limit for the electrode current density, the supply frequency can theoretically increase to :

$$60\ \text{Hz} \times \frac{2\times10^6}{0.8} = 150\ \text{MHz} \qquad \textbf{(6.8)}$$

provided mechanical stress limits on the rotor are not exceeded.

Electrically actuated machines suffer in terms of their average power produced to ohmic power lost ratio when the supply frequency increases. From equation (3.16) we see that the average output power of a variable capacitance motor increases linearly with frequency. From equation (2.16), the conduction losses in the electrodes scale as the square of the current. Since current and frequency are linearly related in a VC machine, power lost to ohmic dissipation (neglecting skin effects) increases with the square of the frequency. Therefore, conduction losses increase at a faster rate than mechanical power produced when excitation frequency increases.

6.3.2 Magnetic Machines (No Permanent Magnet Material)

An estimate for the output coefficient of a "good" conventional magnetic machine design of 5×10^3 J/m^4 was obtained in §6.2. The manner in which this value scales as system

dimensions are reduced depends primarily upon the current density function. Keeping the current density constant, the magnetic flux density decreases linearly with machine size in the absence of permanent magnet material. Hence, the output coefficient decreases linearly with scale as well. Let us assume for purposes of comparison that a certain "macroscopic" synchronous motor 1000 times greater in diameter than the example VC motor possesses an output coefficient of 5×10^3 J/m^4. Using equation (5.1), the transition point in terms of power occurs when the diameter of the magnetic machine is 2.4 mm.

The output coefficient remains constant if the current density function is $s^{-1/2}$. In this event, a magnetic machine operating at the same speed as our example VC motor would need to be an order of magnitude larger than the electrically actuated device. The power crossover point occurs when the diameter of the magnetic machine reaches 0.75 mm. The driving current density in this case is 20 A/mm^2.

Scaling the electric field as $s^{-1/2}$ [2,14,17], transition points analogous to those referred to in figure 2.8 occur at machine diameters of 7.5 mm and 2.4 mm for current density functions s^0 and $s^{-1/2}$ respectively. These are the points at which the electrically actuated VC motor and the magnetic machine produce the same output power for equal machine sizes. In the latter case, the current density level has increased to 2.0 A/mm$^2\times10^{1/4}$=11.2 A/mm^2.

The magnitude of the output coefficient of magnetic machines at small scales can be improved by increasing their operating frequency. In §6.3.1 it was pointed out that conduction losses in a VC motor increase at a faster rate than mechanical power produced when excitation frequency increases. For magnetically actuated devices this is not the case. When current density is constant conduction losses remain fixed while mechanical output

power increases linearly with frequency.

6.3.3 Machines With Permanent Magnets

In chapter two it was shown that when permanent magnet material is introduced into a magnetic actuator, the device's scaling laws become more favourable. From figure 2.8 we see that the static magnetic force produced by an actuator utilizing permanent magnet material decreases at the same rate as the force generated by an electrostatic actuator under conditions of constant electric field. It is worth examining whether a permanent magnet motor enjoys the same favourable scaling laws.

Attempting to keep $\mathbf{V}_\phi$ and $\mathbf{E}_f$ equal, equation (5.10) gives the relationship between phase current and direct axis synchronous reactance which must be maintained in order to keep the power angle δ at 90°. Herein lies the problem with permanent magnet machines. At small scales, the magnitude of $\mathbf{X}_{sd}$ combined with the small area of a slot forces the current density to a prohibitively large value. The only recourse is to limit the current density and reduce δ, an act which we have already seen in §6.1 reduces the output coefficient of the machine.

This problem of a small direct axis synchronous reactance $\mathbf{X}_{sd}$ cannot be overcome by merely adding more turns because both sides of equation (5.10) are scaled by the same power of $\mathbf{N}_c$. Therefore, although static actuators with permanent magnet material scale down favourably, rotating machines requiring a second magnetic field sourced by current-carrying windings are unable to fully exploit the beneficial properties of permanent magnets at very small scales.

As far as a scale at which a permanent magnet machine would be beneficial, let us consider using a current density function of $\mathbf{s}^{-1/3}$ with our example permanent magnet motor. With a macroscopic current density of 2.0 A/mm^2 and a machine diameter of 8.0 cm (1000 times larger than the model examined earlier in this work), the output coefficient of this machine can be obtained. Let $\mathbf{V}_\phi = \mathbf{E}_f$. Equation (6.6) yields a value for sin(δ) of 0.21 and equation (5.1) a value for the output coefficient of:

$$\xi_0 = 3\frac{2.64^2}{4.9\times 10^{-3}}0.21\left(\frac{1}{1800\times(80\times 10^{-3})^3}\right) = 9.7\times 10^2 \qquad \textbf{(6.9)}$$

The transition point (for the average output power) is situated where the outer diameter of the electrically actuated machine takes on a value of approximately 1.9 mm. This is only slightly smaller than the 2.4 mm boundary estimate obtained for machines which do not possess permanent magnet material.

CHAPTER 7

DUAL BOUNDS

7.1 INTRODUCTION

Chapter seven leads a discussion of an alternative method of calculating the torque developed by an electrically actuated micro motor. What is described first is a means of solving for the distribution of the electromagnetic field in a problem domain using a method that places bounds on the stored energy. This method is based upon the fact that the true value for the stored energy (which corresponds to the exact solution of the electromagnetic field distribution) must lie somewhere between a known upper bound and a known lower bound. Once the upper and lower bounds have been calculated, their average value is used as the estimate for the stored energy.

Chapter four describes a procedure whereby the knowledge of the stored energy in a silicon micro motor for specific (direct and quadrature axis) stator electrode excitations is used to estimate the developed torque. The same formulation is applicable with a bounded energy method. What differs is the particular method of extracting, from the given information, a value for the stored energy.

In the method of dual bounds, the basis for the energy estimates under direct and

quadrature axis excitation is no longer the finite element method. Recall that previously, the finite element has been the mathematical formulation employed in generating values for stored energy. The dual bounds approach, although an energy based method, produces estimates for stored energy which are "guaranteed" to be either an upper bound or a lower bound. This is in contrast to the finite element method which yields an electromagnetic field distribution that is stationary. For the set of basis functions chosen, the finite element method will settle on the electromagnetic field (potential) distribution that corresponds to the minimum possible amount of stored energy the field distribution could assume, using the given approximation space.

In the dual bounds approach we are not concerned with finding a stationary distribution since two estimates will be used and subsequently averaged. It suffices only to be assured that each of the estimates that are found are either an upper bound or a lower bound. Therefore, because the developed torque does not rely on an energy value from one estimate solely, the amount of detail in the discretization need not be extensive.

The theory is first described for two dimensional systems and then extended to three dimensional systems. The benefits and the motivation for using the dual bounds method will become apparent when computational requirements are discussed. This is especially true in three dimensional problems where the equations resulting from a detailed finite element discretization of the problem domain result in systems of linear equations that prohibit solution on most affordable hardware platforms. Typically, the storage requirements (memory/disk) are not available or the solution simply takes an extensive amount of time.

The work presented in this chapter has been inspired by the work of Hammond [63,

64, 65, 66], however the application to micro motors in two dimensions and in particular the direct and quadrature axis theory as applied to electrically actuated machines is specific to this thesis. Furthermore, the extension to a three dimensional formulation as it is presented here is unique. Specific information derived within this work is much more detailed and cannot be found in the work conducted by Hammond [63-66] or Sykulski [67] who implemented a form of this work in a two dimensional software package. In particular, the relationship between the shape of a three dimensional structural element and the field intensity in each region is derived. It is shown that commercial finite element mesh generators can be used to discretize a three dimensional problem domain in such a way as to make it amenable to a solution based on bounded energy methods.

A practical application of the concepts presented in this chapter is found in chapter eight. The developed torque of an electrostatic micro motor is calculated in two dimensions and compared with the value obtained from the classical finite element method. An assessment of the methods' accuracy is made and it is found that the accuracy compares to that of the finite element method but requires much less computation. A three dimensional system is also solved. A commercial solid modelling package (XL written by the MacNeal/Schwendler corporation, now owned by the ANSOFT Corp.) is used to discretize the problem domain into a set of hexagons or cuboid shapes suitable for the application of the method of dual bounds. The amount of computation required is found to be significantly less than an equivalent finite element solution involving the same amount of discretization.

7.2 Duality in Variational Methods

The variational principal (from the calculus of variations) is one of the fundamental mathematical premises that, when applied to the appropriate functional, yields the differential equations that describes the behaviour of a physical system. For example, in electro statics or magneto statics, by stipulating that the first variation of the energy stored in the system be zero, we arrive at the elliptical partial differential equations which govern the behaviour of these systems providing that it is the potential functions (electric or magnetic) that are permitted to vary. These differential equations are identical to the differential equations obtained by applying Maxwell's equations.

In the finite element method, we exploit this fact by defining a set of basis functions within which the approximate solution lies. A unique solution is obtained by stipulating that the first variation of the stored energy of the system be zero. The solution, although a stationary one, is not the true (exact) solution since the true solution will not necessarily possess the same amount of stored electric or magnetic energy. What we have found is merely the particular solution within the approximation space used that yields a stationary functional. Note that the very same equations can be arrived at by imposing the condition that the residual error (between the approximate solution and the known sources of the electric or magnetic field) be orthogonal to each and every basis function of the approximation space.

In this latter method, the weighting functions are the basis functions themselves but this does not necessarily have to be the case. When it is the case, the procedure has a special name and is called the Galerkin method. This however is just a special case of a more general class of methods called the method of moments. The reader is referred to references [45, 46,

48] for more details on such methods.

Let us go back to a discussion of variational methods. Assume that an unknown scalar or vector field can be described by some unique member of a known approximation space. We know that the true (exact) solution is one which minimizes an energy functional. By forcing the same condition on the approximate solution we can arrive at a finite set of equations that uniquely define the approximate solution. This solution however, is not the true solution because in the process of approximating the solution, we will have inadvertently introduced new sources into the problem that are not present in the exact solution. This is a direct consequence of the discretization process itself. In the finite element method, these sources are not introduced by the analyst, but indirectly by the method itself in order to achieve a minimum energy configuration.

In the case of electro statics, if we choose the approximation polynomials such that the scalar potential φ and the electric field **E** are related by :

$$\overline{E} = -\overline{\nabla}\varphi \qquad \textbf{(7.1)}$$

We will not satisfy the equation (7.2) exactly because of the added source terms that will be introduced :

$$\overline{\nabla}\cdot\overline{D}=\rho \qquad \textbf{(7.2)}$$

The finite element method chooses the placement of the extra source terms in such a way as to minimize the stored energy in the system. This is achieved by setting the first variation of the energy to zero for all possible first order variations of the potential field. The

extra source terms correspond to charge that is introduced along element edges due to the discontinuity in the normal component of the electric flux density field **D**. Since the first variation of the field energy is zero, the net energy added to the system from the extra charge is zero throughout the system as a whole.

Traditional electrostatic problems are characterized by a known volume charge density distribution within the problem domain and a known electric scalar potential function on the boundary. Wherever the scalar potential is not known on the boundary, the normal component of the gradient of the scalar potential field is usually zero (natural boundary condition). Let us examine how the variational method is applied to such a system in order to generate the governing elliptical partial differential equation. This proves to be useful because it indicates why the first variation of the energy functional is zero for the exact solution and it provides us with one of the bounds we are looking for.

Since it is the volume charge density that is known within the region and the scalar potential that is known on the boundary, let us consider the following energy functional :

$$W_e = -\iiint(\varphi\rho - \frac{\varepsilon}{2}\bar{E}\cdot\bar{E})dv \qquad (7.3)$$

Since the electric field **E** and the electric scalar potential field φ are related through equation (7.1), we can rewrite equation (7.3) as :

$$W_e = -\iiint(\varphi\rho - \frac{\varepsilon}{2}\bar{\nabla}\varphi\cdot\bar{\nabla}\varphi)dv \qquad (7.4)$$

The volume of integration in equations (7.3) and (7.4) is the closed volume of the problem domain. The first variation of this functional is realized by permitting the electric

scalar potential to vary by an amount $\delta\varphi$ everywhere within the problem domain that it is not known. On the boundary where it is known, it is not permitted to vary. The first variation (ignoring second order terms) is as follows :

$$\delta W_e = -\iiint(\rho\delta\varphi - \varepsilon\bar{\nabla}\varphi\cdot\bar{\nabla}\delta\varphi)\,dv \qquad \textbf{(7.5)}$$

Using an identity ($\nabla\varphi\cdot\nabla\delta\varphi = \nabla\cdot(\delta\varphi\nabla\varphi) - \delta\varphi\nabla^2\varphi$) for the last term in equation (7.5) and applying Gauss's Theorem, we rewrite the whole equation as:

$$\delta W_e = -\iiint(\delta\varphi(\rho + \varepsilon\nabla^2\varphi))dv + \iint(\varepsilon\delta\varphi\bar{\nabla}\varphi\cdot\hat{n})dS \qquad \textbf{(7.6)}$$

Note that if φ and ρ satisfy Poisson's equation, and if the normal component of the gradient of φ is zero in all places where φ is not known on the boundary then δW_e will be zero for any arbitrary displacement $\delta\varphi$. The Galerkin method of generating the finite element equations stipulates that the residual error be orthogonal to the basis functions over the entire problem domain. Thus, by starting out with an energy functional and enforcing the constraint that the first order variation be zero, we have actually derived the same equations as if we had employed the Galerkin method from the outset.

The advantage of the variational method is that the approximating polynomials need not be second order or higher in order to implement the variational method. Equation (7.4) can be made stationary by setting the first partial derivatives of the energy functional with respect to the unknown nodal potentials to zero. First order interpolating polynomials can be used in this case but they could not be implemented in equation (7.6) since the Laplacian operator requires functions of order two or more in order not to vanish. Furthermore, along

the boundary where the normal component of the gradient of φ is known to be zero, it is not necessary to impose or force this constraint on the trial functions. By forcing a stationary functional using the partial derivatives, the boundary surface integral from the Galerkin method will naturally be satisfied since we know that the first variation is zero due to the way the partial derivatives have been zeroed.

It should also be noted that the sign of the second variation is positive. The exact term is :

$$\delta^2 W_e = \iiint (\frac{\varepsilon}{2} \bar{\nabla}\delta\varphi \cdot \bar{\nabla}\delta\varphi) dv \qquad (7.7)$$

The fact that the second variation of this functional is positive indicates that for any variation δφ, the energy stored in the system will be greater than the true stored energy. Since the exact solution is one in which the energy functional becomes stationary, we can visualize the behaviour of the stored energy in the system as shown in figure 7.1.

In the event that there are known surface charges resident on the boundary where φ is not known, then an extra term can be added to the functional in order to ensure that its first variation is zero. This extra term is :

$$W_{Ex} = -\iint (\varepsilon\varphi \bar{\nabla}\varphi \cdot \hat{n}) dS \qquad (7.8)$$

To calculate the capacitance using the stored energy use :

$$C = \frac{2W_E}{V^2} \qquad (7.9)$$

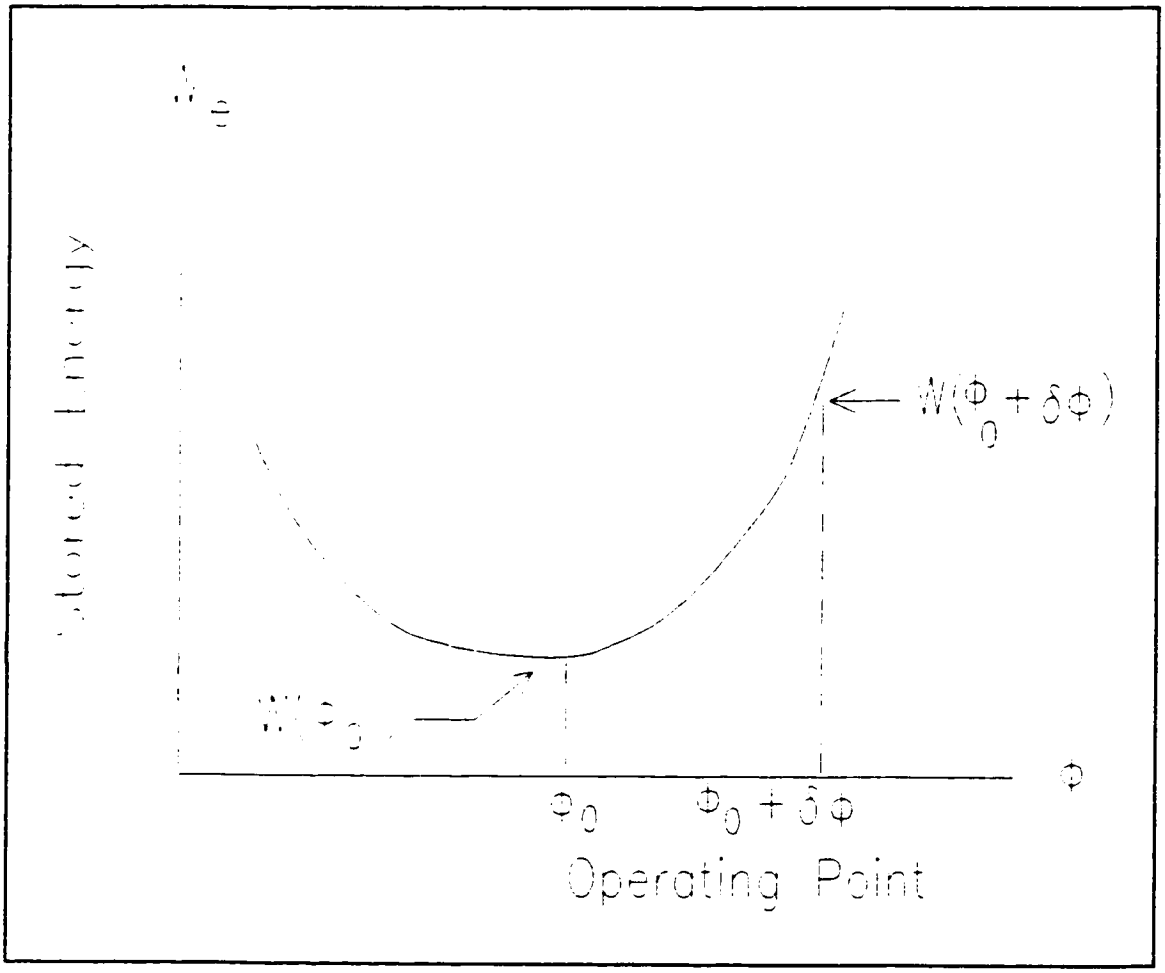

Figure 7.1: Stored Energy

The capacitance calculated via perturbations in scalar potential will be an upper bound based on the nature of the sign of the second variation. This is evident from the fact that any deviation from the exact solution yields a first order variation that is zero and a second order variation that is positive. The positive second variation is the clue to the fact that the actual capacitance must be of lower value than the one computed via equation (7.9).

We will now look at an energy functional that is written in terms of the electric flux density vector **D** rather than the electric field strength vector **E**. There is a reason for choosing different quantities. Recall that in the original discussion of the energy functional, it was the volume charge density ρ that was known in the problem domain and the electric scalar potential φ that was known on the boundary. Now suppose it is the electric scalar potential φ that is known in the problem domain and the surface charge density (which is really the normal component of **D**) that is known on the boundary. The energy functional in this case is :

$$W_e = -\iiint(\varphi\bar{\nabla}\cdot\bar{D} - \frac{1}{2}\frac{\bar{D}\cdot\bar{D}}{\varepsilon})dv \qquad \textbf{(7.10)}$$

The first variation of this functional is :

$$\delta W_e = -\iiint(\varphi\bar{\nabla}\cdot\delta\bar{D} - \frac{\bar{D}\cdot\delta\bar{D}}{\varepsilon})dv \qquad \textbf{(7.11)}$$

Using the identity ($\varphi\nabla\cdot\delta D = \nabla\cdot\varphi\delta D - \delta D\cdot\nabla\varphi$) for the first term in equation (7.11) and applying Gausss's Theorem, we get :

$$\delta W_e = -\iint(\varphi\delta\overline{D}\cdot\hat{n})dS + \iiint\delta\overline{D}\cdot(\overline{\nabla}\varphi + \frac{\overline{D}}{\varepsilon})dv \qquad \textbf{(7.12)}$$

The first variation of this functional when φ and **D** satisfy Maxwell's equations is zero once again provided that φ is zero at all places where the normal component of **D** is not known. If this is not the case, then an extra term can be added to the functional of equation (7.10) in order to force the first variation to zero. The extra added term is :

$$W_{Ex} = +\iint(\varphi\overline{D}\cdot\hat{n})dS \qquad \textbf{(7.13)}$$

This term is added along the boundary of the problem domain in those places where the potential is known but the surface charge density is not known.

The second variation of this function is also positive and is given by :

$$\delta^2 W_e = \iiint(\delta\overline{D}\cdot\delta\overline{D})dv \qquad \textbf{(7.14)}$$

The capacitance will be calculated again, but not using equation (7.9). When the problem is posed using **D** as the quantity that is permitted to vary, the capacitance is most naturally calculated using charge rather than voltage :

$$C = \frac{Q^2}{2W_e} \qquad \textbf{(7.15)}$$

This change is fundamental. Calculating the capacitance in this manner generates the

second bound. We know that any variation from the exact solution will increase the stored energy in the system. Since we are now dividing a known quantity (the square of the charge) by this energy, any and all perturbations yield a smaller value for the capacitance estimate.

7.3 A Second Finite Element Solution

The discussion presented in the previous section is the motivation for the development of a fast economical computational method for obtaining the upper and lower bounds on the capacitance. While a single finite element solution alone can provide us with an estimate for capacitance, the only way to ensure that the energy we arrive at is accurate is to highly discretize the problem domain. For two dimensional linear problems, this approach can be handled on most workstations that are available today at reasonable prices. Having said that, it must be mentioned that one solution only does not provide a means of assessing the accuracy of the result in the absence of experimental data.

It is possible to formulate a dual finite element solution that yields the other bound on the capacitance. The "classical" solution to a problem in electro-statics using the finite element method entails starting with the energy functional in equation (7.4). Trial functions or basis functions for the electric scalar potential φ are defined and substituted into the functional. The first order partial derivatives are calculated and set to zero to generate the final set of linear algebraic equations. The energy of the system is calculated and finally the capacitance estimate is arrived at using the knowledge of the scalar potential.

Keeping the view that the dual solution must involve the electric flux density vector **D**, we start with the functional in equation (7.10). For two dimensional problems, the number

of unknowns can be reduced by using trial basis functions for an electric vector potential **K**. Since the flux density has only *x* and *y* components, the electric vector potential **K** need only possess a *z* component. The relationship between **D** and **K** is defined as follows :

$$\overline{D} = \overline{\nabla} \times \overline{K} \tag{7.16}$$

The energy functional in this case becomes :

$$W_e = -\iiint (\varphi \overline{\nabla} \cdot \overline{\nabla} \times \overline{K} - \frac{1}{2\varepsilon} (\overline{\nabla} \times \overline{K}) \cdot (\overline{\nabla} \times \overline{K})) \, dv \tag{7.17}$$

Since the divergence of the curl of any vector field is zero only the second term in the above functional remains. The first variation of equation (7.17) after **K** is varied is :

$$\delta W_e = \iiint \frac{1}{\varepsilon} \overline{D} \cdot (\overline{\nabla} \times \delta \overline{K}) \, dv \tag{7.18}$$

Using an identity to rewrite equation (7.18), we get :

$$\delta W_e = \iiint \frac{1}{\varepsilon} \delta \overline{K} \cdot (\overline{\nabla} \times \overline{D}) \, dv - \iint \frac{1}{\varepsilon} (\overline{D} \times \delta \overline{K}) \cdot \hat{n} \, dS \tag{7.19}$$

From Maxwell's equations we know that **D** must be proportional to the gradient of the electric scalar potential. Therefore the volume integral will vanish. The second term will also vanish if **D** is zero where **K** is not known. Along the boundary wherever **D** is not zero and the electric vector potential **K** is not known either, an extra surface term must be added to the functional. This term is :

$$W_{Ex} = +\iint \frac{1}{\varepsilon}(\bar{D}\times\bar{K})\cdot\hat{n}\,dS \qquad (7.20)$$

The second variation of this functional is positive and is given by :

$$\delta^2 W_e = \iiint \frac{1}{2\varepsilon}(\bar{\nabla}\times\delta\bar{K})\cdot(\bar{\nabla}\times\delta\bar{K})\,dv \qquad (7.21)$$

To implement this method using the finite element method, it suffices to define the basis functions for **K** in a "weak" sense. In other words the basis functions for **K** need not force the normal component of **D** to zero on the boundary where it is known to vanish provided we minimize the functional given by equation (7.17). To do this, simply substitute the trial functions for **K** into the functional and set the first order partial derivatives equal to zero. Note that method just described will not permit so-called "curl sources". If any volume charge density exists in the problem domain it will not account for any of the stored energy. Therefore, the field will be sourced entirely by the surface electrode charges.

From the above discussion, it is apparent that a dual finite element solution does exist for electrostatic problems. The drawback to implementing this is the fact that a second finite element solution must be solved. While the same mesh could be used, it still means added computational time. For large three dimensional problems this fact makes a second finite element solution too computationally expensive. A better approach entails two solutions which require substantially less computational effort.

7.4 Tubes and Slices

7.4.1 Two Dimensional Analysis

In the previous sections, the mathematical basis behind the dual formulation was outlined. A second finite element formulation was shown to exist but this second formulation requires the solution of another set of equations. As mentioned, this becomes the factor that limits the practicality of this method. Furthermore, since we know that the true solution for the capacitance is bounded by whatever energy value we use, there is no need to minimize the energy in order to produce a bound. Of course, the more accurate the solution, the closer the bounds will be. Keeping this in mind, the method of tubes and slices will be explained in the following sections.

The primary idea behind the tubes and slices method is to discretize the problem domain in such a way that the equipotential surfaces or slices correspond as close as is possible to the actual equipotentials. This concept is therefore fundamentally different from the finite element philosophy. The analyst now has control over the placement of the additional sources whereas in the finite element method, the additional sources are placed into the system in such a way so as to minimize the functional.

In the method of tubes, we have a similar phenomenon. It is the analyst who controls the distribution and path of the lines of flux by the placement of the "walls" of the flux tubes. In the finite element method, additional sources are placed into the system in order to minimize the stored energy. The analyst has no control over the placement of the additional sources.

Giving the analyst control over the placement of the additional sources is the power

of the method of tubes and slices. A knowledgeable analyst will have a good sense of the actual distribution of the equipotential surfaces and flux lines based on experience. It is not necessary to generate one optimal solution when two solutions can be obtained that completely bound the actual solution. These two bounds can be obtained with very little computational expense relative to a finite element solution.

The reason for the computational efficiency is the fact that in the tubes and slices method, it is not necessary to solve a coupled set of equations. When the system has been discretized, the stored energy is obtained by accumulating the energy stored in each of the individual geometrical "shapes" used to discretize the system. In the slice discretization, it is the equipotentials that are placed directly into the system. In the tube discretization, the paths' of the tubes of electrical flux are placed into the system.

A typical quadrilateral element used in slice discretization is shown in figure 7.2. It consists of a quadrilateral in which a centre point and its electric scalar potential are chosen. Two of the four sides of the quadrilateral are prescribed equipotential surfaces and the other two sides are flux lines. The equipotential slice is put into the element by joining the centre point to the flux lines bounding the element so that the joining lines are perpendicular to the flux lines. See figure 7.3 for a pictorial representation of this idea.

Unlike the finite element method, we do not wish to calculate or find the value of the electric scalar potential at the centre node. Nor do we wish to find the scalar potential of the bounding equipotential surfaces that lie on the opposing sides of the element. It is not the objective to minimize the energy functional. Because the functional that is used will yield an upper bound for the capacitance of the system, the values of all equipotential surfaces, and hence of all interior points, can be chosen at will. It is assumed of course that general behaviour of the equipotential surfaces that exist in the system are known.

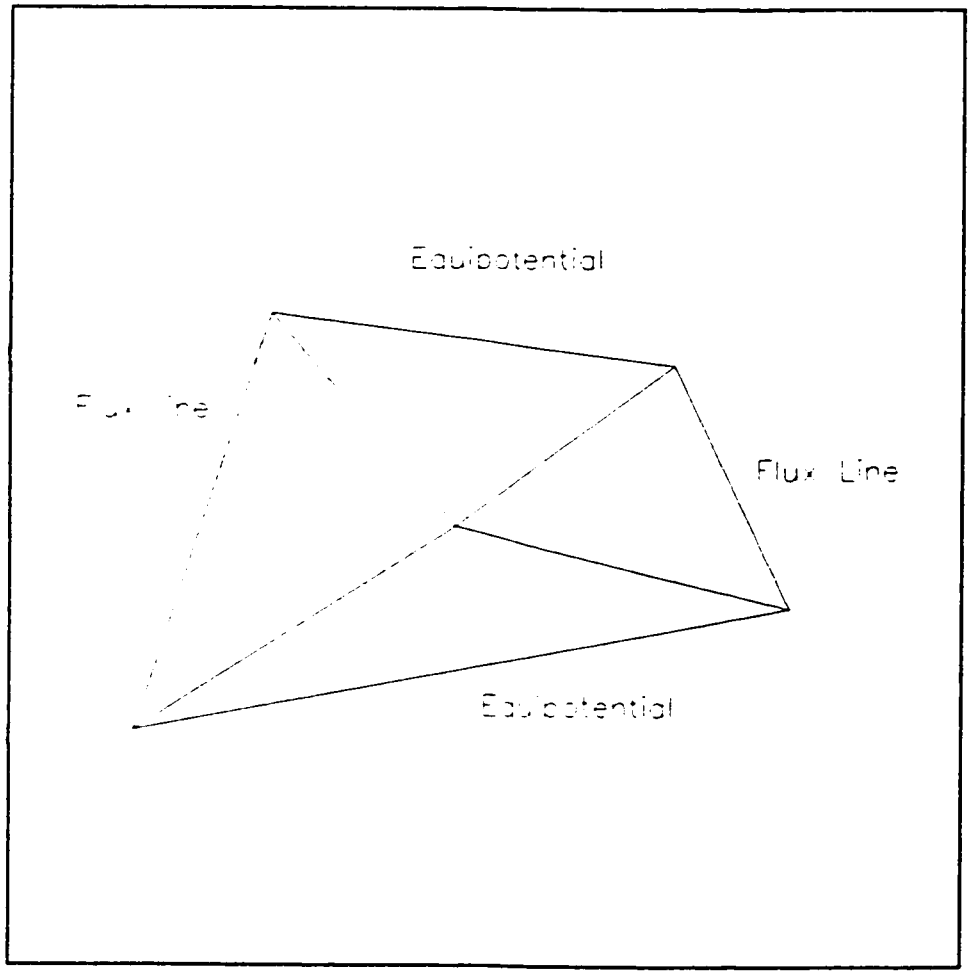

Figure 7.2: Quadrilateral used in two dimensional discretization.

The stored energy in the system is accumulated on a quadrilateral by quadrilateral basis. From figure 7.3 it can be seen that the placement of the centre node creates six triangles within the quadrilateral. This is achieved by connecting the interior point to each of the four vertexes of the quadrilateral. The magnitude of **E** within each triangle is determined in one of two ways. If one side of the triangle corresponds to one of the equipotential surfaces on the edge of the quadrilateral, then the difference between the electric scalar potential on the edge and the electric scalar potential at the interior node is divided by the perpendicular distance to obtain the magnitude of **E**. There are two such triangles in each quadrilateral.

For the other four triangles, the magnitude of the electric field strength is obtained by taking the difference between the electric scalar potential at the edge of the quadrilateral (at the vertex) and the electric scalar potential at the interior point, and then dividing by the distance traversed from the vertex to the perpendicular intersection point. Figure 7.4 shows the six triangles within the quadrilateral and the direction of the electric field within each triangle. The expression for the magnitude of the electric field in each one of the above mentioned triangle "types" within the quadrilateral are given in equations (7.22) and (7.23) respectively.

The additional charges that are introduced into the system will exist along the interior equipotential slice, as well as along the lines that join the verticies of the quadrilateral to the interior point. These additional sources are divergent sources [63, 64, 65, 66] since they permit a net source or sink of electric charge within the quadrilateral. The implication of this is a net difference in the amount of flux that leaves one equipotential surface and the amount of flux that arrives on the other equipotential surface.

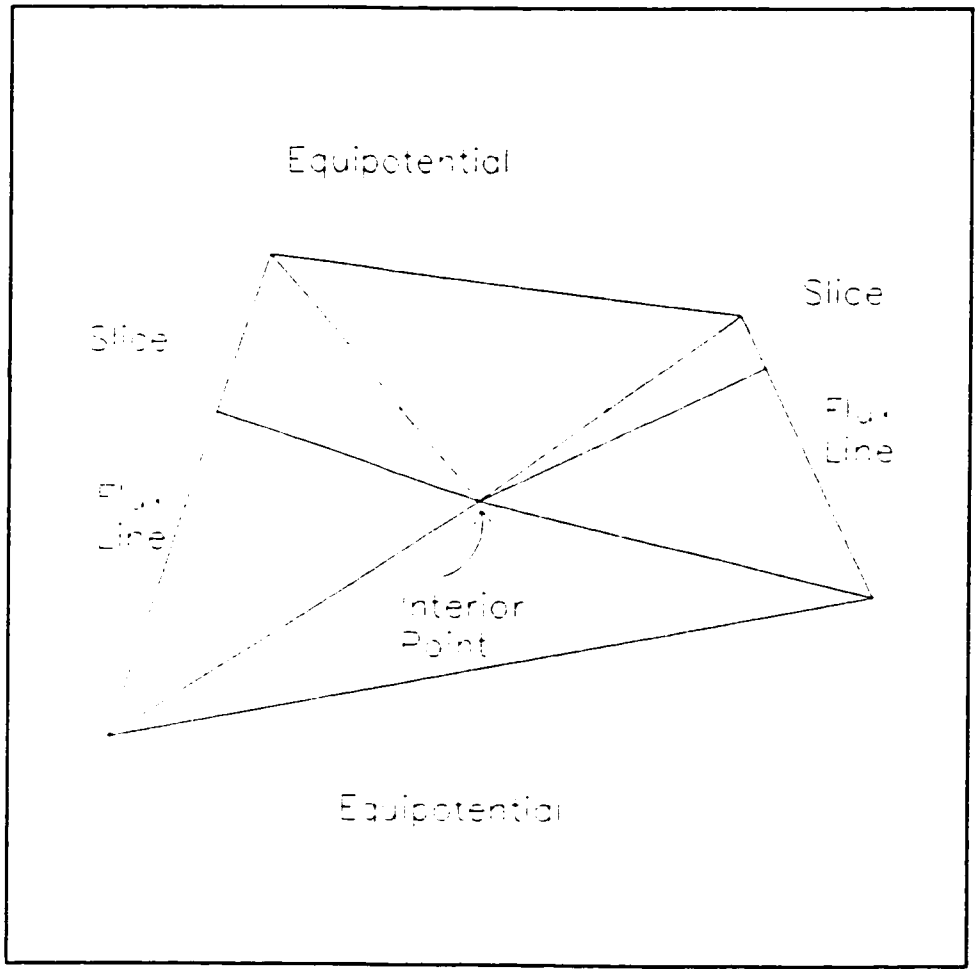

Figure 7.3: Equipotential placement inside a quadrilateral.

$$|\overline{E_1}| = \left| \frac{\varphi_1 - \varphi_{interior}}{\ell_1} \right| \tag{7.22}$$

$$|\overline{E_2}| = \left| \frac{\varphi_2 - \varphi_{interior}}{\ell_2} \right| \tag{7.23}$$

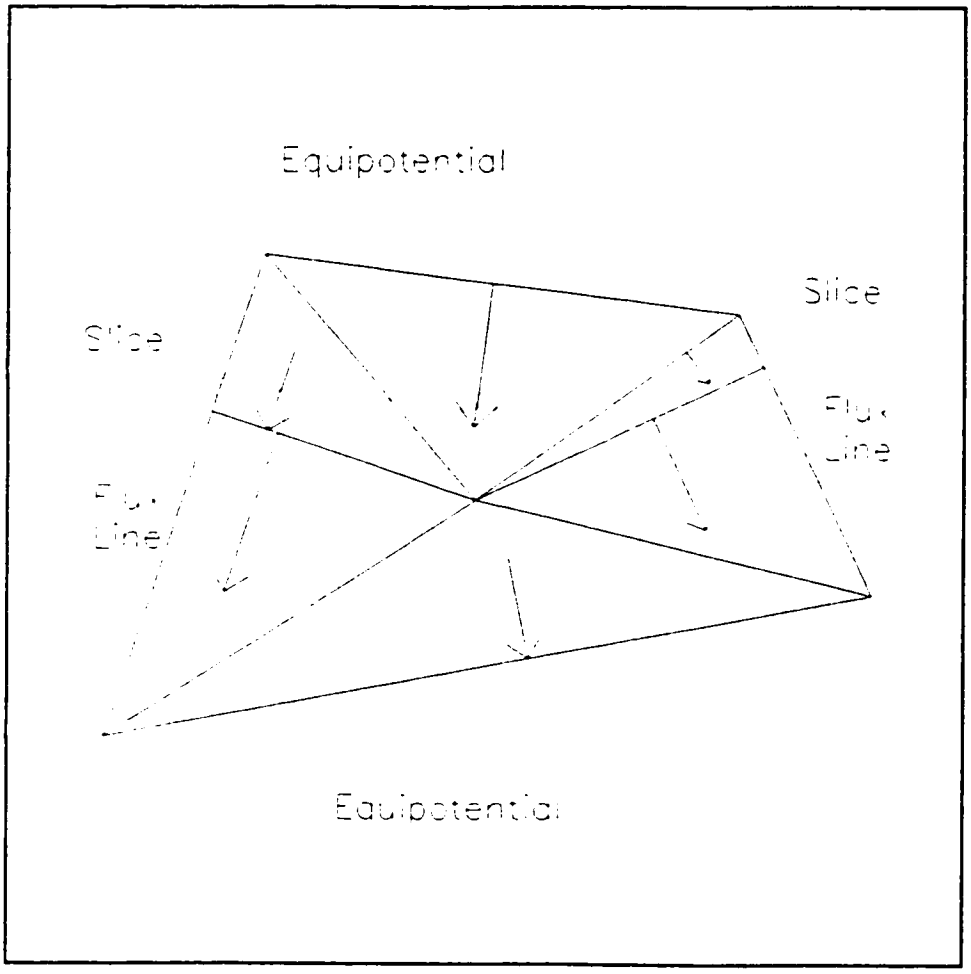

Figure 7.4: Electric field in each triangle - slice discretization.

In the tube discretization, we seek to find a lower bound for the capacitance of the system. Therefore, instead of "slicing" up the problem domain by placing equipotential surfaces at various places, we insert flux tubes. We define the amount of electric flux each tube carries and, in addition, the path the flux takes from one equipotential surface to the next. To start, the problem domain is divided into quadrilaterals, just as is done in the slice discretization. An interior point is placed inside the quadrilateral and lines drawn from the interior point to each of the four verticies. From the interior point, two more lines are drawn. Each of these lines terminates perpendicularly on the two equipotential surfaces of the quadrilateral as shown in figure 7.5.

The direction of the electric flux density vector **D** in each of the six triangles is shown in figure 7.6. The magnitude of the flux density vector is calculated based upon the "type" of triangle the vector lies in. Just as in the case of slice discretization, there are two different types of triangles that exist within the quadrilateral. Four triangles possess an edge coincident with one of the equipotentials. The other two possess an edge coincident with one of the flux lines of the quadrilateral.

In the case of the first triangle type, the electric flux density **D** is determined by initially defining the total amount of electric flux the entire tube carries. Then, a fractional value between zero (0) and one (1) is assigned to the interior point. The amount of flux each interior tube carries divides as the ratio of the interior point's fraction. For example, if we assign the interior point a value of 0.4, then one tube carries 40% of the total tube flux and the other tube carries the remaining 60% of the total tube flux. The magnitude of the electric flux density **D** is obtained by diving the interior tube flux by the length of the edge from the

appropriate vertex to the perpendicular intersection point.

For the remaining two triangles, we use the fact that the flux must remain constant in each interior tube. Since the amount of flux in each tube is constant, the normal component of **D** must be continuous across each of the lines joining the interior point to the four verticies. The tangential component can be calculated knowing the electric flux density vector **D** must be parallel to the side of the quadrilateral because it is a defined flux line. The expressions for the magnitude of the electric flux density in one of each of the two types of triangles are given

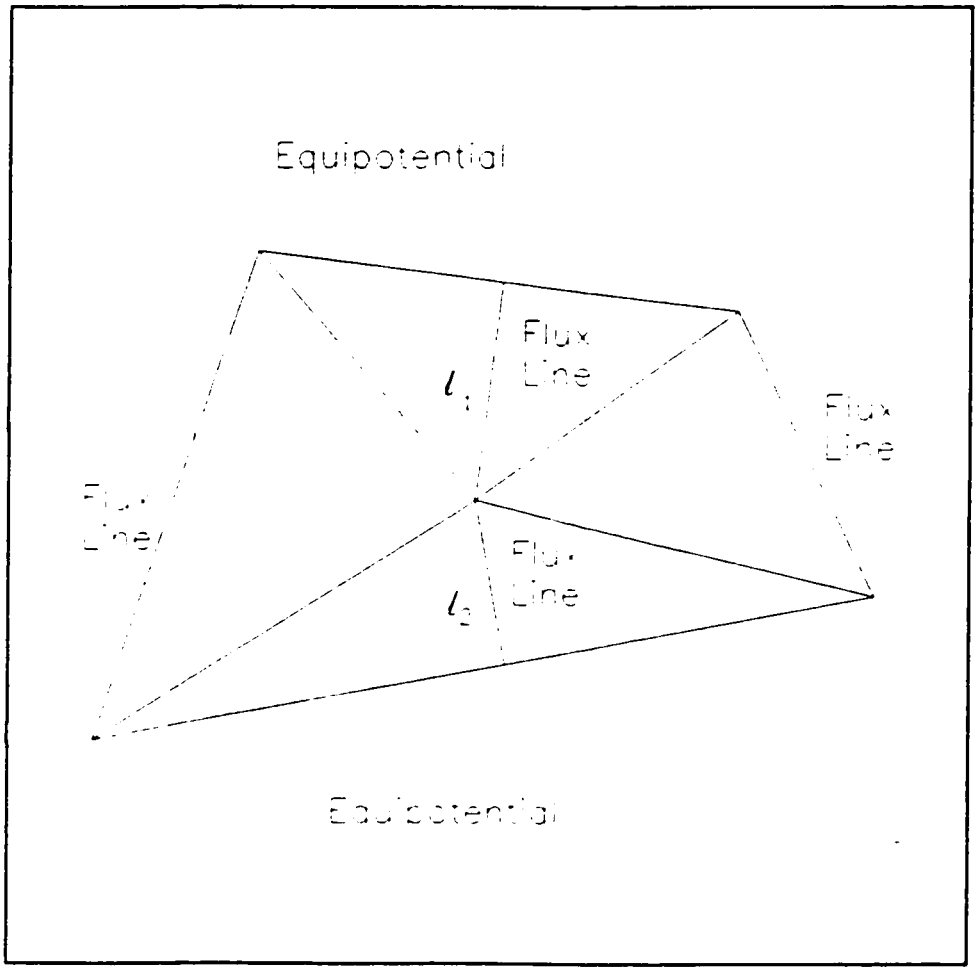

Figure 7.5: Flux lines inside a quadrilateral.

in equations (7.24) and (7.25) respectively.

$$|\overline{D_1}| = \left|\frac{\alpha Q}{\ell_1}\right| \qquad \textbf{(7.24)}$$

$$|\overline{D_2}| = \left|\frac{\alpha Q \ell_2}{2 A_\Delta}\right| \qquad \textbf{(7.25)}$$

In these expressions, α is the fraction of the electrical flux the partial tube carries, Q is the total electrical flux the entire tube carries and A_Δ is the area of the triangle that $\mathbf{D}_2$ is associated with. Alternatively, a coupled set of linear equations in two unknowns can be set up by imposing the continuity of flux across one of the discontinuities and orthogonality with the flux line's normal as the second constraint.

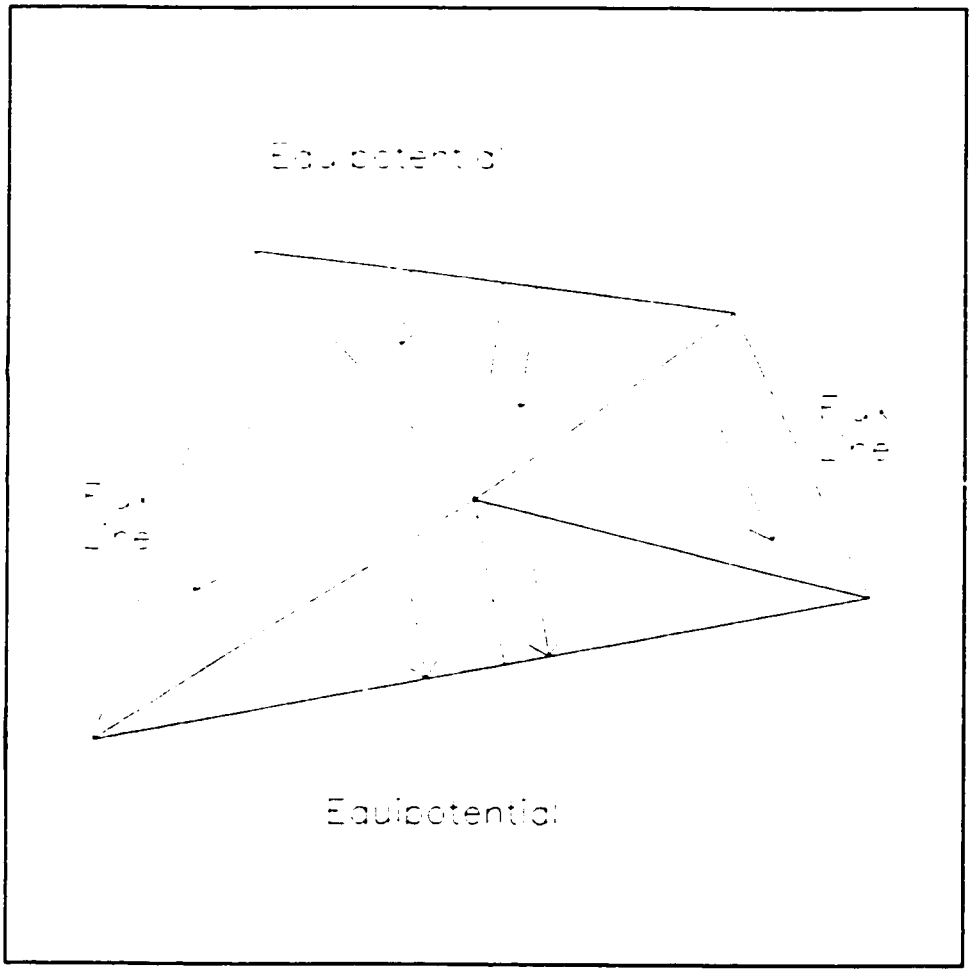

Figure 7.6: Flux density field in each triangle - tube discretization.

7.5 Stationary Functionals in Tubes and Slices

Not mentioned in the literature by other researchers is the fact that a stationary constraint can be imposed on the tube and slice discretization. In the process of stipulating that the functional be stationary, a series of linear equations is generated. It is the main premise of the tube and slice discretization technique to do away with as much computational effort as is possible in order to greatly reduce computation time and hardware requirements

of a solution. It is important to note that the coupling can vary. In the finite element process, the bandwidth of the final matrix is dependent upon the connectivity of the nodes. The equations mentioned here could be uncoupled or highly coupled depending on how the tubes and slices are initially constrained. As an example, the procedure is illustrated here in two dimensions with only one unknown in each quadrilateral.

In general, for the case of slice discretization, there are three independent- unknown values in each quadrilateral. These unknowns represent the electric scalar potential at the interior point of the quadrilateral and of the slice surfaces. For a unique solution, the scalar potential must be known on the boundaries. Since the energy functional is a quadratic function of the scalar potential drop in each of the sub- triangles inside the quadrilaterals, a set of linear equations can be generated. This is accomplished by taking the first partial derivative of the energy functional with respect to each of the unknowns and setting all of the partial derivatives to zero simultaneously. Since the slice cuts through "parallel" quadrilaterals, the coefficients of the polynomials must be summed over each one.

For tube discretization the procedure is similar. The energy functional is written as a sum of the energy stored in each of the quadrilaterals. Within each quadrilateral the unknown quantity is the amount of electric flux within each tube inside the quadrilateral. The total flux present within the system must be known for a unique solution. The functional is, once again, a quadratic function of the unknowns and first order partial derivatives can be taken and set equal to zero to generate a set of linear equations. This time, the tubes that are connected in "series" will contribute to the sum of the coefficient values in the quadratic polynomial.

For example, consider the quadrilateral shown in figure 7.2. It can be shown that the energy functional for the slice discretization for a certain set of (x,y) coordinates for this system is given by :

$$W_e = \frac{1}{2}\varepsilon_0[5\frac{2}{3}p^2 - 10p + 10] \qquad \textbf{(7.26)}$$

For the tube discretization we get :

$$W_e = \frac{1}{2\varepsilon_0}[3\frac{5}{6}q^2 - 10\frac{2}{3}q + 21\frac{1}{3}] \qquad \textbf{(7.27)}$$

Both of the expressions given in (7.35) and (7.36) are quadratic functions of the unknowns p and q. For larger systems, the coefficients would simply be a summation over all of the quadrilaterals that posses that particular unknown.

In these examples, the bounding equipotential surface potentials are assumed known as is the total tube flux. For more complicated geometries, coupled equations result when there are more quadrilaterals. However, the number of unknowns could potentially be orders of magnitude less than in a finite element formulated solution.

7.6 Two Dimensional Applications

In this section, the ideas presented and the methods derived in chapter seven are applied to actual two dimensional silicon micro motor structures and three dimensional geometrical constructs. The objectives are threefold. Firstly, to demonstrate the procedures required to apply the tube and slice discretization methods to micro motor structures. This has not been attempted thus far by other researchers in either two or three dimensions.

Secondly, to assess the accuracy of the dual bounds method in two dimensions by comparison with the previously derived capacitance values obtained through the finite element method. The validity of the two dimensional tube and slice approximation is accomplished by comparing the estimated direct axis capacitance values in two "extreme" cases. Case one consists of the situation in which the stator's emf field is in alignment with the direct axis of the machine. Case two is the situation in which the stator's emf field lies entirely in the quadrature axis. For each of the these cases, a two dimensional slice discretization as well as a two dimensional tube discretization is constructed. A dual bounds approach is implemented by averaging the two values which are known to bound the capacitance.

The third objective of this chapter is to extend the ideas of the two dimensional formulation to three dimensional structures. A geometrical shape and an accompanying discretization is formulated. The goal is to derive the mathematical relationships for the fields in the discretized three dimensional regions. Once the geometrical and mathematical formulation is complete, it is shown that an actual micro motor structure could be discretized in this fashion.

7.7 Two Dimensional Discretization

A silicon micro motor structure with a stator-pole-to-rotor-pole ratio of 3:2 is taken as an example device for purposes of comparison in this chapter. Figure 3.2 shows a scanning electron microscope photograph of such a machine. A pictorial representation of the axial cross section is shown in figure 7.7. The same structure is analysed using both the dual bounds approach as well as the finite element method in order to ascertain the accuracy of the method in a two dimensional example case. Two scenarios in particular are of interest. These configurations correspond to stator emf field alignment with the direct axis and then with the quadrature axis since both situations represent extreme cases of pole surface area alignment and misalignment respectively. It is these two cases that will also be of importance in the three dimensional simulations because it is expected that the amount of stator-to-rotor-pole surface overlap will determine the validity of two dimensional approximations in general [7].

Since the final electrostatic solutions for both the direct axis only excitation as well as the quadrature axis only excitation possess spatial periodicity, the entire structure need not be discretized. With the stator emf field aligned completely with the direct axis, the primary quadrilateral composition of a 180 (electrical) degree sector is broken up as shown in figure 7.8. The same primary quadrilateral scheme is used for both the slice discretization and the tube discretization. What differs for each case is the location of the interior point. In figure 7.9 the slices are shown and in figure 7.10 the tubes are shown.

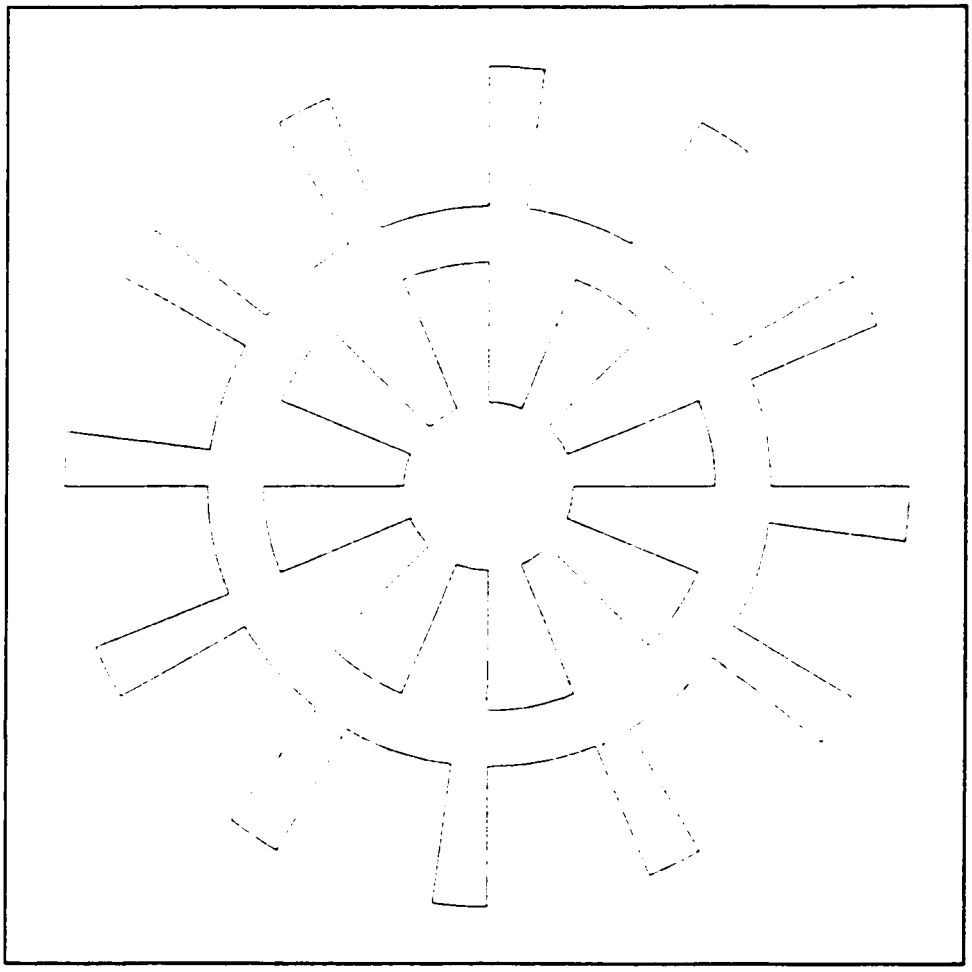

Figure 7.7: Outline of the 3:2 ratio micro motor.

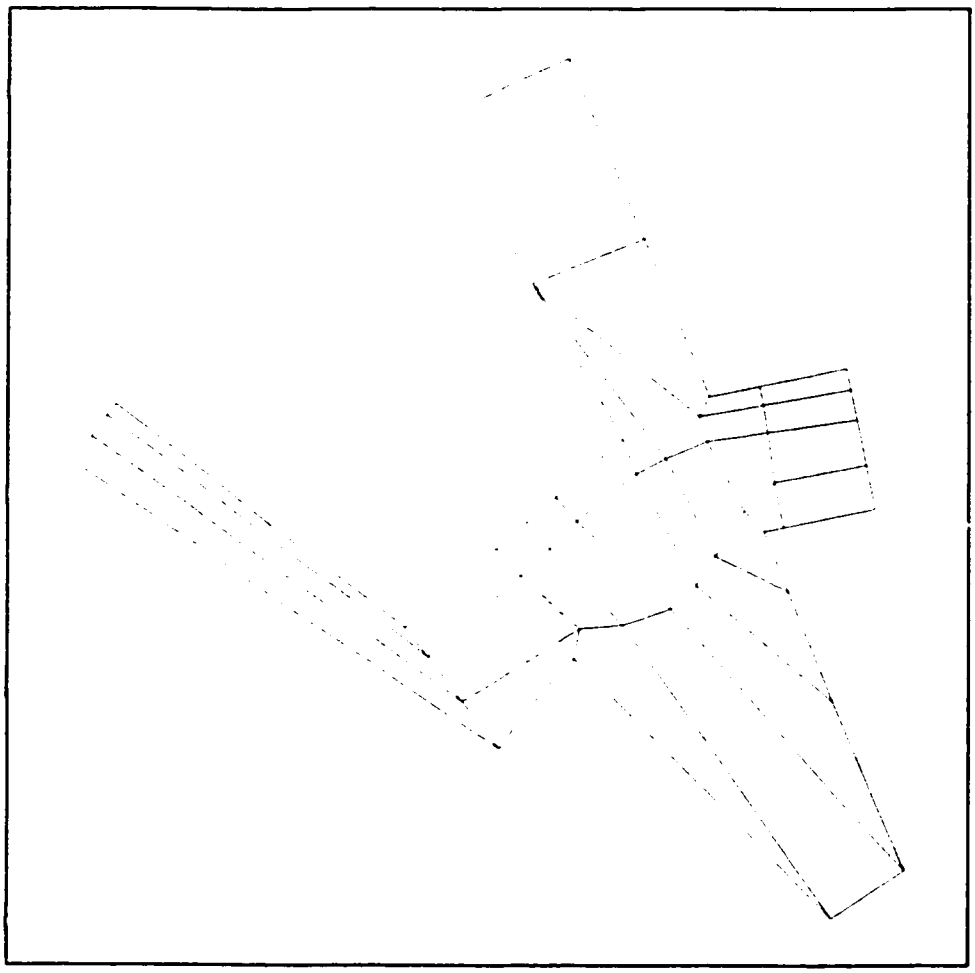

Figure 7.8: Direct axis quadrilateral discretization.

Some of the important features to note in each diagram are the continuity of the slices from one quadrilateral to the next in all cases where the quadrilaterals are in parallel. By this it is meant that the two bounding surfaces on either side of a quadrilateral are at the same electric scalar potential with respect to the reference potential. Every slice that cuts through one quadrilateral must intersect the flux lines of each and every other quadrilateral at a 90 degree spatial angle. Similarly, each tube that passes through one quadrilateral must intersect the equipotential surfaces of all other series quadrilateral elements in a perpendicular fashion.

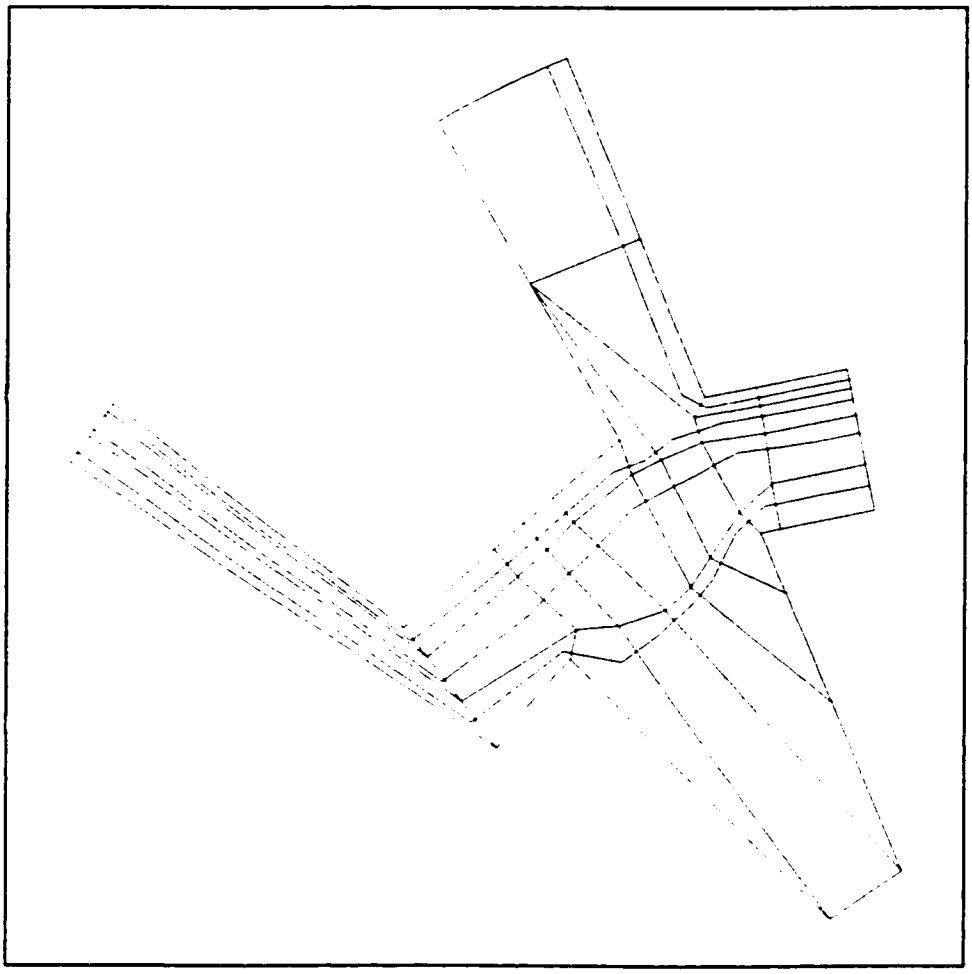

Figure 7.9: Direct axis slice discretization.

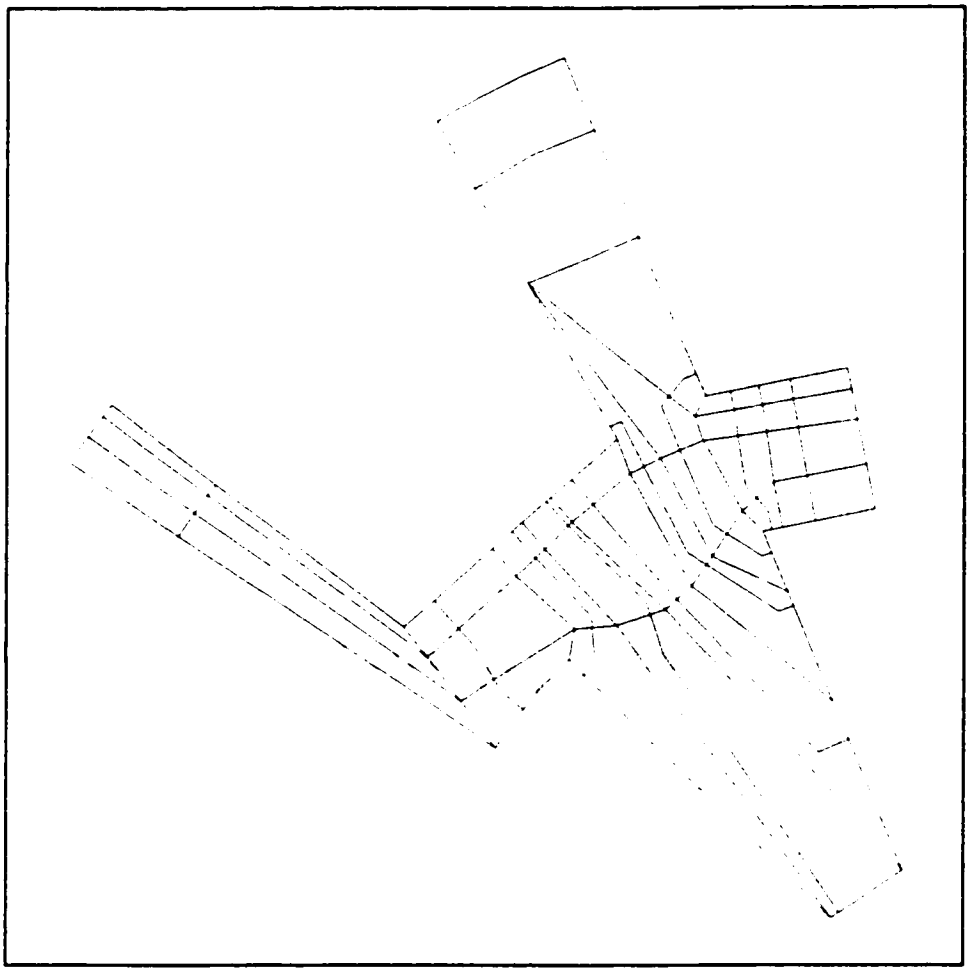

Figure 7.10: Direct axis tube discretization.

For the case of quadrature axis only excitation, the primary set of quadrilaterals for a 180 electrical degree sector is shown in figure 7.11. In this situation, the axis of the stator emf field lies in between two rotor poles and corresponds to the condition of minimum surface area overlap between the stator and the rotor. The quadrature axis slice discretization is shown in figure 7.12 and the tube discretization shown in figure 7.13.

The excitations used to produce the single (direct and quadrature) axis excitations are shown in figure 7.14. For the direct axis case, because the rotor poles are in alignment

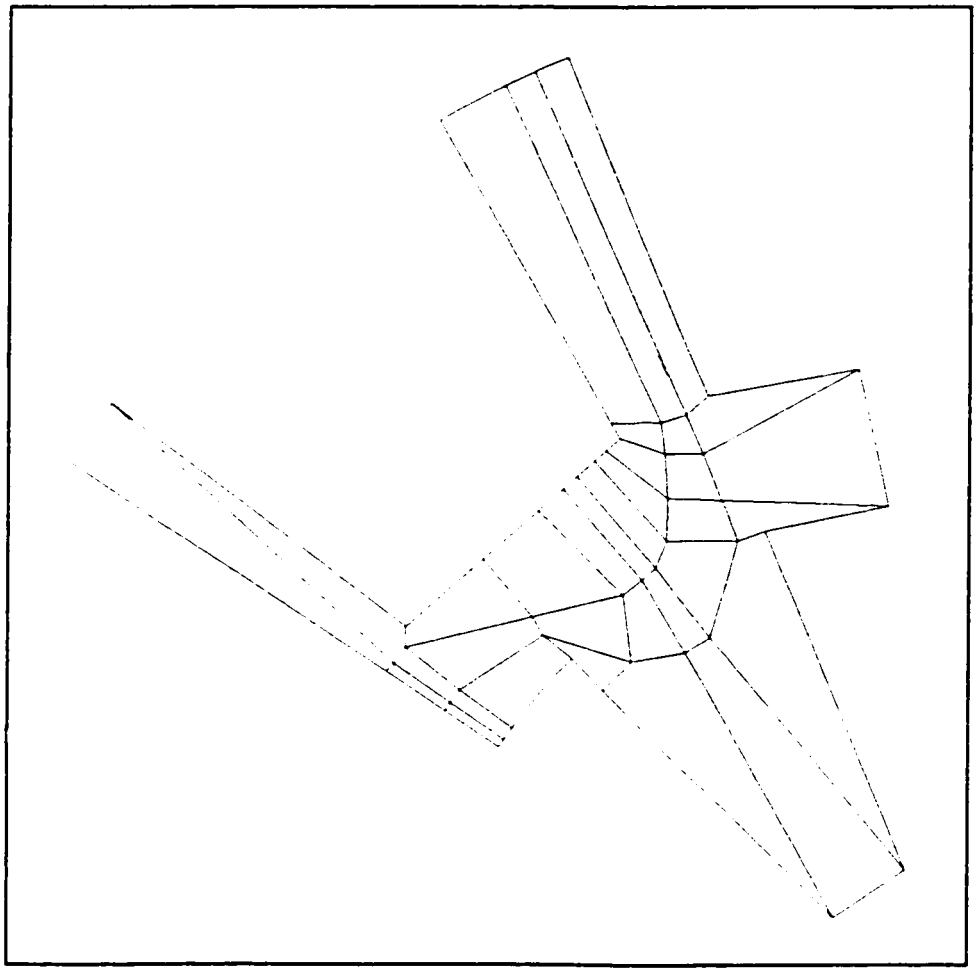

Figure 7.11: Quadrature axis quadrilateral discretization.

with one pair of stator phase electrodes, the voltage of that electrode pair is set to a maximum value while the other two remaining phase electrode pairs are of equal and opposite polarity. Setting electrode potentials corresponds to the slice discretization case. For tube discretization, the electrode charges must be specified. Once again, for the direct axis case, the phase electrode pair in direct spatial alignment with a rotor pole is set to a maximum value. The other two electrode pairs are ascribed equal but opposite amounts of charge. For both slice and tube simulations, the excitations are balanced. There is negative or zero sequence component to the potential or flux excitations. For the quadrature axis situation, the stator emf field must not possess any direct axis component. In order to achieve this condition, the rotor is rotated 90 electrical degrees while the stator electrode excitations remain fixed. The phasor diagram shown in figure 7.14 helps demonstrate how this works. The instantaneous electrode potential or flux is projected spatially onto the desired axis defined by the position of the rotor at the instant in time the phasor diagram is applicable.

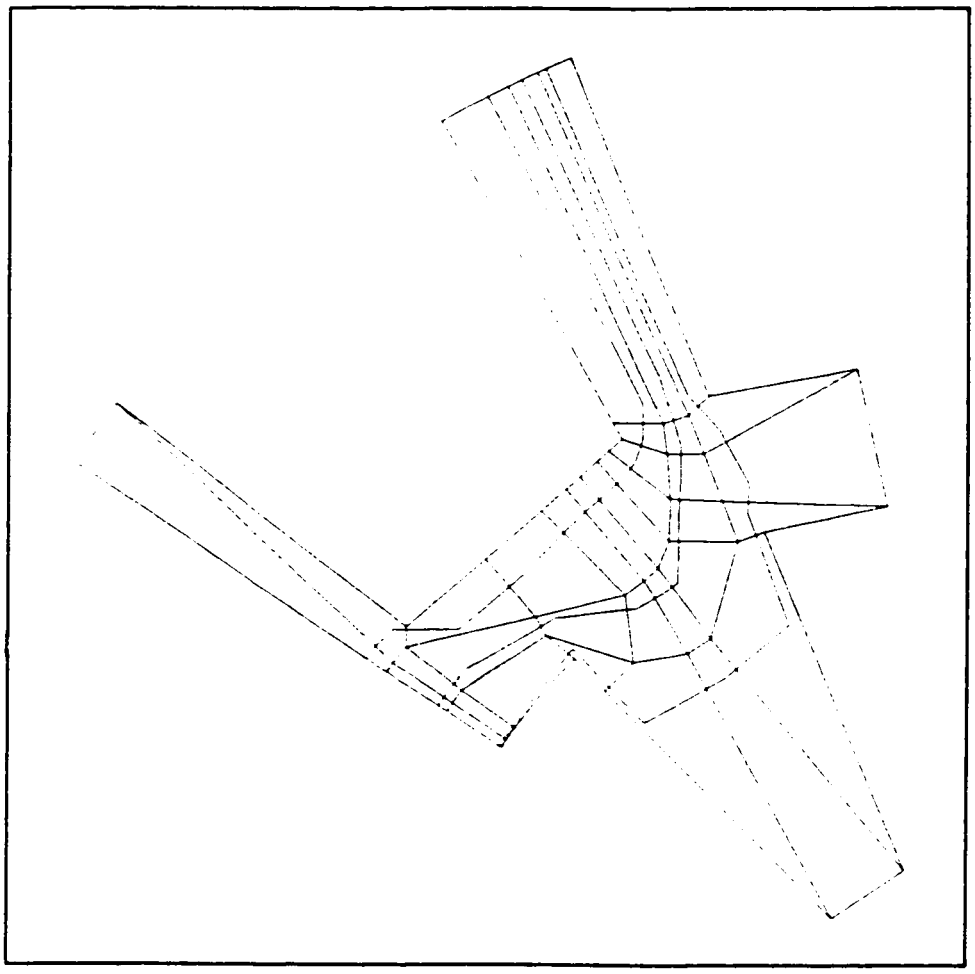

Figure 7.12: Quadrature axis slice discretization.

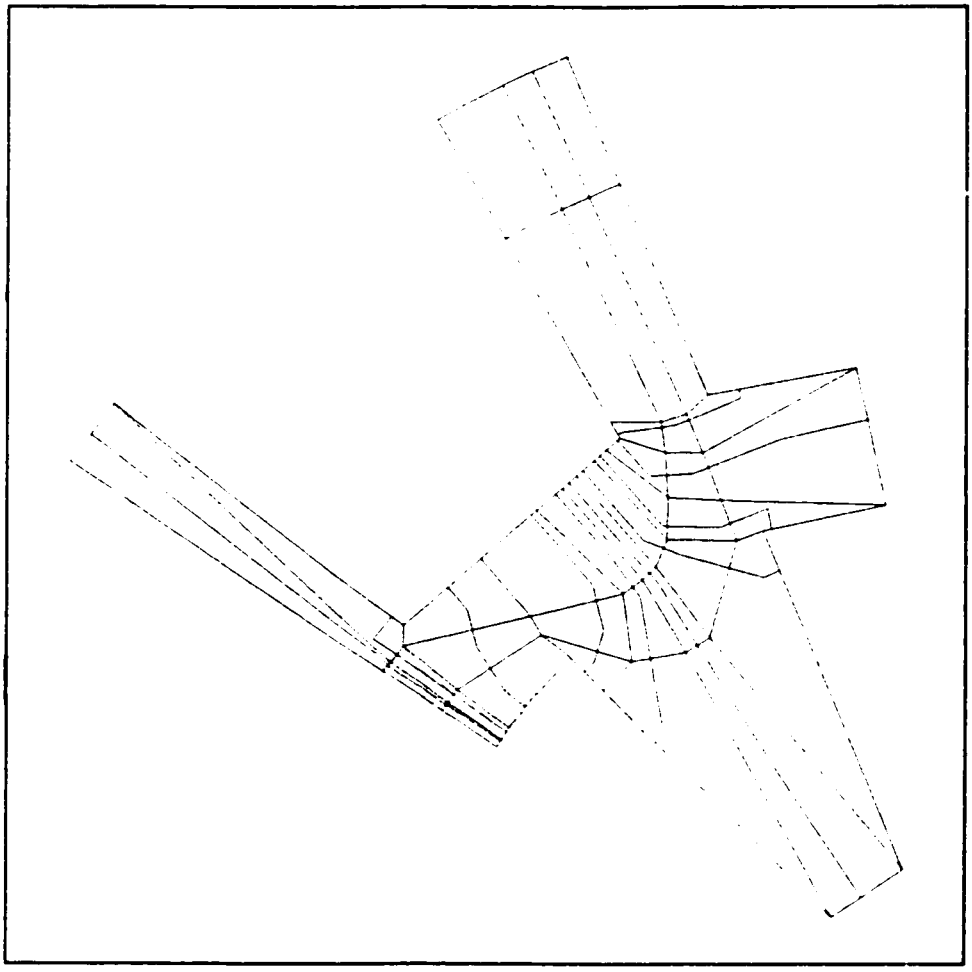

Figure 7.13: Quadrature axis tube discretization.

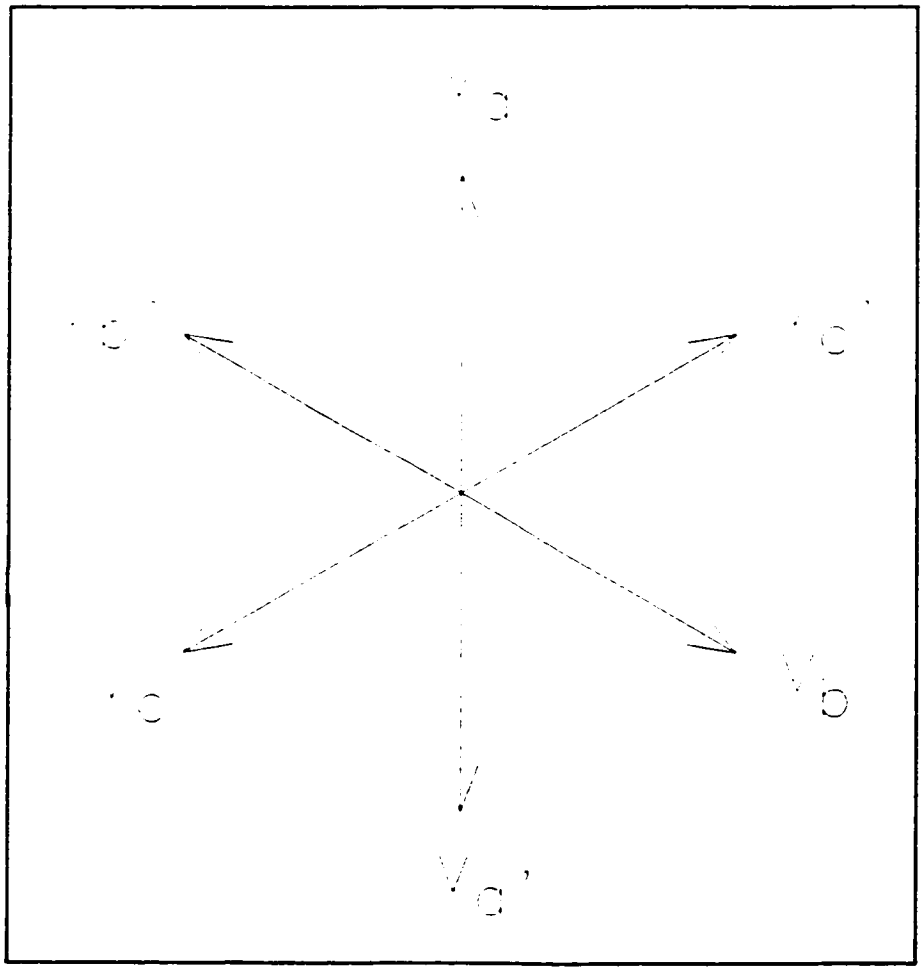

Figure 7.14: Excitation scheme.

7.8 Two Dimensional Results

Two programs were written in 'C' in order to automate the solution process. Each program requires two ASCII input files; a file containing the quadrilateral outline information and another file that contains the interior point information. There is a separate program for slice (SLICENRG.C) and tube (TUBENRG.C) discretization schemes. Two outline files were created; one for the direct axis excitation (OUTLN_D.DAT) and one for the quadrature axis excitation (OUTLN_Q.DAT). Two interior point information files were created to supplement the outline files. For slice discretization interior point information SLICE_D.DAT was created for the direct axis excitation. Similarly, SLICE_Q.DAT was created for the quadrature axis slice excitation.

For the case of tube discretization, the same outline files (OUTLN_D.DAT and OUTLN_Q.DAT) are used. What differs is the interior point information files. For the direct axis simulation, TUBE_D.DAT is used as input and for the quadrature axis case, TUBE_Q.DAT is used as input. The two 'C' programs as well as their associated input data files are presented in appendix A.

A finite element mesh bounded by the same outer contours as the quadrilateral geometry was created for purposes of comparison. What will be compared is the direct axis and the quadrature axis capacitance obtained through the dual bounds method and the finite element method, both in two dimensions. The information expected to be gleaned from this exercise is some expectation about what benefits might be expected from a three dimensional dual bounds solution compared to its finite element counterpart.

The boundary conditions used for both the quadrilateral discretization as well as the

finite element simulations are shown in figures 7.15 and 7.16. Figure 7.15 represents the direct axis discretization and figure 7.16 the quadrature axis discretization. For the direct axis case, one of the stator electrode pairs is aligned with a rotor pole. The boundary conditions are set up such that the rotor pole and the stator pole are split in half along a flux line. The entire sector spans 90 electrical degrees or 45 mechanical degrees. An equipotential line runs from the centre of the adjacent rotor pole to the interior back portion of the stator electrode structure. The value of this equipotential surface is set to zero since it lies at the midpoint of two equal in magnitude but opposite in polarity equipotential surfaces and the spatial geometrical pattern repeats as well.

For the quadrature axis situation, we once again model a 90 electrical degree sector. In this case emf field of the stator axis is aligned with the rotor's quadrature axis. This is implemented by leaving the rotor's position fixed (where it was relative to the stator poles in the direct axis case) and phase advancing the stator electrode scalar potentials by 90 electrical degrees. In this situation, the potential difference between the stator electrode that is aligned with the rotor pole and the rotor's potential is zero. Therefore, the flux line that split the aligned poles in the direct axis case is now an equipotential surface. The equipotential surface from the direct axis case remains becomes an equipotential surface since, in this case, the two stator electrodes that were equal in magnitude but of opposite sign are now equal in magnitude and of equal sign. This forces the midpoint of the boundary at the back of the stator to also be of equal potential.

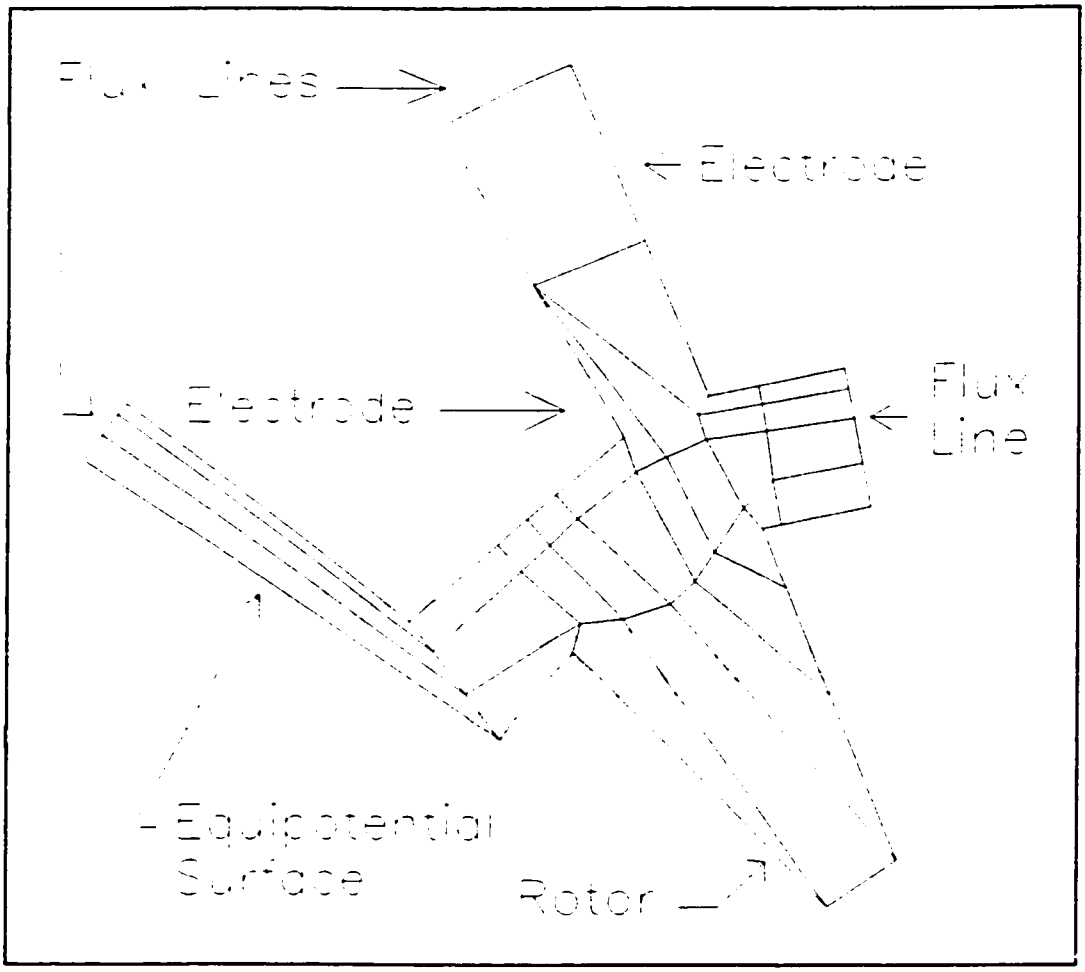

Figure 7.15: Direct axis boundary conditions.

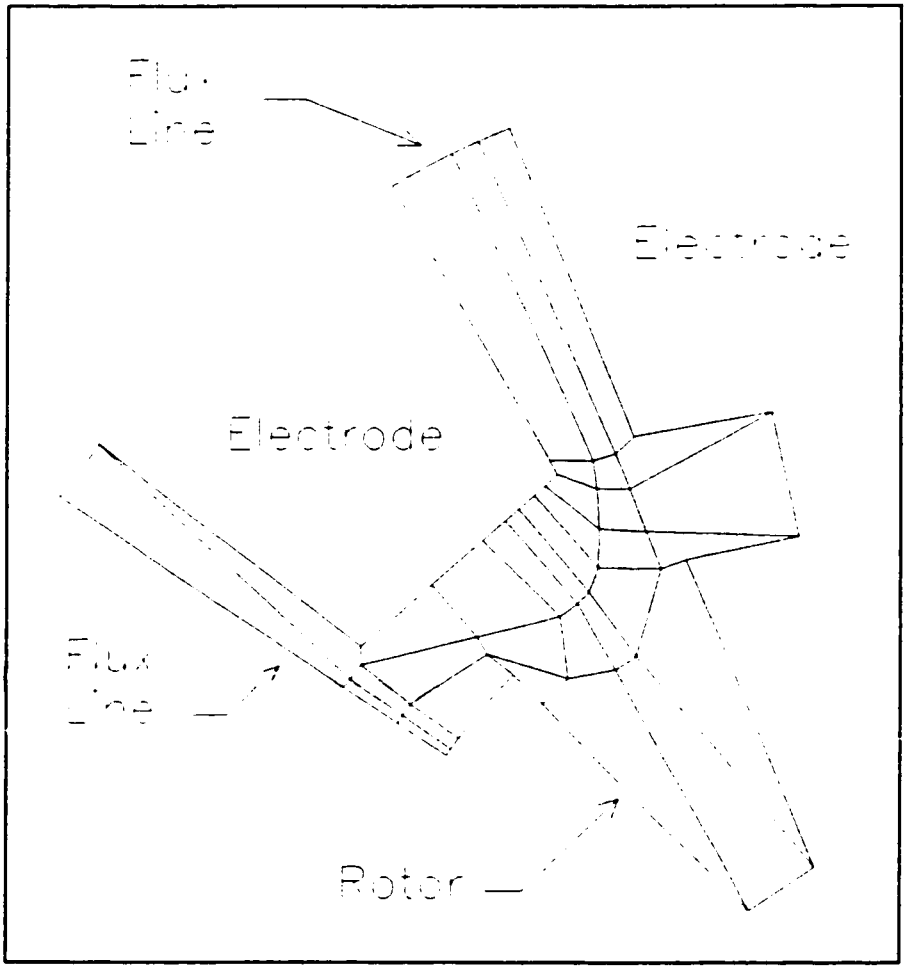

Figure 7.16: Quadrature axis boundary conditions.

7.8.1 Two Dimensional Results Comparison

The results obtained through both methods are tabulated below in table 7.1. For the finite element method, the "classic" denotes a scalar potential formulation where stator electrode potentials are set to known values. A balanced set of voltages is assumed for the stator excitation. The rotor is treated as the reference conductor and is therefore an equipotential surface in a scalar potential formulation.

Table 7.1 Two dimensional capacitance comparison.

Solution Method	Stored Energy {d axis position} (J)	Stored Energy {q axis position} (J)	EMF d-axis Capacitance (pF)	EMF q-axis Capacitance (pF)
Tubes	1.93E+16	6.38E+15	37.4	37.6
Slices	2.66E-06	9.40E-07	237	251
Dual Bound	N/A	N/A	137	144
Classic Finite Element	1.49E-06	4.94E-07	132	132

From the results shown in table 7.1 it is evident that the dual bounds approach has promise as a viable alternative to the finite element method when computational effort is a concern. The direct axis capacitance computed using the average of the slice-based and tube-based direct axis capacitances is within 4 % of the finite element solution. With the field aligned with the quadrature axis, the capacitance calculated by the same averaging technique is within 10 % of the finite element solution. Note that 242 first order elements are included in each of the two-dimensional finite element simulations. No more than 33 quadrilaterals are needed for either of the direct axis or quadrature axis quadrilateral discretizations.

CHAPTER 8

TUBES AND SLICES IN THREE DIMENSIONAL PROBLEMS

8.1 Introduction

It is demonstrated that the concepts discussed in chapter seven that deal with the discretization of a two dimensional region into a set of tubes and slices can be applied to a three dimensional object. All of the geometrical constructs necessary for this procedure are derived in this chapter. It is shown that the fundamental construction elements are consistent with electromagnetic boundary conditions both internally and at the problem outer periphery. It is proved that with appropriate constraints, these fundamental structures can be cascaded to make up a general three dimensional object.

As mentioned before, it is in three dimensional analysis that the method of tubes and slices becomes most attractive. The computations involved in obtaining the upper and the lower bounds do not require the solution of a large system of coupled equations. Furthermore, the amount of discretization need not be excessive. We can arrive at two solutions for the capacitance rather inexpensively, one being an upper bound and one being a lower bound. The average of the two capacitances is guaranteed to be bounded.

The cost of a single three dimensional finite element solution can be very expensive

in terms of the computational demand required. This is especially true in cases where a fine mesh is used. A second solution may not be practical. Furthermore, without a second solution, there is no bound or region wherein the true solution is known to lie. Hence it is difficult to easily assess the accuracy of a single solution using the finite element method.

In a two dimensional problem, the mesh can be refined successively and the system energy determined for each case. It is generally true that as the change in system energy decreases from one solution to the next, the approximate solution becomes more accurate. In a three dimensional problem this procedure is very costly and time consuming.

The information presented in this chapter is a new addition to the concepts first presented by Hammond [66]. In his initial work, there is no detailed derivation of the magnitude of the electric field strength **E** in the slice discretization nor of the magnitude of the electric flux density field **D** in the tube discretization. Furthermore, the exact details of the spatial elements inside the most basic three dimensional element were not presented. To the author's knowledge, this information cannot be found elsewhere in the literature.

8.2 Discretization Constraints

A complex geometrical structure such as the one shown in figure 8.1 can be constructed of a number of smaller fundamental building blocks. To do this without imposing any constraints on the individual elements is quite straight forward. This is one advantage that the finite element method has. Discretizing such a structure in preparation for a computationally expensive finite element solution does not present the analyst with an extraordinary number of constraints on the interconnection of the tetrahedron, brick or other

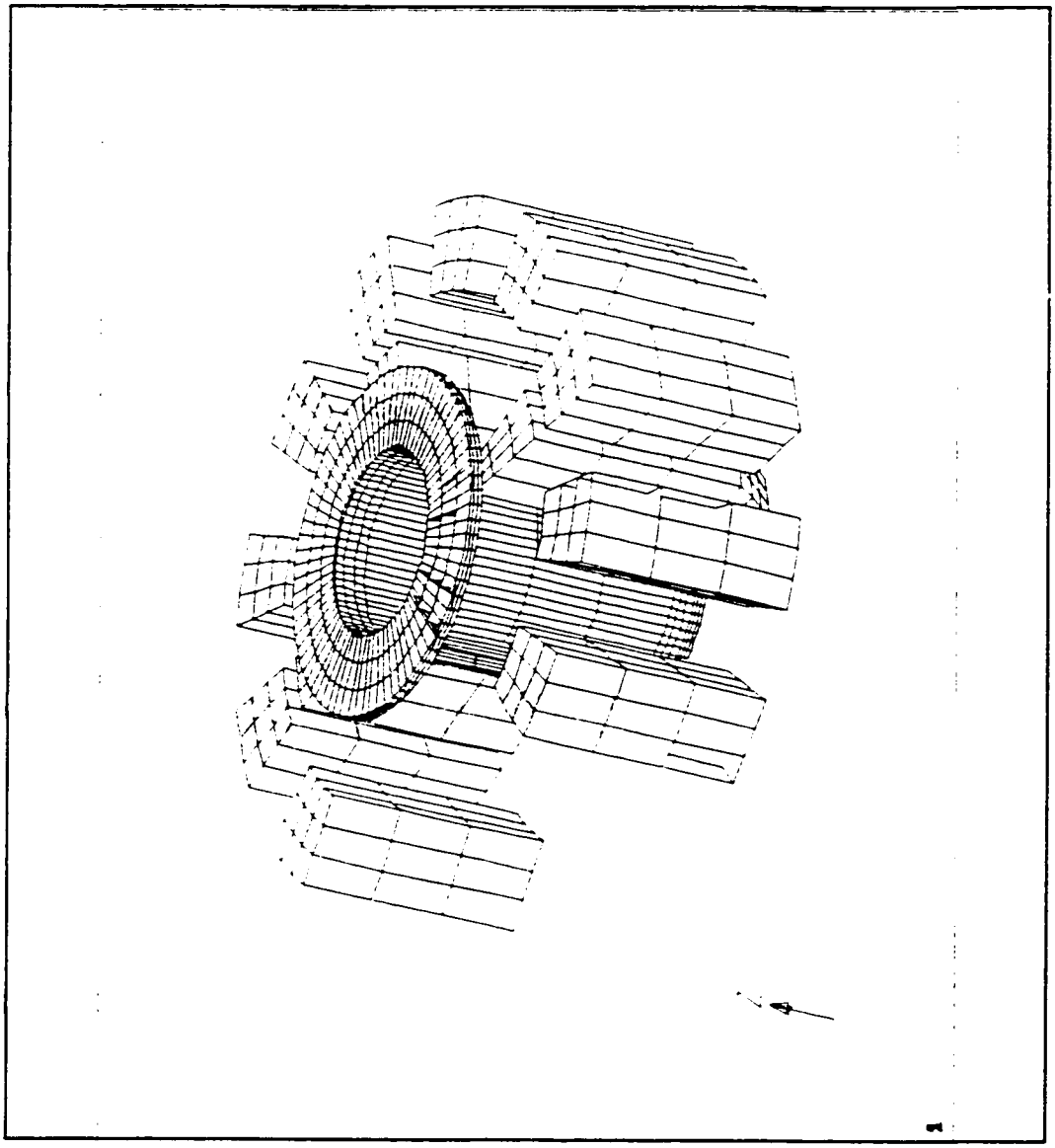

Figure 8.1: A three dimensional model of a silicon micro motor.

elements.

In deriving the method of placement for the tubes and slices which cut through the fundamental base elements, a number of restrictions exist. Because the solution to the overall problem must obey certain boundary conditions, these individual structures must have similar boundary conditions inherent in them. In particular, for electrostatic problems, surfaces of constant electric scalar potential as well as surfaces confining electric flux must be present in the primary element of construction.

A cuboid with six surfaces, two of which are surfaces of constant electric scalar potential and four of which are flux-confining surfaces is shown in figure 8.2. This element is chosen as the base element of construction for the method of tubes and slices in three dimensions. Such a structure is an extension of the quadrilateral structure implemented in two dimensions and was proposed by Hammond in his original work [66].

There are a large number of problems related to the practical implementation of this structure in a three dimensional problem that were not addressed by Hammond or other researchers studying dually bounded methods. These problems are outlined and solved in this chapter.

8.3 Connection of Fundamental Elements

When these fundamental blocks are connected together to form a more complex structure, the basic boundary conditions must still be met. Within the interior of the problem domain, equipotential surfaces must overlay equipotential surfaces and flux surfaces must overlay flux surfaces. The boundary conditions at the physical extremities of the problem

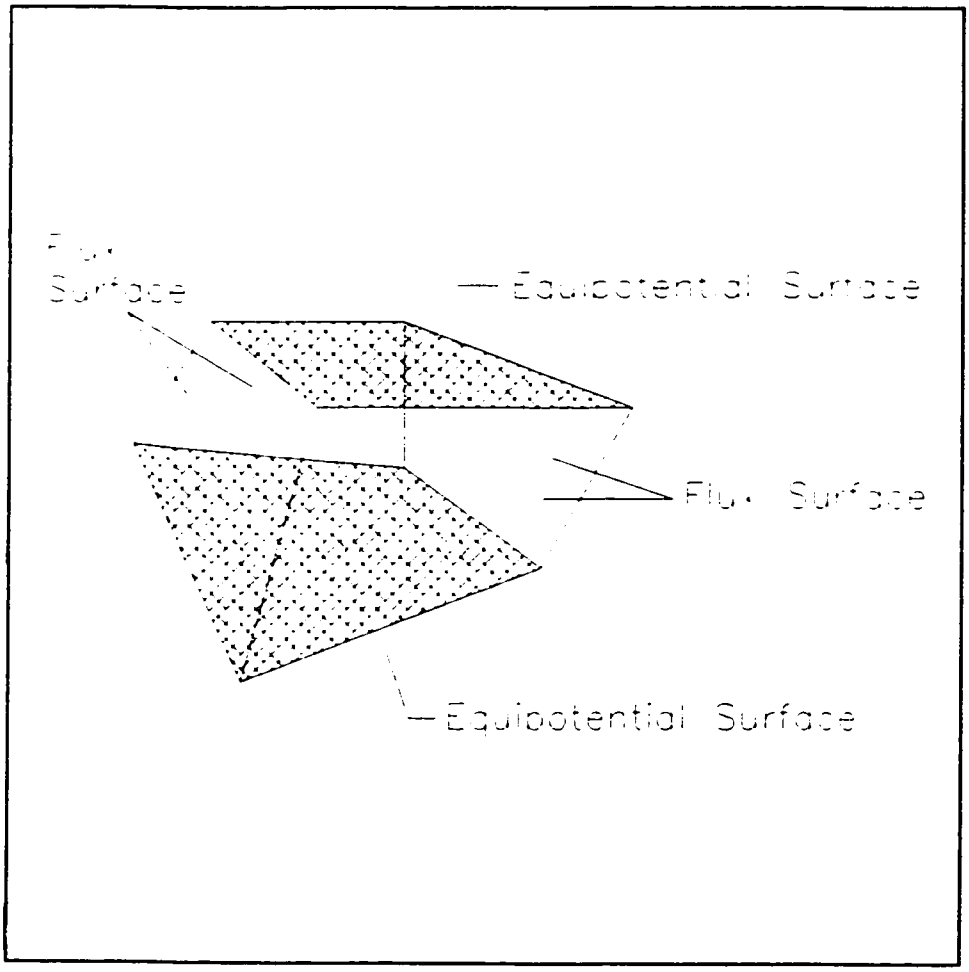

Figure 8.2: Fundamental cuboid structure.

boundary are such that the equipotential surfaces must lie along surfaces with known voltage and the flux surfaces must be used to confine electric flux within the problem domain.

Figure 8.3 illustrates how the individual base elements are connected together. The centre element represents an internal element that physically connects to six other elements. The inner element shares two equipotential surfaces, one with the element above it and one with the element below it. The inner element also shares four flux-confining surfaces belonging to the four adjacent elements.

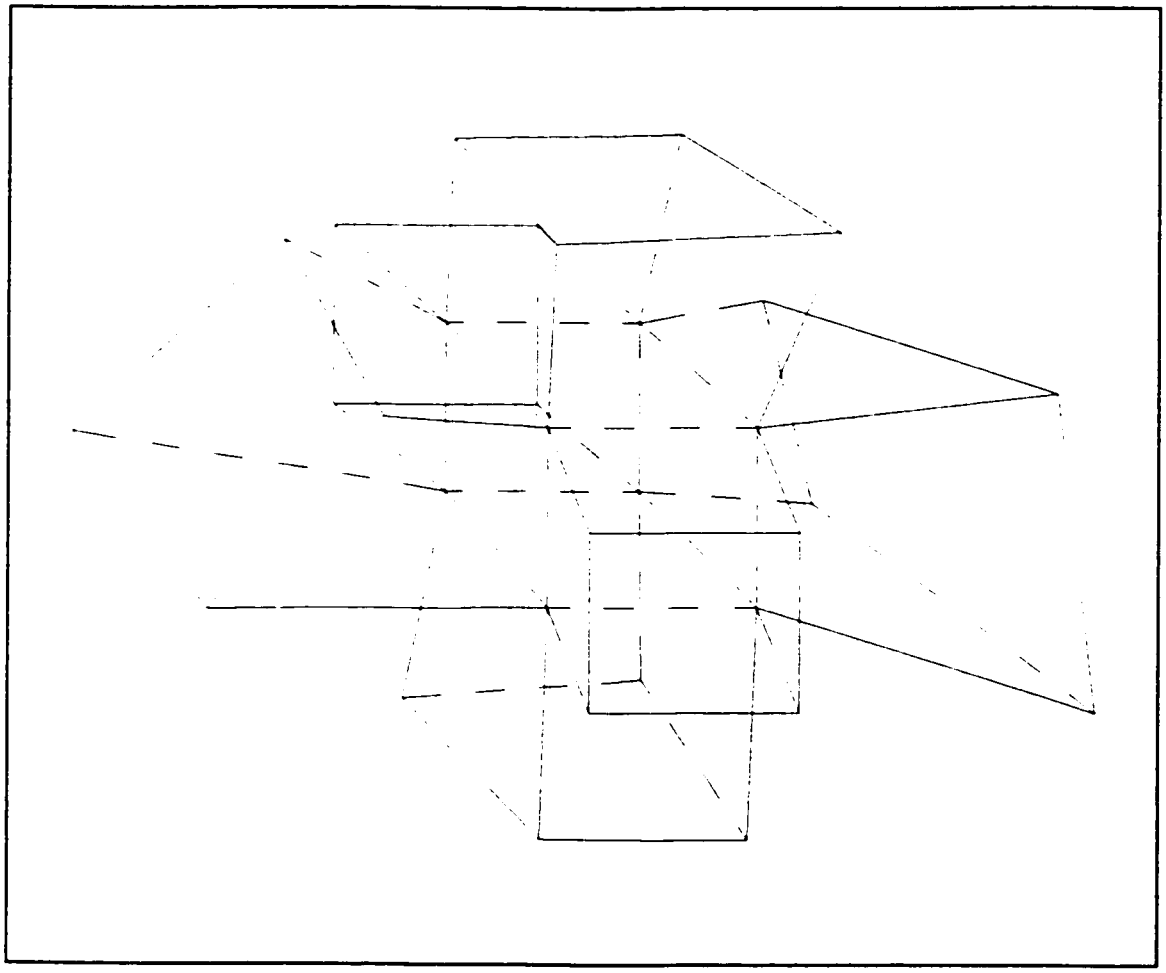

Figure 8.3: Connection of cuboid structures.

Since the inner element shares its top equipotential surface with the above element's bottom equipotential surface, we are guaranteed to have continuity of electric scalar potential across that surface. The same is true for the inner element's bottom equipotential surface and the underlying element's top equipotential surface. As the elements are cascaded "laterally" outward from the inner element we are guaranteed that the surfaces of constant electric scalar potential will be continuous. See figure 8.4.

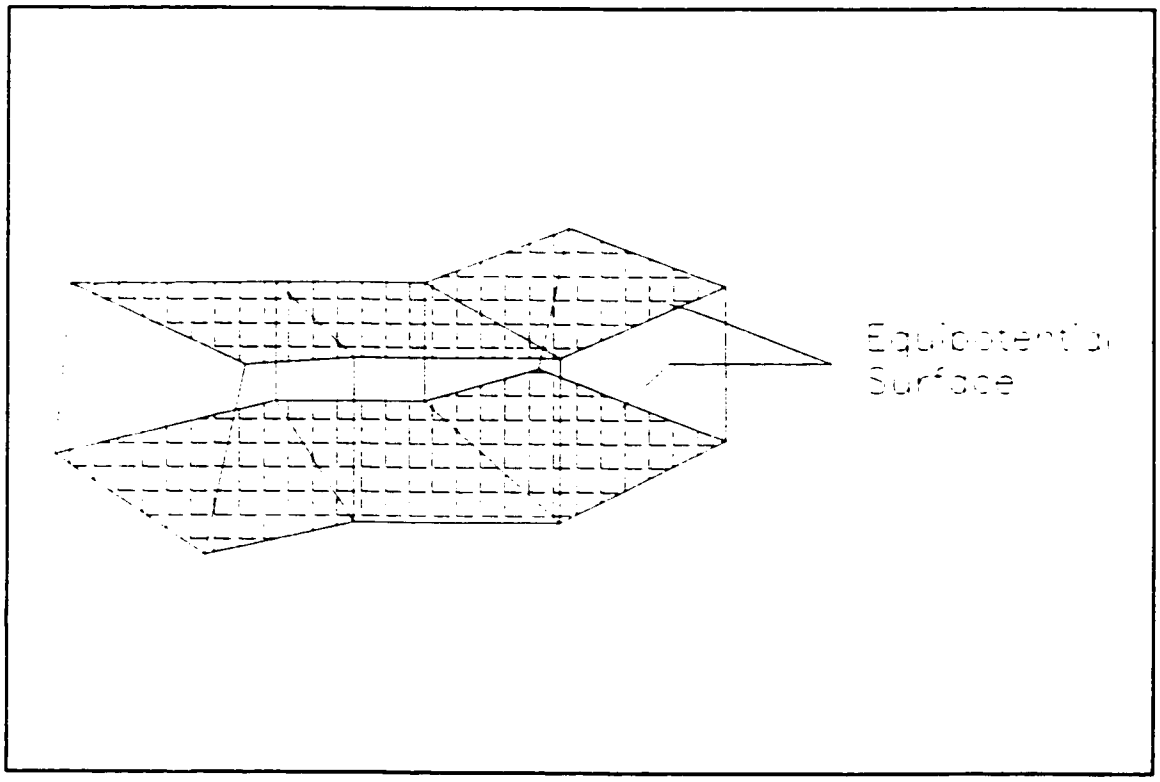

Figure 8.4: Continuity of equipotential surfaces.

The four flux-confining surfaces serve to keep the quantity of electric flux entering the top equipotential surface equal to the amount of electric flux leaving the bottom equipotential surface. The continuity of the normal component of electric flux density **D** is guaranteed. The electric field terminates perpendicularly on the top and bottom surfaces. Since each equipotential surface is shared by two elements, the cross sectional area through which the flux passes as it crosses this surface is equal. Because the amount of flux is also equal, we are guaranteed that the normal component of **D** remains continuous.

At the problem's outer boundary, we must ensure that the equipotential surfaces of the boundary elements coincide with known surfaces of electric scalar potential. On the remaining unconstrained boundary surfaces, the built in flux-confining surfaces of the

boundary elements need to be used to confine the electric flux to the problem domain. In finite element terminology, this is merely a Neuman or natural boundary condition enforcement. It guarantees that there is no normal component to the gradient of the electric field at these surfaces. Figure 8.5 illustrates the enforcement of boundary conditions on boundary surfaces.

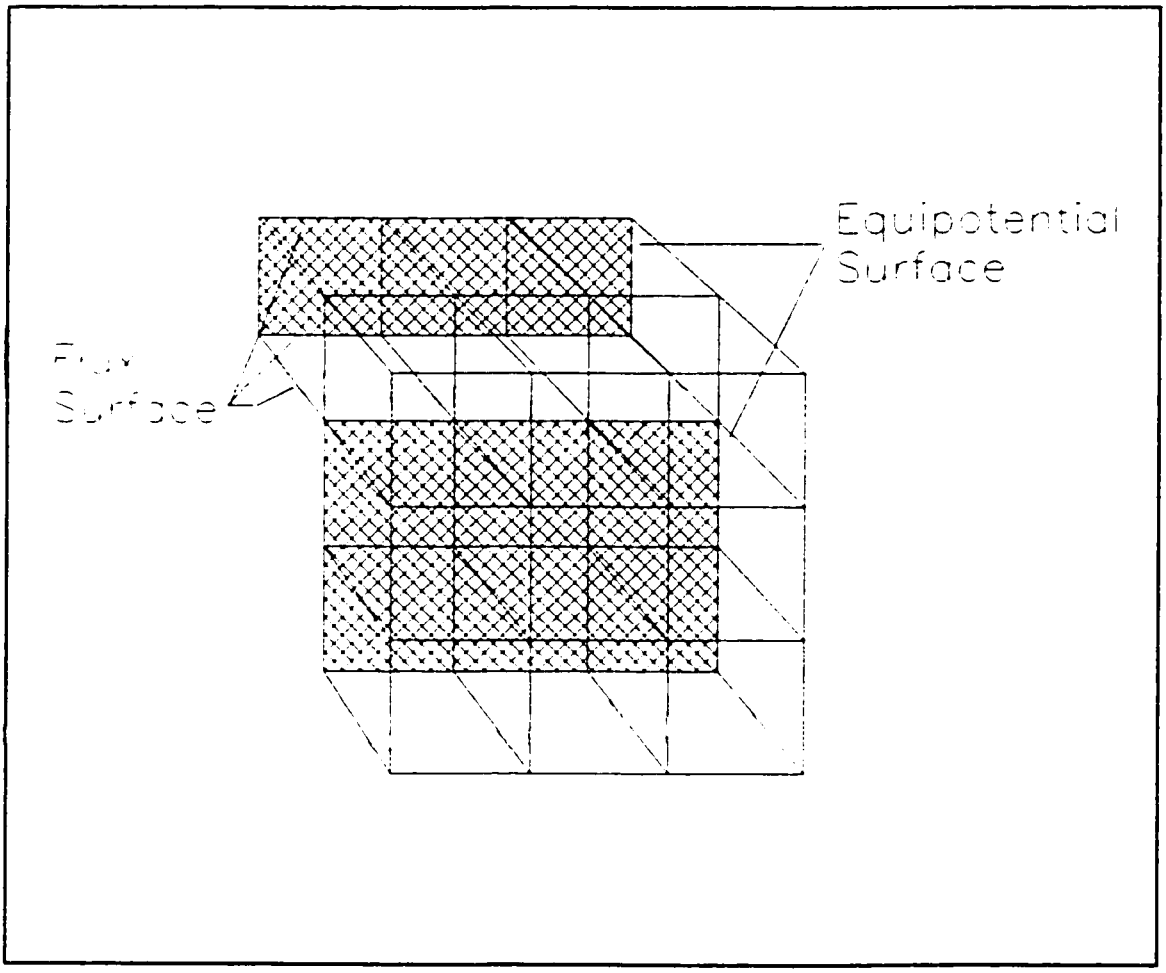

Figure 8.5: Enforcement of boundary conditions.

8.4 Equipotential Slices in Three Dimensions

For the method of slices in three dimensions, we start with a basic geometrical unit that consists of a cuboid. It has eight vertices and six faces. Two of the faces are equipotential surfaces and the other four represent flux surfaces. A slice is to be placed inside the structure. The slice is a surface of constant electric scalar potential that will be assigned a value later on in the analysis. For the moment, it suffices only to state the constraints that apply to the location and geometrical properties of this surface:

1. Because the slice is a surface of constant electric scalar potential, it must be perpendicular to all four of the flux-confining surfaces where it intersects these surfaces.
2. The slice surface must be connected within the cuboid structure.
3. The slice surface must be continuous at the interface with neighbouring cuboid elements. This is a consequence of the fact that each of the four flux-confining surfaces is shared by two elements.
4. The placement of a slice surface in neighbouring elements must not prohibit the placement of a slice surface within an element. This statement essentially states that the ability of the individual base elements to be cascaded must be preserved in order for an arbitrary geometry to be discretized.

8.5 Interior Planes

In a two dimensional slice discretization, an interior point is uniquely defined by the intersection of two equipotential lines. Each of these lines represents a slice that is

perpendicular to the flux edge it originates from. Refer to figure 7.3. In three dimensional problems, the situation is more complex. In this section, we derive the procedure and state the conditions in which an interior point can be located such that the aforementioned constraints are met. It will also be proven that if this point is not unique, a slice discretization is still possible.

Three planes that possess linearly independent normal vectors will intersect at only one point in three dimensional space. If two or three of these planes are parallel, then the number of points of intersection are infinite. Two parallel planes and a third independent plane will intersect in a line if the two parallel planes contain a common point. Three parallel planes will intersect in a plane provided all three planes posses a common point.

Let us choose as a set of basis vectors any combination of three direction vectors corresponding to the edges of intersection of the flux-confining surfaces. See figure 8.6. The problem at hand is to devise a method in which we are guaranteed that there will be at least one point of intersection of the three planes having these three direction vectors as their normal vectors. There may be an infinite number of points of intersection if any of these three edges are parallel to one or both of the other two. A fourth plane must also be found that contains this point in order to meet the second constraint stated earlier.

An essential part of the derivation of the slice placement is to first note that each of the four direction vectors $\mathbf{n}_1$, $\mathbf{n}_2$, $\mathbf{n}_3$ and $\mathbf{n}_4$ can be obtained by taking the vector cross product of two flux surface normal vectors.

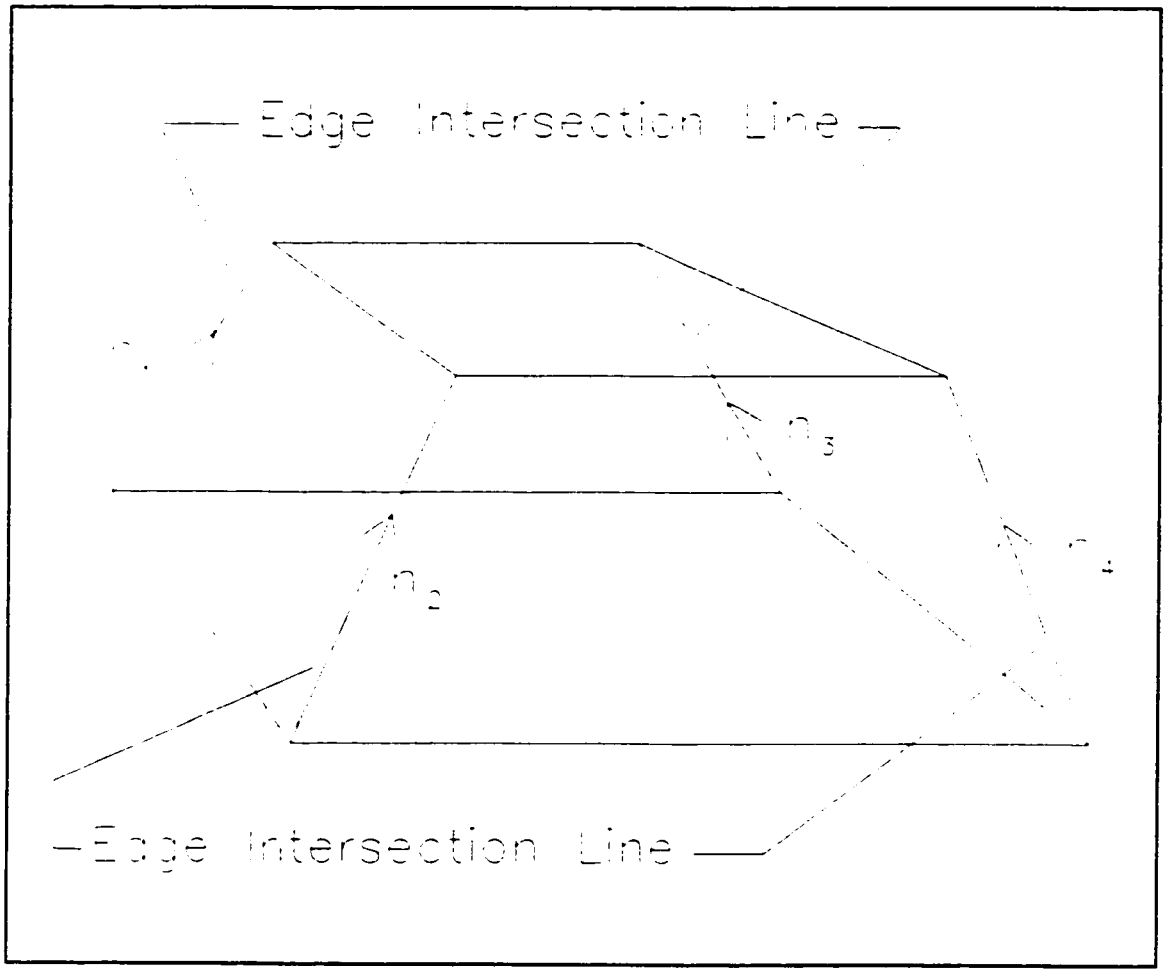

Figure 8.6: Slice surface normal vectors.

PROOF I

Given that each of the direction vectors $\mathbf{n}_1, \mathbf{n}_2, \mathbf{n}_3$ *and* $\mathbf{n}_4$ *lie along an edge defined by the intersection of two planes, then each vector must lie within both planes.*

Since the direction vector lies within both planes, it must be perpendicular to the normal vector of each of the two planes.

The resultant of the cross product of two vectors $\mathbf{A}$ *and* $\mathbf{B}$ *is orthogonal to both* $\mathbf{A}$ *and* $\mathbf{B}$.

Therefore, if the normal vectors of each of the two flux surfaces are "crossed" vectorially, the resultant must be parallel to the line of intersection.

Now let us choose an arbitrary point within the interior of the cuboid structure. We then define eight more points in the following manner. The first four points are the projection of the interior point onto each of the four flux surfaces. The remaining four points are projections of the interior point onto the four edge direction vectors. See figure 8.7.

We are now in a position to define four interior planes. Recall that each plane must contain the interior point chosen previously in order to maintain the continuity of the slice within the cuboid. Suppose we choose the four interior planes such that each plane has as its normal vector the direction vector of one of the four edges of intersection of the flux surfaces. Each of these planes will pass through the four edge intersection points defined previously. Furthermore, along the lines of intersection within the cuboid, the four planes are continuous.

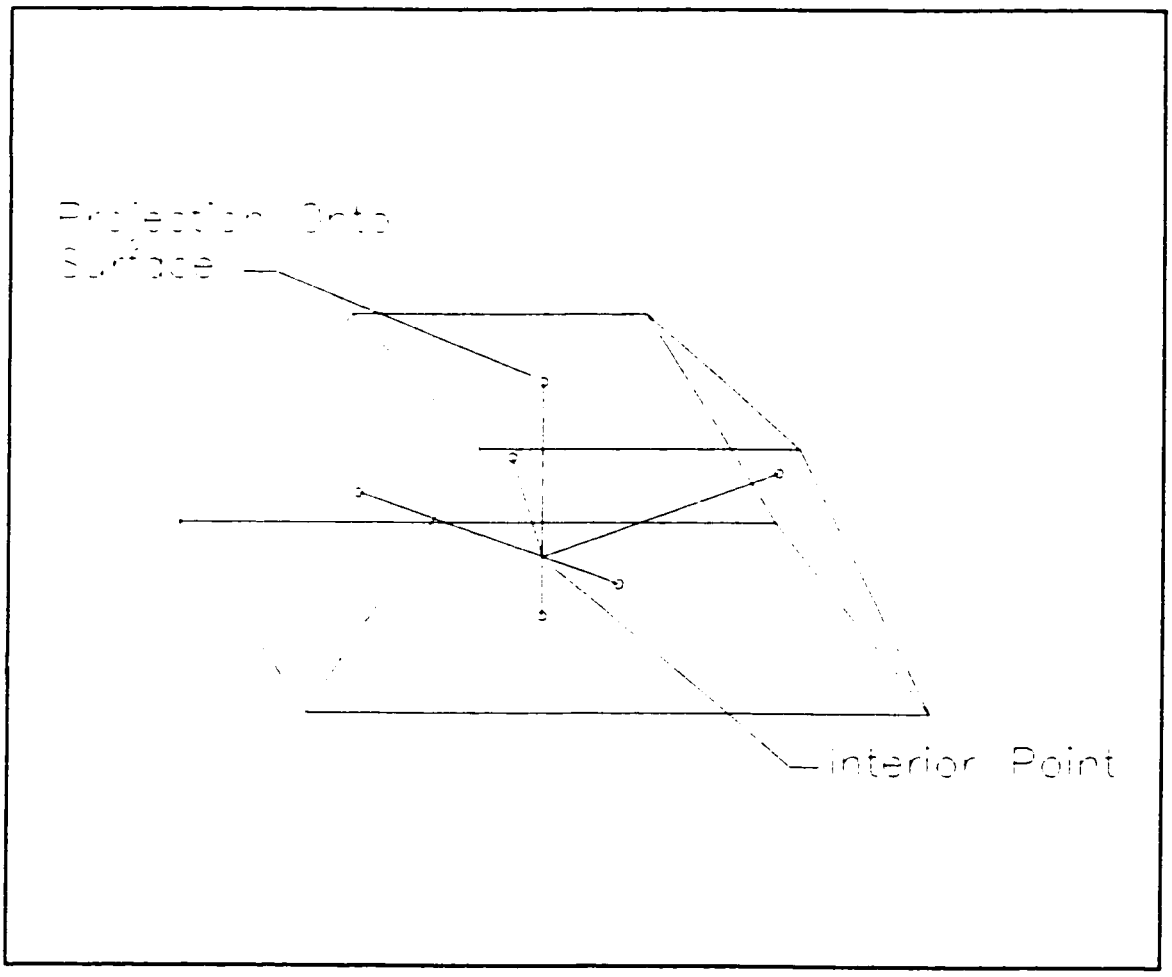

Figure 8.7: Projection of interior point onto flux surfaces.

PROOF 2

Recall that earlier, we proved that the direction vector of each of the four planes could be derived from the cross product of two flux surface normal vectors.

We now impose the constraint that the normal vectors used to derive the direction vectors pass through the interior point. We then have four vector originating at the interior point and terminating on the flux surfaces.

Since each of the four normal vectors is used to derive two direction vectors, the corresponding planes must intersect along the shared normal vector.

Therefore, although the four planes do not necessarily possess the same normal vector, they constitute a continuous surface.

The four internal planes within the cuboid that constitute the slice are shown in figure 8.8. The four planes are guaranteed to intersect in at least one point - the chosen interior point. If there are an infinite number of points of intersection, the pre-defined interior point is a member of this set.

PROOF 3

The fact that all of the normal vectors used to generate the direction vectors pass through the interior point guarantees that the interior point is a member of all four planes.

This point will be unique if any three of the four planes possess linearly independent normal vectors. This follows from the fact that three planes with linearly independent normals can only intersect at one point. There is a constraint imposed on the fourth plane in that it must also contain the interior point.

If the normals are not linearly independent then the interior point could be translated along a line (if two of the three normal vectors are parallel) or within a plane (if all three normals are parallel).

There will always be a constraint imposed on the fourth plane on where it intersects the edge of the cuboid. This must be taken into consideration when discretizing the problem domain and cascading the cuboids. More will be said about this later.

In addition to the main slice that passes through the interior point, all other slices that pass through the cuboid must meet the same constraints. The next problem to be addressed is the placement of the slice surfaces as one moves away from the four planes and towards the top and bottom equipotential surfaces.

Consider the lines formed by the interior slice as it intersects the four flux surfaces. Figure 8.9 shows the general case. Note the similarity to the two dimensional case. The "bend" in the slice occurs at the projection of the interior node onto the flux surface. Now suppose we wish to locate a slice above or below the main slice. We wish to derive the placement of this slice within the cuboid.

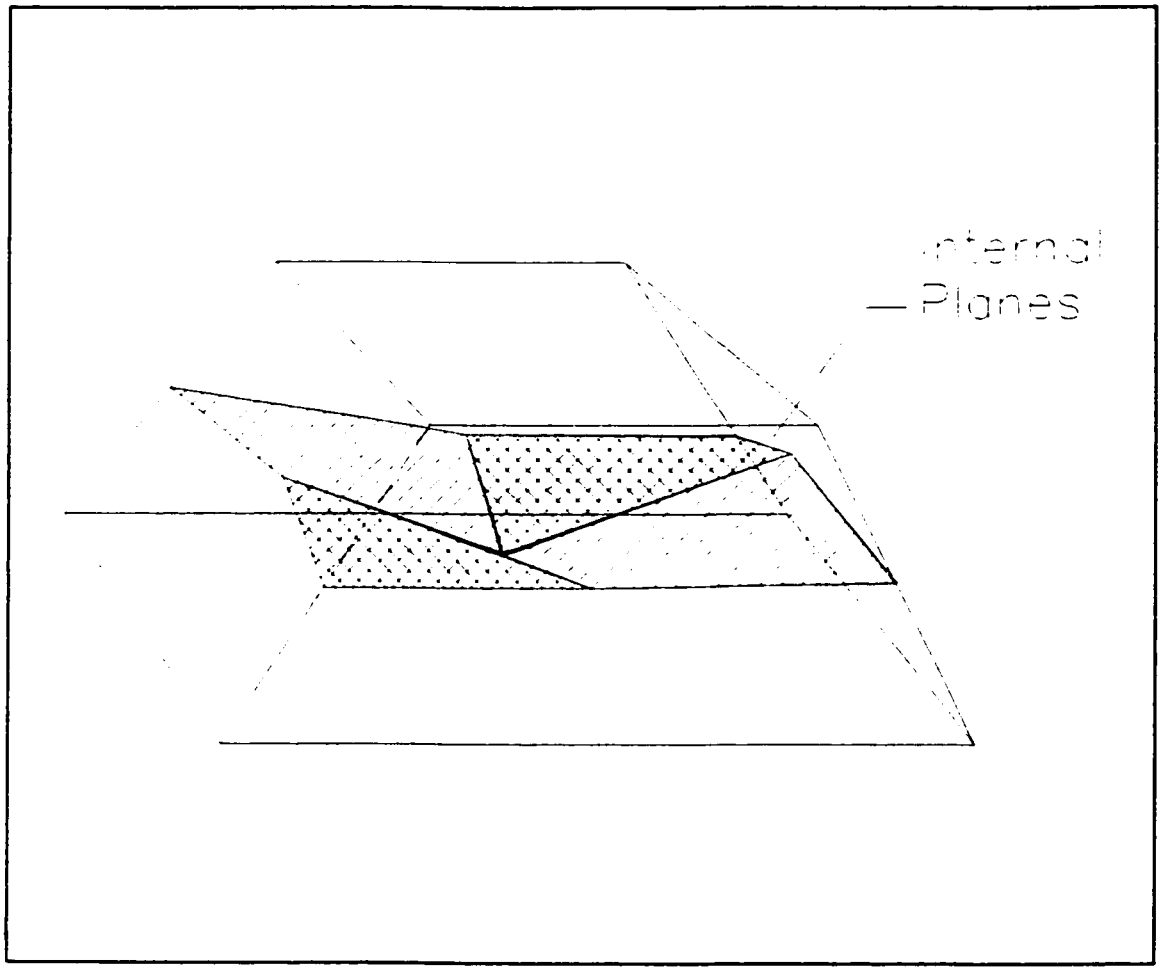

Figure 8.8: Four primary interior planes.

As one moves away from the four interior planes and moves towards the top and bottom equipotential surfaces, the slice becomes much more complex because of the constraints. For instance, just below the top equipotential surface, and just above the bottom equipotential surface, the slice must be parallel to the top and bottom surface respectively. Furthermore, within a flux surface and regions close to a flux surface, the slice must bend. The exact positioning of the bend must be derived since the magnitude of the electric field **E** within the cuboid depends on the slice separation.

8.6 A Complete Internal Slice

The problem of describing the slice that passes through the arbitrarily chosen interior point has been solved. It still remains to fully describe a slice internal to the cuboid that does not pass through the interior node. Only after this problem has been solved can the cuboid structure be employed in the dual bounds analysis.

Since the slice must be parallel to the equipotential surface it resides near, let us take this as a starting point. The rest of the slice will be built around this portion of the slice. Consider the pyramid formed by the top equipotential surface and the four surfaces that arise by joining the interior point to the top four vertices. Refer to figure 8.10.

Suppose we pass a plane through this structure that is parallel to the rectangular base

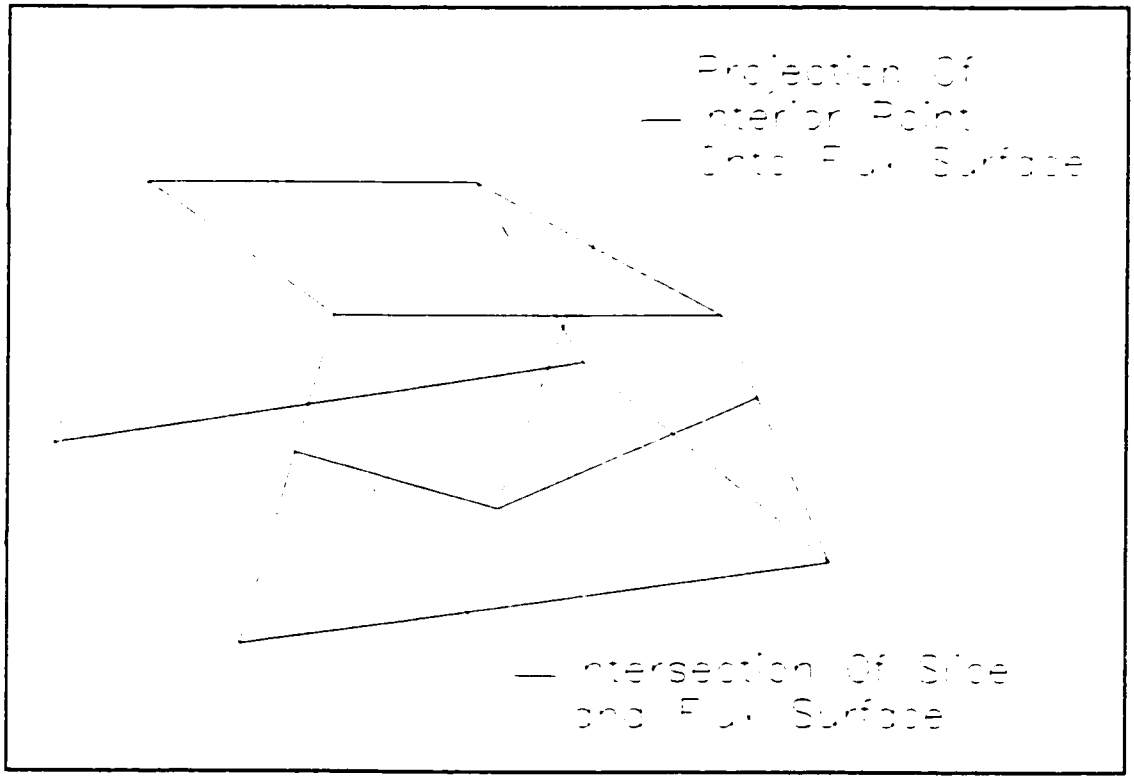

Figure 8.9: Intersection of slices and flux surface.

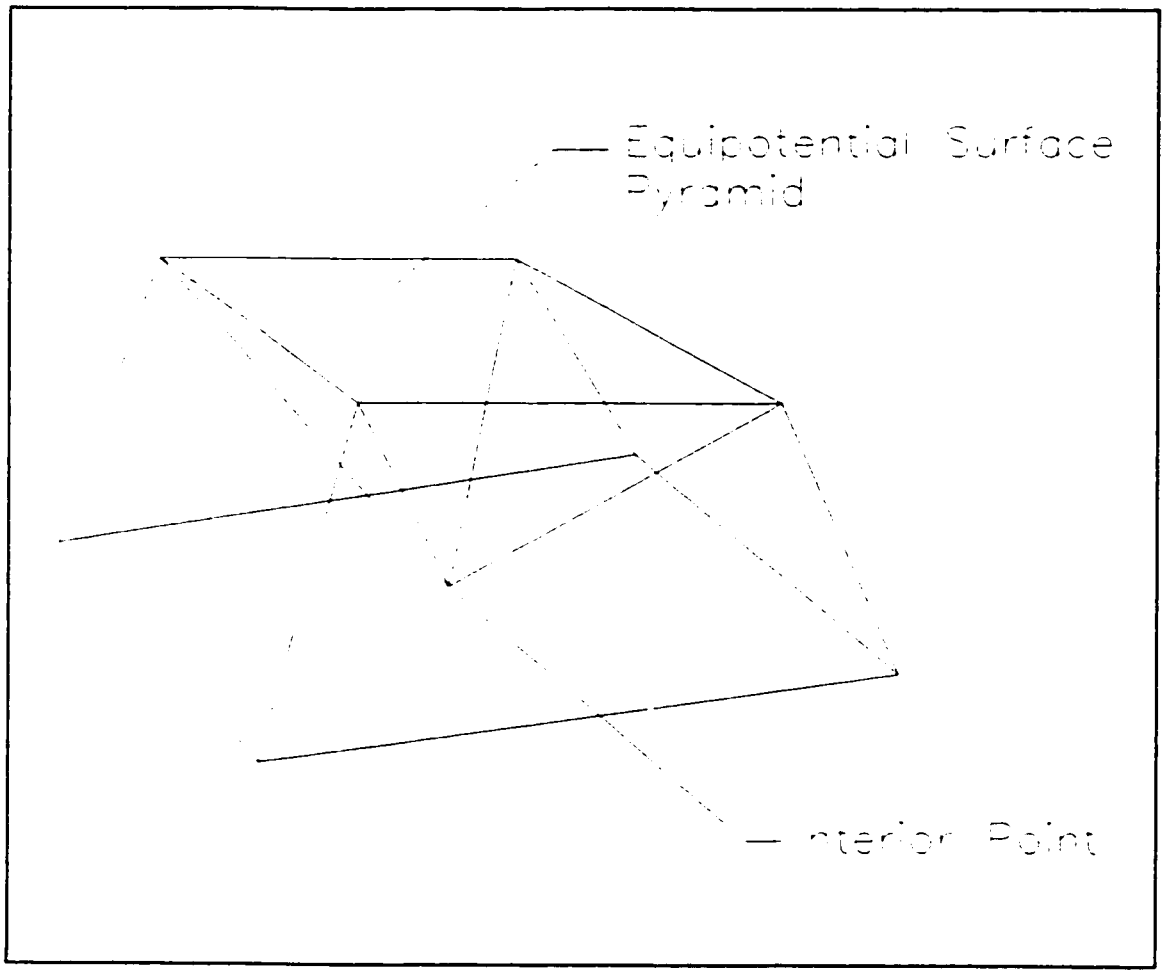

Figure 8.10: Equipotential surface based pyramid.

of the pyramid (ie. the top equipotential surface). This slice will intersect the four other triangular surfaces of the pyramid creating a rectangular surface. See figure 8.11.

We need to allow this surface to "propagate" to the outer four flux surface while still following the constraints stated earlier in this chapter. By projecting the lines formed between each of the eight vertices and the interior point onto the flux surfaces, we can predict where the bend in the slice will take place. The bend within the flux surface appears just as it does in the two dimensional case. See figure 8.12. What must be solved is the situation inside the

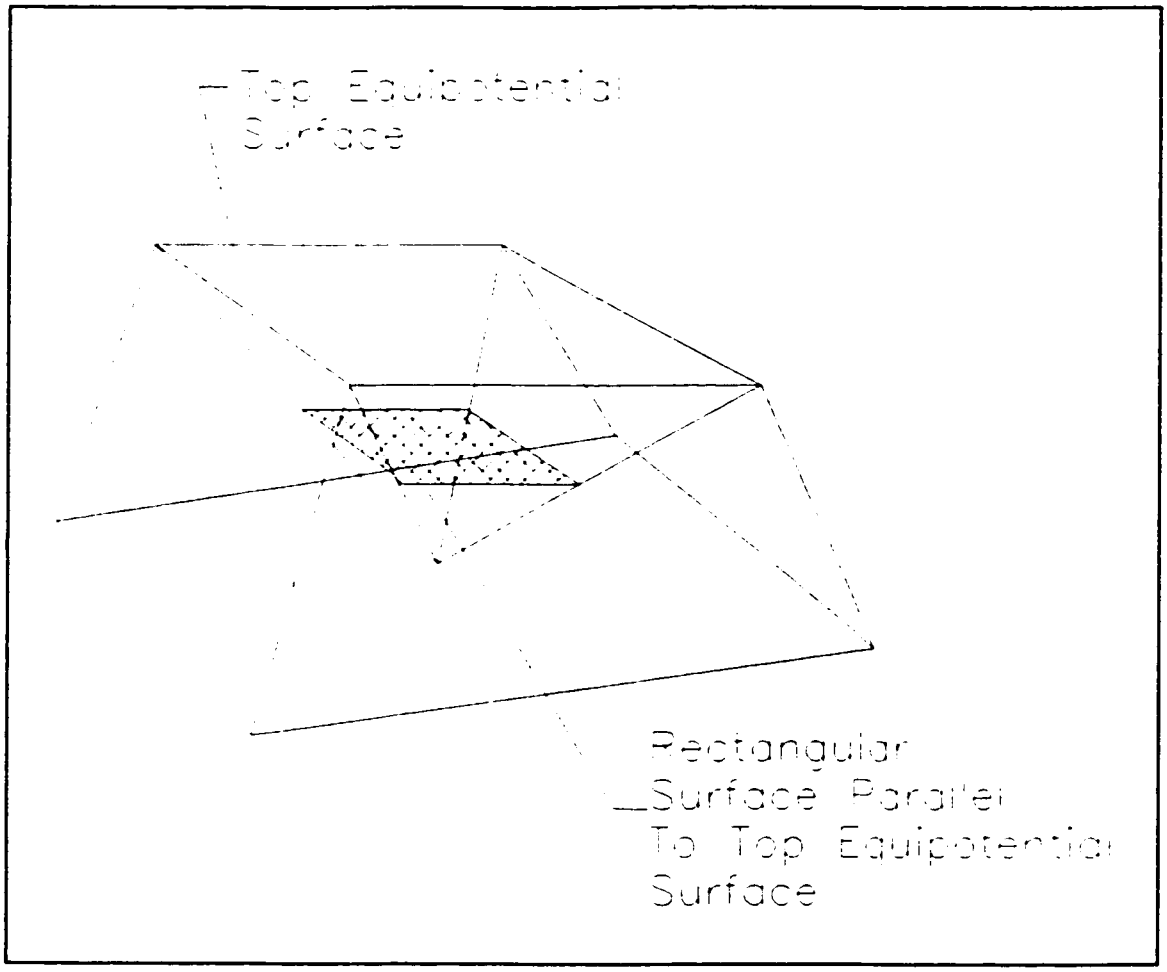

Figure 8.11: Slice passing through equipotential surface based pyramid.

cuboid.

The rectangular surface of figure 8.11 scribes four lines on the four triangular surfaces of the pyramid. The projection of each of these lines onto the flux surface facing it yields the path the slice will take within that flux surface. At the same time, an equipotential surface is formed normal to that flux surface. The intersection between this surface and the rectangular slice parallel to the top equipotential surface is automatically continuous. This slice surface can be extended in a continuous fashion to the edges of intersection of the flux surfaces.

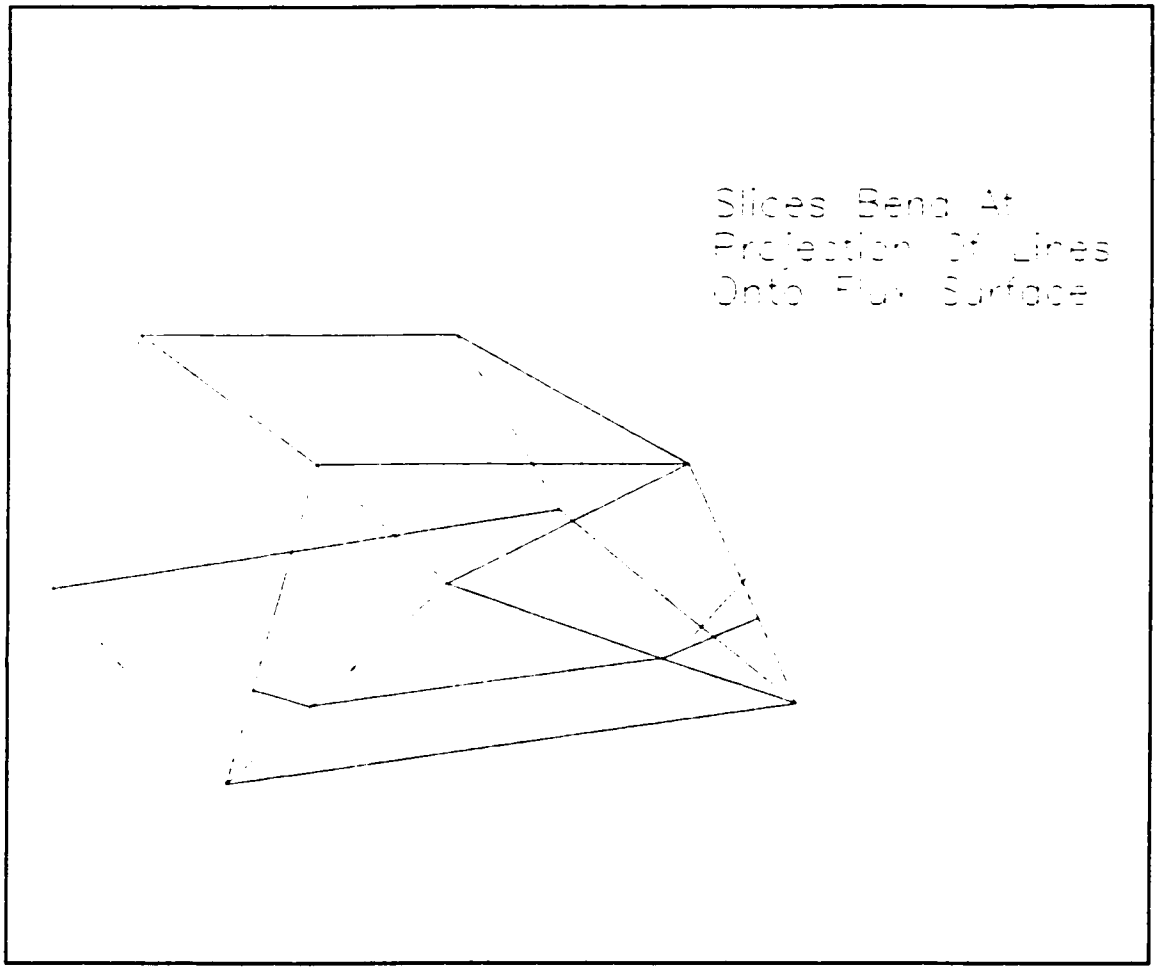

Figure 8.12: Bending of slice on flux surface.

PROOF 4

We know that the slice parallel to the top equipotential surface will scribe a line in the triangular face of the pyramid.

Take a point on the edge of this face and project it onto both of the adjacent flux surfaces. The plane swept out by these two vectors must be parallel to the slice that passes through the edge pyramid. Refer to figure 8.13.

Each of these projections also forms one edge of the slice that passes through the flux surface tetrahedron. Slice this plus the slice that extends through the edge pyramid completely fill the surface area of the slice.

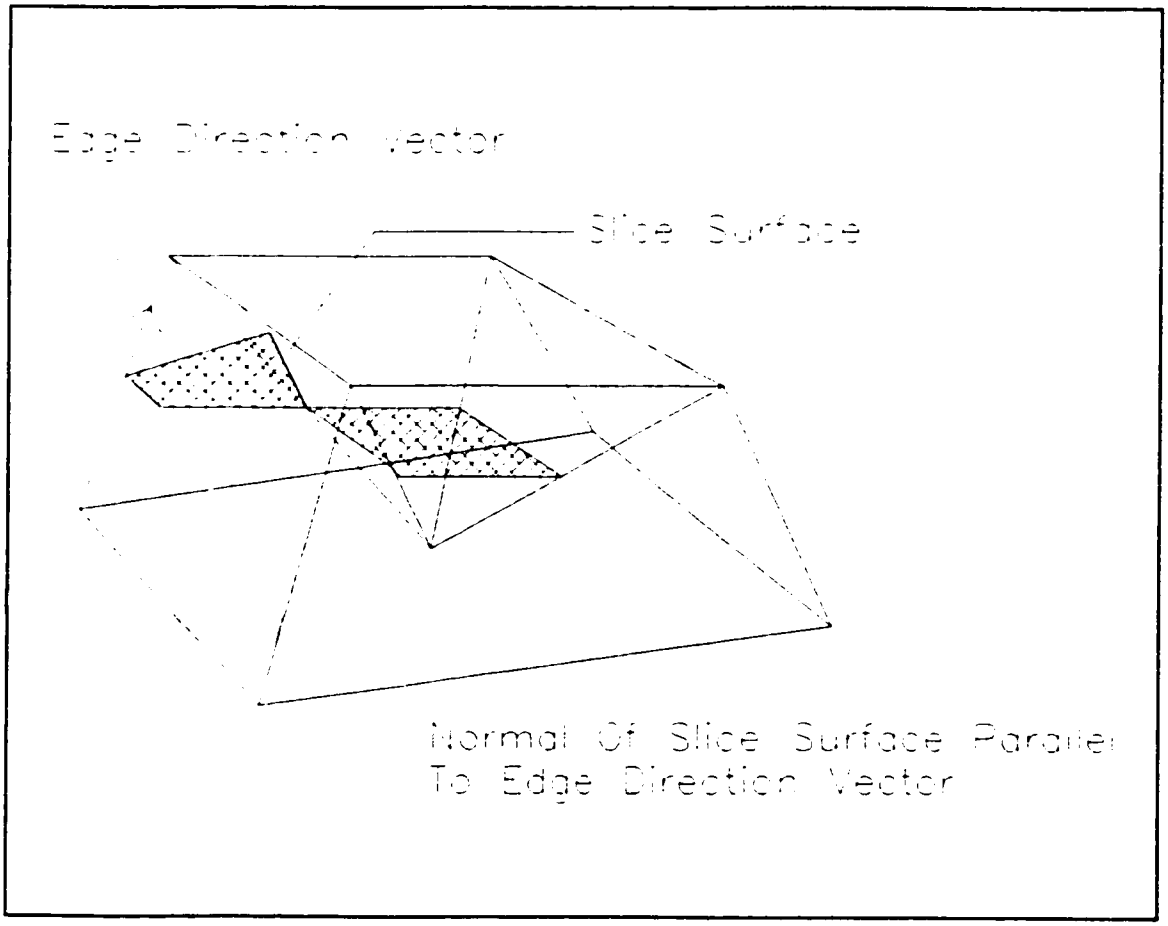

Figure 8.13: Slice in the vicinity of the cuboid's edge.

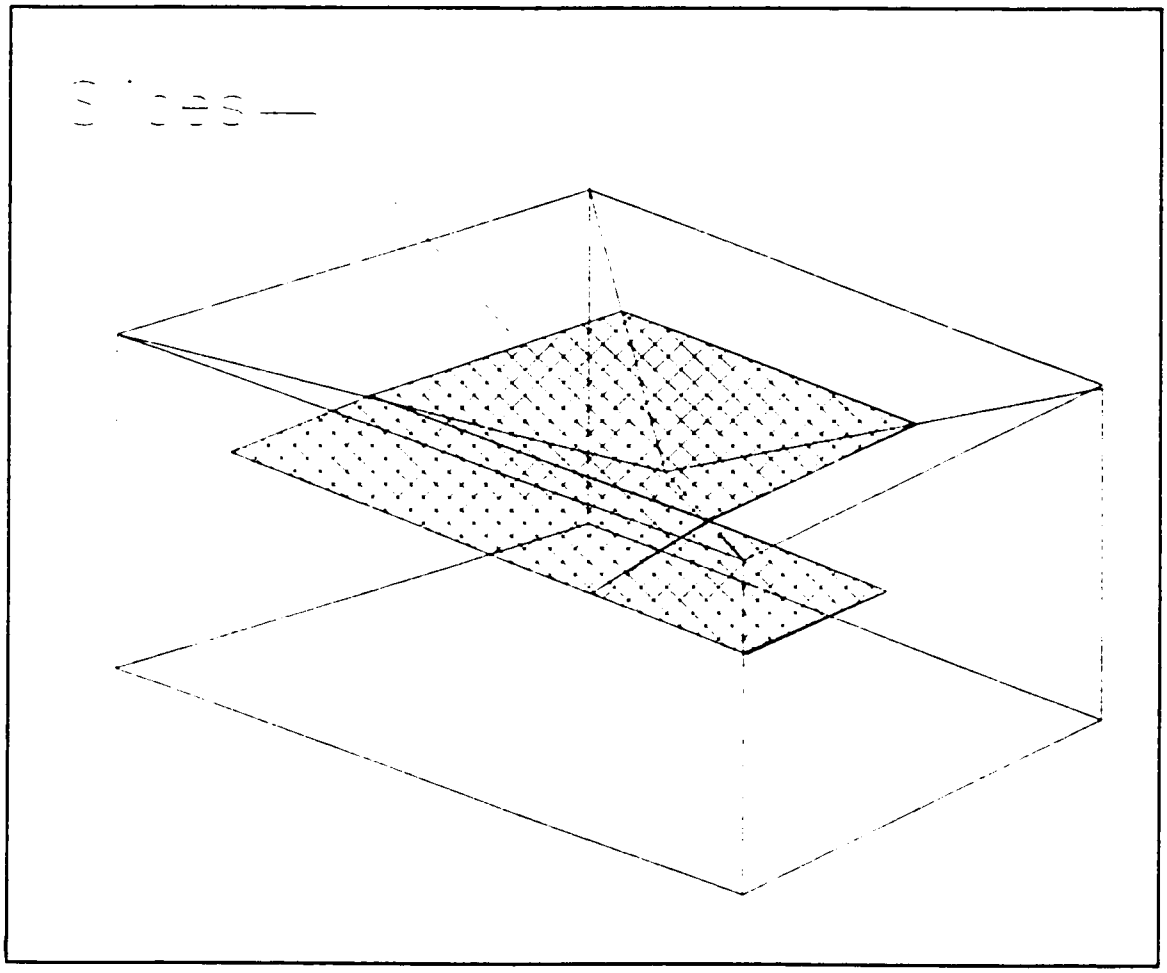

Figure 8.14: Portion of a full slice.

A portion of a complete internal slice is shown in figure 8.14. The three primary segments shown extend out to the flux surface. Additional planes (not shown for clarity) added around the rest of the cuboid's interior periphery make up the rest of the continuous slice.

8.7 Volumes Within the Cuboid

In order to implement a slice discretization as part of a dual bounds method, the total system energy must be obtained by summing the energy contributed by each of the individual geometrical constructs. In two dimensions, the fundamental geometrical constructs contained within the quadrilaterals are triangles. In this section, the three dimensional volume elements are derived. The key to deriving the volume elements is to start with the placement of the slices within the cuboid structure.

The volumes are characterized by the direction of the electric field within it. Each volume element within the cuboid will have an electric field associated with it. The direction of the electric filed is a function of the placement of the equipotential slice that passes through that volume. As we have shown, there are a number of directions that the equipotential slice assumes at it passes through the cuboid. Consequently, the volume within the fundamental cuboid is divided up in a complex manner.

8.7.1 Equipotential Surface Based Pyramids

Consider the pyramid shown in figure 8.11 and the slice that passes through it. Everywhere inside this pyramid structure the electric field must be perpendicular to the slice. There are two of these structures contained in the elemental cuboid, one at each of the two boundary equipotential surfaces. These two pyramids share the same apex located at the interior point. See figure 8.15.

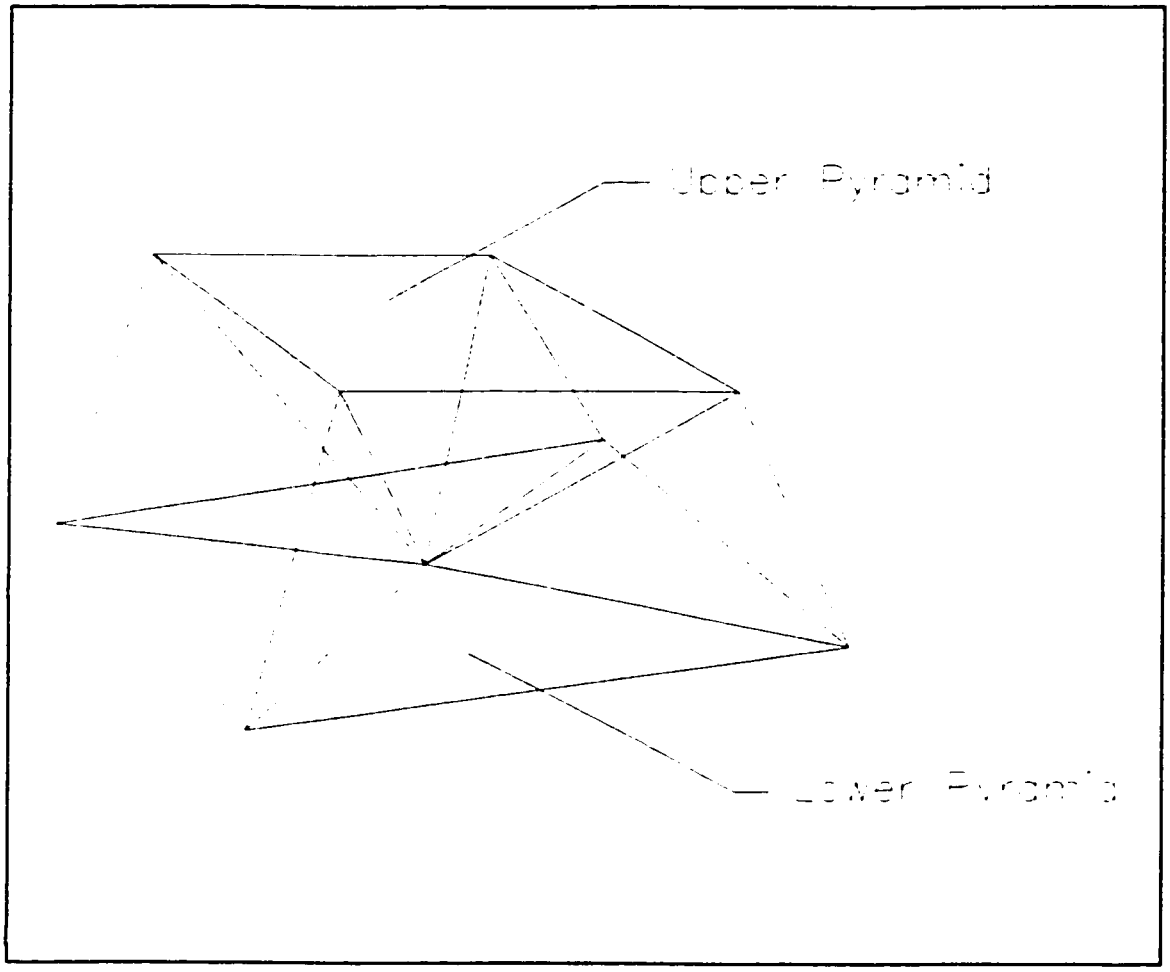

Figure 8.15: Pyramids that share the same apex - the interior point.

8.7.2 Edge Based Pyramids

Recall that the slice passing through the interior point consists of four separate planes. The normal vector associated with each of these planes is defined by the direction vector of and edge. The electric field in the vicinity of each edge must also be parallel to this edge. We will construct a second pyramidal structure whose rectangular base derives from the following four points;

1. The interior node.

2. The projection of the interior node onto the edge of intersection of the flux surfaces.

3. The projection of the interior node onto the two flux surfaces that share the edge.

The fifth node in the pyramid is the cuboid vertex along that particular edge. Since there are two such vertices, there are two edge pyramids along each edge. See figure 8.16. There are thus eight edge pyramids in total. Within each pyramid, the electric field is perpendicular to the plane that forms its base.

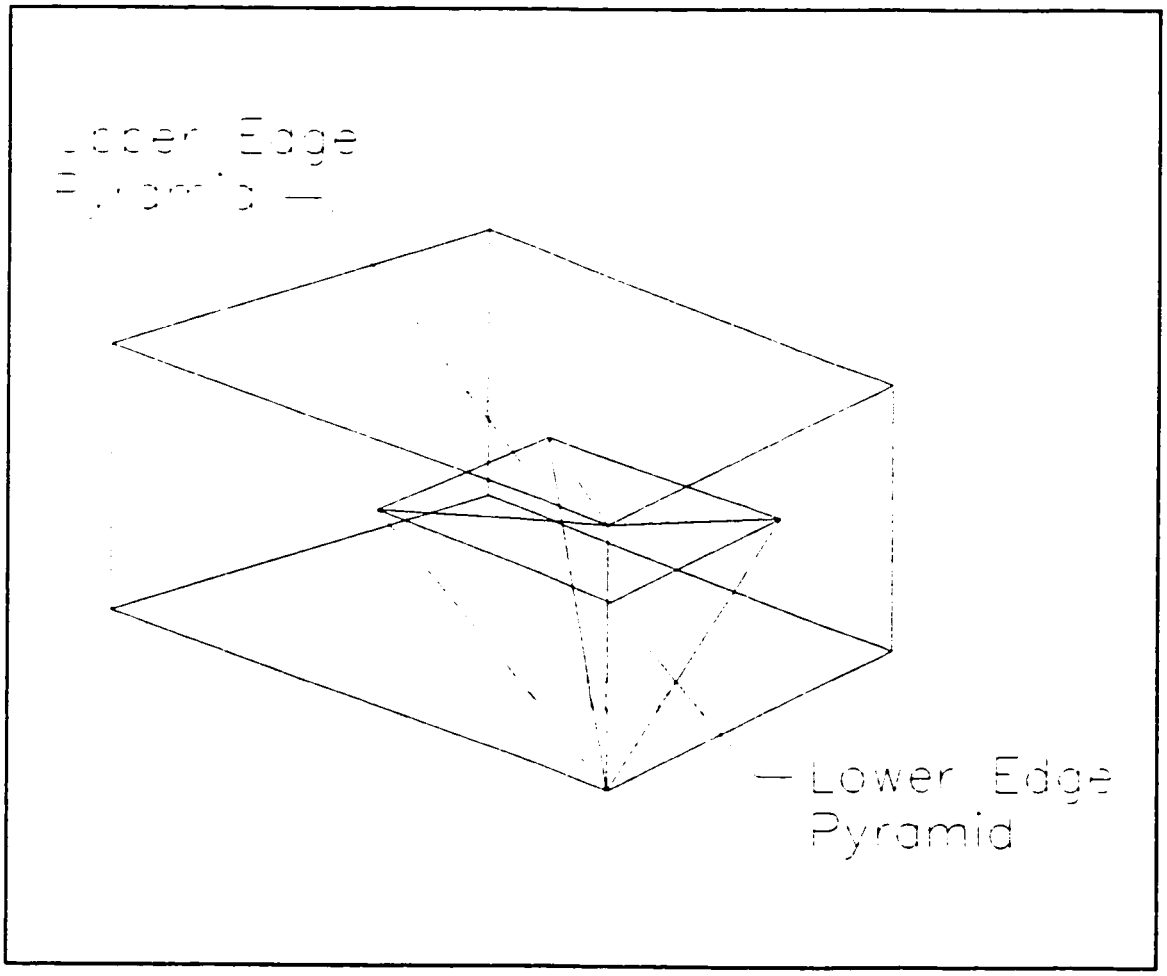

Figure 8.16: Two edge-based pyramids.

8.7.3 Flux Surface Tetrahedrons

The final structure required to fill the internal volume of the cuboid is a tetrahedron. It contains four triangular faces, three of which overlay surfaces belonging to already defined pyramids. One face overlays a surface of the top (or bottom) pyramid while the other two overlay the surfaces of the edge pyramids. The fourth face lies within a flux surface of the cuboid. This face is defined by the projection of the lines joining the interior point to two vertices of the top (or bottom) equipotential surface.

Within the tetrahedron, the electric field is perpendicular to the slice that passes through it. Earlier it was stipulated that any slice intersecting a flux surface must do so perpendicular to that flux surface. In the case of the tetrahedron, the slice must be normal to the flux surface and parallel to the projection vector that defines the triangular face on the flux surface. The placement of this slice within the tetrahedron is shown in figure 8.17.

8.8 Cascading Cuboids for Slice Discretization

The last point that needs consideration is that of proving that constraint 4 can be met. The fourth constraint states that the choice of slices in one cuboid will not prohibit the placement of consistent slices within the rest of the cuboids. To help illustrate the process of cascading, consider the grid pattern of figure 8.18. The two dimensional array represents the connection of a large number of cuboids that share a common upper and lower equipotential surface.

We can consider such a grouping since the top and bottom equipotential surfaces serve to decouple the cuboid layers. Completing the interconnection of a set of slices in this

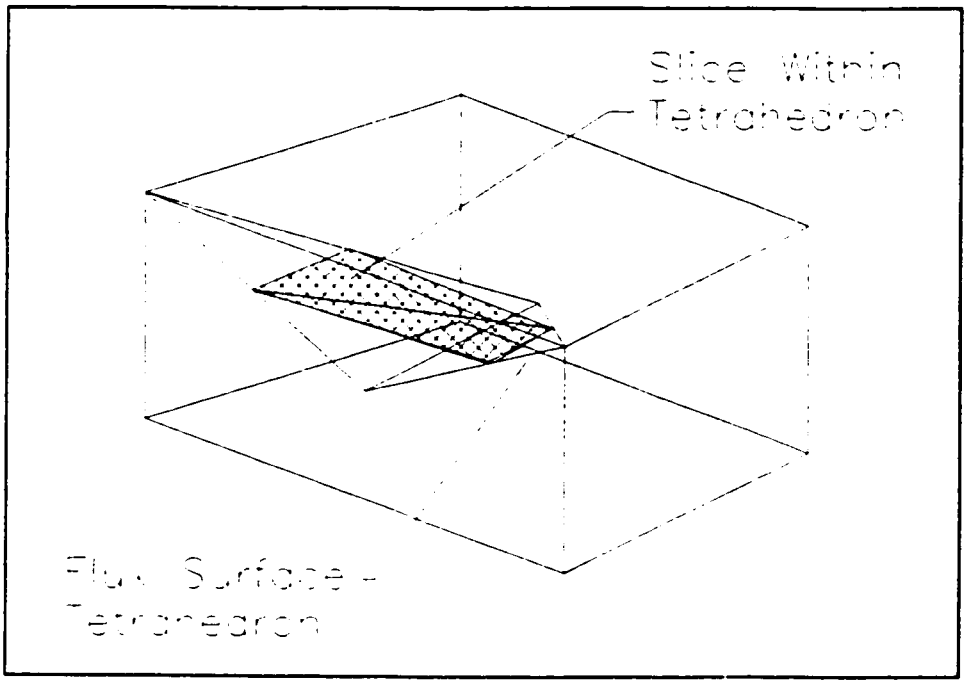

Figure 8.17: Flux surface tetrahedron and slice.

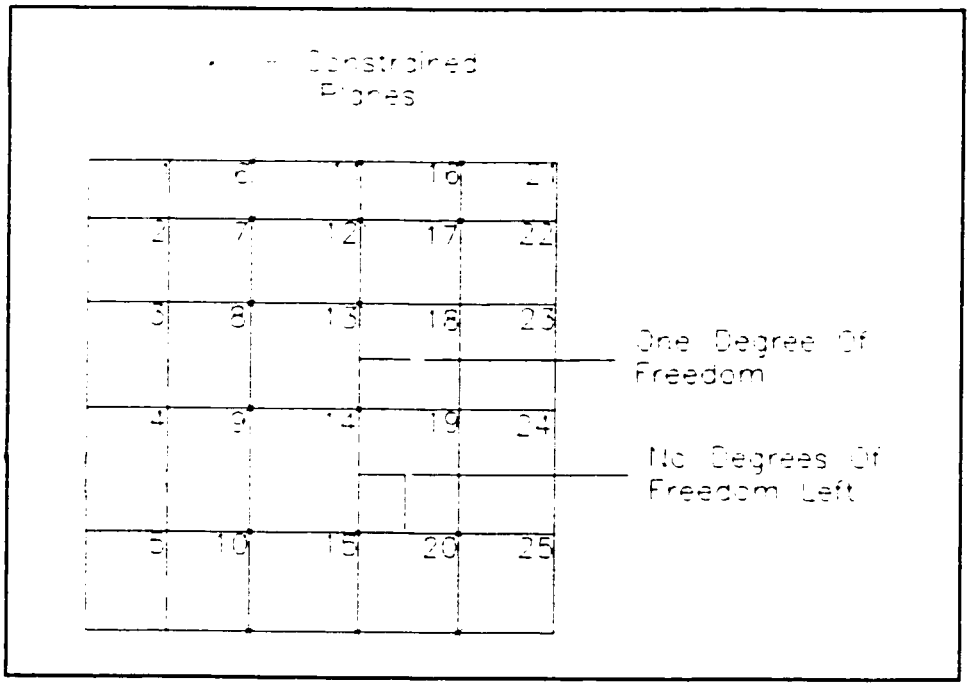

Figure 8.18: Cascading of cuboids for slice discretization.

group can be done independently. This layer will not influence, and is not influenced by the geometry of any other layer.

Suppose we start with the cuboid labelled 11 at the top-centre of the grid. If we choose the position of the interior node in this cuboid, it will reduce the number of degrees of freedom we have when locating the interior node in the adjacent cuboids. The reason for this is the four planes that pass through the interior point of this cuboid must also contain the interior point of the four surrounding cuboids.

Hence, we have potentially restricted the location of the interior point in those cuboids to a line rather than a volume. The reason being that two of the four edge intersections and hence planes are now defined on the four adjacent cuboids. Since the interior point must lie within each plane, we have potentially reduced the location to a line. If the two planes happen to be parallel, we still have the degree of freedom of a plane in which to locate the interior point.

If we work outwards from the initial cuboid, we can expect that some cuboids will have more than two of the four interior planes dictated by the placement of slices in adjacent cuboids. For example, if the sequence we follow is 12, 13, 14, 15, 16 then by the time we get to cuboid 17, three of the four internal planes in that cuboid will have been defined already. If the planes have normal vectors that are all linearly independent, then the interior point will have been located automatically. We do not have the freedom to choose its location in this cuboid.

Provided we do not progress in such a way so as to "hook" ourselves by forcing all four internal planes we can discretize the entire layer. This can be accomplished by working

in strips from boundary to boundary or from the interior to the boundary, always ensuring that the last cuboid has an unconstrained edge intersection. Not following this pattern and starting the placement of interior points in two different locations and working inwards can lead to the situation of figure 8.19. In this instance, we have produced a potential problem at the centre cuboid. All four edge intersections (hence interior planes) have been chosen and there are no remaining degrees of freedom. We have no guarantee that the interior point will lie within all four planes.

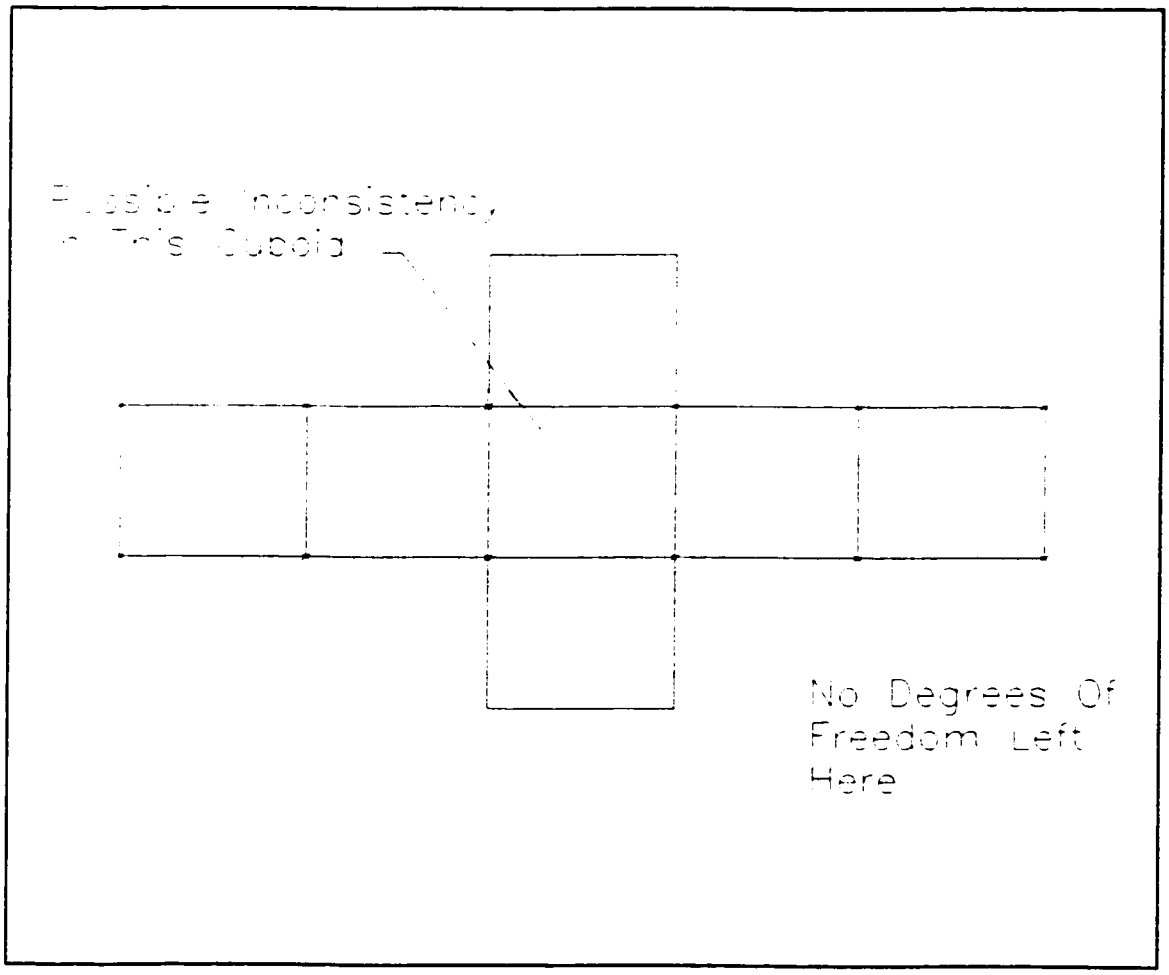

Figure 8.19: Possible improper cascading of cuboids.

8.9 The Electric Field After Slice Discretization

We have shown that the interior point chosen inside the cuboid discretizes the inside of the cuboid into different regions. We have also proved that the direction of the electric field **E** within each of the volumes is perpendicular to the equipotential slice that passes through that volume. The final step is to derive the magnitude of the electric field within each volume. Knowing the magnitude of the electric field and the volume of the structure it pertains to, we can calculate the energy stored by the electric field in the volume.

The first type of interior three dimensional structure consists of a pyramid. Inside the pyramid, the electric field strength **E**, depends upon two factors. The first factor is the difference in the electric scalar potential φ between one of the bounding equipotential surfaces and the scalar potential ascribed to the interior point. This potential difference is divided by the second factor which is the distance along the previously mentioned edge from the bounding equipotential surface to the perpendicular intersection point. This type of interior substructure is shown in figure 8.20. The direction of **E** is parallel to the common edge that forms the intersection between the two flux surfaces.

The next type of substructure is a tetrahedron. A tetrahedron is formed by four (4) surfaces. These surfaces are all triangular and are shown in figure 8.21. One of these surfaces lies within a flux surface of the larger cuboid structure. Therefore, the electric field **E** must also lie within this plane. What makes the electric field direction unique in this type of structure is the fact that the electric field must also be perpendicular to the edge which forms the intersection between one of the cuboid's equipotential surfaces and the flux surface that the field lies within. The magnitude of **E** is determined by the difference in the electric

scalar potential at one of the cuboid's bounding equipotential surfaces and the scalar potential at the interior point. This potential difference is then divided by the perpendicular distance from the bounding equipotential surface to the interior point's projection onto the flux surface.

The final type of substructure is another pyramidal element. The base is comprised of one of the equipotential surfaces of the cuboid. Within the pyramid, the electric field **E** is perpendicular to the equipotential surface, its magnitude determined by two factors; firstly,

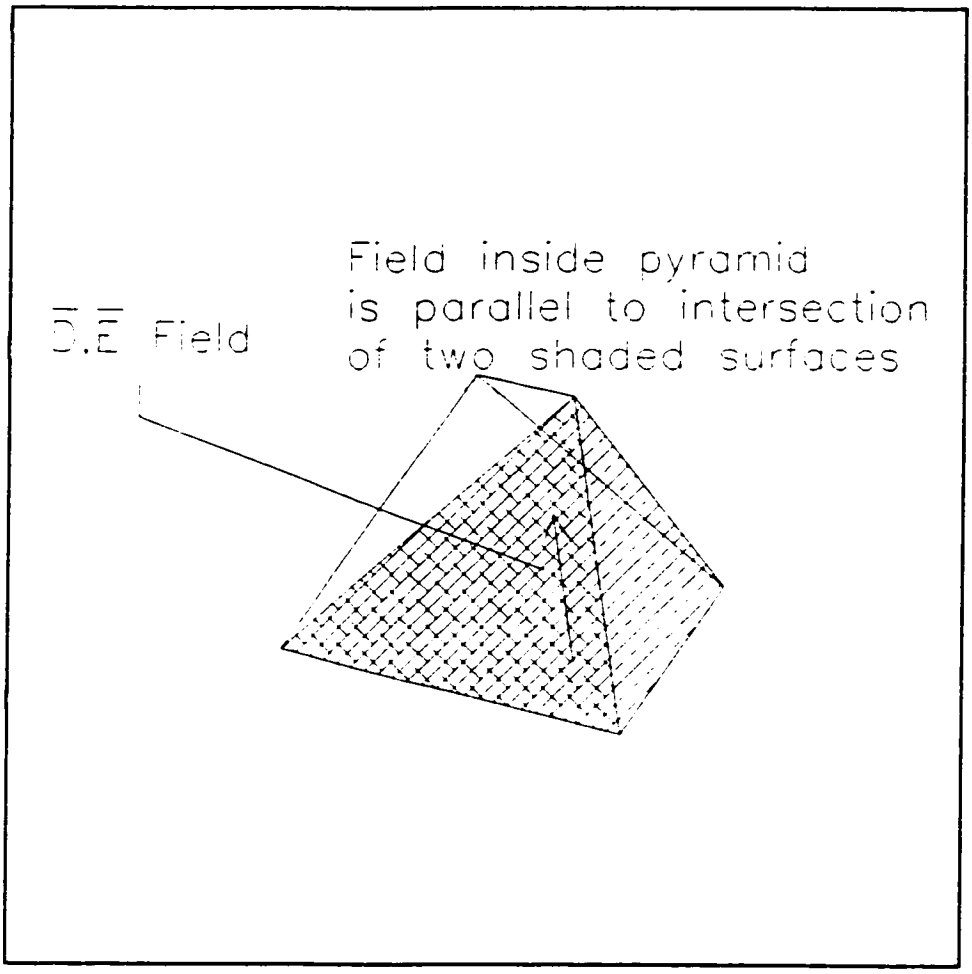

Figure 8.20: Field parallel to edge of intersection of two flux surfaces.

the difference between the electric scalar potential at the equipotential surface and the scalar potential of the interior point; secondly, the perpendicular distance from the equipotential surface to the interior point. This final pyramidal structure is shown in figure 8.22.

The expressions for the electric field strength in each of the three regions are given in equations (8.1) through (8.3) for the three regions in the order that they were presented. When implemented in practice, the volume of each of the three types must also be known, since the energy density within each region must be multiplied by the volume of the element

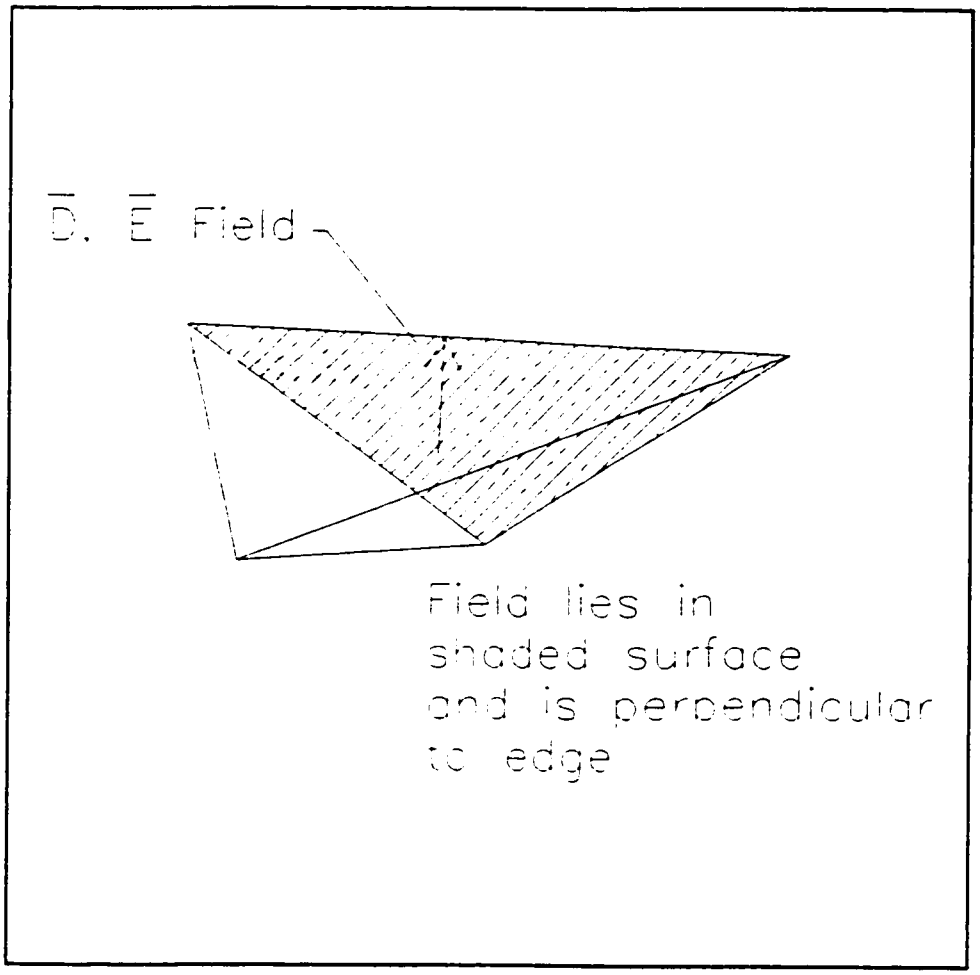

Figure 8.21: Tetrahedral structure with a flux surface as one face.

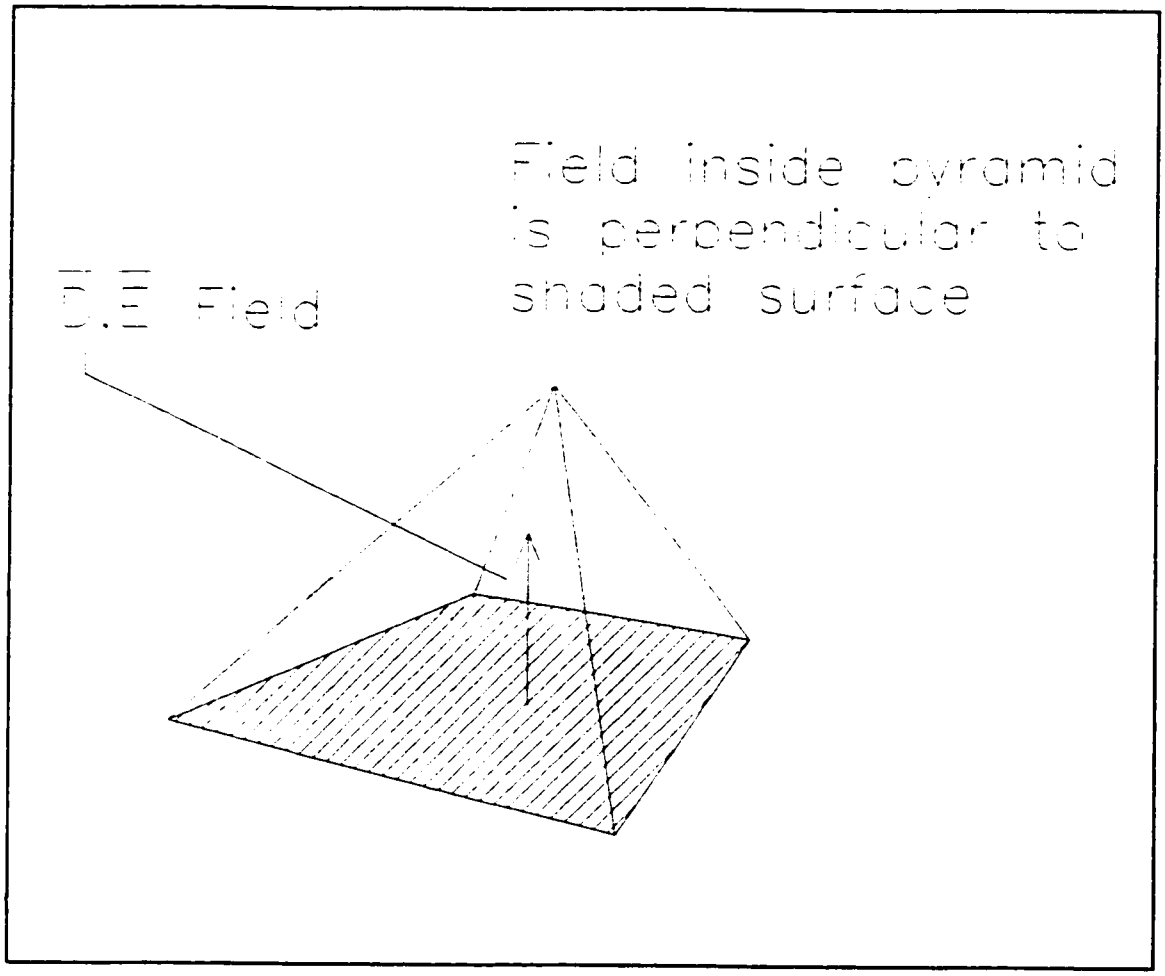

Figure 8.22: Pyramidal structure with an equipotential surface as one face.

in order to obtain that particular structure's contribution to the overall stored energy within the system.

$$|E_1| = \frac{\varphi_{surf} - \varphi_i}{\ell_1} \qquad \textbf{(8.1)}$$

$$|E_2| = \frac{\varphi_{surf} - \varphi_i}{\ell_2} \tag{8.2}$$

$$|E_3| = \frac{\varphi_{surf} - \varphi_i}{\ell_3} \tag{8.3}$$

where φ_i and φ_{surf} are the electric scalar potential of the interior point and the electric scalar potential of the equipotential surface respectively. The lengths ℓ_1, ℓ_2 and ℓ_3 represent the heights' of the structures in question.

The expressions for the volumes are presented in equations (8.4) through (8.6).

$$\text{Volume}_{\text{pyramid 1}} = \frac{\ell_1 \times A_{\text{pyramid 1 base}}}{3} \tag{8.4}$$

$$\text{Volume}_{\text{tetrahedron}} = \frac{\ell_2 \times A_{\text{tetrahedron base}}}{3} \tag{8.5}$$

$$\text{Volume}_{\text{pyramid 2}} = \frac{\ell_3 \times A_{\text{pyramid 2 base}}}{3} \tag{8.6}$$

8.10 Tubes in Three Dimensions

Discretization for the case of tubes in three dimensions follows a similar procedure

as that for slice discretization. The basic building block is a six sided cuboid or hexahedron in which an interior point is chosen. The location of this interior point is, once again, arbitrary but only to a certain degree. The positioning of the interior point and the interior walls of the flux tubes that pass through it are subject to a number of constraints that will be defined subsequently.

Once again there are two equipotential surfaces and four flux surfaces. We begin the construction by joining the interior point to each of the eight vertices of the hexahedron. The projection of each of these lines onto any of the four (4) flux surfaces will yield a two dimensional pattern similar to that described in the two dimensional tube case. The projection of the interior point onto the flux surface locates the interior point of the quadrilateral on the surface.

On each of the cuboid flux surfaces, we seek to define the path of intersection the internal flux planes make. Since there are four bounding flux surfaces per cuboid, we divide the total flux leaving one equipotential surface and terminating on the other into four parts. The projection of the interior point onto each of the equipotential surfaces denotes the centre point of the division. Refer back to figure 8.7 for an illustration of the projection of the interior point onto the various surfaces of the cuboid.

For the walls of the flux tubes the constraints are as follows:

1. Because the flux tube is a surface in which there is no normal component of electric flux density, it must be parallel to all four of the flux-confining surfaces when "running" in the vicinity of the flux surface.
2. Because the flux tube eliminates a normal component of the flux density, it must be

perpendicular to the top and bottom equipotential surfaces where it intersects them.

3. The flux tube must be continuous within the cuboid structure.

4. The flux tube must be continuous at the interface with neighbouring cuboid elements. This is a consequence of the fact that each of the two equipotential surfaces is shared by two cuboid elements.

5. The placement of a tube in neighbouring elements must not prohibit the placement of a tube within an element. This statement essentially states that the ability of the individual base elements to be cascaded must be preserved in order for an arbitrary geometry to be discretized.

8.11 Interior Planes For Tube Discretization

We will now define eight planes within the cuboid. The normal vector of each plane will be parallel to the vector cross product of the vector joining the interior point to one equipotential surface and the vector joining the interior point to one flux surface. Following a similar argument to that presented in *PROOF 1* of this chapter, the normal vector of each plane must be parallel to the edge of intersection of the equipotential surface and a flux surface. Refer to figure 8.23.

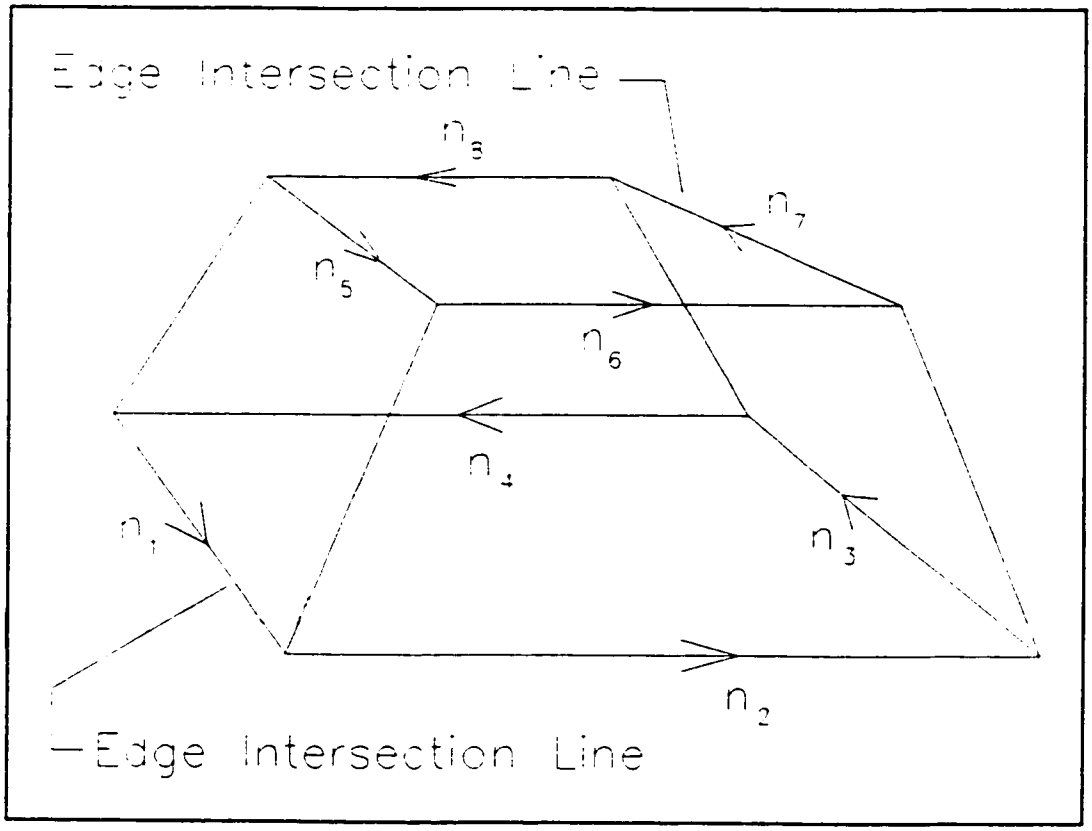

Figure 8.23: Normal vectors for flux tube walls.

These eight planes must be continuous from the bottom equipotential surface right on through to the top equipotential surface. Furthermore, each of these planes must pass through the interior point. The intersection of each of these planes with the flux surface and equipotential surface defining its normal will pass through the projection of the interior point onto the corresponding surface.

PROOF 5

> *Let* $\mathbf{n}$ *denote the normal vector of a plane that possesses the interior point. The direction of* $\mathbf{n}$ *is defined by the vector cross product of two vectors that originate at the interior point. One vector terminates on a flux surface of a cuboid and the other on an equipotential surface of the same cuboid.*
>
> *Since the origin of both of these vectors lie in the plane, so must their termination points.*

These eight planes confine the flux within the cuboid by forcing the normal component of the flux density along their surface to be zero. The actual direction of the flux density is still determined by the constraints listed previously. Two of the eight planes and their location within the cuboid are shown in figure 8.24. Note that each plane passes through the interior point and the eight planes form a continuous surface. The upper four planes intersect along a line joining the interior point to its projection of the top equipotential surface. Likewise for the lower four planes. The intersection of the two lines uniquely identifies the interior point.

For the positioning of the walls of a flux tube that does not pass through the interior point, consider the two dimensional situation shown in figure 7.4. We know that the wall of the flux tube will produce a pattern similar to that of the two dimensional case when in intersects the plane of the flux surface. Therefore, the surface along which the plane of the

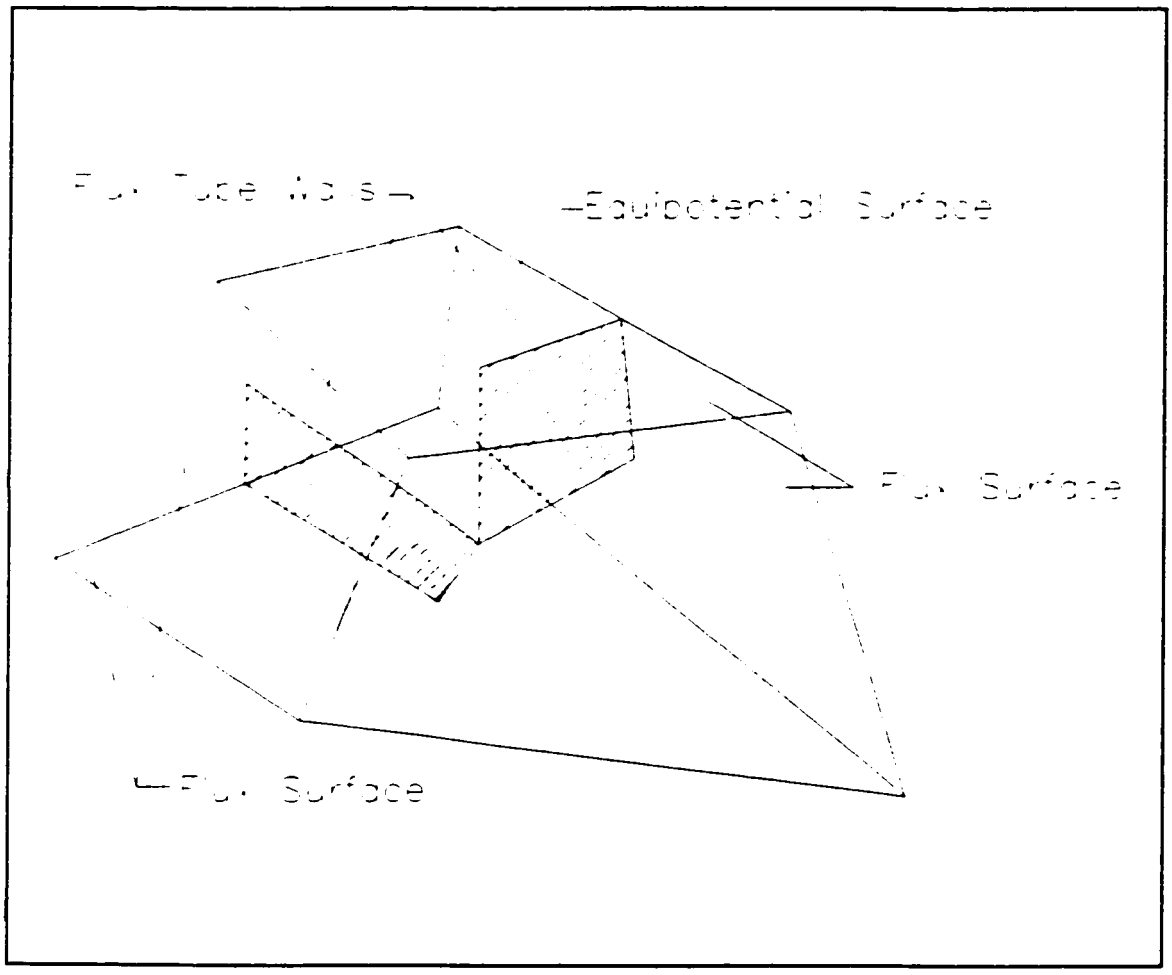

Figure 8.24: Flux tube walls passing through interior point.

flux tube bends is defined by three points. These points are firstly, the interior point, secondly, the projection of the interior point onto the flux surface and thirdly, one of the cuboid vertices.

We continue the wall of the flux tube back to the adjacent flux surface as shown in figure 8.25. The projection of the line between the interior point and a cuboid vertex onto the equipotential surfaces locates the point at which the cut back of the flux tube wall to the adjacent flux surface is made.

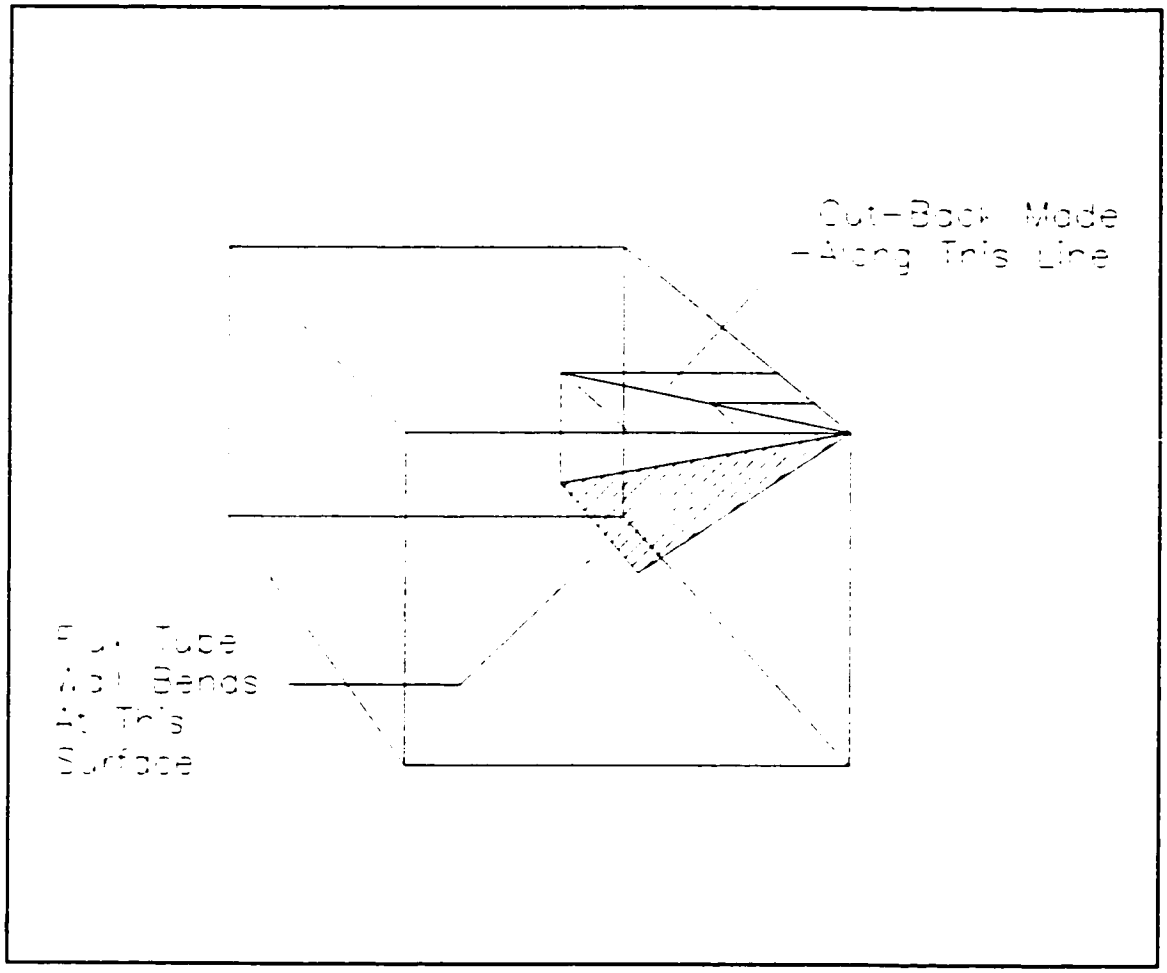

Figure 8.25: Flux tube wall cut-back made along projection onto equipotential surface.

This choice of positioning the internal walls of the flux tubes is what enables us to divide the total flux passing through the cuboid into four parts. In essence we form a cross pattern on the equipotential surfaces. It will be proved later that this cross pattern can be continued across an entire layer of cuboids in a continuous fashion. This same pattern can be propagated down through the layers of the cuboids as well.

8.12 Volumes For Tube Discretization

The same basic internal volume structures that were employed for slice discretization can be used again for tube discretization. The only difference is that some of thc volumes can be joined to form one and other volumes have to be subdivided.

The top and bottom pyramids who have as their rectangular base an equipotential surface will be divided into four smaller pyramids. Each of these smaller pyramids has a rectangular base as well. The lines of division are formed by the cross pattern the primary walls of the flux tubes make as they intersect the top and bottom equipotential surfaces. See figure 8.26.

The edge pyramids that were used in the slice discretization can be reused as they were. The only difference is that the flux density value for the two pyramids along one edge will be the same. In slice discretization, the electric filed strength in each of these was different because the primary equipotential slices that passed through the cuboid forced the field strengths to differ. More will be said about the flux density values later in this chapter.

Each of the flux surface tetrahedrons from slice discretization are divided into two portions by the primary walls of the flux tube as they intersect the flux surface.

8.13 Cascading Cuboids For Tube Discretization

This sections serves to prove that the cuboid structures can be cascaded in much the same way as is done for slice discretization. After the placement of the interior point in one cuboid, we will show that the degrees of freedom for the placement of the interior point in surrounding cuboids decreases but does not prohibit the full geometry from being discretized.

Let us consider one layer of cuboids that share the same upper and lower equipotential surface. Suppose we choose the location of the interior point in one of the cuboids. We wish to determine the degrees of freedom we have left in the remaining cuboids for locating the interior point such that the flux tubes are continuous throughout the entire cuboid layer.

We will prove that a grid pattern can be generated on the upper surface that denotes the intersection of the primary walls of the flux tubes with that equipotential surface. We then go on to prove that the choice of an interior point within one cuboid leads to the successful

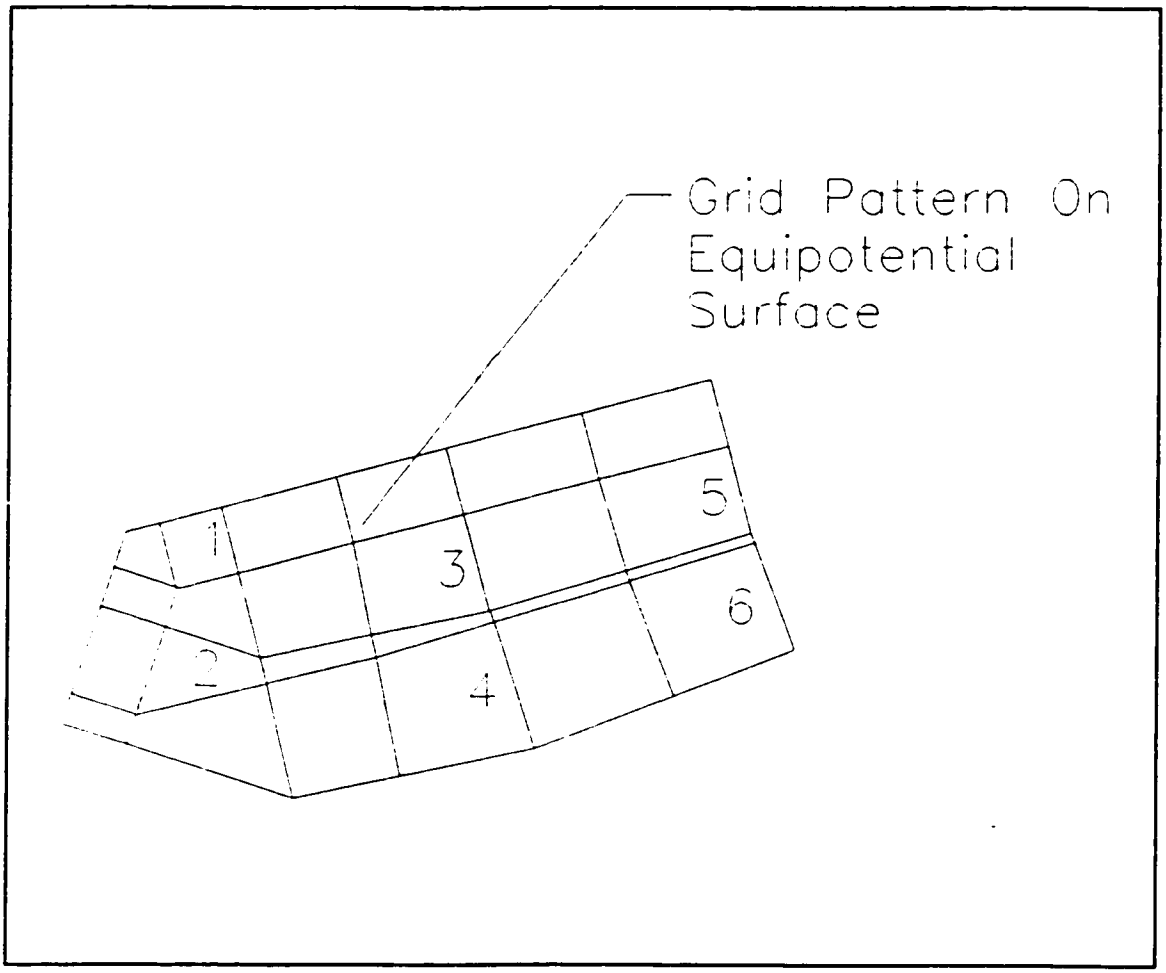

Figure 8.26: Placement of grid pattern on equipotential surface.

discretization of that layer. Moreover, the grid pattern for the next layer is generated at the same time. By applying the same procedure, that layer can be discretized as well. Repeated applications of this procedure lead to a fully discretized set of tubes from the upper most equipotential surface to the lower most.

Suppose we start with the cuboid labelled 1 in figure 8.26. We choose a point on the upper equipotential surface that is the projection of the interior point onto that surface. The entire layer is then subdivided into a grid pattern, following the rules that apply when the wall of a primary flux tube crosses a flux surface. Specifically, the rule that is enforced is that the path of intersection that the wall of the flux tube makes as it passes from one cuboid to the next is perpendicular to the flux surface it crosses. Note that we have not yet located the interior point of any cuboid yet. All that we have located are their projections onto the top equipotential surface.

After the entire equipotential surface has been divided up into a grid pattern, we choose the interior point of one of the cuboids as a starting point. Let us choose the interior point of cuboid 1 as the starting point. The interior point of the three surrounding cuboids (cuboids 2, 6 and 7) is automatically determined after this. The reason being that the plane that intersects the projection line of the interior point of cuboid 1 must possess a normal vector that is parallel to the edge line connecting cuboids 2, 6, and 7. This fact was established by virtue of the direction of the flux density in the vicinity of the flux surfaces.

We work our way down the cuboids in column wise fashion, producing two more interior nodes at a time. Once we get to the bottom of the column we start back up the next column. Note that for cuboids such as that labelled 14, the plane that intersects the projection

of the normal vector is already defined since the two vectors that form the plane have been defined. See figure 8.27.

Once the entire cuboid layer is complete in the sense that every cuboid now has an interior point defined, we proceed to the next layer. On the next level down, all of the projections of the interior points are defined due to the discretization that took place in the layer above. We start the entire process again by choosing an interior point on one of the cuboids and working our way through the layer. The process can be repeated down to the

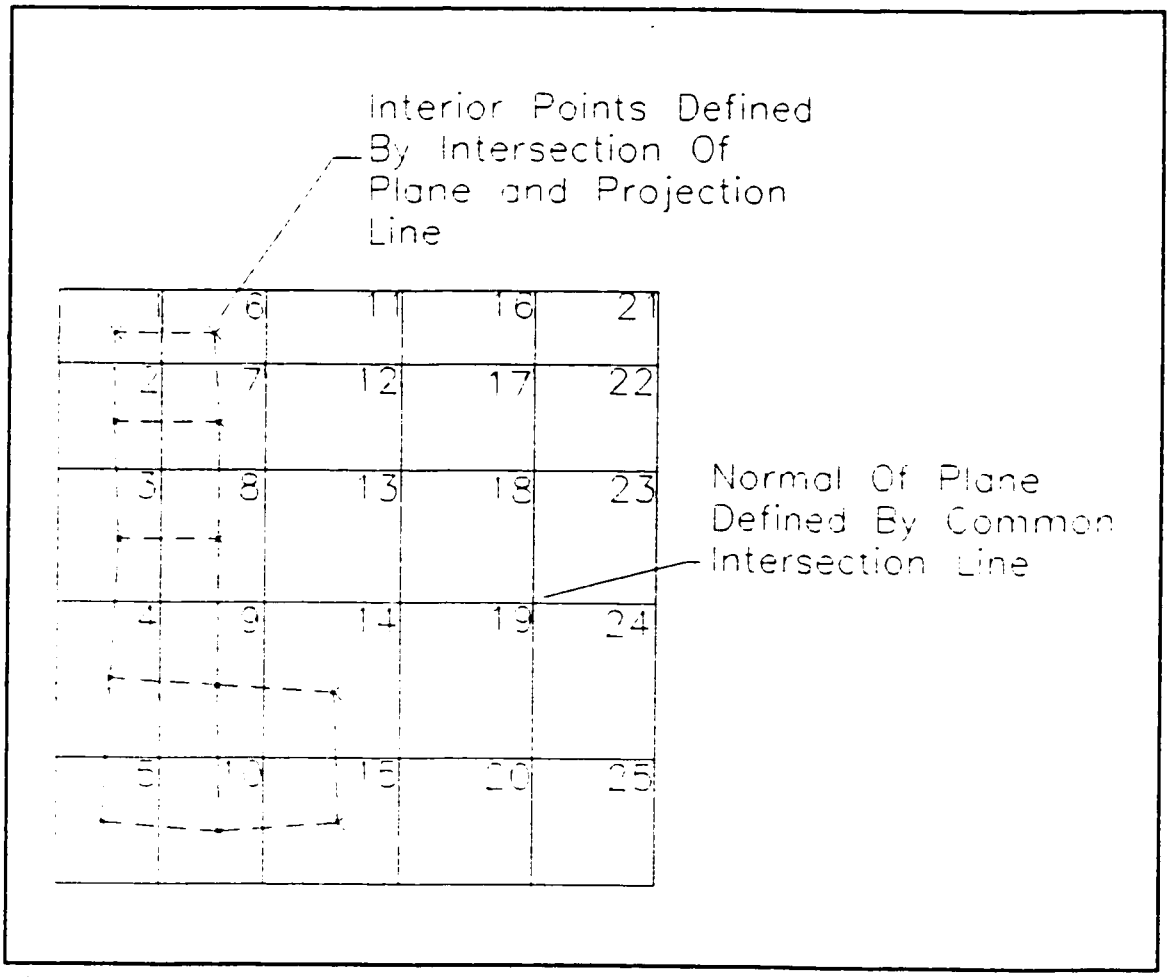

Figure 8.27: Cascading of cuboids for tube discretization.

lower level of cuboids since the equipotential surfaces tend to decouple the layers. Forcing the projection of all the interior points onto the equipotential surface has not restricted the process.

The other alternative is to reuse the interior points employed in the slice discretization. The projection of the interior node and the four lines that join the interior node to its projection on the four flux surfaces constitutes the consistent grid pattern required for tube discretization when projected back onto the two equipotential surfaces. In fact, the eight planes that were derived earlier actually form the grid pattern required on the top and bottom equipotential surfaces.

PROOF 6

We have already proved that the walls of the flux tubes that pass through the interior point also contain the projection points of the interior point onto the equipotential surfaces of the cuboid.

What needs to be proved is that the line formed by the intersection of the flux tube and the equipotential surface intersect the edge line of the cuboid perpendicularly.

We know that the flux tube wall is perpendicular to the equipotential surface. Therefore, the edge line of the cuboid is parallel to the normal vector of the flux wall.

Since the line formed by the intersection of the flux plane and the equipotential surface lines in the plane of flux wall, these two lines must meet at right angles.

8.14 The Flux Density After Tube Discretization

In two dimensions, it was natural to divide the flux tube into two portions. As shown

previously in this chapter, dividing the total flux leaving one equipotential surface (and hence terminating on the second) into four parts is a logical progression in three dimensions.

Again, in total there, are a maximum of three different types of electric flux density field configurations. The three types of regions are identical to the regions generated by the slice discretization, two pyramids and a tetrahedron. The direction of the flux density vector **D** and its magnitude will depend on the subregions' position inside the larger hexahedron.

For the two pyramids located along an edge which is formed by the intersection of two flux surfaces, the flux density vector is directed along the edge. The magnitude of the flux density vector will depend on the amount of flux this tube carries. In three dimensional problems, the amount of flux each tube carries will depend on the fractional value ascribed to the interior point. The total flux must split up into four sections rather than just two as in the two dimensional case. The flux density in both pyramids is equal to the amount of electric flux passing through this tube divided by the area of the quadrilateral base. The magnitude of **D** is equal in both pyramids since they share a common base. The equation which governs the magnitude of the flux density in these pyramids is given below in equation (8.7) :

$$|D_1| = \frac{Q_{tube}}{Area_{pyramid\ 1}} \qquad \textbf{(8.7)}$$

For the pyramids which have as their base one of the equipotential surfaces, the magnitude of the flux density is equal to the amount of electric flux the tube must carry divided by the quadrilateral base area. Each of the two pyramids whose base lies coplanar with an equipotential surface is divided into four smaller sub-pyramids by the interior flux

surfaces that are placed into the system by the tube discretization. The common point to each of the four quadrilateral bases is the interior point's projection onto the equipotential surface. Equation (8.8) describes the calculation of the magnitude of **D** in these pyramids :

$$|D_2| = \frac{Q_{tube}}{Area_{pyramid\ 2}} \tag{8.8}$$

The final structure that must be considered is the tetrahedral structure. Insertion of the interior flux surfaces divides each of these tetrahedral structures into two smaller tetrahedrons. The magnitude of **D** in each of these structures depends upon the area and the orientation of the bounding surfaces that make up the tetrahedrons through which the tube flux must pass. The primary constraint that must be met is the continuity of flux. All of the electric flux that is sourced from one of the equipotential surfaces must eventually terminate on the other within one flux tube. On two of the tetrahedron's surfaces this continuity constraint can be imposed. On the third surface, which is the inserted flux surface, the flux density vector must be perpendicular to that surface's normal. A set of three equations in three unknowns can be set up to solve for the unique electric flux density vector **D** in the tetrahedron. This procedure is described in equation (8.9) where $\mathbf{D}_3$ is the electric flux density vector in the tetrahedron :

$$\begin{aligned} \overline{D_3}\cdot\hat{n}_1 A_1 &= Q_{tube} \\ \overline{D_3}\cdot\hat{n}_2 A_2 &= Q_{tube} \\ \overline{D_3}\cdot\hat{n}_3 &= 0 \end{aligned} \tag{8.9}$$

8.15 Three Dimensional Application Results

For the first shape, which is the "perfect" cuboid of figure 8.28, the top and bottom surfaces are constrained to be at a potential difference of 10 volts. The interior node which is geometrically centred is placed at a scalar potential of +5 volts with respect to the bottom surface. The total volume of the cuboid is 8 m^3. The stored energy for the slice discretization is $100.0\varepsilon_0$ Joules. The capacitance is $2\varepsilon_0$ Farads.

For the tube discretization, the total electric flux (ie. charge) is assigned to be 20 Coulombs and is equally divided among the four inner tubes. The stored energy in this case is $100/\varepsilon_0$ Joules yielding a capacitance of $2\varepsilon_0$ Farads. By ignoring the fringing fields, the solution to this problem is exact and both methods should have arrived at the same final capacitance value. The average value of these two values is the exact value as well.

To illustrate the implementation of the method with a cuboid that does not have flux surfaces that are perpendicular to the equipotential surfaces, consider figure 8.29. Assigned potentials and tube flux remain as previously defined. The stored energy for the slice discretization is $310\varepsilon_0$ Joules and the estimated capacitance is 55 pF. For the tube discretization, the stored energy is $81/\varepsilon_0$ J and the capacitance estimate is 22 pF. The dual bounds estimate for the capacitance, which is the average of the slice and tube estimates is 38 pF.

The programs used to obtained these values are listed in appendix B. The coordinates for the eight vertexes and the interior point are contained in one file (CUBOID.DAT) while the potential and flux distributions are contained in two additional files called SLCEDATA.DAT and TUBEDATA.DAT for the slice and tube discretizations respectively.

8.16 Three Dimensional Silicon Micro Motor Structures

The three dimensional structures analysed in the previous section can be combined to form a solid model of a three dimensional silicon micro motor. Shown in figure 8.1 is a portion of a solid model of a 3:2 ratio silicon micro motor structure. The solid modelling graphical user interface provided with ANSOFT (formerly MacNeal/Schwendler) corporation's EMAS software is the commercial software package used to implement the three dimensional geometry. For clarity, portions of the air-gap's geometrical constructs are removed. This particular silicon micro motor is a three dimensional implementation of the two dimensional structure shown in the scanning electron micrograph of figure 3.2.

The primary components of the structure are a rotor; a set of stator electrodes; a pin bearing; a substrate shield and bushings on the underside of the rotor. Each of these components can be seen in the two dimensional cut-away view of a micro motor structure which is shown in figure 3.1.

Once the initial cuboids are in place, the slices and tubes can be generated by choosing an inner point in each cuboid following the guidelines presented earlier in this chapter. The desired capacitance values can then be calculated and finally the desired torque estimates. The effects of the fringing fields will now be included since the initial discretization took them into account.

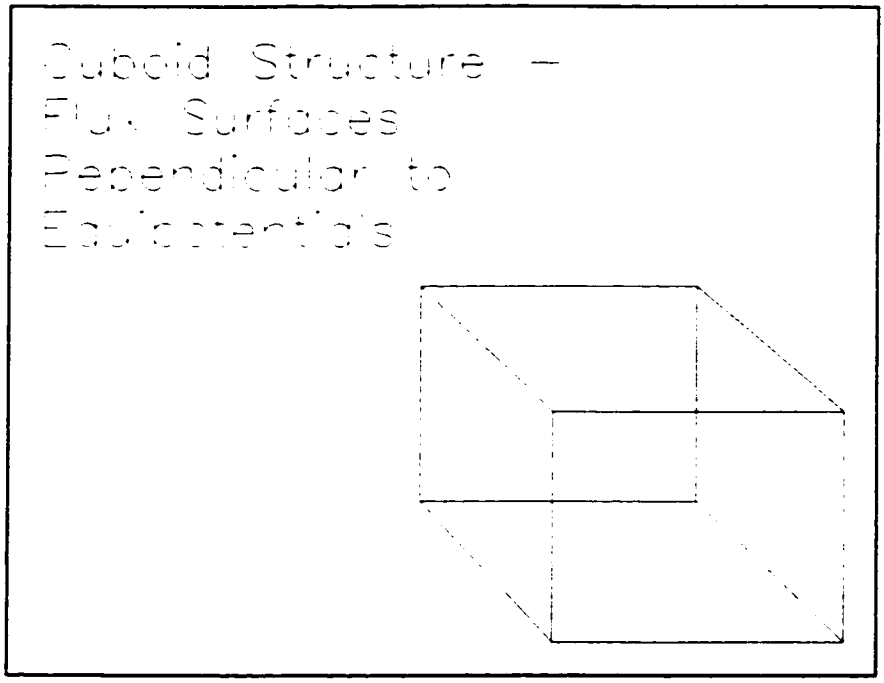

Figure 8.28: Cuboid flux surfaces perpendicular to equipotentials

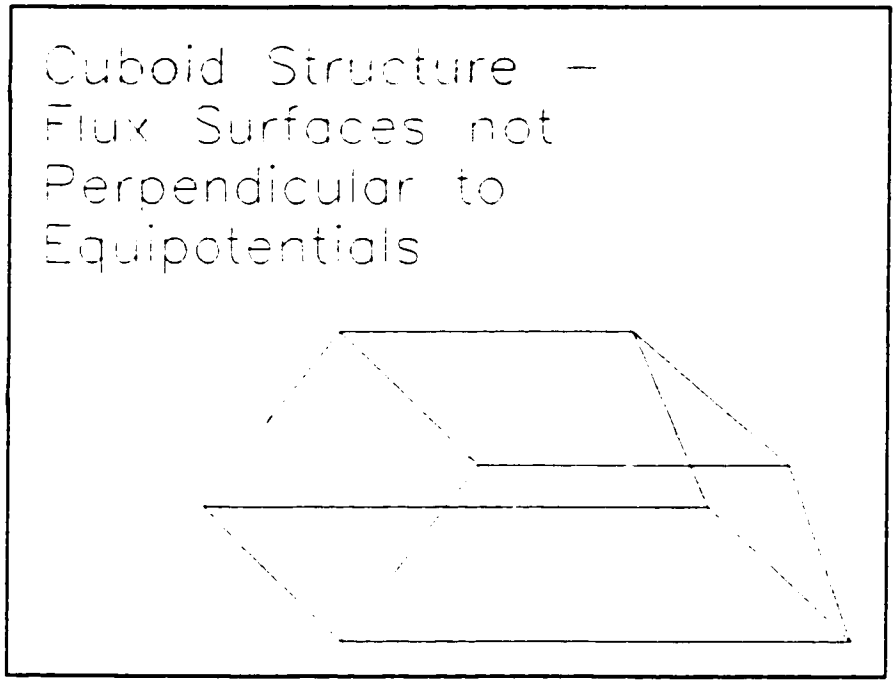

Figure 8.29: Cuboid flux surfaces not perpendicular to equipotentials.

CHAPTER 9

SUMMARY AND CONCLUSIONS

1) It is possible to implement the output coefficient of a motor sizing equation as a measure of performance. Since the output coefficient is a measure which is independent of actuation scheme, it can be employed as a comparative measure in a scaling analysis between motors that do not share the same actuation schemes.

2) The performance capabilities of a practical electrically actuated variable capacitance motor have been compared to those of magnetically actuated alternatives and found to be superior at small scales. The output coefficient of the example variable capacitance micromotor is calculated to be 5×10^{6} J/m^{4}. Compare this with 5×10^{3} J/m^{4}, the estimated output coefficient of a "good" conventional macro domain sized machine and also the value of the output coefficient of the example interior type permanent magnet motor operating at a current density level of 10 A/mm^{2}. Furthermore, at 60 Hz, current density levels in the stator electrodes of the variable capacitance machine are far below the 2 A/mm^{2} level. Unless mechanical stress limits in the rotor are exceeded, operating frequencies as high as 150 MHz may be possible.

3) The disadvantage of using higher frequencies for variable capacitance machines is that the power lost to ohmic dissipation increases at a faster rate than mechanical power

produced when excitation frequency increases.

4) For synchronous motors with an equal number of poles and operating at the same frequency, the transition from magnetic to electric actuation should be made when device outer diameters are of the order of 2 mm. This estimate is based on the output coefficient possessed by each type of machine and assumes that the current density level in magnetic machines can safely reach 10 A/mm^2.

5) Incorporating permanent magnet material into magnetically actuated synchronous motors of the type considered in this thesis is found to be of little added benefit at scales below 2 mm. The product of the RMS phase current and the direct axis synchronous reactance is insufficient to permit maximum rotor angles. As a result, substantial amounts of power/torque cannot be generated unless current density values are raised to extreme levels ($\sim 10^{10}$ A/m^2).

6) The two axis or **dq0** method of analysing conventional magnetically actuated machines can be extended and applied to the topology of electrically actuated variable capacitance silicon micro motors. The two axis method is suitable for both two dimensional and three dimensional structures because it utilizes lumped electrical circuit parameters. Since energy based methods can be used to derive lumped electrical circuit values, the two axis method is also suited for numerical analysis.

7) The finite element method can be used to obtain estimates for the direct axis and quadrature axis synchronous capacitive susceptances. The energy based formulation employed eliminates the need to extract self and mutual phase capacitances and produces the desired axis capacitances directly.

8) Higher order space harmonics present in the air-gap flux density distribution can be

obtained without the need for numerical differentiation of the air-gap potential field. For example, the pronounced sixth harmonic in the direct axis and quadrature axis charge versus rotor angular position curves arises out of the seventh (positive sequence) and fifth (negative sequence) phase charge harmonics.

9) The dual bounds approach of estimating lumped circuit parameter values for silicon micromotor structures requires far less computation than the "classical" finite element approach. How much less computation can be controlled by the analyst. This is in contrast to the finite element method in which the connectivity of the nodes determines the bandwidth of the final matrix equation. Because the small 4%-10% deviation from the finite element simulation results was accomplished without having to solve a system of linear equations, the method shows great promise as a bounds check for the finite element method as well as a viable alternative.

10) The method of tubes and slices can be implemented in three dimensional structures by applying the concepts derived in this work. The equipotential surfaces and flux surfaces can be placed inside the fundamental cuboid structures such that the surfaces are continuous. By following the guidelines set out in chapter eight, complicated three dimensional structures can be discretized using six sided cuboid structures which possess two equipotential surfaces and four flux confining surfaces.

RECOMMENDATIONS FOR FUTURE WORK

In addition to work being conducted on minimizing torque ripple, ways of reducing the undesirable current harmonics should be investigated. An experimental verification of the magnitudes of the higher frequency current harmonics needs to be performed. It is

recommended that harmonic currents be considered at the design stage because of the additional torques they develop.

To demonstrate the advantages of the dual bounds approach in three dimensions, a silicon micro motor solid model should be "outfitted" with the tube and slice discretization and the direct and quadrature axis capacitances calculated. More comparisons need to be performed between three dimensional finite element simulations and three dimensional tube and slice discretizations. Since some existing three dimensional meshes could be turned into a tube and slice discretization, automated methods for doing this should be investigated. The motivation for this is low cost built in bounds checking for three dimensional finite element solutions. This is an attractive feature to add to commercial finite element software.

It was shown that an optimization can be performed on the discretization implemented in the method of dual bounds. The amount of computational effort can be controlled in a number of ways. In the slice discretization, we can choose to fix the equipotential surfaces or to keep them as degrees of freedom. For tube discretization, we can choose the total tube flux for each tube and constrain the sum of the fractional fluxes to be one, or, apply no constraints other than that of total system charge.

The structure of the resulting equations should be investigated. The optimization process should be employed with varying amounts of coupling between the degrees of freedom in order to assess the sensitivity of the method to the optimization process.

REFERENCES

[1] Oleg D. Jefimenko, "Electrostatic Motors", Chapter 7 in Electrostatics and its Applications by A. D. Moore, Wiley, New York, 1973.

[2] W. S. N Trimmer, "Micro Robots and Micro Mechanical Systems", Sensors and Actuators, 19 (1989), pp. 267-287.

[3] T. W. Dakin, G. Luxa, G. Opperman, J. Vigreux, G. Wind, H. Winkelnkemper, "Breakdown of Gases in Uniform Fields", Electra, (32), 1974, pp. 61-82.

[4] Stephen F. Bart, Theresa A. Lober, Roger T. Howe, Jeffrey H. Lang, Martin F. Schlecht, "Design Considerations for Micro Machined Electric Actuators", Sensors and Actuators, 14 (1988), pp. 269-292.

[5] K. J. Gabriel, F. Behi, R. Mahdevan, M. Mehregany, "*In situ* Friction and Wear Measurements in Integrated Polysilicon Mechanisms", Sensors and Actuators, A21-A23 (1990) pp. 184-188.

[6] Yu-Chong Tai, Richard S. Muller, "Frictional Study of IC-Processed Micro Motors", Sensors and Actuators, A21-A23 (1990) pp. 180-183.

[7] Modelling and Design of Electroquasistatic Micro Actuators by Stephen F. Bart, Ph.D Thesis, M.I.T., Cambridge, MA, September 1990.

[8] Long-Shen Fan, Yu-Chong Tai, Richard S. Muller, "IC-Processed Electrostatic Micro Motors", Sensors and Actuators, 20 (1989), pp. 41-47.

[9] Roger T. Howe, Richard S. Muller, Kaigham J. Gabriel, William S. N. Trimmer, "Silicon Micro Mechanics: Sensors and Actuators on a Chip", IEEE. Spectrum, July 1990, pp. 29-35.

[10] M. Mehregany, S. F. Bart, L. S. Tavrow, J. H. Lang, S. D. Senturia, M. F. Schlecht, "A Study of Three Micro Fabricated Variable-Capacitance Motors", Sensors and Actuators, A21-A23 (1990), pp. 173-179.

[11] Yu-Chong Tai, Richard S. Muller, "IC-Processed Electrostatic Synchronous Micro Motors", Sensors and Actuators, 20 (1989), pp.49-55.

[12] Lee S. Tavrow, Stephen F. Bart, Jeffrey H. Lang, Martin F. Schlecht, "A LOCOS Process for an Electrostatic Micro Fabricated Motor", Sensors and Actuators, A21-A23 (1990) pp. 893-898.

[13] J. H. Lang, "Electric Micro Motors - A Status Report", unpublished.

[14] William Trimmer, "Micro Mechanical Systems", The Third Toyota Conference Program, October 22-25, 1989, Toyota Motor Corporation, Nisshin International Education Building, pp. 1.1-1.20.

[15] W. S. N. Trimmer, K. J. Gabriel, "Design Considerations for a Practical Electrostatic Micro-Motor", Sensors and Actuators, 11 (1987) pp. 189-206.

[16] D. K. MacKay, R. D. Findlay, "An Examination of the Scaling Properties of Electric Micro Motors and Their Magnetic Duals", a paper presented at the 1991 IEE Conference on Electrical Machines and Drives, London, U.K.

[17] R. Belmans, T. B. Johansson, D. Verdyck, W. Geysen, R. Hanitsch, "Contribution to the Design of Micro Motors", 1991 University Power Engineering Conference (UPEC '91).

[18] P J. Clarkson, P. P. Acarnley, "Reluctance Stepping Motor Systems", IEE Proceedings, Vol. 135, Pt. B, No. 6, November 1988, pp. 308-317.

[19] P. J. Clarkson, P. P. Acarnley, "Simplified Approach to the Dynamic modelling of Variable-Reluctance Stepping Motors", IEE Proceeedings, Vol. 136, Pt. B, No. 1, January 1989, pp. 1-10.

[20] George C. Verghese, Jeffrey H. Lang, Leo. F. Casey, "Analysis of Instability in Electrical Machines", IEEE Transactions on Industry Applications, Vol. IA-22, No. 5, September/October 1986, pp. 853-862.

[21] Jeffrey H. Lang, "Initial Thoughts on the Dynamics and Control of Electric Micro Motors", The Third Toyota Conference Program, October 22-25, 1989, Toyota Motor Corporation, Nisshin International Education Building, pp. 9.1-9.14.

[22] Mehran Mehregany, Kaigam J. Gabriel, William S. N. Trimmer, "Integrated Fabrication of Polysilicon Mechanisms", IEEE Transactions on Electron Devices, Vol. 35, No. 6, June 1988, pp. 719-723.

[23] Long-Shen Fan, Yu-Chong Tai, Richard S. Muller, "Integrated Movable Micro Mechanical Structures for Sensors and Actuators", IEEE Transactions on Electron Devices, Vol. 35, No. 6, June 1988, pp. 724-730.

[24] National Semiconductor Catalogue, Transducers; Pressure and Temperature, August 1974.

[25] Kurt E. Petersen, "Dynamic Micromechanics on Silicon: Techniques and Devices", IEEE Transactions on Electron Devices, Vol. ED-25, No. 10, October 1978, pp. 1241-1249.

[26] E. Bassous, H. H. Taub, L. Kuhn, "Ink Jet Printing Nozzle Arrays Etched", Appl. Phys. letters, Vol. 31, No. 2, 15 July, 1977, pp. 135-137.

[27] S. C. Jacobsen, R. H. Price, J. E. Wood, T. H. Rytting, M. Rafaelof, "A Design Overview of an Eccentric-Motion Electrostatic Micro Actuator (the Wobble Motor)", Sensors and Actuators, 20 (1989), pp. 1-16.

[28] Mark G. Allen, Martin Scheidl, Rosemary L. Smith, Aleks D. Nikolich, "Moveable Micro Machined Silicon Plates with Integrated Position Sensing", Sensors and Actuators, A21-A23 (1990), pp. 211-214.

[29] Y. Nosé, M. Zborowski, P. S. Malchesky, "Application of Micro Machine Systems in Medicine", The Third Toyota Conference Program, October 22-25, 1989, Toyota Motor Corporation, Nisshin International Education Building, pp. 24.1-24.20.

[30] Electromagnetic Fields, Energy and Forces, by Robert M. Fano, Lan Jen Chu and Richard B. Adler,Wiley, New York, 1960.

[31] Electromechanical Energy Conversion, by David C. White and Herbert H. Woodson, Wiley, New York, 1959.

[32] Electric Machinery, by A. E. Fitzgerald and Charles Kingsley Jr., McGraw Hill, New York, 1961.

[33] V. B. Honsinger, "The Fields and Parameters of Interior Type AC Permanent Magnet Machines", IEEE Transactions on Power Apparatus and Systems, Vol. PAS-101, No. 4, April 1982, pp. 867-875.

[34] D. Pavlik, V. K. Garg, J. R. Repp, J. Weiss, "A Finite Element Technique for Calculating the Magnet Sizes and Inductances of Permanent Magnet Machines", IEEE Transactions on Energy Conversion, Vol. 3. No. 1, March 1988, pp. 116-122.

[35] Teck-Seng Low, Mohammed A. Jabbar, M. Azizur Rahman, "Permanent Magnet Motors for Brushless Operation", IEEE Transactions on Industry Applications, Vol. 26, No. 1, January/February 1990, pp. 124-129.

[36] R. T. Howe, R. S. Muller, "Polycrystalline Silicon Micro Mechanical Beams", Journal of the Electrochemical Society: Solid-State Science and Technology, Vol. 130, No. 6, June 1983, pp. 1420-1423.

[37] Micro Fabricated Silicon Electric Mechanisms, by M. Mehregany, Ph.D Thesis, M.I.T., Cambridge, MA, 1990.

[38] J. F. Lindsay, R. Arumugam, R. Krishnan, "Finite-Element Analysis Characterisation of a Switched Reluctance Motor With Multitooth Per Stator Pole", IEE Proceedings, Vol. 133, Pt. B, No. 6, November 1986, pp. 347-353.

[39] K. C. Mukherji, S. Neville, "Magnetic Permeance of Identical Double Slotting", Proceedings IEE, Vol. 118, No. 9, September 1971, pp. 1257-1268.

[40] B. Bollée, "Electrostatic Motors", Philips Technical Review, Volume 30, No. 6/7, 1969, pp. 178-194.

[41] W. Trimmer, R. Jebens, "Harmonic Electrostatic Motors", Sensors and Actuators, 20 (1989), pp. 17-24.

[42] H. Guckel, T. Randazzo, D. W. Burns, "A Simple Technique for the Determination of Mechanical Strain in Thin Films With Applications to Polysilicon", Journal of Applied Physics, Vol. 57, No. 5, March 1985, pp. 1671-1675.

[43] C. H. Lee, "Vernier Motor and its Design", IEEE Transactions on Power Apparatus and Systems, Vol. PAS-82, 1963, pp. 343-349.

[44] K. C. Mukherji, A. Tustin, "Vernier Reluctance Motor", Proceedings of the IEE, Vol. 121, No. 9, September 1974, pp. 965-974.

[45] Computer-Aided Analysis and Design of Electromagnetic Devices, by S. Ratnajeevan H. Hoole, Elsevier, New York, 1989.

[46] Finite Elements for Electrical Engineers, by P. P. Silvester and R. L. Ferrari, Cambridge University Press, Cambridge, 1990.

[47] Magnet 2D Manual, Infolytica Corporation, Montreal, Canada, 1991.

[48] Computer-Aided Design in Magnetics, by D. A. Lowther and P. P. Silvester, Springer-Verlag, Berlin, 1986.

[49] C. N. Ashtiani, D. A. Lowther, "Simulation of Steady State Reactances of a Large Water Wheel Generator by Finite Elements", IEEE Transactions on Power Apparatus and Systems, Vol. PAS-103, No. 7, July 1984, pp. 1781-1787.

[50] V. B. Honsinger, "Sizing Equations for Electrical Machinery", IEEE Transactions on Energy Conversion, Vol. EC-2, No. 1, March 1987, pp. 116-121.

[51] An Introduction to Electrical Machines and Transfomers, by George McPherson, Wiley, New York, 1981.

[52] Stephen F. Bart, Mehran Mehregany, Lee S. Tavrow, Jeffrey H. Lang and Stephen D. Senturia, "Electric Micro Motor Dynamics", IEEE Transactions on Electron Devices, Vol. 39, No. 3, March 1992, pp. 566-575.

[53] Mehran Mehregany, Stephen D. Senturia, Jeffrey H. Lang and Pradnya Nagarkar, "Micro Motor Fabrication", IEEE Transactions on Electron Devices, Vol. 39, No. 9, September 1992, pp. 2060-2069.

[54] Suresh Kumar, Dan Cho and William N. Carr, "Experimental Study of Electric Suspension for Micro Bearings", Journal of Micro Electromechanical Sysytems Vol. 1, No. 1, March 1992, pp. 23-30.

[55] Mohd P. Omar, Mehran Mehregany and Robert L. Mullen, "Electric and Fluid Field Analysis of Side-Drive Micro Motors", Journal of Micro Electromechanical Systems, Vol. 1, No. 3, September 1992, pp. 130-140.

[56] Chong H. Ahn and Mark G. Allen, "A Fully Integrated Surface Micro Machined Magnetic Micro Actuator with a Multilevel Meander Magnetic Core", Journal of Micro Electromechanical Systems, Vol. 2, No. 1, March 1993, pp. 15-22.

[57] B. Wagner, M. Kreutzer and W. Benecke, "Permanent Magnet Micro Motors on Silicon Substrates", Journal of Micro Electromechanical Systems, Vol. 2, No. 1, March 1993, pp. 23-28.

[58] Bruno Frazier, Johnathon W. Babb, Mark G. Allen and David G. Taylor, "Design and Fabrication of Electroplated Micro Motor Structures", ASME Journal of Micro Mechanical Sensors, Actuators and Systems, Vol. DSC-32, 1991, pp. 135-146.

[59] G. Meunier, J. L. Coulomb and J. C. Sabonnadiere, "2D and 3D Finite Element Modelling of Small Electrical Machines",

[60] Stephen F. Bart, Mehran Mehregany, Lee S. Tavrow and Stephen Senturia, "Measurements of Electric Micro Motor Dynamics", ASME Dyn Sys Contr Div, Publ DSC v.19, Microstructures Sensors and Actuators, Winter Annual Meeting of ASME, Dallas, TX, USA, Nov 25-30 1990. Publ by ASME NY, NY 1990, pp. 19-29.

[61] J. H. Lang, M. F. Schlecht, R. T. Howe, "Electric Micro Motors: Electromechanical Characteristics",

[62] Suresh Kumar and Dan Cho, "Electrostatically-Levitated Micro Actuators", ASME

Journal of Micro Mechanical Systems, Vol. DSC-40, 1992, pp. 53-67.

[63] P. Hammond, T. D. Tsiboukis, "Dual Finite-Element Calculations for Static Electric and Magnetic Fields", IEE Proceedings, Vol 130, Part A, No. 3, 1983, pp. 105-111.

[64] P. Hammond, M. C. Romero-Fuster and S. A. Robertson, "Fast Numerical Method for Calculation of Electric and Magnetic Fields Based on Potential-Flux Duality", IEE Proceedings, Vol. 132, Pt. A, No. 2, March 1985, pp. 84-94.

[65] P. Hammond and Zhan Qionghua, "Calculation of Poissonian Fields by Means of the Method of Tubes and Slices", IEE Proceedings, Vol. 132, Pt. A, No. 4, July 1985, pp. 149-157.

[66] P. Hammond and D. Baldomir, "Dual Energy Methods in Electromagnetism Using Tubes and Slices", IEE Proceedings, Vol. 135, Pt. A, No. 3, March 1988, pp. 167-172.

[67] J. K Sykulski, "Computer Package for Calculating Electric and Magnetic Fields Exploiting Dual Energy Bounds", IEE. Proceedings, Vol 135, Pt A, March 1988, pp. 145-150.

[68] S. D. Senturia, "CAD Challenges for Micro Sensors, Micro Actuators, and Micro Systems", Proceedings IEEE., Vol 86, No. 8, August 1998, pp. 1611-1626.

[69] T. B. Johansson, M. Van-Dessel, R. Belmans, "Technique for Finding the Optimum Geometry of Electro Static Micro Motors", IEEE Trans. Industry Applications, Vol. 30, July-August 1994, pp. 912-919.

[70] Leo O' Connor, "Micro Machines Tap Actuating Principles", Mechanical Engineering, Vol. 116, August 1994, pp. 58-60.

[71] H. Fujita, "Micro Actuators and Micro Machines", Proc. IEEE., Vol. 86, No. 8, Aug 1998, pp. 1721-1732.

[72] D. S. Eddy, D. R. Sparks, "Application of MEMS Technology in Automotive Sensors and Actuators", Proc. IEEE., Vol. 86, No. 8, August 1998, pp. 1747-1755.

[73] J. Campbull, "Magnetism Motivates Micro Actuator Research", Electronics World, Vol. 102, April 1996, p. 275.

[74] J. B. Morrell, J. K. Salisbury, "Parallel-Coupled Micro-Macro Actuators", International Journal of Robotics Research, Vol. 17, No. 7, July 1998, pp. 773-791.

[75] K. F. Bohringer, B. R. Donald, N. C. MacDonald, "Programmable Force Fields for Distributed Manipulation", International Journal of Robotics Research, Vol. 18, No. 2, February 1999, pp. 168-200.

[76] P. T. Krein, "Analysis of Corona Motors and Micro Motors by Means of Effective Gap Conductivity", IEEE. Trans. Industry Applications, Vol. 31, July-August 1995, pp. 752-760.

[77] Leo O'Connor, "Miniature Motors for Future PCs", Mechanical Engineering, Vol. 117, February 1995, pp. 63-65.

[78] S. L. Garverick, M. L. Nagy, N. K. Rao, "A Capacitive Sensing Integrated Circuit for Detection of Micro Motor Critical Angles", IEEE Journal of Solid State Circuits, Vol. 32, Jan 1997, pp. 23-30.

APPENDIX A

SLICENRG.C

```
#define _HPUX_SOURCE
#include <stdio.h>
#include <math.h>
#include <stdlib.h>
#include <string.h>
#ifndef EPS0
#define EPS0 8.85416e-12
#endif

/* Author: D. Kyle MacKay */

/* ================================================================== */
double cross_prod (double x_diff1, double x_diff2,
                   double y_diff1, double y_diff2) {
/* ================================================================== */

/* This function calculates the magnitude of the cross product
of two vectors */

return ( fabs( x_diff1*y_diff2-x_diff2*y_diff1 ) ) ;
}

/* ================================================================== */
double length (double x_diff, double y_diff) {
/* ================================================================== */
/* This function returns the square of the length of a vector */

return ( x_diff*x_diff+y_diff*y_diff );
}

/* ================================================================== */
int check_flux (double x1, double y1, double x2, double y2,
                double x3, double y3)
/* ================================================================== */
{

if ( fabs ( length (x1-x2, y1-y2) -
            length (x2-x3, y2-y3) -
            length (x3-x1, y3-y1) -
```

```
        2.0*sqrt(length (x2-x3,y2-y3))*
          sqrt(length (x3-x1,y3-y1)))
    > 1.0e-01 ) return (1);
return (0);
}

/* ========================================================== */
double main (void) {
/* ========================================================== */

/* This program calculates the energy based upon a slice discretization
of a physical geometry */

FILE *outline, *interior;
char line[81];
double equi_line[2][2][2], flux_line[2][2][2], interior_x,
     interior_y, edge_x[2], edge_y[2], area, energy;
double x[4], y[4], edge_val[2], inner_val;
double E_squared, total_area;
int num_quad, quad_count, i, j;
int pot_order[4]  = {0, 1, 2, 3} ;
int flux_order[4] = {1, 2, 0, 3} ;

energy=0.0;
total_area=0.0;

outline=fopen("outln_d.dat","r");
if (outline==NULL) {
  printf("Erorr! Cannot find file OUTLN_D.DAT\n");
  return (energy);
}

interior=fopen("slice_d.dat","r");
if (interior==NULL) {
  printf("Error! Cannot find file SLICE_D.DAT\n");
  return (energy);
}

while ( fscanf(outline,"%s",line) && (line[0] != '#'))

/* This while loop is executed so long as a # sign has not been
  encountered.  The number sign indicates that the end of the
  information header has been reached. */
```

```
{
  if ( !strcasecmp("Number", line) )
  {
    while ( fscanf(outline,"%s\n", line) && strcasecmp("=",line)) ;
    fscanf (outline,"%d",&num_quad);

  } /* end if */

} /* end while */

/* Read to the end of the header in the interior file. */

while ( fscanf(interior,"%s\n",line) && (line[0] != '#')) ;

for (quad_count=1; quad_count<=num_quad; quad_count++)
{
  printf("Quadrilateral number %d\n", quad_count);
  for (i=0; i<4; i++) fscanf(outline,"%lf %lf\n", x+i, y+i);
  fscanf(interior, "%lf %lf %lf\n", edge_x, edge_y, edge_val) ;
  fscanf(interior, "%lf %lf %lf\n", edge_x+1, edge_y+1, edge_val+1) ;
  fscanf(interior, "%lf %lf %lf\n", &interior_x, &interior_y, &inner_val) ;

  if ( (inner_val<edge_val[0]&&inner_val<edge_val[1])||
     (inner_val>edge_val[0]&&inner_val>edge_val[1]) )
  {printf("An error has occurred!  Inner value out of range.\n");
   return (0.0);
  } /* end if */

  /* Assign values to endpoints of equipotential lines and flux lines
  */

  for (i=0; i<2; i++) /* Loop for the number of pot and flux edges */
  {
    for (j=0; j<2; j++) /* Loop once for start and once for stop */
    {
    equi_line[i][j][0]=x[ pot_order[2*i+j] ];
    equi_line[i][j][1]=y[ pot_order[2*i+j] ];
    flux_line[i][j][0]=x[ flux_order[2*i+j] ];
    flux_line[i][j][1]=y[ flux_order[2*i+j] ];
    } /* end for loop */
  } /* end for loop */

/* Check to see if the edge point is actually along the flux line */
```

```
for (i=0; i<2; i++)
  if (check_flux (flux_line[i][0][0],
                  flux_line[i][0][1],
                  flux_line[i][1][0],
                  flux_line[i][1][1],
                  edge_x[i],
                  edge_y[i]) ) return (0.0) ;

for (i=0; i<2; i++) /* Loop for the number of flux lines */
{
  for (j=0; j<2; j++) /* Loop for the number of triangles along edge */
  {
    E_squared=(edge_val[j]-inner_val)*(edge_val[j]-inner_val)/
            length( (flux_line[i][j][0]-edge_x[i]),
                    (flux_line[i][j][1]-edge_y[i]) ) ;
    area=0.5*cross_prod( (flux_line[i][j][0]-edge_x[i]),
                         (edge_x[i]-interior_x),
                         (flux_line[i][j][1]-edge_y[i]),
                         (edge_y[i]-interior_y));
    printf("%14.6e %14.6e %14.6e\n",edge_val[j], flux_line[i][j][0],
                                    flux_line[i][j][1]);
      energy+=0.5*E_squared*area;
    total_area+=area;
  } /* end for loop */
} /* end for loop */

/* Now add the contribution made to the energy from the triangles
  not along the flux lines */

  for (i=0; i<2; i++)
  { area=0.5*cross_prod ( (equi_line[i][1][0]-equi_line[i][0][0]),
                          (interior_x-equi_line[i][0][0]),
                          (equi_line[i][1][1]-equi_line[i][0][1]),
                          (interior_y-equi_line[i][0][1]) ) ;
    E_squared= (edge_val[i]-inner_val)*(edge_val[i]-inner_val)*
            length ( (equi_line[i][1][0]-equi_line[i][0][0]),
                     (equi_line[i][1][1]-equi_line[i][0][1]) )/
            (4.0*area*area);
    energy+=0.5*E_squared*area;
    total_area+=area;
    printf("%14.6e %14.6e %14.6e\n",0.5*E_squared*area,area,E_squared);
  } /* end for loop */
```

```
} /* end for loop */

fclose (outline);
fclose (interior);

printf("Y E A H ! Completed Entire Slice Calculation!%14.6e\n", energy);
printf("total area = %14.6e\n", total_area);

return (energy);
}
```

TUBENRG.C

```
#define _HPUX_SOURCE
#include <stdio.h>
#include <math.h>
#include <stdlib.h>
#include <string.h>
#ifndef EPS0
#define EPS0 8.85416e-12
#endif

/* Author: D. Kyle MacKay */

/* ================================================================== */
double cross_prod (double x_diff1, double x_diff2,
                   double y_diff1, double y_diff2) {
/* ================================================================== */

/* This function calculates the magnitude of the cross product
of two vectors */

return ( fabs( x_diff1*y_diff2-x_diff2*y_diff1 ) ) ;
}

/* ================================================================== */
double length (double x_diff, double y_diff) {
/* ================================================================== */
/* This function returns the square of the length of a vector    */

return ( x_diff*x_diff+y_diff*y_diff );
}

/* ================================================================== */
int check_flux (double x1, double y1, double x2, double y2,
                double x3, double y3)
/* ================================================================== */
{

if ( fabs ( length (x1-x2, y1-y2) -
            length (x2-x3, y2-y3) -
            length (x3-x1, y3-y1) -
            2.0*sqrt(length (x2-x3,y2-y3))*
               sqrt(length (x3-x1,y3-y1)))
```

```
    > 1.0e-01 ) return (1);
return (0);
}

/* ================================================================== */
double main (void) {
/* ================================================================== */

/* This program calculates the energy based upon a tube discretization
of a physical geometry                                          */

FILE *outline, *interior;
char line[81];
double equi_line[2][2][2], flux_line[2][2][2], interior_x,
     interior_y, edge_x[2], edge_y[2], area, energy;
double x[4], y[4], flux_frac[2], tot_flux;
double D_squared, total_area;
int num_quad, quad_count, i, j;
int pot_order[4]  = {0, 1, 3, 2} ;
int flux_order[4] = {3, 0, 1, 2} ;

energy=0.0;
total_area=0.0;

outline=fopen("outln_d.dat","r");
if (outline==NULL) {
  printf("Erorr! Cannot find file OUTLN_D.DAT\n");
  return (energy);
} /* end if */

interior=fopen("tube_d.dat","r");
if (interior==NULL) {
  printf("Error! Cannot find file TUBE_D.DAT\n");
  return (energy);
} /* end if */

while ( fscanf(outline,"%s",line) && (line[0] != '#'))

/* This while loop is executed so long as a # sign has not been
  encountered.  The number sign indicates that the end of the
  information header has been reached.                          */
{
  if ( !strcasecmp("Number", line) )
```

```
  {
    while ( fscanf(outline,"%s\n", line) && strcasecmp("=",line)) ;
    fscanf (outline,"%d",&num_quad);

  } /* end if */

} /* end while */

/* Read to the end of the header in the interior file.        */

while ( fscanf(interior,"%s\n",line) && (line[0] != '#')) ;

for (quad_count=1; quad_count<=num_quad; quad_count++)
{
  printf("Quadrilateral number %d\n", quad_count);
  for (i=0; i<4; i++) fscanf(outline,"%lf %lf\n", x+i, y+i);
  fscanf(interior, "%lf %lf %lf\n", edge_x, edge_y, flux_frac) ;
  fscanf(interior, "%lf %lf %lf\n", edge_x+1, edge_y+1, flux_frac+1) ;
  fscanf(interior, "%lf %lf %lf\n", &interior_x, &interior_y, &tot_flux) ;

  if ( fabs (1.0-flux_frac[0]-flux_frac[1]) > 1.0e-08 )
  {printf("An error has occurred!  Fractions don't add to 1.0.\n");
   return (0.0);
  } /* end if */

  /* Assign values to endpoints of equipotential lines and
     flux lines                                          */

  for (i=0; i<2; i++) /* Loop for the number of pot and flux edges */
  {
    for (j=0; j<2; j++) /* Loop once for start and once for stop */
    {
    equi_line[i][j][0]=x[ pot_order[2*i+j] ];
    equi_line[i][j][1]=y[ pot_order[2*i+j] ];
    flux_line[i][j][0]=x[ flux_order[2*i+j] ];
    flux_line[i][j][1]=y[ flux_order[2*i+j] ];
    } /* end for loop */
  } /* end for loop */

/* Check to see if the edge point is actually along the equi pot line */

  for (i=0; i<2; i++)
    if (check_flux (equi_line[i][0][0],
```

```
                equi_line[i][0][1],
                equi_line[i][1][0],
                equi_line[i][1][1],
                edge_x[i],
                edge_y[i]) ) return (0.0) ;

  for (i=0; i<2; i++) /* Loop for the number of equi lines    */
  {
    for (j=0; j<2; j++) /* Loop for the number of triangles along edge */
    {
      D_squared=(tot_flux*flux_frac[j])*(tot_flux*flux_frac[j])/
              length( (equi_line[i][j][0]-edge_x[i]),
                   (equi_line[i][j][1]-edge_y[i]) ) ;
      area=0.5*cross_prod( (equi_line[i][j][0]-edge_x[i]),
                    (edge_x[i]-interior_x),
                    (equi_line[i][j][1]-edge_y[i]),
                    (edge_y[i]-interior_y));
      printf("%14.6e %14.6e %14.6e\n", flux_frac[j], equi_line[i][j][0],
                                        equi_line[i][j][1]);
        energy+=0.5*D_squared*area;
      total_area+=area;
    } /* end for loop */
  } /* end for loop */

/* Now add the contribution made to the energy from the triangles
   not along the equi pot lines                              */

  for (i=0; i<2; i++)
  {  area=0.5*cross_prod ( (flux_line[i][1][0]-flux_line[i][0][0]),
                    (interior_x-flux_line[i][0][0]),
                    (flux_line[i][1][1]-flux_line[i][0][1]),
                    (interior_y-flux_line[i][0][1]) ) ;
     D_squared= (tot_flux*flux_frac[i])*(tot_flux*flux_frac[i])*
              length ( (flux_line[i][1][0]-flux_line[i][0][0]),
                   (flux_line[i][1][1]-flux_line[i][0][1]) )/
              (4.0*area*area);
     energy+=0.5*D_squared*area;
     total_area+=area;
     printf("%14.6e %14.6e %14.6e\n",0.5*area*D_squared,area,D_squared);
  } /* end for loop */

} /* end for loop */
```

```
fclose (outline);
fclose (interior);

printf("Y E A H ! Completed Entire Tube Calculation!%14.6e\n", energy);
printf("total area = %14.6e\n", total_area);

return (energy);
}
```

APPENDIX B

```
#include<math.h>
#include<stdio.h>
#define EPS0 (double) 8.85E-12
/*************************************************************************

This is the function file for the 3D enery calculations for the
tube and slice simulation .

The functions include ;

- VectorFromTo
double  *VectorFromTo (double *From , double *To , double *Result)

- VectorCrossProduct
double *VectorCrossProduct (double *V1 , double *V2 , *Result )

- VolumeOfPyramid
double VolumeOfPyramid (double *P , double *Height)

- VolumeOfTetrahedron
double VolumeOfTetrahedron (double *Height, double *V1, double *V2 )

- InterSectionPIEdgeFluxSurface
double *InterSectionPIEdgeFluxSurface ( double *Normal, double *PI , double *P , double
*Result)

- InterSectionPIFluxSurface
double *InterSectionPIFluxSurface ( double *Normal, double *PI , double *P , double
*Result)

- VectorMagnitude
double VectorMagnitude ( double *Vector )

- VectorDotProduct
double VectorDotProduct (double *V1 , double *V2 )

- InterSectionPIEquipotentials
double *InterSectionPIEquipotentials ( double *Normal, double *PI , double *P , double
*Result)

*************************************************************************/
```

```
/*
The structures that follow immediately should also be defined in the
threeD.h file.

Some of the result structures can be filled in by one function call and
others will require data to be filled in in some structure elements before
they can be filled in.
*/

double VectorFromTo (double *From , double *To, double *Result ) ;
double VectorCrossProduct (double *V1 , double *V2 , double *Result ) ;
double VolumeOfPyramid (double P[][3] , double *Height ) ;
double VolumeOfTetrahedron (double *Height , double *V1, double *V2 ) ;
double VectorMagnitude ( double *Vector ) ;
double InterSectionPIEdgeFluxSurface ( double *Normal, double *PI , double *P , double
*Result );
double VectorDotProduct (double *V1 , double *V2 );
double InterSectionPIFluxSurface ( double *Normal, double *PI , double *P , double *Result
) ;
double InterSectionPIEquipotentials ( double *Normal, double *PI , double *P , double
*Result );
double InterSectionOtherEdges ( double Face[][3], double P[][3], double Result[][3] ) ;
double ESquared (double PHI1, double PHI2, double *P1, double *P2) ;
double DSquared (double Q, double Fraction, double *P1, double *P2, double *PCentre) ;



double  VectorFromTo (double *From , double *To, double *Result)

{

int i ;
double Magnitude = 0.0 ;

for (i = 0; i < 3; i++)
{
  *(Result + i) = *(From + i) - *(To + i) ;
  Magnitude = Magnitude + (*(Result + i))*(*(Result + i)) ;

}

Magnitude = sqrt (Magnitude) ;
```

```
if ( Magnitude == 0.0) printf ("The magnitude of the vector is zero.\n") ;

return (Magnitude) ;

}


double VectorCrossProduct (double *V1 , double *V2 , double *Result )

{

int i ;
double Magnitude = 0.0 ;

for (i = 0; i < 3; i++)
{

  *(Result + i) = ( *(V1 + (i+1)%3) ) * ( *(V2 + (i+2)%3) ) - ( *(V2 + (i+1)%3) ) * ( *(V1
+ (i+2)%3) );
  Magnitude = Magnitude + (*(Result + i))*(*(Result + i)) ;
}

Magnitude = sqrt (Magnitude) ;

if ( Magnitude <= 0.0) printf ("The magnitude of the cross product is zero.\n") ;

return (Magnitude);

}

double VolumeOfPyramid (double P[][3] , double *Height)

{
double TempResult[2][3] ;

double Volume, Check ;

Check = VectorFromTo ( *(P+1), P[0], TempResult[0] ) ;

if (Check <= 0.0) printf ("Bad VectorFromTo\n") ;

Check = VectorFromTo ( P[3], P[0], TempResult[1] ) ;
```

```
if (Check <= 0.0) printf ("Bad VectorFromTo\n") ;

Volume = VolumeOfTetrahedron ( Height , TempResult[0], TempResult[1]) ;

Check = VectorFromTo (P[3], P[2], TempResult[0]) ;

if (Check <= 0.0) printf ("Bad VectorFromTo\n") ;

Check = VectorFromTo (P[1], P[2], TempResult[1]) ;

if (Check <= 0.0) printf ("Bad VectorFromTo\n") ;

Volume = Volume + VolumeOfTetrahedron ( Height , TempResult[0] , TempResult[1] ) ;

return (Volume) ;

}

double VolumeOfTetrahedron (double *Height , double *V1, double *V2 )

{

doubie TempResult[2][3] ;

double Volume , Check;
double BaseArea  ;

Check = VectorCrossProduct (V1, V2, TempResult[0]) ;

if (Check <= 0.0) printf ("Bad VectorCrossProduct.\n") ;

BaseArea = VectorMagnitude( TempResult[0] ) ;

Volume = BaseArea * (VectorMagnitude (Height)) / 6.0 ;

return (Volume) ;

}

double VectorMagnitude ( double *Vector )
```

```
{

int i ;
double Magnitude = 0.0 ;

for (i=0; i < 3 ; i++)
  {
    Magnitude = Magnitude + ( *(Vector + i) )*( *(Vector + i) ) ;
  }

Magnitude = sqrt (Magnitude) ;

if (Magnitude <= 0.0) printf ("The magnitude of the vector is zero.\n") ;

return (Magnitude) ;

}


double InterSectionPIEdgeFluxSurface ( double *Normal, double *PI , double *P , double
*Result)

{

int i ;
double Magnitude = 0.0 , k  ;

k = VectorDotProduct(Normal, PI) - VectorDotProduct (Normal, P) ;
k = k / ((VectorMagnitude (Normal))*(VectorMagnitude (Normal))) ;

for (i = 0 ; i < 3 ; i++)
{

  Result[i] = P[i] + (k * Normal[i]) ;
  Magnitude = Magnitude + (Result[i])*(Result[i]) ;
  printf ("PIEdgeFlux surface intersection[%d] = %lf\n", i, Result[i]) ;

}


return (Magnitude) ;
```

```
}

double VectorDotProduct (double *V1 , double *V2 )

{

int i ;
double Magnitude = 0.0 ;
for (i = 0; i < 3; i++)
  {

    Magnitude = Magnitude + V1[i]*V2[i] ;

  }

return (Magnitude) ;

}

double InterSectionPIFluxSurface ( double *Normal, double *PI , double *P , double
*Result)

{

int i ;
double Magnitude = 0.0 , k  , c ;

c = VectorDotProduct(Normal, P) ;

k = (c - VectorDotProduct(PI, Normal) ) / ( (VectorMagnitude (Normal))*(VectorMagnitude
(Normal)) ) ;

for (i = 0 ; i < 3 ; i++)
{

  Result[i] = PI[i] + (k * Normal[i]) ;
  Magnitude = Magnitude + (Result[i]*Result[i]) ;
  printf ("PIFlux surface intersection[%d] = %lf\n", i, Result[i]) ;

}

return (Magnitude) ;
```

```
}

double InterSectionPIEquipotentials ( double *Normal, double *PI , double *P , double
*Result)

{

int i ;
double Magnitude = 0.0 , k , c  ;

c = VectorDotProduct(Normal, P) ;

k = (c- VectorDotProduct(PI, Normal)) / ( (VectorMagnitude (Normal))*(VectorMagnitude
(Normal)) ) ;

for (i = 0 ; i < 3 ; i++)
{

  Result[i] = PI[i] + (k * Normal[i]) ;
  Magnitude = Magnitude + (Result[i]*Result[i]) ;
  printf ("PIEquipotential surface intersection[%d] = %lf\n", i, Result[i]) ;
}

return (Magnitude) ;

}

double InterSectionOtherEdges ( double Face[][3], double P[][3], double Result[][3]  )

{

int i, j ;
double Magnitude = 0.0 , k  ;
double TempVector[3] ;


for (j=0;j<4;j++)

{

VectorFromTo ( *(P+j), *(P+((j+1)%4)), TempVector) ;

k = VectorDotProduct(TempVector, Face[j]) - VectorDotProduct (TempVector, *(P+j)) ;
```

```
k = k / ((VectorMagnitude (TempVector))*(VectorMagnitude (TempVector))) ;

for (i = 0 , i < 3 , i++)
{

  Result[j][i] = P[j][i] + (k * TempVector[i]) ;
  Magnitude = Magnitude + (Result[j][i])*(Result[j][i]) ;
  printf ("Other Edge intersection[%d] = %lf\n", i, Result[j][i]) ;
}
}

return (Magnitude) ;


}

double ESquared (double PHI1, double PHI2, double *P1, double *P2)

{

double EE, TempVector[3] ;

printf ("Magnitude = %lf.\n", VectorFromTo (P1, P2, TempVector)) ;

EE = (PHI1 - PHI2) / VectorMagnitude (TempVector) ;
EE = 0.5*(EE*EE);
return (EE) ;

}

double DSquared (double Q, double F, double *P1, double *P2, double *PCentre)

{

double DD, TempVector[3][3] ;

VectorFromTo (P1, PCentre, TempVector[0]) ;
VectorFromTo (P2, PCentre, TempVector[1]) ;
VectorCrossProduct (TempVector[0], TempVector[1], TempVector[2]) ;

DD = (F*Q) / ( VectorMagnitude (TempVector[2]) / 2.0 ) ;
DD = 0.5*(DD*DD);
return (DD) ;
```

```
}

/*****************************************************************************
This is the main function of the three dimensional energy calculation
routines.  It calls all of the required functions in order and does all
of then required IO as well.
*****************************************************************************/
#include <stdio.h>
#include <math.h>
#include "threed.h"

extern double VectorFromTo (double *From , double *To, double *Result) ;
extern double VectorCrossProduct (double *V1 , double *V2 , double *Result ) ;
extern double VolumeOfPyramid (double *P , double *Height) ;
extern double VolumeOfTetrahedron (double *Height, double *V1, double *V2 ) ;
extern double VectorMagnitude ( double *Vector ) ;
extern double InterSectionPIEdgeFluxSurface ( double *Normal, double *PI , double *P ,
double *Result);
extern double VectorDotProduct (double *V1 , double *V2 );
extern double InterSectionPIFluxSurface ( double *Normal, double *PI , double *P , double
*Result) ;
extern double InterSectionPIEquipotentials ( double *Normal, double *PI , double *P ,
double *Result);
extern double InterSectionOtherEdges ( double *Face, double *P, double *Result ) ;
extern double ESquared (double PHI1, double PHI2, double *P1, double *P2) ;
extern double DSquared (double Q, double Fraction, double *P1, double *P2, double
*PCentre) ;

RAWCUBOIDDATA RawCuboidData[MAXIMUM_NUMBER_OF_CUBOIDS] ;

void main (void)

{

CALCULATEDCUBOIDDATA CalculatedCuboidData ;
RAWSLICEDATA RawSliceData ;
RAWTUBEDATA RawTubeData ;
CALCULATEDSLICEDATA CalculatedSliceData ;
CALCULATEDTUBEDATA CalculatedTubeData ;
CALCULATEDTUBEVOLUMES CalculatedTubeVolumes ;
CALCULATEDSLICEVOLUMES CalculatedSliceVolumes ;

FILE *GeometryFile, *SliceFile, *TubeFile ;
```

```
int i, j, k, l, loop ;
double Check, TotalVolume = 0.0 ;
double Height[2][3] ;
double TempResult[2][3] ,D0, D1, D2, D3 ;
double EETotal = 0.0 , DDTotal = 0.0 ;
double PyramidBase[4][3] ;

GeometryFile = fopen("Cuboid.dat","r") ;
SliceFile = fopen("slicedat.dat","r") ;
TubeFile = fopen("tubedata.dat","r") ;

for (loop=0;loop<MAXIMUM_NUMBER_OF_CUBOIDS;loop++)
{

fscanf(TubeFile, "%lf", &RawTubeData.TubeFlux) ;
printf ("Total Tube Flux = %lf.\n", RawTubeData.TubeFlux) ;

for(k = 0 ; k < 4 ; k++)
{

fscanf(TubeFile, "%lf", RawTubeData.EdgeTubeFlux+k) ;
printf ("Fraction of Tube Flux = %lf.\n", RawTubeData.EdgeTubeFlux[k]) ;

for(l = 0 ; l < 3 ; l++)
{

fscanf(GeometryFile,"%lf", (RawCuboidData[loop].TopSurfaceCornerPoints[k]+l)) ;

}
}

printf ("Address = %x %x\n", SliceFile, TubeFile) ;
fscanf (SliceFile, "%lf", &RawSliceData.TopSurfacePotential) ;
fscanf (SliceFile, "%lf", &RawSliceData.BottomSurfacePotential) ;
fscanf (SliceFile, "%lf", &RawSliceData.InteriorPotential) ;

printf ("Potential = %lf.\n", RawSliceData.TopSurfacePotential) ;
printf ("Potential = %lf.\n", RawSliceData.BottomSurfacePotential) ;
printf ("Potential = %lf.\n", RawSliceData.InteriorPotential) ;

for(k = 0 ; k < 4 ; k++)

{
```

```
for(l = 0 ; l < 3 ; l++)

{

fscanf(GeometryFile,"%lf", (RawCuboidData[loop].BottomSurfaceCornerPoints[k]+l)) ;

}
}

for(l = 0 ; l < 3 ; l++)

{
fscanf(GeometryFile,"%lf", (RawCuboidData[loop].InternalPoint+l)) ;
}

/* Calculate the edge vectors */

for (i = 0 ; i < 4 ; i++)
{

Check = VectorFromTo(RawCuboidData[loop].TopSurfaceCornerPoints[i],
                RawCuboidData[loop].BottomSurfaceCornerPoints[i],
                CalculatedCuboidData.EdgeVectors[i]) ;

if (Check <= 0.0) printf("Bad Flux Surface Edge Detected.\n") ;

}

printf ("Done edge vectors.\n") ;

/* Calculate the Normal Generator Vectors */

for (i = 0 ; i < 8 ; i+=2)
{

j = i / 2 ;

Check = VectorFromTo(RawCuboidData[loop].TopSurfaceCornerPoints[j],
                RawCuboidData[loop].BottomSurfaceCornerPoints[j],
                CalculatedCuboidData.NormalGeneratorVectors[i]) ;

if (Check <= 0.0) printf("Bad Flux Surface Normal Generator Vector Detected.\n") ;
```

```
Check = VectorFromTo(RawCuboidData[loop].BottomSurfaceCornerPoints[(j+1)%4],
            RawCuboidData[loop].BottomSurfaceCornerPoints[j],
            CalculatedCuboidData.NormalGeneratorVectors[i+1]) ;

if (Check <= 0.0) printf("Bad Flux Surface Normal Generator Vector Detected.\n") ;

}

printf("Done generator vectors.\n") ;

/* Calculate the Flux Surface Normal Vectors */

for (i = 0 ; i < 8 ; i+=2)

{

j = i / 2 ;

Check = VectorCrossProduct(CalculatedCuboidData.NormalGeneratorVectors[i],
                CalculatedCuboidData.NormalGeneratorVectors[i+1],
                CalculatedCuboidData.FluxSurfaceNormalVectors[j]) ;

if (Check <= 0.0) printf("Bad Flux Surface Normal Vector Detected.\n") ;

}

/* Calculate the equipotential surface normal generators */

Check = VectorFromTo(RawCuboidData[loop].TopSurfaceCornerPoints[3],
            RawCuboidData[loop].TopSurfaceCornerPoints[0],
            CalculatedCuboidData.EquiNormalGenerators[0]) ;

if (Check <= 0.0) printf("Bad Equi Generator Detected \n") ;

Check = VectorFromTo(RawCuboidData[loop].TopSurfaceCornerPoints[1],
            RawCuboidData[loop].TopSurfaceCornerPoints[0],
            CalculatedCuboidData.EquiNormalGenerators[1]) ;

if (Check <= 0.0) printf("Bad Equi Generator Detected.\n") ;

Check = VectorFromTo(RawCuboidData[loop].BottomSurfaceCornerPoints[1],
            RawCuboidData[loop].BottomSurfaceCornerPoints[0],
            CalculatedCuboidData.EquiNormalGenerators[2]) ;
```

```
if (Check <= 0.0) printf("Bad Equi Generator Detected.\n") ;

Check = VectorFromTo(RawCuboidData[loop].BottomSurfaceCornerPoints[3],
            RawCuboidData[loop].BottomSurfaceCornerPoints[0],
            CalculatedCuboidData.EquiNormalGenerators[3]) ;

if (Check <= 0.0) printf("Bad Equi Generator Detected.\n") ;

/* Calculate the Equipotential Surface Normal Vectors */

for (i = 0 ; i < 4 ; i+=2)

{
printf ("Now calculating the equipotential surface normals.\n") ;

j = i/2 ;

Check = VectorCrossProduct(CalculatedCuboidData.EquiNormalGenerators[i],
                CalculatedCuboidData.EquiNormalGenerators[i+1],
                CalculatedCuboidData.EquipotentialSurfaceNormalVectors[j]) ;

if (Check <= 0.0) printf("Bad Equipotential Normal Vector Detected.\n") ;

}

/* Calculate the Flux Surface Intersections */

for (i = 0 ; i < 4 ; i++)

{

Check = InterSectionPIFluxSurface ( CalculatedCuboidData.FluxSurfaceNormalVectors[i],
                        RawCuboidData[loop].InternalPoint,
                        RawCuboidData[loop].BottomSurfaceCornerPoints[i],
                        CalculatedCuboidData.FluxSurfaceIntersectionPoints[i]) ;

if (Check <= 0.0) printf("Bad PI Edge Flux Surface Intersection Detected.\n") ;

}

/* Calculate the Equipotential Surface Intersection points */

printf ("Equipotential surface intersection points.\n") ;
```

```
Check = InterSectionPIEquipotentials (
CalculatedCuboidData.EquipotentialSurfaceNormalVectors[0],
                        RawCuboidData[loop].InternalPoint,
                        RawCuboidData[loop].TopSurfaceCornerPoints[0],
                        CalculatedCuboidData.EquipotentialIntersectionPoints[0]) ;

if (Check <= 0.0) printf("Bad PI Edge Flux Surface Intersection Detected.\n") ;

Check = InterSectionPIEquipotentials (
CalculatedCuboidData.EquipotentialSurfaceNormalVectors[1],
                        RawCuboidData[loop].InternalPoint,
                        RawCuboidData[loop].BottomSurfaceCornerPoints[0],
                        CalculatedCuboidData.EquipotentialIntersectionPoints[1]) ;

if (Check <= 0.0) printf("Bad PI Edge Flux Surface Intersection Detected.\n") ;

/* Calculate the PI - Edge Flux Surface Intersection Points */

for (i = 0 ; i < 4 ; i++)

{

Check = InterSectionPIEdgeFluxSurface ( CalculatedCuboidData.EdgeVectors[i],
                        RawCuboidData[loop].InternalPoint,
                        RawCuboidData[loop].BottomSurfaceCornerPoints[i],
                        CalculatedCuboidData.EdgeIntersectionPoints[i]) ;

if (Check <= 0.0) printf("Bad PI Edge Flux Surface Intersection Detected.\n") ;

}

/* Calculate the other edge intersection points */

printf("Top edges.\n") ;

Check = InterSectionOtherEdges (*CalculatedCuboidData.FluxSurfaceIntersectionPoints,
                        RawCuboidData[loop].TopSurfaceCornerPoints[0],
                        *CalculatedCuboidData.OtherEdgeInterSectionPoints) ;

printf("Bottom edges.\n") ;

Check = InterSectionOtherEdges (*CalculatedCuboidData.FluxSurfaceIntersectionPoints,
                        RawCuboidData[loop].BottomSurfaceCornerPoints[0],
```

```
                    *(CalculatedCuboidData.OtherEdgeInterSectionPoints+4)) ;

/********** VOLUME CALCULATIONS **********/

/* Calculate the volume of the top equipotential surface pyramid */

Check = VectorFromTo (RawCuboidData[loop].InternalPoint,
            CalculatedCuboidData.EquipotentialIntersectionPoints[0],
            Height[0]) ;

if (Check <= 0.0) printf("Bad Pyramid Height Detected.\n") ;

Check = VolumeOfPyramid (RawCuboidData[loop].TopSurfaceCornerPoints[0] ,
              Height[0]) ;

if (Check <= 0.0) printf("Bad Pyramid Volume Detected.\n") ;
else
{
  TotalVolume+=Check ;
  CalculatedSliceVolumes.TopEquipotentialSurfacePyramid = Check ;
}

printf("The Volume of the top pyramid is = %lf\n", Check) ;

for (i=0;i<4;i++)
{
  for (j=0;j<3;j++)
  {
    PyramidBase[0][j]=RawCuboidData[loop].TopSurfaceCornerPoints[i][j] ;
    PyramidBase[1][j]=CalculatedCuboidData.OtherEdgeInterSectionPoints[i][j];
    PyramidBase[2][j]=CalculatedCuboidData.EquipotentialIntersectionPoints[0][j];
    PyramidBase[3][j]=CalculatedCuboidData.OtherEdgeInterSectionPoints[((i+3)%4)][j];
  }
Check = VolumeOfPyramid (PyramidBase[0],Height[0]);
printf("Quarter pyramid volume = %lf.\n", Check);
CalculatedTubeVolumes.TopEquipotentialSurfacePyramid[i] = Check ;

}

/* Calculate the volume of the bottom equipotential surface pyramid */

Check = VectorFromTo (RawCuboidData[loop].InternalPoint,
```

```
                CalculatedCuboidData.EquipotentialIntersectionPoints[1],
                Height[1]) ;

if (Check <= 0.0) printf("Bad Pyramid Height Detected.\n") ;

Check = VolumeOfPyramid (RawCuboidData[loop].BottomSurfaceCornerPoints[0] ,
                  Height[1]) ;

if (Check <= 0.0) printf("Bad Pyramid Volume Detected.\n") ;
else
{
  TotalVolume+=Check ;
  CalculatedSliceVolumes.BottomEquipotentialSurfacePyramid = Check ;
}
printf("The Volume of the bottom pyramid is = %lf\n", Check) ;

for (i=0;i<4;i++)
{
  for (j=0;j<3;j++)
  {
    PyramidBase[0][j]=RawCuboidData[loop].BottomSurfaceCornerPoints[i][j] ;
    PyramidBase[1][j]=CalculatedCuboidData.OtherEdgeInterSectionPoints[i+4][j];
    PyramidBase[2][j]=CalculatedCuboidData.EquipotentialIntersectionPoints[1][j];
    PyramidBase[3][j]=CalculatedCuboidData.OtherEdgeInterSectionPoints[((i+3)%4)+4][j];
  }
Check = VolumeOfPyramid (PyramidBase[0],Height[1]);
printf("Quarter pyramid volume = %lf.\n", Check);
CalculatedTubeVolumes.BottomEquipotentialSurfacePyramid[i] = Check ;

}

/* Calculate the volume of the eight flux surface tetrahedrons */

for (i = 0; i<4; i++)
{

Check = VectorFromTo (RawCuboidData[loop].InternalPoint,
                CalculatedCuboidData.FluxSurfaceIntersectionPoints[i],
                Height[0]) ;

if (Check <=0.0) printf("Bad VectorFromTo.\n") ,

Check = VectorFromTo (RawCuboidData[loop].TopSurfaceCornerPoints[i],
```

```
                CalculatedCuboidData.FluxSurfaceIntersectionPoints[i],
                TempResult[0]) ;

if (Check <=0.0) printf("Bad VectorFromTo.\n") ;

Check = VectorFromTo (RawCuboidData[loop].TopSurfaceCornerPoints[(i+1)%4],
                CalculatedCuboidData.FluxSurfaceIntersectionPoints[i],
                TempResult[1]) ;

if (Check <=0.0) printf("Bad VectorFromTo.\n") ;

Check = VolumeOfTetrahedron (Height[0], TempResult[0], TempResult[1] ) ;
CalculatedSliceVolumes.TopFluxSurfaceTetrahedrons[i] = Check ;

TotalVolume+=Check ;

printf("The volume of a flux surface tetrahedron is = %lf\n", Check) ;

Check = VectorFromTo (RawCuboidData[loop].InternalPoint,
                CalculatedCuboidData.FluxSurfaceIntersectionPoints[i],
                Height[1]) ;

if (Check <=0.0) printf("Bad VectorFromTo.\n") ;

Check = VectorFromTo (RawCuboidData[loop].BottomSurfaceCornerPoints[i],
                CalculatedCuboidData.FluxSurfaceIntersectionPoints[i],
                TempResult[0]) ;

if (Check <=0.0) printf("Bad VectorFromTo.\n") ;

Check = VectorFromTo (RawCuboidData[loop].BottomSurfaceCornerPoints[(i+1)%4],
                CalculatedCuboidData.FluxSurfaceIntersectionPoints[i],
                TempResult[1]) ;

if (Check <=0.0) printf("Bad VectorFromTo.\n") ;

Check = VolumeOfTetrahedron (Height[1], TempResult[0], TempResult[1] ) ;
CalculatedSliceVolumes.BottomFluxSurfaceTetrahedrons[i] = Check ;

TotalVolume+=Check ;

printf("The volume of a flux surface tetrahedron is = %lf\n", Check) ;
```

```
}

for (i=0;i<4;i++) CalculatedSliceVolumes.TopEdgePyramids[i]=0.0 ;
for (i=0;i<4;i++) CalculatedSliceVolumes.BottomEdgePyramids[i]=0.0 ;

/* Calculate the volume of the eight edge pyramids (sixteen tetrahedrons)*/
for (i = 0; i<4; i++)
{

Check = VectorFromTo (RawCuboidData[loop].TopSurfaceCornerPoints[i],
            CalculatedCuboidData.EdgeIntersectionPoints[i],
            Height[0]) ;

Check = VectorFromTo (CalculatedCuboidData.EdgeIntersectionPoints[i],
            CalculatedCuboidData.FluxSurfaceIntersectionPoints[i],
            TempResult[0]) ;

Check = VectorFromTo (RawCuboidData[loop].InternalPoint,
            CalculatedCuboidData.FluxSurfaceIntersectionPoints[i],
            TempResult[1]) ;

Check = VolumeOfTetrahedron (Height[0], TempResult[0], TempResult[1] ) ;
CalculatedSliceVolumes.TopEdgePyramids[i] += Check ;
TotalVolume+=Check ;
printf("The volume of an edge tetrahedron is = %lf\n", Check) ;

Check = VectorFromTo (RawCuboidData[loop].TopSurfaceCornerPoints[(i+1)%4],
            CalculatedCuboidData.EdgeIntersectionPoints[(i+1)%4],
            Height[1]) ;

Check = VectorFromTo (CalculatedCuboidData.EdgeIntersectionPoints[(i+1)%4],
            CalculatedCuboidData.FluxSurfaceIntersectionPoints[i],
            TempResult[0]) ;

Check = VectorFromTo (RawCuboidData[loop].InternalPoint,
            CalculatedCuboidData.FluxSurfaceIntersectionPoints[i],
            TempResult[1]) ;

Check = VolumeOfTetrahedron (Height[1], TempResult[0], TempResult[1] ) ;
CalculatedSliceVolumes.TopEdgePyramids[(i+1)%4] += Check ;
TotalVolume+=Check ;
printf("The volume of an edge tetrahedron is = %lf\n", Check) ;
```

```
Check = VectorFromTo (RawCuboidData[loop].BottomSurfaceCornerPoints[i],
                CalculatedCuboidData.EdgeIntersectionPoints[i],
                Height[0]) ;

Check = VectorFromTo (CalculatedCuboidData.EdgeIntersectionPoints[i],
                CalculatedCuboidData.FluxSurfaceIntersectionPoints[i],
                TempResult[0]) ;

Check = VectorFromTo (RawCuboidData[loop].InternalPoint,
                CalculatedCuboidData.FluxSurfaceIntersectionPoints[i],
                TempResult[1]) ;

Check = VolumeOfTetrahedron (Height[0], TempResult[0], TempResult[1] ) ;
CalculatedSliceVolumes.BottomEdgePyramids[i] += Check ;
TotalVolume+=Check ;
printf("The volume of an edge tetrahedron is = %lf\n", Check) ;

Check = VectorFromTo (RawCuboidData[loop].BottomSurfaceCornerPoints[(i+1)%4],
                CalculatedCuboidData.EdgeIntersectionPoints[(i+1)%4],
                Height[1]) ;

Check = VectorFromTo (CalculatedCuboidData.EdgeIntersectionPoints[(i+1)%4],
                CalculatedCuboidData.FluxSurfaceIntersectionPoints[i],
                TempResult[0]) ;

Check = VectorFromTo (RawCuboidData[loop].InternalPoint,
                CalculatedCuboidData.FluxSurfaceIntersectionPoints[i],
                TempResult[1]) ;

Check = VolumeOfTetrahedron (Height[1], TempResult[0], TempResult[1] ) ;
CalculatedSliceVolumes.BottomEdgePyramids[(i+1)%4] += Check ;
TotalVolume+=Check ;
printf("The volume of an edge tetrahedron is = %lf\n", Check) ;

/* Start the 16 flux surface tetrahedrons */
/* Volumes are stored as [FACE][TOP/BOTTOM][SIDE OF FACE] */

Check = VectorFromTo (RawCuboidData[loop].InternalPoint,
                CalculatedCuboidData.FluxSurfaceIntersectionPoints[i],
                Height[0]) ;

Check = VectorFromTo (CalculatedCuboidData.OtherEdgeInterSectionPoints[i],
                CalculatedCuboidData.FluxSurfaceIntersectionPoints[i],
```

```
                TempResult[0]) ;

Check = VectorFromTo (RawCuboidData[loop].TopSurfaceCornerPoints[i],
                CalculatedCuboidData.FluxSurfaceIntersectionPoints[i],
                TempResult[1]) ;

Check = VolumeOfTetrahedron (Height[0], TempResult[0], TempResult[1] ) ;
printf("The volume of half surface tetrahedron is = %lf\n", Check) ;
CalculatedTubeVolumes.SurfaceTetrahedrons[i][0][0]=Check ;

Check = VectorFromTo (RawCuboidData[loop].InternalPoint,
                CalculatedCuboidData.FluxSurfaceIntersectionPoints[i],
                Height[0]) ;

Check = VectorFromTo (CalculatedCuboidData.OtherEdgeInterSectionPoints[i],
                CalculatedCuboidData.FluxSurfaceIntersectionPoints[i],
                TempResult[0]) ;

Check = VectorFromTo (RawCuboidData[loop].TopSurfaceCornerPoints[(i+1)%4],
                CalculatedCuboidData.FluxSurfaceIntersectionPoints[i],
                TempResult[1]) ;

Check = VolumeOfTetrahedron (Height[0], TempResult[0], TempResult[1] ) ;
printf("The volume of half surface tetrahedron is = %lf\n", Check) ;
CalculatedTubeVolumes.SurfaceTetrahedrons[i][0][1]=Check ;

/* Do the bottom ones */
Check = VectorFromTo (RawCuboidData[loop].InternalPoint,
                CalculatedCuboidData.FluxSurfaceIntersectionPoints[i],
                Height[1]) ;

Check = VectorFromTo (CalculatedCuboidData.OtherEdgeInterSectionPoints[i+4],
                CalculatedCuboidData.FluxSurfaceIntersectionPoints[i],
                TempResult[0]) ;

Check = VectorFromTo (RawCuboidData[loop].BottomSurfaceCornerPoints[i],
                CalculatedCuboidData.FluxSurfaceIntersectionPoints[i],
                TempResult[1]) ;

Check = VolumeOfTetrahedron (Height[1], TempResult[0], TempResult[1] ) ;
printf("The volume of half surface tetrahedron is = %lf\n", Check) ;
CalculatedTubeVolumes.SurfaceTetrahedrons[i][1][0]=Check ;
```

```
Check = VectorFromTo (RawCuboidData[loop].InternalPoint,
                CalculatedCuboidData.FluxSurfaceIntersectionPoints[i],
                Height[1]) ;

Check = VectorFromTo (CalculatedCuboidData.OtherEdgeInterSectionPoints[i+4],
                CalculatedCuboidData.FluxSurfaceIntersectionPoints[i],
                TempResult[0]) ;

Check = VectorFromTo (RawCuboidData[loop].BottomSurfaceCornerPoints[(i+1)%4],
                CalculatedCuboidData.FluxSurfaceIntersectionPoints[i],
                TempResult[1]) ;

Check = VolumeOfTetrahedron (Height[1], TempResult[0], TempResult[1] ) ;
printf("The volume of half surface tetrahedron is = %lf\n", Check) ;
CalculatedTubeVolumes.SurfaceTetrahedrons[i][1][1]=Check ;

}

for (i=0;i<4;i++) {
CalculatedTubeVolumes.TopEdgePyramids[i]      =
CalculatedSliceVolumes.TopEdgePyramids[i] ;
CalculatedTubeVolumes.BottomEdgePyramids[i]      =
CalculatedSliceVolumes.BottomEdgePyramids[i] ;
    }

printf("The Total Volume is = %lf\n", TotalVolume) ;

/************** FIELD CALCULATIONS ***************/

/* Calculate the Electric field strength.

There are the following structures to consider here :

- the top pyramid
- the bottom pyramid
- the 4 edge pyramids on the top
- the 4 edge pyramids on the bottom
- the 4 tetrahedrons on the top
- the 4 tetrahedrons on the bottom

In all there are 18 field strengths but 14 direction vectors to compute.

*/
```

```
/* Top pyramid */
Check = ESquared (RawSliceData.TopSurfacePotential,
            RawSliceData.InteriorPotential,
            CalculatedCuboidData.EquipotentialIntersectionPoints[0],
            RawCuboidData[loop].InternalPoint) ;
printf ("EE = %lf.\n", Check) ;
EETotal += Check*CalculatedSliceVolumes.TopEquipotentialSurfacePyramid ;

/* Bottom pyramid */
Check = ESquared (RawSliceData.BottomSurfacePotential,
            RawSliceData.InteriorPotential,
            CalculatedCuboidData.EquipotentialIntersectionPoints[1],
            RawCuboidData[loop].InternalPoint) ;
printf ("EE = %lf.\n", Check) ;
EETotal += Check*CalculatedSliceVolumes.BottomEquipotentialSurfacePyramid ;

for (l=0;l<4;l++)
{
/* Do four top edge pyramids */
Check = ESquared (RawSliceData.TopSurfacePotential,
            RawSliceData.InteriorPotential,
            RawCuboidData[loop].TopSurfaceCornerPoints[l],
            CalculatedCuboidData.EdgeIntersectionPoints[l]) ;

printf ("EE = %lf.\n", Check) ;
EETotal += Check*CalculatedSliceVolumes.TopEdgePyramids[l] ;

/* Break up top pyramid into 4 regions for D calculations*/
Check = DSquared (RawTubeData.TubeFlux,
            RawTubeData.EdgeTubeFlux[l],
            CalculatedCuboidData.OtherEdgeInterSectionPoints[(l+3)%4],
            RawCuboidData[loop].TopSurfaceCornerPoints[l],
            CalculatedCuboidData.OtherEdgeInterSectionPoints[(l+1)%4]) ;

printf ("DD = %lf.\n", Check) ;
DDTotal += Check*CalculatedTubeVolumes.TopEquipotentialSurfacePyramid[l] ;

/* Do four edge pyramids */
Check = DSquared (RawTubeData.TubeFlux,
            RawTubeData.EdgeTubeFlux[l],
            CalculatedCuboidData.FluxSurfaceIntersectionPoints[(l+3)%4],
            CalculatedCuboidData.EdgeIntersectionPoints[l],
            CalculatedCuboidData.FluxSurfaceIntersectionPoints[(l+1)%4]) ;
```

```
printf ("DD = %lf.\n", Check) ;
DDTotal+=Check*(CalculatedTubeVolumes.TopEdgePyramids[l]
        +CalculatedTubeVolumes.BottomEdgePyramids[l]);

/* Now apply continuity of normal D to get 4 more values for surface tetrahedrons */
VectorFromTo (CalculatedCuboidData.OtherEdgeInterSectionPoints[l],
        CalculatedCuboidData.FluxSurfaceIntersectionPoints[l],
        TempResult[0]) ;

D0 = Check * (VectorDotProduct (TempResult[0], CalculatedCuboidData.EdgeVectors[l]))
/(      (VectorMagnitude      (TempResult[0]))      *      VectorMagnitude
(CalculatedCuboidData.EdgeVectors[l]) ) ;

printf ("D0 = %lf.\n", D0) ;
D0=labs(D0);
DDTotal += D0*CalculatedTubeVolumes.SurfaceTetrahedrons[l][0][0];

VectorFromTo (CalculatedCuboidData.OtherEdgeInterSectionPoints[(l+3)%4],
        CalculatedCuboidData.FluxSurfaceIntersectionPoints[(l+3)%4],
        TempResult[0]) ;

D1 = Check * (VectorDotProduct (TempResult[0], CalculatedCuboidData.EdgeVectors[l]))
/(      (VectorMagnitude      (TempResult[0]))      *      VectorMagnitude
(CalculatedCuboidData.EdgeVectors[l]) ) ;

printf ("D1 = %lf.\n", D1) ;
D1=labs(D1);
DDTotal += D1*CalculatedTubeVolumes.SurfaceTetrahedrons[(l+3)%4][0][1] ;

VectorFromTo (CalculatedCuboidData.OtherEdgeInterSectionPoints[l+4],
        CalculatedCuboidData.FluxSurfaceIntersectionPoints[l],
        TempResult[0]) ;

D2 = Check * (VectorDotProduct (TempResult[0], CalculatedCuboidData.EdgeVectors[l]))
/(      (VectorMagnitude      (TempResult[0]))      *      VectorMagnitude
(CalculatedCuboidData.EdgeVectors[l]) ) ;

printf ("D2 = %lf.\n", D2) ;
D2=labs(D2);
DDTotal += D2*CalculatedTubeVolumes.SurfaceTetrahedrons[l][1][0] ;

VectorFromTo (CalculatedCuboidData.OtherEdgeInterSectionPoints[((l+3)%4)+4],
        CalculatedCuboidData.FluxSurfaceIntersectionPoints[(l+3)%4],
```

```
        TempResult[0]) ;

D3 = Check * (VectorDotProduct (TempResult[0], CalculatedCuboidData.EdgeVectors[l]))
/(      (VectorMagnitude      (TempResult[0]))      *      VectorMagnitude
(CalculatedCuboidData.EdgeVectors[l]) ) ;

printf ("D3 = %lf.\n", D3) ;
D3=labs(D3);
DDTotal += D3*CalculatedTubeVolumes.SurfaceTetrahedrons[(l+3)%4][1][1] ;

/* Break up bottom pyramid into 4 regions for D calculations*/
Check = DSquared (RawTubeData.TubeFlux,
            RawTubeData.EdgeTubeFlux[l],
            CalculatedCuboidData.OtherEdgeInterSectionPoints[((l+3)%4)+4],
            RawCuboidData[loop].BottomSurfaceCornerPoints[l],
            CalculatedCuboidData.OtherEdgeInterSectionPoints[((l+1)%4)+4]) ;

printf ("DD = %lf.\n", Check) ;
DDTotal += Check*CalculatedTubeVolumes.BottomEquipotentialSurfacePyramid[l] ;

/* Four lower edge pyramids */
Check = ESquared (RawSliceData.BottomSurfacePotential,
            RawSliceData.InteriorPotential,
            RawCuboidData[loop].BottomSurfaceCornerPoints[l],
            CalculatedCuboidData.EdgeIntersectionPoints[l]) ;

printf ("EE = %lf.\n", Check) ;
EETotal += Check*CalculatedSliceVolumes.BottomEdgePyramids[l] ;

/* Top Surface tetrahedrons */
Check = ESquared (RawSliceData.TopSurfacePotential,
            RawSliceData.InteriorPotential,
            CalculatedCuboidData.OtherEdgeInterSectionPoints[l],
            CalculatedCuboidData.FluxSurfaceIntersectionPoints[l]) ;

printf ("EE = %lf.\n", Check) ;
EETotal += Check*CalculatedSliceVolumes.TopFluxSurfaceTetrahedrons[l] ;

/* Bottom Surface tetrahedrons */
Check = ESquared (RawSliceData.BottomSurfacePotential,
            RawSliceData.InteriorPotential,
            CalculatedCuboidData.OtherEdgeInterSectionPoints[l+4],
            CalculatedCuboidData.FluxSurfaceIntersectionPoints[l]) ;
```

```
printf ("EE = %lf.\n", Check) ;
EETotal += Check*CalculatedSliceVolumes.BottomFluxSurfaceTetrahedrons[l] ;

}


/* Calculate the Electric flux density.

In all there are 22 field strengths but 14 direction vectors to compute.

*/

/* Calcualte the stored energy in the pyramid */

/* Calcualte the stored energy in the pyramid */

/* Calcualte the stored energy in the tetrahedron */

}

fclose (GeometryFile) ;
fclose (SliceFile) ;
fclose (TubeFile) ;

printf("EETotal = %lf\nDDTotal = %lf\nDONE !!!!!\n", EETotal, DDTotal);
return ;

}

#define MAXIMUM_NUMBER_OF_CUBOIDS 1


typedef struct tagRAWCUBOIDDATA {

double TopSurfaceCornerPoints[4][3] ;
double BottomSurfaceCornerPoints[4][3] ;
double InternalPoint[3] ;

} RAWCUBOIDDATA ;

typedef struct tagRAWSLICEDATA {

double TopSurfacePotential ;
```

```
double BottomSurfacePotential ;
double InteriorPotential ;

} RAWSLICEDATA ;

typedef struct tagRAWTUBEDATA {

double TubeFlux ;
double EdgeTubeFlux[4] ;

} RAWTUBEDATA ;


typedef struct tagCALCULATEDCUBOIDDATA {

double EdgeVectors[4][3] ;

double NormalGeneratorVectors[8][3] ;

double FluxSurfaceNormalVectors[4][3] ;

double EquiNormalGenerators[4][3] ;

double EquipotentialSurfaceNormalVectors[2][3] ;

double FluxSurfaceIntersectionPoints[4][3] ;

double EquipotentialIntersectionPoints[2][3] ;

double EdgeIntersectionPoints[4][3] ;

double OtherEdgeInterSectionPoints[8][3] ;

} CALCULATEDCUBOIDDATA ;

typedef struct tagCALCULATEDSLICEDATA {

double EquiSurfacePyramidEField[2] ;
double FluxSurfaceTetrahedronEField[8] ;
double EdgeIntersectionPyramidEField[8] ;

} CALCULATEDSLICEDATA ;
```

```
typedef struct tagCALCULATEDTUBEDATA {

double EquiSurfacePyramidDField[2] ;
double FluxSurfaceTetrahedronDField[8] ;
double EdgeIntersectionPyramidDField[8] ;

} CALCULATEDTUBEDATA ;

typedef struct tagCALCULATEDSLICEVOLUMES {

double TopEquipotentialSurfacePyramid ;
double BottomEquipotentialSurfacePyramid ;
double TopEdgePyramids[4] ;
double BottomEdgePyramids[4] ;
double TopFluxSurfaceTetrahedrons[4] ;
double BottomFluxSurfaceTetrahedrons[4] ;

} CALCULATEDSLICEVOLUMES ;

typedef struct tagCALCULATEDTUBEVOLUMES {

double TopEquipotentialSurfacePyramid[4] ;
double BottomEquipotentialSurfacePyramid[4] ;
double TopEdgePyramids[4] ;
double BottomEdgePyramids[4] ;
double SurfaceTetrahedrons[4][2][2] ;

} CALCULATEDTUBEVOLUMES ;
```

APPENDIX C

MESH SCRIPT FILE (INPUT TO MESH2D)

```
para
y
1.0E-10 20 1.0E-04
n
dele ELMM
stat ROTO
copy ELMM
rota blin 5.0
join MMST blin
fini
```

PROBLEM SCRIPT FILE (INPUT TO PROB2D)

```
n
n
new
ELMM
y
y
n
y
scal real line cart vert soft
n
n
n
prob p1
Conditions for direct axis capacitance.
para
n
n
y
n
y
0.1 0.1
n
n
auto
kcon
1
```

```
150.0
2
0.0
3
-75.0
4
0.0
5
-75.0
6
0.0
a
150.0
b
0.0
c
-75.0
d
0.0
e
-75.0
f
0.0
r
0.0
quit
kelm
a
DAIR 0.0 TOTA
quit
sequ
1 p1 (p1)
none
fini
```